

LASER SURFACE ALLOYING OF CHROMIUM AND NICKEL  
ON IRON AND CARBON STEELS

Palaniappa Amutha Molian

B.Sc., University of Madras, Madras, India, 1972

B.E., Indian Institute of Science, Bangalore, India, 1975

M.E., Indian Institute of Science, Bangalore, India, 1977

A dissertation submitted to the faculty  
of the Oregon Graduate Center  
in partial fulfillment of the  
requirements for the degree  
Doctor of Philosophy  
in  
Materials Science and Engineering

March, 1982

The dissertation "Laser Surface Alloying of Chromium and Nickel on Iron and Carbon Steels" by Palaniappa Amutha Molian has been examined and approved by the following Examination Committee:

---

William E. Wood, Thesis Advisor  
Professor

---

Jack H. Devletian  
Associate Professor

---

Lawrence E. Murr  
Professor  
Vice President for Academic Affairs  
and Research

---

Richard A. Elliott  
Associate Professor

ACKNOWLEDGEMENTS

Supported by the U.S. Army Research Office

## TABLE OF CONTENTS

Title Page . . . . .	i
Approval Page . . . . .	ii
Acknowledgement . . . . .	iii
Table of Contents . . . . .	iv
List of Tables . . . . .	vi
List of Figures . . . . .	vii
Abstract . . . . .	xiv
1. INTRODUCTION . . . . .	1
2. REVIEW OF LITERATURE . . . . .	4
2.1. Process Variables . . . . .	5
2.2. Solidification and Solid State Transformations . . . . .	7
3. EXPERIMENTAL PROCEDURE . . . . .	11
3.1. Materials . . . . .	11
3.2. Electrodeposition . . . . .	11
3.3. Laser . . . . .	11
3.4. Measurement of Laser Beam Parameters . . . . .	12
3.5. Cooling Rate Determinations . . . . .	13
3.6. Compositional Analysis . . . . .	13
3.7. Microscopy . . . . .	14
3.7.1. Optical Metallography . . . . .	14
3.7.2. Transmission Electron Microscopy . . . . .	14
3.7.3. Scanning Electron Microscopy . . . . .	15
3.8. Microhardness . . . . .	15
4. RESULTS AND DISCUSSION . . . . .	16
4.1. Optimization of Process Variables . . . . .	16
4.1.1. Effects of Laser Beam Parameters . . . . .	17
4.1.2. Optimization of Coating Variables . . . . .	19
4.2. Fusion Zone Defects Characterization . . . . .	22

4.2.1.	Porosity . . . . .	22
4.2.2.	Nonuniform Composition of the Fusion Zone . . . . .	24
4.2.3.	Cracking . . . . .	28
4.3.	Solidification Studies of Laser Processed Fe-C-Cr Alloys	30
4.3.1.	Heat Flow Models . . . . .	30
4.3.2.	Solidification Structures . . . . .	32
4.3.3.	Composition Studies of Laser Alloyed Fusion Zones . . . . .	33
4.4.	Solid State Transformation Structures . . . . .	34
4.4.1.	Fe-Cr System . . . . .	34
4.4.2.	Fe-Ni and Fe-Cr-Ni Systems . . . . .	39
4.4.3.	Fe-0.2%C-Cr System . . . . .	41
4.4.4.	Fe-0.5%C-Cr System . . . . .	51
4.4.5.	Fe-1.0%C-Cr System . . . . .	55
4.4.6.	General Discussion/Summary of Solid State Trans- formation Structures . . . . .	60
5.	CONCLUSIONS . . . . .	64
	REFERENCES . . . . .	65
	Tables I-V . . . . .	71
	Figures 1-106 . . . . .	76
	VITA . . . . .	186

## LIST OF TABLES

I.	Chemical Compositions of Materials . . . . .	71
II.	Electroplating Conditions . . . . .	72
III.	CO <sub>2</sub> Gas Transport Laser Specifications . . . . .	73
IV.	Beam Size Determination . . . . .	74
V.	Laser Operating Parameters . . . . .	75

## LIST OF FIGURES

1.	A Schematic of Laser Surface Alloying Process . . . . .	76
2.	The CO <sub>2</sub> Gas Transport Laser . . . . .	77
3.	Surface Appearances of Laser Alloyed Specimens . . . . .	78
4.	Scanning Electron Micrographs Showing the Transverse Section of Chromium Coating on an Iron Substrate and a Laser Alloyed Fusion Zone . . . . .	79
5.	Effect of Laser Power on Melt Penetration of Fe-Cr Alloys .	80
6.	Effect of Laser Power on Melt Width of Fe-Cr Alloys . . . .	81
7.	Scanning Electron Micrographs Showing the Variation of Fusion Zone Size with Laser Power at 900-1200 Watts . . . .	82
8.	Effect of Focal Position on Melt Penetration of Fe-Cr Alloys	83
9.	Effect of Focal Position on Melt Width of Fe-Cr Alloys . .	84
10.	Scanning Electron Micrographs Showing the Effect of Focusing on Fusion Zone Geometry . . . . .	85
11.	Effect of Scan Rate on Melt Penetration of Fe-Cr Alloys . .	86
12.	Effect of Scan Rate on Melt Width of Fe-Cr Alloys . . . . .	87
13.	Scanning Electron Micrographs of the Transverse Sections of Electrodeposited Coatings . . . . .	88
14.	Effect of Coating Composition on Melt Penetration of Fe-Cr, Fe-Ni and Fe-Cr-Ni Alloys for Various Laser Powers . . . .	89
15.	Effect of Coating Composition on Melt Penetration of Fe-Cr, Fe-Ni and Fe-Cr-Ni Alloys for Various Focal Positions . . .	90
16.	Effect of Coating Composition on Melt Penetration of Fe-Cr, Fe-Ni and Fe-Cr-Ni Alloys for Different Scan Rates . . . .	91
17.	Scanning Electron Micrographs Showing the Electrodeposited Coating Morphologies . . . . .	92
18.	Thermal Properties of Alloying Elements . . . . .	93
19.	Effect of Coating Morphology on Melt Penetration of Fe-Cr Alloys . . . . .	94

20.	Effect of Coating Morphology on Melt Width of Fe-Cr Alloys	95
21.	Scanning Electron Micrographs Showing the Coating Morphologies and the Transverse Sections of Fusion Zones . . . . .	96
22.	Scanning Electron Micrographs Showing the Coating Morphologies and the Transverse Sections of Fusion Zones . . . . .	97
23.	Effect of Chromium Coating Thickness on Melt Penetration of Fe-Cr Alloys . . . . .	98
24.	Effect of Chromium Coating Thickness on Melt Width of Fe-Cr Alloys . . . . .	99
25.	Scanning Electron Micrographs Showing the Effect of Trapped Hydrogen on the Laser Alloyed Surfaces Before and After Degassing . . . . .	100
26.	Optical and Scanning Electron Micrographs Showing the Effect of Trapped Hydrogen on Porosity of Laser Alloyed Surfaces as a Function of Scan Rate . . . . .	101
27.	Optical and Scanning Electron Micrographs Showing the Effect of Trapped Hydrogen on Porosity of Laser Alloyed Surfaces as a Function of Coating Thickness . . . . .	104
28.	Optical Micrograph Showing the "Keyhole" Porosity in Deep Penetration Fusion Zones . . . . .	107
29.	Effect of Fusion Zone Shape on the Composition Uniformity of Fusion Zone . . . . .	108
30.	Scanning Electron Micrographs Showing the Effect of Fusion Zone Size and Shape on the Crack Susceptibility of Fe-1.0% C-Cr Alloys . . . . .	109
31.	Scanning Electron Micrographs Showing the Effect of Fusion Zone Size on the Crack Susceptibility of Fe-1.0%C-Cr Alloys	110
32.	Scanning Electron Micrographs Showing the Heat Affected Zone Cracks and Cracks in the Coating Adjacent to the Melt Pass . . . . .	111
33.	Scanning Electron Micrographs Showing the Semicircular Fusion Zones . . . . .	112
34.	Effect of Scan Rate on Melt Penetration of Fe-Cr Alloys as Predicted by a One-Dimensional Heat Transfer Model . . .	113

35.	Scanning Electron Micrographs Showing the Triangular Fusion Zones . . . . .	114
36.	Effect of Scan Rate on Melt Penetration of Fe-Cr Alloys as Predicted by a Three-Dimensional Heat Transfer Model . . .	115
37.	Scanning Electron Micrographs Showing the Hour-Glass Fusion Zones . . . . .	116
38.	Effect of Scan Rate on Melt Penetration of Fe-Cr Alloys as Predicted by a Three-Dimensional Heat Transfer Model . . .	117
39.	Scanning Electron Micrographs Showing the Solidification Structures of Fe-1.0%C-Cr Alloys with Penetration Depths from 1150-1500 $\mu$ m . . . . .	118
40.	Scanning Electron Micrographs Showing the Solidification Structures of Fe-1.0%C-Cr Alloys with Penetration Depths from 700-1000 $\mu$ m . . . . .	119
41.	Effect of Penetration Depth on the Cell Spacing of Solidification Structures of Fe-C-Cr Alloys . . . . .	120
42.	Effect of Penetration Depth on the Cell Spacing of Solidification Structures of Fe-C-Cr Alloys . . . . .	121
43.	Effect of Penetration Depth on the Solidification Cooling Rates as Predicted by Heat Transfer Models and Solidification Structures . . . . .	122
44.	Effect of Coating Thickness and Fusion Zone Cross Sectional Area on the Alloy Content of Fusion Zone . . . . .	123
45.	The Fe-Cr Phase Diagram . . . . .	124
46.	Light Micrographs of Laser Processed Fe-Cr Alloys Showing the Massive Ferrite Structures . . . . .	125
47.	Effect of Quench Rate on the Transformation Temperature and Structure of Fe-10%Cr Alloy . . . . .	126
48.	A TTT Diagram for Fe-10%Cr Alloy . . . . .	127
49.	Light Micrograph of a Fe-Cr Alloy Showing The Variation in the Morphology of Ferrite from the Bottom to the Top Surface of Fusion Zone as a Function of Chromium Content . . .	128
50.	Light Micrographs of Laser Processed Fe-Cr Alloys Showing the Equiaxed Ferritic Structures . . . . .	129

51.	The Longitudinal and Transverse Sections of "Multiple Scan" Laser Alloyed Surfaces . . . . .	130
52.	Transmission Electron Micrographs of Laser Processed Fe-Cr Alloys Showing the Ferritic Structures 5-50% Cr . . . . .	131
53.	Transmission Electron Micrographs of Laser Processed Fe-Cr Alloys Showing the Ferritic Structures . . . . .	132
54.	Transmission Electron Micrographs of Laser Processed Fe-10% Cr Alloy . . . . .	133
55.	Transmission Electron Micrographs of Laser Processed Fe-10% Cr Alloy . . . . .	134
56.	Effect of Composition and Cooling Rate on the Microhardness of Fe-Cr Alloys . . . . .	135
57.	The Fe-Ni Equilibrium Diagram . . . . .	136
58.	Light Micrographs of Laser Processed Fe-Ni Alloys . . . . .	137
59.	Light Micrographs of Laser Processed Fe-Ni Alloys . . . . .	138
60.	Light Micrographs of Laser Processed Fe-Cr-Ni Alloys . . . . .	139
61.	Light Micrographs of Laser Processed Fe-Cr-Ni Alloys . . . . .	140
62.	Transmission Electron Micrographs of Laser Processed Fe-5%Ni Alloy . . . . .	141
63.	Transmission Electron Micrographs of Laser Processed Fe-6%Cr-2%Ni Alloy . . . . .	142
64.	Effect of Quench Rate on the Transformation Temperature and Structure of Fe-5%Ni Alloy . . . . .	143
65.	Effect of Quench Rate on the Transformation Temperature and Structure of Fe-5%Ni Alloy . . . . .	144
66.	The Fe-0.2%C-Cr Phase Diagram . . . . .	145
67.	Light Micrographs of Laser Processed Fe-0.2%C-Cr Alloys . . . . .	146
68.	Light Micrographs of Laser Processed Fe-0.2%C-Cr Alloys . . . . .	147
69.	Light Micrographs of Laser Processed Fe-0.2%C-Cr Alloys . . . . .	148
70.	Light Micrographs of Laser Processed Fe-0.2%C-Cr Alloys . . . . .	149

71.	Transmission Electron Micrography of Laser Processed Fe-0.2%C-5%Cr Alloy Showing the Lath Martensitic Structures .	150
72.	Transmission Electron Micrographs of Laser Processed Fe-0.2%C-5%Cr Alloy Showing the Lath Martensitic Structures .	151
73.	Transmission Electron Micrographs of Laser Processed Fe-0.2%C-5%Cr Alloy Showing the Lath Martensitic Structures .	152
74.	Transmission Electron Micrographs of Laser Processed Fe-0.2%C-10%Cr Alloy Showing the Lath Martensitic Structures .	153
75.	Transmission Electron Micrographs of Laser Processed Fe-0.2%C-10%Cr Alloy Showing the Lath Martensitic Structures .	154
76.	Transmission Electron Micrographs of Laser Processed Fe-0.2%C-10%Cr Alloy Showing the Lath Martensitic Structures .	155
77.	Transmission Electron Micrographs of Laser Processed Fe-0.2%C-5%Cr Alloy . . . . .	156
78.	Transmission Electron Micrographs of Laser Processed Fe-0.2%C-5%Cr Alloy . . . . .	157
79.	Transmission Electron Micrographs of Laser Processed Fe-0.2%C-10%Cr Alloy . . . . .	158
80.	Transmission Electron Micrographs of Laser Processed Fe-0.2%C-5%Cr Alloy . . . . .	159
81.	Effect of Cooling Rate on the Microhardness of Fe-0.2%C-Cr Alloys . . . . .	160
82.	Scanning Electron Micrographs Showing the Transverse Sections of Fusion Zones Containing 20%Cr . . . . .	161
83.	Scanning Electron Micrographs Showing the Microstructures of Laser Processed Fe-0.2%C-20%Cr Alloys . . . . .	162
84.	Transmission Electron Micrographs of Laser Processed Fe-0.2%C-20%Cr Alloy Showing the Austenitic Needles in a Ferritic Matrix . . . . .	163
85.	Transmission Electron Micrographs of Laser Processed Fe-0.2%C-20%Cr Alloy . . . . .	164
86.	Transmission Electron Micrographs of Laser Processed Fe-0.2%C-20%Cr Alloy . . . . .	165

87.	Transmission Electron Micrographs of Laser Processed Fe-0.2%C-20%Cr Alloy . . . . .	166
88.	Transmission Electron Micrographs of Laser Processed Fe-0.2%C-20%Cr Alloy . . . . .	167
89.	Light Micrographs of Conventionally Furnace Heat Treated and Water Quenched "Single Scan" Fe-0.2%C-20%Cr Alloys . . .	168
90.	Transmission Electron Micrographs of Laser Processed Fe-0.2%C-30%Cr Alloy Showing the Ferritic Structures . . . . .	169
91.	Transmission Electron Micrographs of Laser Processed Fe-0.2%C-30%Cr Alloy . . . . .	170
92.	Scanning Electron Micrographs of Laser Processed Fe-0.5%C-Cr Alloys . . . . .	171
93.	Transmission Electron Micrographs of Laser Processed Fe-0.5%C-10%Cr Alloy Showing the Lath Martensitic Structures .	172
94.	Transmission Electron Micrographs of Laser Processed Fe-0.5%C-10%Cr Alloy . . . . .	173
95.	Transmission Electron Micrographs of Laser Processed Fe-0.5%C-20%Cr Alloy Showing the Austenite/Ferrite Structures	174
96.	Transmission Electron Micrographs of Laser Processed Fe-0.5%C-20%Cr Alloy . . . . .	175
97.	Transmission Electron Micrographs of Laser Processed Fe-0.5%C-40%Cr Alloy Showing the Ferritic Structures . . . . .	176
98.	Transmission Electron Micrographs of Laser Processed Fe-0.5%C-40%Cr Alloy . . . . .	177
99.	Scanning Electron Micrographs of Laser Processed Fe-1.0%C-Cr Alloys . . . . .	178
100.	Transmission Electron Micrographs of Laser Processed Fe-1.0%C-10%Cr Alloy Showing the Plate Martensitic Structures	179
101.	Transmission Electron Micrographs of Laser Processed Fe-1.0%C-10%Cr Alloy Showing the Twinned Plate Martensites and Dislocated Lath Martensites . . . . .	180
102.	Transmission Electron Micrographs of Laser Processed Fe-1.0%C-20%Cr Alloy Showing the Austenitic Structures Containing a High Density of Lattice Defects . . . . .	181

103.	Transmission Electron Micrographs of Laser Processed Fe-1.0%C-20%Cr Alloy . . . . .	182
104.	Transmission Electron Micrographs of Laser Processed Fe-1.0%C-40%Cr Alloy Showing the Ferritic Structures . . . . .	183
105.	Transmission Electron Micrographs of Laser Processed Fe-1.0%C-40%Cr Alloy . . . . .	184
106.	A Non-Equilibrium Diagram for "Splat Cooled" Fe-C-Cr Alloys	185

## ABSTRACT

Laser Surface Alloying of Chromium and Nickel  
on Iron and Carbon SteelsP. A. Molian, Ph.D.  
Oregon Graduate Center, 1982

Supervising Professor: William E. Wood

The effects of rapid melting and subsequent quenching on the solidification behavior and solid state transformation structures of laser surface alloyed Fe-Cr, Fe-Ni, Fe-Cr-Ni and Fe-C-Cr systems were investigated as functions of composition (0-50%Cr, 0-20%Ni, 0-20%Cr/Ni, 0-1% C) and cooling rate ( $10^3$ - $10^6$ °C/s). The microstructures were characterized by optical, scanning and thin foil transmission electron microscopy. The effects of laser parameters (laser power, beam size and scan rate) and coating variables (composition, thickness and morphology) on the penetration depth and melt width were also evaluated.

The microstructures of Fe-Cr alloys were ferritic in nature, irrespective of the composition (0-50%Cr) and cooling rate ( $10^3$ - $10^6$ °C/s). The transformation structures of Fe-5%Ni and Fe-6%Cr-2%Ni alloys exhibited a mixture of martensite and ferrite. The transformation structures of Fe-C-Cr alloys were studied as functions of the carbon (0.2-1.0%C) and chromium contents (0-40%Cr). The alloys containing up to 10%Cr exhibited a martensitic structure with fine precipitates of  $M_3C$  carbide and small amounts of retained austenite. The 20%Cr alloys consisted of duplex austenite/ferrite structures. The morphology and substructure of austenite were a function of the carbon content. Carbide precipitation

was identified only in a 1.0%C alloy. The 40%Cr alloys were ferritic and the morphology changed from equiaxed grains to regular cells with increasing carbon content. Significant amounts of  $M_{23}C_6$  carbide were also observed in these alloys.

The rapid solidification effects including the retention of super-saturated austenite, lack of carbide precipitation and the morphology of phases are discussed as functions of alloy content and cooling rate.

## 1. INTRODUCTION

In recent years, significant advances have been made in the field of rapid solidification processing. A number of innovative new techniques have been developed for the production of rapidly solidified splats, powders, ribbons and thin sections. High power energy sources, such as electron beams and continuous CO<sub>2</sub> lasers, are being used for surface melting, alloying, cutting, drilling, heat treating and welding of metals and alloys. Among the potential applications, surface alloying is unique as a process designed to produce different alloy compositions and microstructural features on the surface of a substrate material, thereby improving its resistance to wear, corrosion and fatigue. The basic process consists of applying a thin coating, on the order of 10 to 200 microns in thickness, to the surface of a substrate and then scanning the surface with a laser beam to melt and fuse the coating into the substrate to form an alloy (Figure 1). The characteristics of this process include high melting efficiency, rapid melting and cooling, minimum distortion, small heat affected zone, retention of high temperature phases, fine grain/dendrite size and other modified microstructural features.

Limited work has been done<sup>2-5</sup> to explain the resulting surface properties on the basis of microstructural features and solidification behavior. To exploit the full range of applications of this process, it is essential to develop a detailed study of the microstructures of laser treated surface layers in order to achieve a complete understanding of

the associated solidification mechanisms. The observations of unusually fine structures, increased solid solubilities and alloy elements, non-equilibrium crystalline and amorphous phases, modification of segregation patterns and achievement of high point defect concentrations<sup>100-110</sup> in rapidly quenched metals and alloys have stimulated efforts among many investigators to develop theories explaining the observed phenomena. However, the mechanisms of phase transformations at high cooling rates were not completely elucidated and often subject to conflicting results. For instance, rapid quenching of high carbon steels in the solid state resulted<sup>77</sup> in an increase in  $M_s$  temperature and also an increase in austenite transformed with an increase in quench rates. But the results obtained in splat quenched Fe-Ni, Fe-Mn and Fe-Ni-C steels indicated an enhancement of austenite retention in the microstructure which was attributed to the depression of  $M_s$  temperature. Certainly, additional experimental data are required in this field before any responsible mechanism can fully be identified. While the microstructures of rapidly solidified, splat quenched steels had been extensively studied, little attention has been paid to the allied process of laser melting, which has an additional feature of rapid melting.

In the light of these observations, the present investigation has been undertaken to study the effects of rapid melting and subsequent quenching on the solidification behavior and solid state transformation structures of laser surface alloyed Fe-Cr, Fe-Ni, Fe-Cr-Ni and Fe-Cr-C systems as functions of composition (5-50%Cr, 0-1%C, 5-20%Ni and 5-10% Cr/Ni) and cooling rate ( $10^3$ - $10^6$ °C/s). In addition, the effects of

laser beam parameters (laser power, beam size, and scan rate) and coating variables (coating composition, thickness, and morphology) on fusion zone penetration depth and melt width have been evaluated. The binary Fe-Cr, Fe-Ni and ternary Fe-Cr-C, Fe-Cr-Ni systems were chosen for study not only because a large volume of information is already available in the literature but also because they possess superior mechanical and service properties.

## 2. REVIEW OF LITERATURE

It is common to observe that the majority of engineering failures are surface oriented and occur through such phenomena as friction, wear, fatigue and corrosion. The two specific reasons are (1) stress levels are highest at the surface, and (2) surface is subjected to environment. The correct engineering approach to such a situation is to provide different surface material properties from those of the bulk material. This may be achieved by surface coatings of different materials, but the inherent defects associated with coatings do not permit achievement of this purpose unless the coatings are fused into the substrate. A high power continuous laser is one of the recent and most effective sources used to fuse the coating into the substrate to depths of 50-300 microns by melting and subsequent rapid solidification, which resulted in layers exhibiting enhanced wear resistance, hardness and corrosion resistance.<sup>1</sup>

Prior to laser treatment, all materials are surface coated by many methods including: (1) Flame spraying, (2) Plasma spraying, (3) Electroplating, (4) Sputtering, (5) Ionplating, and (6) CVD weld overlay. Protective coatings applied by these processes are widely used in industries, but as such they have some drawbacks including inhomogeneous structure, porosity, nonuniform thickness, and poor adhesion. Laser remelting can substantially improve the chemical and mechanical properties of such coatings. Ayers and Schaefer<sup>2</sup> investigated the effects of laser remelting of plasma sprayed coatings of titanium and 316L stainless steel on steel substrates and demonstrated the improvement in corrosion

resistance and strong adhesion to the substrate. Weinman et al.<sup>3</sup> had shown that laser melting of electroplated or sputter deposited chromium and bimetallic layers of chromium and nickel on AISI 1018 resulted in a mechanically stable coating and improved resistance against corrosion. Seaman and Gnanamutha<sup>4</sup> added small amounts of chromium in the form of powder onto the surfaces of valve seats of internal combustion engines and laser melted them to increase their service life. Studies at the Oregon Graduate Center<sup>5</sup> have shown that laser remelted flame sprayed coatings on AISI 6150 steel possess high hardness.

### 2.1. Process Variables

The key variables controlling the efficiency of the laser surface alloying process are laser power, beam size, scan rate, coating composition, coating thickness, and coating morphology. Several investigators<sup>2-7</sup> reported the following effects of laser parameters on the characteristics of this process. Increasing laser power increases melt penetration, ensures uniform mixing, introduces surface rippling, increases heat affected zone, alters the shape of the fusion zone, increases absorptivity, and increases the tendency to crack. Focusing the beam ensures the maximum achievable power density, but the melting area becomes narrow. Increasing the beam diameter increases the width of the fusion zone but reduces the intensity of the heat input and, thereby, diminishes melt penetration. Increasing the scan rate decreases the melt depth and width, reduces the homogenization of the fusion zone, changes the shape of the fusion zone from semicircular to elliptical, decreases

the roughness of the melt, increases the tendency to crack, and reduces the dendrite arm spacing. Ferrous metals like iron and steel have low reflectivity while nonferrous metals like aluminum and copper show almost 100% reflectivity.<sup>18</sup> Cold rolling of 304 stainless steel decreased the reflectivity by 25%. This was attributed to increased scattering from nonplanar defects within the surface layer.<sup>20</sup> Stainless steels exhibited a weak temperature dependence to laser beam reflectivity up to 1000°C. This was attributed to the relatively small effect of phonon scattering.<sup>21</sup> Growth of an oxide layer on the surface of 304 stainless steel changed the reflectivity.<sup>22</sup> Reflectivity of a metal surface also increases with an increase in the wavelength of the laser beam. Thus, metals and alloys show a complex behavior in their ability to reflect infrared energy. Almost all metals have poor absorption of infrared energy at low power densities. But, when power densities are in excess of  $10^6 \text{ w/cm}^2$ , the effective absorption reaches 90%.<sup>18</sup>

Generally, the materials are laser processed under an inert gas atmosphere to prevent the oxidation of the metal surface and suppress the formation of plasma. Studies on laser melted aluminum and titanium alloys<sup>11</sup> revealed that surface appearance and coupling could be affected by gas pressure and flow rate. Changes in the surface appearance were observed in laser melted chromium steels and were attributed to shielding gas.<sup>10</sup> Coating thickness is an important variable that influences the extent of dilution of the alloying element into the substrate and also the melt depth and width. Various coating thicknesses were employed in many investigations and are listed on the next page.

Reference	Coating Material	Substrate	Coating Thickness ( $\mu\text{m}$ )	Coating Technique
3	Chromium	1018 Steel	2-16	Electroplating
3	Chromium-Nickel	1018 Steel	2-18	Electroplating
4	Chromium rich alloy	Cast Iron	500	Powder Addition
2	316L Stainless Steel	1020 Steel	120-500	Plasma Spray
2	Metco 16C	4340 Steel	520	Plasma Spray
2	Metco 16C	1020 Steel	70-100	Plasma Spray
2	Ti-Amdry	1020 Steel	300-380	Plasma Spray
5	Metco 19E, 36C, 81 VF-NS, 34F, 101 SF, 350, T-700	6150 Steel	50-100	Flame Spray

## 2.2. Solidification and Solid State Transformations

The potential for future application of laser surface alloying lies in its ability to control the microstructures on a finer scale than previously has been possible. Rapid solidification produces smaller grain/dendrite sizes which are responsible for the improved properties. Laser melting of aluminum<sup>6</sup> alloys produced a dendrite arm spacing of 0.25-0.60 micron. In laser melted M2 tool steel,<sup>15</sup> the dendrite arm spacing was found to be 1-2 microns. Strutt et al.<sup>15-17</sup> had shown that the solidification structure at maximum melt depth was plane front and towards the

surface, the change was to columnar and finally to equiaxed structure. Further ferrite and austenite were observed in the lower and upper melt zones, respectively. Rapid solidification sequence was generally controlled by laser beam parameters and composition, conductivity, thermal diffusivity and surface free energy of substrate and coating materials.<sup>27</sup>

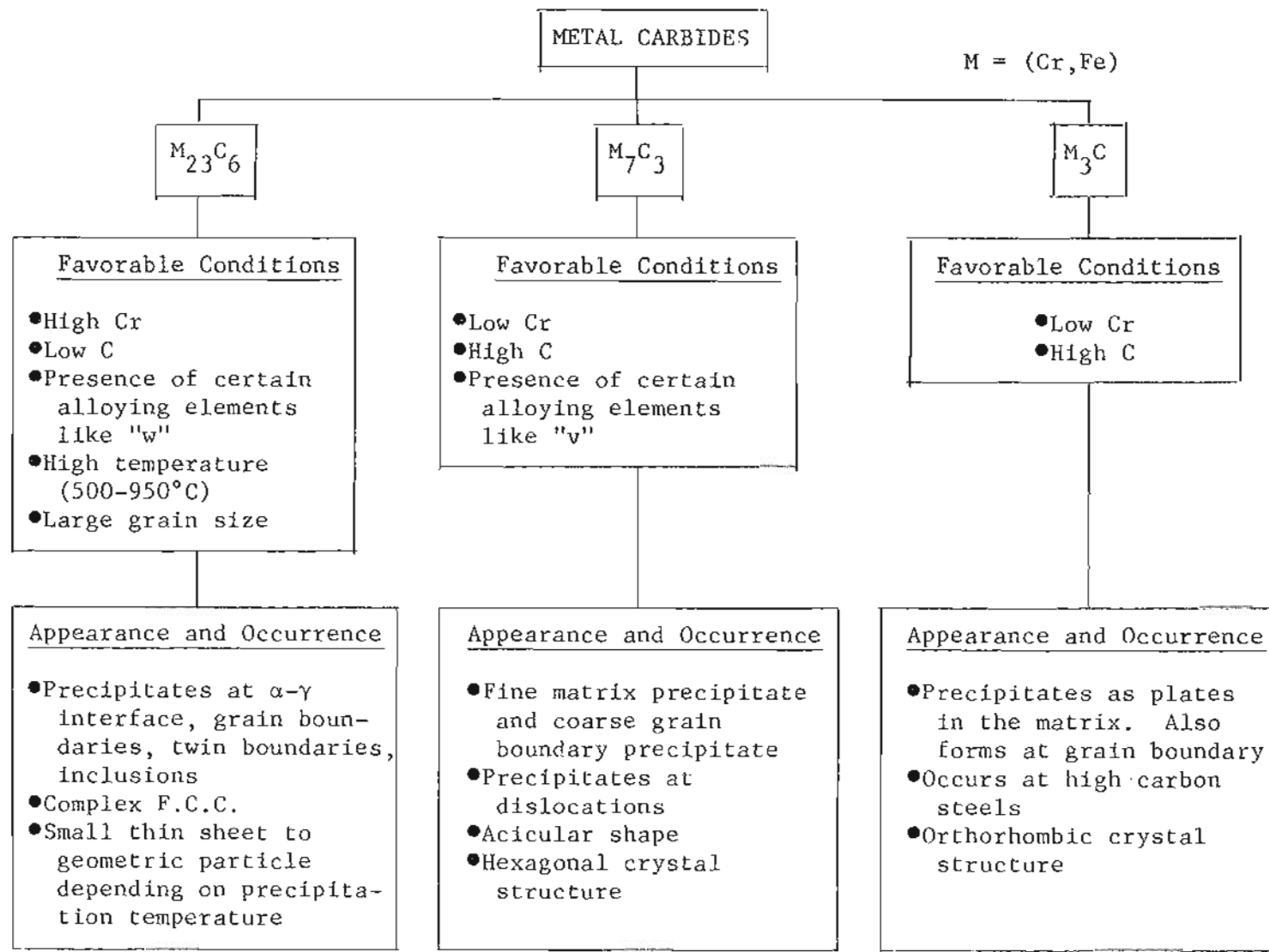
A variety of microstructures were produced by the laser melting process<sup>12</sup> and these included amorphous surface layers on bulk crystalline substrates, super saturated solid solutions, ultra fine eutectics, and nonequilibrium phases. Moore et al.<sup>14</sup> reported martensitic structures in laser melted titanium alloys which had a high resistance against stress corrosion cracking. Strutt et al.<sup>15-17</sup> extensively worked on the microstructural characterization of laser surface melted M2 and 440C tool steels. They observed a simple coupled growth of delta ferrite/ $\text{Cr}_7\text{C}_3$  eutectic structure in 440C alloy. Further laser melted M2 tool steel contained a mixture of ferrite and austenite in contrast to martensite and carbide structures obtained in conventional solid state quenching. Cline and Anthony<sup>25</sup> reported acicular bands of martensite in laser melted 304 stainless steel which on subsequent corrosion tests exhibited a high resistance against intergranular corrosion.

Chromium and nickel are widely used as alloying elements to impart corrosion resistance, high-temperature resistance, and mechanical properties on steels. Chromium exhibits isomorphous with iron while nickel forms peritectic with iron. Chromium is a ferrite stabilizer, but nickel is austenite stabilizer. Chromium forms carbides of the type  $\text{Cr}_{23}\text{C}_6$ ,

$\text{Cr}_7\text{C}_3$ ,  $\text{Cr}_6\text{C}$ , etc., while nickel has no tendency to form carbides.

Chromium poses embrittling effects by forming a brittle sigma phase at high chromium contents. Alloys of chromium and iron in the presence or absence of nickel show several metal carbides of the type  $(\text{Cr,Fe})_{23}\text{C}_6$ ,  $(\text{Cr,Fe})_7\text{C}_3$ , and  $(\text{Cr,Fe})_3\text{C}$  under different conditions.

These metal carbides constitute an important source in affecting corrosion, wear, fatigue and other mechanical properties. The following chart gives a brief history of the carbides present in iron-carbon-chromium-nickel systems.



### 3. EXPERIMENTAL PROCEDURE

#### 3.1. Materials

The substrate materials used in this investigation were pure iron (Ferro vac E) and commercial quality 0.2, 0.5 and 1.0% carbon steels. The chemical compositions of these steels are given in Table 1. The steels, received in the form of cold rolled ingots, plates and bars, were thoroughly vacuum degassed at 600°C and cut to specimens of size 7.5 x 2.5 x 0.64 cm (3.0 x 1.0 x 0.25 inch). Prior to applying the coating, the specimens were surface ground using a 400-grit grinder.

#### 3.2. Electrodeposition

The substrate materials were electrodeposited with chromium or nickel or chromium over nickel using conventional electroplating methods. Electroplating conditions are given in Table 2 for each category. The coating thicknesses ranged from 10 to 200 microns. Electrodeposition techniques were chosen as coating methods for their simplicity, controllability, and uniformity. After electrodeposition, the samples were vacuum degassed ( $10^{-7}$  torr) at 205°C (400°F) for 10 to 12 hours to remove the entrapped hydrogen in the coating.

#### 3.3. Laser

A GTE Sylvania Model 971 CO<sub>2</sub> gas transport laser which provided 1500 watts continuous infrared laser radiation at a wavelength of 10.6 microns was used in the present investigation (Figure 2). The laser output beam

can be focused optically to a very small area to achieve power densities of up to  $10^8$  watts per square centimeter. The system specifications are shown in Table 3. A helium-neon laser was used in conjunction with a  $\text{CO}_2$  laser to produce a beam of red light coaxial with the infrared laser beam. The red beam has been used for the alignment of external optics and for the positioning of the workpiece.

#### 3.4. Measurement of Laser Beam Parameters

A power meter (GTE Sylvania Model 491) was used to determine the total laser output beam power. The beam was directed into a watercooled calorimeter and the temperature drop associated with the heat flow across a copper element lamination was amplified through an amplifier built into the power meter head. The amplifier output was fed to a display readout containing 100, 300, 1000 and 3000-watt scales. This arrangement did not permit power monitoring when the laser beam was scanned across the metal surface. However, the output power from the laser was stable enough over extended time periods to make this method satisfactory. The laser power stability during the course of an 8 hour run has been determined to be typically within  $\pm 0.5\%$ . Due to relatively high power densities and small size, direct measurements of the focused optical spot diameter are in practice quite difficult to perform. In this study, the beam size was measured by an indirect method. First, the actual focal point of the lens was determined directly from experiments on thin plexiglass sheet. The effective spot size of the beam at the sample surface was then calculated using appropriate optical relationships (Table 4). A numerically

controlled X-Y table beneath the stationary laser nozzle has been used to control laser beam scan rate. Both single and overlapping multiple scan laser melting were employed. The distance between successive laser scans was fixed to be 50% of the beam diameter. Helium and argon shielding gas mixture (90%Ar/10%He) was introduced coaxially with the laser beam at a flow rate of 50 cfh through a cone-shaped nozzle of 0.25 inch diameter during laser melting. The shield gas served two purposes-- first to protect the lens from debris collecting on it, and second to suppress oxidation of the metal surface and formation of an absorptive plasma.

The laser operating parameters used in this investigation are shown in Table 5.

### 3.5. Cooling Rate Determinations

Owing to the experimental difficulties (due to rapid melting and subsequent quenching) involved in measuring directly the cooling rates in this process, they were estimated based on heat transfer models. However, the present study utilized solidification structures in addition to two heat transfer models<sup>44,45,47</sup> to calculate the solidification cooling rates.

### 3.6. Compositional Analysis

Energy and wavelength dispersive X-ray microprobe analysis were used to determine the compositions of surface alloys produced. A working curve of the concentrations of alloys by x-ray microprobe and wet chemical

analysis methods were plotted using several standards of known composition. The compositions of laser alloyed fusion zones were then determined using this plot.

### 3.7. Microscopy

3.7.1. Optical Metallography. Small sections were cut from laser treated specimens using a 1/32 inch thick abrasive wheel with flood cooling. The samples were mounted and successively ground in 120, 240, 400 and 600 grit SiC emery papers. The samples were then polished using 5.0, 0.3 and 0.05 micron alumina powders and etched. Various etchants, including 2% nital, Vilella's reagent and mixed acid etchants, were used in accordance with the effects desired. The samples were then examined in a Carl Zeiss optical microscope.

3.7.2. Transmission Electron Microscopy. Thin foils for transmission work were taken from the mid region of transverse sections of laser alloyed zones (perpendicular to the scanning direction). Slices of about 0.6mm thick were mechanically sectioned using flood cooling to avoid heating. A series of 120, 240, 400 and 600 grit SiC papers were then used to reduce the thickness to 0.10 mm. Discs of 3 mm diameter were then punched and electrolytically thinned in a solution containing 5% perchloric acid in 2-butoxy ethanol with 80 volts applied voltage at -10°C using a twin jet polisher. The foils were examined in a Hitachi HU-11B electron microscope operated at 100 Kv.

3.7.3. Scanning Electron Microscopy. Using a JEOL JSM-35 scanning electron microscope operated at a secondary electron voltage of 25 Kv, scanning electron microscopy of polished and etched samples were carried out to record fusion zone depth, width, geometry and coating thickness.

### 3.8. Microhardness

Knoop microhardness tests were conducted on the transverse sections of laser alloyed fusion zones with a Leitz miniload hardness tester using 100 and 500 gms loads. The hardness values were expressed as knoop hardness number.

## 4. RESULTS AND DISCUSSION

This section is divided into three parts. The first part describes the effects of laser beam parameters and coating variables on the laser alloyed fusion zones. The second part discusses the factors governing the formation of porosity, cracks and non-uniform composition of laser alloyed fusion zones. The third part summarizes the solidification, solid state transformation microstructures and microhardness data of the fusion zones.

### 4.1. Optimization of Process Variables

Figure 3 shows the macrographs of typical surface appearances of laser alloyed specimens processed under different laser beam conditions. Figure 4 depicts the transverse sections of a deposited coating and laser alloyed fusion zone typically observed in single scan laser treated samples. Two parameters of interest, namely penetration depth and melt width describing the fusion zone geometry, have been defined in Figure 4b and are the direct consequences of laser beam parameters and coating/substrate materials properties. Penetration depth and melt width control the compositions, cooling rates and microstructures of alloys produced. Hence, the effects of laser beam parameters, such as laser power, beam size and scan rate, and coating variables, including coating thickness, composition and morphology on penetration depth and melt width of fusion zones have been evaluated in the following sections.

#### 4.1.1. Effects of Laser Beam Parameters.

LASER BEAM POWER--Penetration depth and melt width of fusion zones of chromium alloyed iron as a function of laser beam power at different scan rates are shown in Figures 5 and 6. Penetration depth increases linearly with power but melt width remains almost independent of power. The sensitivity of laser beam power to penetration depths rather than melt widths is attributed to a higher power density peak at the center of the focal spot. Figure 7 shows the transverse sections of fusion zones at various laser powers. The penetrations are significantly greater and such "deep penetration" melts are primarily caused by small beam size and high laser power. It is also seen that the liquid zone extends deeply into the material relative to the width of the fusion zone. Deep penetration melting occurs due to "key holing"<sup>18</sup> in which the beam delivers energy more rapidly than it can be removed by thermal conduction. A hole is then drilled so that laser energy can penetrate deep into the workpiece. A flow of molten material then recloses the hole after the passage of the beam to a new area. Deep penetration melts, characterized by an hour-glass shape with a high aspect ratio (aspect ratio = penetration depth/melt width), have been shown by many investigators in laser and electron beam welds.<sup>30-35</sup> It has been suggested and substantiated experimentally that under the conditions of deep penetration melting,<sup>33</sup> the laser power is completely absorbed. This was explained by the multiple reflections that occur in the cavity in the liquid which increase the absorption of light. According to Breinan and Banas,<sup>32</sup> when a laser beam was focused on a material surface with

sufficient power density, an in-depth vapor column is created and maintained in equilibrium with a liquid pool which surrounds it. Evidence for the formation of vapor during laser surface alloying of chromium on steels in deep penetration melts had been verified experimentally by collecting and analyzing the vapors on a filter paper. Figures 5 and 6 also show that the penetration depth is as high as 1500 microns at a scan rate of 50 in/min and 1200 watts power and still higher penetrations can be achieved by reducing the scan rate.

FOCAL POSITION/BEAM SIZE--The shape of laser alloyed fusion zones is determined by a number of characteristics. One such controllable characteristic is the location of the focal point relative to the surface of the specimen. This is also directly related to the beam size at the specimen surface. The results of experiments performed on the effect of the focal position on penetration depths and melt widths are summarized in Figures 8 and 9 for chromium alloyed iron. It can be seen that maximum penetration had occurred when the beam was focused slightly (0.025") inside the surface. Similar results were reported by Locke and Hella<sup>30</sup> for 304 stainless steel (0.060" below the surface) and Engel<sup>35</sup> for 1018 steel (0.050" below the surface). These plots also indicate that higher penetrations were always obtained when the beam was focused below the specimen surface rather than above for a given beam size. The shape of this plot appears as parabolic but essentially depends on focal length of lens,<sup>35</sup> laser power, scan rate and material system. Figure 10 shows the cross sections of fusion zones of chromium

alloyed iron at different locations of the focal point relative to the specimen surface. The shape of fusion zones indicates that the aspect ratio decreases and the shape changes from hour-glass to semicircular through triangular when the specimen surface is moved away from the focal point. The hour-glass shape corresponds to "deep penetration" melting for conditions of focusing to a higher power density such that substantial vaporization occurs. The triangular and semicircular fusion zones correspond to "conduction" melting for conditions of focusing such that no substantial amounts of vaporization occurs.

SCAN RATE--Figures 11 and 12 summarize data on the penetrations and widths achieved in chromium alloyed iron at various rates of beam traverse for values of laser power from 900 to 1200 watts. Both penetration depth and melt width decrease with an increase in scan rate. Similar results were obtained by several investigators for different materials.<sup>30-35</sup>

Thus, laser beam parameters, such as laser power, focal position/beam size and scan rate have been manipulated to obtain penetration depths from 100 to 1500 microns, melt widths from 300 to 1200 microns, and fusion zone shapes from hour-glass to semicircular. Consequently, the compositions, cooling rates, microstructures, and mechanical properties of the alloys produced were controlled.

4.1.2. Optimization of Coating Variables. This section examines the effects of coating composition, morphology and thickness on penetration depth and melt width of laser surface alloyed steel.

COATING COMPOSITION--The final alloy composition of the fusion zone is primarily determined by the initial coating composition. Since penetration depth also controls the resulting alloy composition, it is imperative to study the effects of coating composition on penetration depth. Figure 13 shows the transverse sections of chromium, nickel and chromium deposited over nickel coatings on pure iron. Figures 14 to 16 present the data on the effects of these coatings on penetration depths as a function of laser beam parameters. It is evident from these plots that laser alloying of chromium/nickel coating exhibited a greater penetration compared to laser alloying of either chromium or nickel. This increase was obtained under all laser beam conditions. This also implies that higher penetration in Fe-Cr-Ni systems over Fe-Cr and Fe-Ni was achieved independently of melting modes such as deep penetration or conduction. However, the amount of increase in penetration appears to be influenced by laser beam parameters. For given laser parameters, there is no appreciable difference in penetration depths between Fe-Cr and Fe-Ni systems. Another interesting aspect of Figure 22 is that the Fe-Cr-Ni system is more sensitive to the position of the focal point relative to the material surface than the Fe-Cr and Fe-Ni systems, thereby indicating the differences in laser response to individual material systems.

These observations suggest that the probable mechanism in controlling penetrations is a combined effect of the initial surface condition (which controls the initial absorption) and the thermal properties of alloys formed (which controls the heat flow) during solidification.

Figures 17 and 18 are the top views of chromium, nickel, and chromium over nickel coatings in conjunction with thermal properties of chromium, nickel and 304 stainless steel (which represent the Fe-Cr-Ni system), thus illustrating the differences in the morphology and heat transfer properties.

COATING MORPHOLOGY--To date there has been no reported data on the response of coating morphology to high power laser beam absorptivity in the laser surface alloying process, though it has been frequently said that the initial surface appearance alters the penetration through its affects on absorption. The results of tests conducted on the influence of chromium and alloy coating morphologies on penetration depth, melt width and fusion zone shape are shown in Figures 19 to 22. Figures 21 and 22 show the coating morphologies and the laser alloyed surfaces of black and bright chromium and co-deposited iron-chromium coatings for the given laser parameters. The coating morphologies, as seen in these micrographs, largely differ from each other in terms of particle size and surface defects such as porosity, cracking, pitting, oxidation and roughness. The results obtained indicate that there is no significant effect of coating morphology on penetration depth and melt width excepting for a small change in fusion zone geometry. This suggests further that the heat transfer properties of the coating are more important in deciding the laser beam absorptivity rather than the coating morphology.

COATING THICKNESS--Initial coating thickness controls the extent of dilution of the alloying element and constitutes a versatile parameter to obtain the desired alloy composition. The results of studies performed on the influence of chromium coating thickness on penetration depths and melt widths are summarized in Figures 23 and 24. These experiments were repeated on several steel substrates to assess and confirm that the effects are caused only by chromium coating thickness variations and also to produce different surface alloy compositions (0-50%Cr) and, thereby, study their microstructures. As seen from these plots, there is no substantial influence of chromium coating thickness on penetration depth and melt width. However, the amount of variation in penetrations suggests that chromium coating thickness has some role in controlling the fusion zone size, the reasons for which are not fully understood. It is believed that the thermal properties of the alloys formed and their variation with temperature are responsible for the observed variation in penetration depth with respect to coating thickness.

#### 4.2. Fusion Zone Defects Characterization

This section deals with the factors that favor the formation of porosity, cracks and nonuniform composition of fusion zones and with methods to eliminate them.

##### 4.2.1. Porosity.

EFFECTS OF ENTRAPPED HYDROGEN--Hydrogen entrapped during the application of the coating appears to play a significant role in determining

the porosity formation. Figure 25 shows the top views of laser alloyed surfaces with and without trapped hydrogen. It is apparent from Figure 25a that hydrogen had been expelled from the melt towards the free surface and remained as surface pore. Contrary to vacuum degassed samples (Figure 25b), considerable amounts of porosity were observed in samples that were not degassed. The pores appear as elongated and irregular in shape, similar to the observations of Kim and Weinman<sup>36</sup> in laser melted aluminum alloys. A significant amount of hydrogen is introduced into the coating during the chromium electrodeposition process as a result of high current density ( $0.3\text{A}/\text{cm}^2$ ) and high temperatures ( $65^\circ\text{C}$ ). When the laser beam rapidly heats the samples to the melting temperature and above of the coating, the hydrogen trapped within the pores of the coating would experience an increase in temperature and also an increase in pressure, particularly if the pores are of the closed type.<sup>2</sup> Consequently, the expanding and pressurized gases tend to escape the fusion zone prior to the onset of solidification. If the rate of solidification is less than the rate at which these gas bubbles rise to the surface, then they either remain as enlarged residual pores or force out portions of the resulting fusion zone surface (Figure 27c).

Figures 26 and 27 show the longitudinal and transverse sections of laser alloyed zones as functions of chromium coating thickness and laser beam scan rate. The amount of porosity, as seen from these micrographs, appears to be strongly dependent on the initial coating thickness and scan rate. Under the conditions of the electrodeposition process,

increasing chromium coating thickness generally increases the concentration of entrapped hydrogen gas. As a result, extensive amounts of porosity were developed in alloys produced from thicker coatings (Figure 26). Increasing scan rate also increases the amount of porosity in the fusion zone (Figure 27). At low scan rates, there is sufficient time for the gas to escape through the surface during solidification resulting in a relatively porous-free fusion zone (Figure 27a). However, as the scan rate increases, there is less time for the gases to escape and, subsequently, these gas bubbles were caught by the advancing solidification front to form pores in the fusion zone. These results suggest that hydrogen gas porosity in laser alloyed surfaces can be avoided by employing either a thin coating or a low scan rate.

KEY HOLE POROSITY--In addition to hydrogen porosity, another form of porosity has been observed but only in deep penetration melts. Figure 28 shows this type of porosity near the bottom of the fusion zones. This was attributed<sup>38</sup> to the entrapment of primary shielding gas by collapsing the key hole.

4.2.2. Nonuniform Composition of the Fusion Zone. High energy density ( $10^6 - 10^8 \text{ w/cm}^2$ ) and short interaction times ( $10^{-6} - 10^{-2} \text{ sec}$ ) involved in this process raise the question whether uniform composition can be achieved in laser alloyed fusion zones. Weinman et al.<sup>3</sup> had shown by electron microprobe analysis of laser alloyed chromium on AISI 1018 steel that uniform mixing of chromium had occurred in the melt pool within 50 microseconds. In this study, the composition uniformity had been

studied as a function of fusion zone shape. Figure 29 shows the transverse sections of laser alloyed zones produced under different laser beam conditions and the corresponding chromium concentration profile plots from the top surface of fusion zone to the fusion/base interface. It is seen that the variation in chromium content is more pronounced in an hour-glass shaped fusion zone (Figure 29a), intermediate in a triangular fusion zone (Figure 29b) and relatively none in a semicircular fusion zone (Figure 29c).

The following table shows the laser parameters employed in this study to obtain the previously described fusion zones. In addition, the resulting penetration depths of fusion zones and the depth of uniform concentration of chromium that can be obtained in the fusion zones based on the models proposed by Cline and Anthony<sup>8,9</sup> are given.

For uniform composition to occur in the fusion zone, two mechanisms have been postulated.<sup>8,9</sup> One is based on the diffusion of solute in the melt pool and the other on the surface tension effects caused by the temperature gradients in the melt pool and surrounding area. The diffusion model involves the laser beam interaction time ( $t$ ) and the diffusivity of solute in the liquid ( $D_L$ ) as given by the equation  $X = (D_L t)^{0.5}$ , where  $X$  is the diffusion distance over which the concentration homogenization can occur. Cline and Anthony reported that with interaction times of 50 microseconds to 2 milliseconds, the diffusion distances in the melt pool are too small to obtain uniform mixing in ferrous systems. Surface tension gradient mechanism was also not expected to be operative within this time frame since the convection currents produced

Laser Beam Parameters	Hour-Glass	Fusion Zone Shape	
		Triangular	Semicircular
Power density, watts/ cm <sup>2</sup>	$3.5 \times 10^7$	$2.4 \times 10^6$	$1.0 \times 10^6$
Interaction time, seconds	$3.12 \times 10^{-3}$	$1.2 \times 10^{-2}$	$1.9 \times 10^{-2}$
Penetration depth, microns	1430	880	250
*Depth of uniform concentration of chromium (diffusion model), microns	190	380	470
*Time that the alloy was in molten state, seconds	$5.8 \times 10^{-2}$	$4.6 \times 10^{-2}$	$1.7 \times 10^{-2}$
*Fluid flow velocity required to achieve homogenization (sur- face tension model), cm/sec	4500	2550	500

\*Estimated based on diffusion and surface tension models<sup>2,3</sup>

in the melt pool by surface tension gradients had been shown to lag the advance of solidification front and, hence, could not cause enough stirring. For a moment, let us assume that the fluid flow in molten iron, induced by surface tension gradients, would produce a more uniform alloyed region than the diffusion of solute in the melt pool. Then the time that the alloy was in the liquid state ( $t'$ ) and the fluid flow velocity [ $U(y,t')$ ] required to homogenize the liquid were estimated (see the above

table) employing the appropriate equations, developed by Cline and Anthony,<sup>8,9</sup> which are given as follows:

$$U(y, t') = \frac{1}{\mu} \left( \frac{d\sigma}{dt} \right) \Delta T \left[ (D_u t')^{0.5} - y \right]$$

where  $y$  = penetration depth (cm)

$t'$  = time that the alloy was in molten state (sec)

$\mu$  = surface energy per unit area (dyne-sec/cm<sup>2</sup>)

$\frac{d\sigma}{dt}$  = surface tension temperature gradient (ergs/cm<sup>2</sup> °K)

$\Delta T$  = temperature difference between the liquid below the laser beam and the liquid at the solid-liquid interface of the melt pool (°K)

$D_u = \mu/\rho$ , "diffusivity" of velocity profile (dyne-sec/gm)

Contrary to these mechanisms, Weinman et al.<sup>3</sup> have shown, using electron microprobe analysis of laser surface alloyed 1018 steel, that complete mixing occurred in 50 microseconds of interaction time. They postulated a different mechanism, namely, that the mixing effects caused by superheated gases above the melt pool were sufficient to stir the melt pool. However, in the present investigation, the diffusion model has been followed to explain the uniform concentration of chromium in semicircular fusion zones. However, the uniform compositions obtained in hour-glass and triangular fusion zones other than predicted by diffusion models (see the above table) suggest that the surface tension gradient and superheated gas mechanisms are also operative.

4.2.3. Cracking. The most serious limitation of laser alloying chromium on medium (0.5%C) and high (1.0%C) carbon steels is the frequent occurrence of cracks. The contraction of alloys formed during rapid cooling sets up internal tensile stresses in the fusion zone and surrounding heat affected zone causing the formation of cracks. Several distinct types of cracks have been observed depending upon laser processing variables and the chemistry of substrate and coating materials. The cracks have been classified (according to their locations) as follows: (1) cracks in the fusion zone, (2) cracks in the heat affected zone, and (3) cracks in the coating adjacent to the melt pass. Figures 30 and 32 illustrate these cracks of laser alloyed 1.0%C steels formed by substantially different mechanisms of nucleation and propagation.

Cracks of type 1--namely the centerline cracks in the fusion zone--are identified as "hot cracking" or "solidification cracking" and are due to both inadequate "feeding" and tensile stresses developed by contraction. The word "feeding" is used here in the same sense as in foundry technology. Among the several variables, the base metal composition and laser processing parameters were found to control the solidification cracking to a greater extent. In contrast to laser alloyed pure iron and 0.2%C steels, where no evidence of any cracking was observed, laser alloying of chromium on 0.5 and 1.0%C steels had produced a significant amount of cracking in the fusion and heat affected zones. The effect of carbon in enhancing the centerline cracking is attributed to its effects in increasing the liquid to solid freezing range. This long freezing range allows small amounts of molten metal to be present for a longer

time. Subsequently, the liquid film present between grains or cells builds up stresses and causes the cracks.<sup>39</sup> Laser beam parameters (thereby, fusion zone shape) also determine the propensity of cracking in the fusion zone. Studies carried out with different laser parameters (for example, increasing the beam size or decreasing scan rate) have shown that the fusion zone susceptibility to cracking decreases with a decrease in heat input and aspect ratio of fusion zone (Figures 30-31). Solidification cracks, similar to the present findings, have been observed in conventional welds containing a high aspect ratio.<sup>39</sup> Linnert<sup>40</sup> reported that solidification cracks are favored in welding processes involving large heat inputs. The formation of this type of cracking, however, does not appear to depend on the solid state transformation structures. Figures 30a,b correspond to fusion zones containing martensitic structures, while Figures 31a-c correspond to fusion zones containing ferrite/austenite and ferrite structures. The presence of cracks in all these figures show that microstructure did not play any role in controlling this type of crack forming tendency.

Cracks of Type 2--namely, cracks in the heat affected zone--were produced by thermal stresses induced by the rapid rise of temperature over a small area. This type of cracking appears to be initiated by the physical defects in the coating. Figures 30 and 32 show the cracks in the heat affected zone as having originated from the cracks already present in the coating. During electrodeposition or laser melting, the cracks are initiated in the unmelted coating and act as stress

raisers. They also serve as suitable sites for the nucleation and propagation of cracks in the heat affected zone.

Cracks of Type 3--namely cracks in the coating adjacent to the alloyed zone (Figure 32b) and along the edge of the melt pass--are relatively common since the melted portion of the coating is stronger than the unmelted portion. These cracks generally do not present a problem since they lie in the path of subsequent melt passes.

#### 4.3. Solidification Studies of Laser Processed Fe-C-Cr Alloys

4.3.1. Heat Flow Models. Because of the experimental difficulties involved in measuring the temperature and cooling rates in this process (due to high energy density and short interaction time) several heat flow models based on theoretical concepts have been addressed. The details of the mathematical descriptions and the numerical computation techniques used are available in many publications<sup>41-45</sup> dealing with one, two or three dimensional heat flow analyses. In this study, two such models<sup>44,45</sup> have been followed to predict the cooling rates during solidification. Both models use the following assumptions: (1) semi-infinite solid, (2) constant heat input, (3) conduction heat transfer, (4) homogeneous material with constant thermal properties, (5) no latent heat effect, and (6) temperature independent absorptivity. These models are usually applied to laser melting of single material. However, the present study involved three materials--namely the coating, substrate and alloy formed during solidification. Nevertheless, only the thermal properties of initial coating are considered in applying these models.

The first model, described by Greenwald et al.,<sup>45</sup> is a one dimensional semi-infinite conduction heat transfer model and applicable only when the aspect ratio is less than one (Figure 33). The results of this model and the experimental points are shown in Figure 34 for chromium alloyed iron. Considering the uncertainties in the thermal properties under actual melting conditions and other assumptions, the observed and predicted values of penetration depth are in fairly good agreement. In contrast with the preceding model, the moving Gaussian energy source models (3-Dimensional) by Cline and Anthony<sup>44</sup> are applied to fusion zones having an aspect ratio equal to or greater than one (Figures 35 and 37). Figures 36 and 38 present the data on the predicted and experimentally obtained values of penetration depths in the range 400 to 1500 microns. This model is in reasonably good agreement with experimental values in the range 400 to 600 microns. When the penetration depth exceeds 600 microns, the predicted values underestimate the actual values. The melting mode could provide an explanation. Generally, the deep penetration mode of melting begins to operate when the penetration depth exceeds 500 microns. The concepts and properties of "key holes" formed during deep penetration melting, which basically determine penetrations, are not fully understood and evaluated. It is, therefore, concluded that heat transfer models can be applied reasonably for penetration depths 10 to 500 microns. The overprediction of penetrations by heat flow models in all three cases may probably be due to the assumptions involved in these models.

4.3.2. Solidification Structures. Both the uncertainties implicit in the prediction of cooling rates and temperature distributions and the difficulties involved in measuring these quantities directly by thermal analysis stimulated many investigators to determine their values from the dimensions of microstructural features. These features include the matrix grain size,<sup>46</sup> dendrite or cell spacing,<sup>47,48</sup> inclusion size,<sup>47</sup> eutectic interphase spacing,<sup>49</sup> the width of vacancy denuded zones along side grain boundaries,<sup>50</sup> dislocation array size,<sup>51</sup> radius of GP zones,<sup>46</sup> and wavelength of spinodal decomposition.<sup>52</sup>

In this study, the fineness of cellular solidification structures has been related to the cooling rates during solidification. Fusion zones containing 0 and 0.2%C did not reveal the presence of any solidification structure. Several etchants were tried and none found to be effective. But laser alloying of chromium on 0.5 and 1.0%C steels readily exhibited the cellular/dendrite solidification structures. Figures 39 and 40 are the scanning electron micrographs showing the cell/dendrite structures observed at the top views of laser alloyed zones. The cell/dendrite spacing ranged from 0.1 to 4 microns depending on penetration depths, indicating the high cooling rates attained in this process.

The appropriate equation employed here to establish the cooling rates based on cell/dendrite spacing is given by Flemings et al.<sup>47</sup> as  $d = 60 r^{-0.41}$ , where  $d$  is the dendrite arm spacing in microns and  $r$  is the cooling rate in °C/s. This equation has been experimentally determined for Fe-1.0%C-15%Cr alloy and for cooling rates in the range

$10^0 - 10^5$  °C/s. Figures 41 and 42 show the cooling rates as a function of cell/dendrite spacing, which in turn depends on penetration depth and alloy content of fusion zones. Generally, the nature of the surface alloying process is such that it is difficult to isolate the effects of composition from penetration depth. Assuming that the composition effects are minimum in altering the cell spacing, Figure 43 provides the cooling rate as a function of penetration depth. This plot also presents the predicted values of cooling rates by heat flow models as described earlier.

4.3.3. Composition Studies of Laser Alloyed Fusion Zones. The composition of fusion zones was determined from energy and wavelength X-ray microprobe analysis. The compositions of the fusion zones were also theoretically calculated from the volumes of coating melted and the fusion zone as per the following equation,

$$\text{Percentage of alloying element in the fusion zone} = \frac{\text{Vol. of coating melted}}{\text{Vol. of fusion zone}} \times \frac{\text{Density of alloy} \times 10}{\text{Density of coating}}$$

The results, plotted in Figure 44 for chromium alloyed iron, are in good agreement with theoretical calculations. However, the variation in composition within the fusion zone cannot be determined from the above equation.

#### 4.4. Solid State Transformation Structures

A detailed characterization of the microstructures by optical, scanning, and thin foil transmission electron microscopy was performed on all the alloy systems produced through the laser surface alloying process. Since extensive microscopy work was involved in this study, the microstructures were classified on the basis of alloy compositions and cooling rates.

4.4.1. Fe-Cr System. Referring to the Fe-Cr equilibrium diagram (Figure 45), the transformation structures of Fe-Cr alloys were investigated as a function of chromium content. Alloys containing chromium up to 12% undergo austenite to ferrite transformation, while alloys containing more than 12% chromium do not undergo any solid state transformation except for an extremely sluggish transformation from ferrite to sigma phase at high chromium contents.

#### OPTICAL METALLOGRAPHY--

##### Transformation Structures of Alloys within gamma phase field--

Figures 46a-d present the optical micrographs of Fe-Cr alloys (4-10%Cr) produced with similar cooling rates. The microstructures appeared to consist of massive ferrite (also described as "bainitic ferrite" by Bee and Honeycombe;<sup>62</sup> furthermore, the morphology of ferrite grains, being irregular in shape, illustrated no apparent features (suggesting that) they had arisen from shear transformation. This was also confirmed by thin foil transmission electron microscopy studies described in a

later section. A comparison of Figures 46a-d reveals that there is no apparent change in the morphology of ferrite grains with an increase in composition.

Massive transformation was first recognized in Cu-Ga and other copper base alloys.<sup>63</sup> Transformation by massive mechanism has been reported to occur in rapidly cooled ( $5.5 \times 10^3$  °C/s), solid state quenched Fe-Cr (0-10%Cr), Fe-Ni (0-15%Ni) and Fe-Si (0.2-7%Si) alloys by Gilbert and Owen.<sup>54</sup> By applying Kaufmann and Cohen's thermodynamic data of regular solution analysis, they had shown that the free energy change accompanying the massive transformation (10-80 cal/mole) was smaller than that of martensitic transformation (260-320 cal/mole) in these alloy systems. Hence, they concluded that rapidly quenched Fe-Cr alloys can undergo only massive transformations. Pascover and Radcliffe<sup>53</sup> reported equiaxed ferrite (also designated as "massive" by them) transformations in solid state quenched Fe-Cr alloys (0-10%Cr) up to quench rates of  $4 \times 10^4$  °C/s. They also observed<sup>71</sup> that the structures of Fe-Cr alloys remained as equiaxed ferrite by quenching at a pressure of 25 Kbar (quench rate  $10^2$  °C/s). They attributed that both pressure and quench rates were insufficient to inhibit the short range diffusion involved in the formation of ferrite. However, Wallbridge and Parr<sup>55</sup> had shown martensitic transformation in solid state quenched Fe-Cr alloys (0-10%Cr) with a quench rate of  $1.5 \times 10^4$  °C/s based on surface rumbling criterion. Bee and Honeycombe<sup>62</sup> also observed martensitic transformation in water quenched Fe-10%Cr alloy. In fact, Pascover and Radcliffe<sup>53</sup> reported martensitic transformations in Fe-Cr alloys with quench rates greater than

$7 \times 10^3$ °C/s but at an alternate and lower transformation temperature of about 500°C.

Transformation temperature, i.e., the temperature at which austenite transforms to martensite or massive ferrite, plays an important role in determining the type of transformation as massive, equiaxed, or martensitic. While it is well established that the transformation temperature exhibited a progressive decrease with the increase in cooling rate to a constant value in iron binary alloys, there is a discrepancy in reported values of transformation temperature for a constant cooling rate by several investigators.<sup>53-59</sup> Pascover and Radcliffe<sup>53</sup> had shown that, regardless of quench rates, martensitic transformation was observed in Fe-10%Cr alloy when the transformation temperature was around 500°C and equiaxed ferrite transformation had prevailed when the transformation temperature was around 600°C (Figure 47). Bee and Honeycombe<sup>62</sup> reported the transformation temperatures of martensite and massive to be 500°C and 580°C, respectively, for Fe-10%Cr alloy (Figure 48). Although transformation temperatures could not be determined in the present study, the observed characteristics of transformation behavior in laser processed Fe-Cr alloys (up to quench rates of  $10^6$ °C/s) suggest that the transformation temperature is higher than necessary to produce martensitic transformation. Unfortunately, there are no published data on the rapid solidification of Fe-Cr alloys with which the present results can be compared. However, the pattern of transformation behavior in laser processed Fe-Cr alloys appears to be consistent with the current understanding of the characteristic non-martensitic mode of decomposition of

Transformation Structures of alloys beyond gamma phase field--In contrast to massive ferrite structures that developed in low chromium alloys, metallographic examination of laser processed high chromium alloys revealed equiaxed ferrite structures. These ferrite grains contained several subgrains oriented in the direction of the heat flow. Solute dumping lines were also evident. Figures 49 and 50 illustrate these aspects of ferritic morphology. It is interesting to note in Figure 49 that the microstructures varied from massive to equiaxed ferrite in the same fusion zone depending on the chromium content.

Transmission electron microscopy--Transmission electron microscopy studies were carried out only on multiple scan laser treated samples. There was no observable differences in the microstructures between single and multiple scan laser melted samples. Figure 51 shows the longitudinal and transverse sections of laser alloyed zones.

Effect of Composition--Transmission electron microscopy studies revealed that all the laser processed Fe-Cr alloys were essentially ferritic in nature, the substructure of which contained dislocations. For a given cooling rate ( $8.0 \times 10^4$  °C/s), an increase in dislocation density was observed qualitatively with an increase in chromium content. Figures 52a-d are the bright field micrographs obtained in 5, 10, 20 and 50%Cr alloys illustrating this aspect. It appears that an increase in chromium content of the alloy caused an increase in the thermal gradient and compositional differences, thereby, enhanced the dislocation density.

Effect of cooling rate--Figures 53a-d illustrate that increasing cooling rates from  $8.0 \times 10^4$  to  $9.0 \times 10^5$  °C/s did not produce a significant effect on the dislocation structures in Fe-5%Cr and Fe-20%Cr alloys. Wilson et al.<sup>58</sup> reported that there was no appreciable increase in dislocation density when the cooling rate was increased from  $2 \times 10^2$  to  $5 \times 10^4$  °C/s for Fe-5%Ni alloy.

Carbide Precipitation-- $M_3C$  and epsilon carbides were observed in laser processed Fe-Cr alloys and are shown in Figures 54 and 55 for Fe-10%Cr alloy. Both carbides decreased with increased chromium content of the alloy. This is attributed to the effect of chromium in reducing the diffusivity of carbon and, thereby, keeping it in solution. Generally low carbon steels are not expected to contain any epsilon carbide<sup>64</sup> and a minimum of 0.25%C is necessary for the precipitation of epsilon carbide.<sup>65</sup> This is contrary to Tekin's results<sup>66</sup> who obtained epsilon carbide in quenched 0.1%C steels. Further, the presence of epsilon carbide in aged low carbon (C = 0.01%) irons indicates that epsilon carbide forms in iron containing less than 0.25%C.<sup>67,69</sup> Epsilon carbide has also been shown to be preferentially precipitated on dislocations in low carbon irons.<sup>68</sup>

Microhardness--Conducted on the fusion zones using a load of 100 gms, Knoop microhardness results as functions of composition and cooling rate are shown in Figure 56. It is apparent that an increase in hardness was obtained with an increase in composition but not with cooling rate. These results were consistent with the observed dislocation structures in Fe-Cr

alloys. High hardness in high chromium alloys is attributed to substitutional solid solution hardening effects coupled with increased dislocation density.

#### 4.4.2. Fe-Ni and Fe-Cr-Ni Systems.

OPTICAL METALLOGRAPHY--Figure 57 presents the equilibrium diagram of the Fe-Ni system. Figures 58 and 59 show the microstructures of laser processed Fe-Ni alloys of various compositions. The microstructures of alloys appear to be martensitic, but the presence of cellular solidification structures have masked the solid state transformation structures. However, there is a variation in the morphology of martensites when the nickel content exceeds 8%. It is interesting to note that the solidification structures are readily apparent in Fe-Ni alloys in contrast to Fe-Cr alloys.

Unlike Fe-Cr and Fe-Ni alloys, laser processed Fe-Cr-Ni alloys exhibited a microstructure typical of martensitic transformation. Figures 60 and 61 are the optical micrographs of various combinations of chromium and nickel, thus illustrating the acicular morphology of martensite.

TRANSMISSION ELECTRON MICROSCOPY--Thin foil transmission electron microscopy studies were carried out only on Fe-5%Ni and Fe-6%Cr-2%Ni alloys as representative of these two alloy systems. In contrast to massive ferrite structures that formed in Fe-5%Cr alloy, transmission electron metallographic examination of Fe-5%Ni and Fe-6%Cr-2%Ni alloys revealed that the microstructures were composed of mixtures of ferrite and

martensite (Figures 62 and 63). The Fe-Ni system is of special interest in that massive transformation was observed in alloys containing less than 15%Ni while alloys having more than 18%Ni transformed by the conventional martensitic mechanism.<sup>54,59</sup> Gilbert and Owen<sup>54</sup> attributed the reason for obtaining martensite in alloys containing more than 18%Ni, even at a low quench rate of 5°C/s, to be due to the lower transformation temperature. Wilson et al.<sup>58</sup> reported massive ferrite transformation in solid state quenched Fe-5%Ni alloy at a quench rate of  $5 \times 10^4$ °C/s and at a transformation temperature of 525°C (Figure 64). But Swanson and Parr<sup>57</sup> were able to suppress the massive transformation in alloys containing 0-10%Ni at a quench rate of  $1.5 \times 10^4$ °C/s and produced martensitic transformation as revealed by surface relief (Figure 65). They also observed that the critical cooling rate required to produce martensitic transformation is  $3 \times 10^4$ °C/s for 1%Ni alloy and  $1.5 \times 10^4$ °C/s for 10%Ni alloy. Goodenow and Hehemann<sup>59</sup> reported a lathlike substructure in rapidly quenched ( $2.5 \times 10^3$ °C/s) Fe-9%Ni alloy analogous to that of low carbon martensite. Speich and Swann,<sup>70</sup> using thin foil electron microscopy, identified a lathlike cell structure in ice-brine quenched alloys containing 6 to 25%Ni. But they observed that the structure of alloys containing 0 to 4%Ni were blocky grains of ferrite with low dislocation density. They attributed that the discontinuous change in the transformation behavior at 6%Ni was due to a change in the transformation mechanism from massive to martensitic. Unlike Fe-Cr and Fe-Ni alloy systems, there is very limited data reported on the effect of high quench rate on the microstructures of Fe-Cr-Ni alloys. Speich<sup>72</sup> has plotted a

nonequilibrium diagram for Fe-Cr-Ni alloy quenched from 1100°C. According to this plot, 6%Cr-2%Ni alloy should exhibit both massive ferrite and lath martensite.

The presence of ferrite and martensite in laser processed Fe-5%Ni and Fe-6%Cr-2%Ni alloys suggest that there is a change in the solid state transformation mechanisms during rapid quenching. Under equilibrium conditions, as predicted by the constitution diagrams, both alloys should undergo a transformation from austenite/ferrite to ferrite. It is believed that rapid quenching, as achieved in the laser alloying process, is able to suppress the transformation of the austenite/ferrite mixture to ferrite but permits the austenite to transform to martensite, resulting in a microstructure consisting of martensite and ferrite.

#### 4.4.3. Fe-0.2%C-Cr System.

OPTICAL METALLOGRAPHY--Figure 66 is the vertical section of the ternary equilibrium diagram of Fe-0.2%C-Cr system, illustrating different phase transformations at different chromium contents. Figures 67 to 70 present the optical micrographs of single scan laser processed Fe-0.2%C-Cr alloys at various chromium contents except Figure 67c-d which represent the microstructures of multiple scan laser melted specimens. The microstructures of alloys containing chromium up to 13% were fully martensitic in nature. Single scan vs. multiple scan laser melted alloys (Figure 67) revealed a difference in the fineness of martensite. These microstructures show neither the presence of carbides nor the resolution of any other second phase. When the chromium content exceeded 14%, a new type of

microstructure characterized by the presence of needles embedded in a matrix was observed. The density of such needles was found to increase with an increase in chromium contents up to 23%. In accordance with the phase diagram, these alloys should undergo a solid state transformation of austenite/ferrite mixture to ferrite/carbide mixture. The final microstructures of laser processed alloys containing 15 to 23%Cr might have contained a ferrite matrix concurrent with the equilibrium diagram, but the needles could not be identified by optical microscopy. When the chromium content of the alloy reached 30% and beyond, the microstructures consisted of equiaxed ferrite grains.

#### TRANSFORMATIONS OF ALLOYS(0-10%Cr) WITHIN THE GAMMA PHASE FIELD--

##### Transmission Electron Microscopy--(Martensitic Substructure)--

Transmission electron microscopy studies of laser processed 5 and 10%Cr alloys resulted in a microstructure consisting of lath martensite occurring in packets. Figures 71 to 76 are the bright field micrographs of 5 and 10%Cr alloys at various cooling rates. The laths were predominantly dislocated, however, some internal microtwinning in a few laths was also observed. Internal twinning in some individual laths has also been shown by many previous investigators for plain carbon and alloy steels.<sup>81,86</sup> The laths within a packet of martensite were separated by low angle boundaries, although in some regions twin related laths were also observed. In concurrence with the observations of other investigators,<sup>87</sup> these laths of martensite are predominantly in juxtaposition to  $(100)_M$  and  $(111)_M$  orientations. Careful analysis of lath martensitic structures

indicated the presence of at least three types of lath morphologies, viz. convergent laths, regular parallel laths and large laths containing extensive autotempered carbides. Regular parallel laths were most frequently observed with individual laths having planar boundaries. Large laths containing carbides were also observed and most probably they might have formed in the early stages of transformation.<sup>76</sup>

The cooling rate did not have a significant effect on the morphology and substructure of martensites. For all the cooling rates, the martensitic substructures were made up of packets of fine parallel laths. Messler et al.<sup>78</sup> reported that at slow quench rates, the martensite laths consisted of less parallel, thicker, more lenticular laths, but the degree of perfection of alignment among parallel laths increased as the quench rate increased. Messler et al. explained the appearance of particular morphology based on the conditions under which growth takes place. Donachie and Ansell<sup>77</sup> observed twinned laths in fast quenched ( $4 \times 10^4$  °C/s) low carbon steel. They attributed the morphology change to the deformation mode of austenite. The presence of twins, however, was seldom observed in this investigation in spite of very high quench rates ( $7 \times 10^5$  °C/s). It is possible that the twins in martensite may not have been induced because the limiting dislocation density has not yet been attained.<sup>75</sup> There was no change in morphology and substructures of martensite observed between 5 and 10%Cr alloys. Kelly and Nutting<sup>73</sup> attributed the change in morphology and substructure of austenite to stacking fault energy and  $M_s$  temperature. Lowering  $M_s$  temperature or raising stacking fault energy favor the formation of twinned martensite.

The addition of chromium to a steel lowers the  $M_s$  temperature and also lowers the stacking fault energy, thereby producing opposing effects.<sup>73</sup>

Transmission Electron Microscopy--(Retained Austenite)--Although retained austenite was not identified in x-ray diffraction work, transmission electron microscopy studies of 5 and 10%Cr alloys clearly proved the existence of thin films of retained austenite at interlath boundaries and at prior austenite grain boundaries. Figures 77 to 79 illustrate the typical interlath film morphology of retained austenite in laser processed 5 and 10%Cr alloys at various cooling rates. Analysis of SAD patterns, as illustrated in these Figures, revealed that the orientation relationship between the austenite and martensite was the Kurdjumov-Sachs type, i.e.,  $(011)_\alpha \parallel (111)_\gamma$ ,  $[111]_\alpha \parallel [110]_\gamma$  and the Nishiyama-Wessermann type, namely  $(011)_\alpha \parallel (111)_\gamma$ ,  $[100]_\alpha \parallel [101]_\gamma$ . The most significant conclusion in this study is that with an increase in the cooling rate, there is a decrease in the amount of retained austenite. At this point, it is important to emphasize that the above conclusion is based upon the examination of a number of thin foils. Unlike the cooling rate, the chromium contents did not exhibit any difference in the amounts of retained austenite.

The presence of retained austenite in quenched steels is attributed to the following factors: (1) Grain size, (2)  $M_s$  temperature, (3) carbide precipitation, (4) austenite shear strength, and (5) alloy content. Several models have been proposed<sup>77-80,82,83</sup> to explain the stabilization of austenite at room temperature. They primarily include chemical

stabilization (carbon partitioning from lath martensite to the surrounding austenite during transformation or carbon-dislocation interactions inhibiting transformation), thermal stabilization (lowering  $M_s$  temperature), and mechanical stabilization (plastic deformation in austenite accompanying the shear transformation). The effect of the quench rate in reducing the amount of austenite in the present study appears to be a combined effect of thermal and chemical stabilization. It is generally agreed that<sup>77-80</sup>  $M_s$  temperature increases with increases in quench rates in solid state quenched martensitic steels. In terms of Ansell and Arrot's model,<sup>79</sup> increasing quench rate decreases the time available for carbon segregation to the structural imperfections in the austenite. As a result, the equilibrium carbon concentration in the carbon-defects atmospheres is not obtained. The austenite is no longer as effectively strengthened by the segregation of carbon to imperfections and the transformation to martensite can occur more easily. Thus, an increase in  $M_s$  temperature and a reduction in austenite shear strength with an increase in quench rate are probably responsible for the observed decrease in the amounts of retained austenite.

Transmission Electron Microscopy--(Carbide Precipitation)-- $\epsilon$ -carbide and  $M_3C$  carbide were observed in both 5 and 10%Cr alloys irrespective of quench rates (Figures 77 and 80). But the carbides were more pronounced in 5%Cr than 10%Cr alloy. The carbides were present both at the lath boundaries and within the laths. The shape and size of carbide particles was not influenced by the quench rates.

Microhardness--Knoop microhardness tests (load 500 gms) as functions of the composition and cooling rate, and single vs. multiple pass laser melted alloys (Figure 81), had shown that an increase in hardness was obtained with an increase in chromium contents of the alloy; nevertheless, cooling rate did not influence the hardness. Further single pass alloys exhibited higher hardness than multiple pass alloys for a given composition and cooling rate.

TRANSFORMATIONS OF ALLOYS (15-25%Cr) WITHIN GAMMA/ALPHA PHASE FIELD--An alloy containing 20%Cr was selected as a representative of alloys within austenite/ferrite phase field for detailed microstructural investigations.

Scanning Electron Microscopy--Figure 82a-c shows the transverse sections of single scan and multiple scan laser processed 20%Cr alloys. Figure 83a is a scanning electron micrograph of a single pass laser alloyed zone (penetration depth: 600 microns) showing austenite needles in a ferrite matrix. But, the microstructure of the multiple pass laser alloyed zone (penetration depth: 600 microns) contained a mixture of martensite and ferrite (Figure 83b). However, when the same alloy was produced by multiple pass to a penetration depth of 120 microns (using different laser parameters and thin coating), the austenite did not transform to martensite (Figure 83c). Though scanning electron microscopy could not positively identify these phases, transmission electron microscopy studies, shown in the following section, confirmed these microstructural features.

Transmission Electron Microscopy--("Single Scan" Laser Processed Alloy)--Transmission electron microscopy studies of a single scan laser processed alloy resulted in a microstructure consisting of internally twinned austenite needles in a dislocated ferrite matrix (Figures 84 and 85). The presence of strong FCC reflections and the associated twin spots in the electron diffraction patterns implied that these needles were austenite containing a high density of twins. The formation of twins in face centered austenite is believed to be due to the enrichment of carbon and chromium caused by rapid quenching. Recently, Sandvik and Nevalainen<sup>94</sup> have reported the presence of transformation twins in austenite of isothermally transformed high carbon high silicon steels.

Transmission Electron Microscopy--("Multiple Scan" Laser Processed Alloy)--When the alloy was produced to a penetration depth of 600 microns by multiple scan laser processing, the austenite transformed to dislocated lath martensite resulting in a mixture of martensite and ferrite (Figures 86 and 87). Thin films of retained austenite were observed at interlath boundaries, but the carbide precipitation was not identified. However, when the alloy was produced to a penetration depth of 120 microns (using a thin coating), the austenite did not transform to martensite (Figure 88). This might very well explain the fact that the transformation reaction from austenite to martensite is strongly dependent on laser beam parameters (or penetration depth) which, in turn, decide the degree of rapid thermal cycles (temperature and quench rate) involved in multiple scan laser processing.

Tempering Behavior of "Single Scan" Laser Processed Alloys--Single scan laser processed alloys were solution treated at various temperatures (100 to 1200°C) and times (5 min to 1 hr) and then water quenched to study the stability of austenite in the microstructures. The results obtained indicate that the austenite needles remained stable up to 900°C without any subsequent transformation. At 1000°C (1 hr), the austenite needles were partially decomposed giving rise to a mixture of ferrite and carbide. At 1200°C (5 min), the austenite had completely transformed to ferrite and fine carbides. Figures 89a-c illustrate the effects of tempering on the microstructures of single pass laser processed alloys.

Microhardness--Knoop microhardness tests (load 500 gms) were carried out on the fusion zones of single and multiple pass laser processed alloys and also on the furnace heat treated single pass alloys. The results are summarized in the table on the next page.

Discussion--Thin foil transmission electron microscopy studies of laser processed Fe-0.2%C-20%Cr alloys revealed several unique microstructural features and also indicated the complex phase transformation mechanisms associated with rapid quenching. The as-quenched "single pass" processed alloys contained austenite and ferrite and were observed independently of melt penetration depths. But the multiple pass laser processed alloys (quenched and tempered) exhibited a mixture of martensite and ferrite depending on melt penetration depths (or heat input).

Treatment	Microhardness KHN
1. SINGLE PASS	
A. As-quenched	390 (R <sub>c</sub> 39)
B. Heat treated at 1000°C for 1 hr and water quenched	316 (R <sub>c</sub> 31)
C. Heat treated at 1200°C for 5 min and water quenched	219 (R <sub>B</sub> 94)
2. MULTIPLE PASS	430 (R <sub>c</sub> 43)

During multiple pass laser processing, high heat inputs resulted in the transformation of austenite to martensite, while low heat inputs retained the stability of austenite. The results obtained in conventional solid solution treated and water quenched single pass alloys substantiated the effect of heat input on the stability of austenite. The most significant observation in this investigation is the absence of carbide precipitation in both single and multiple pass laser processed alloys.

The retention of nonequilibrium face centered austenite along with equilibrium body centered ferrite is essentially a consequence of rapid solidification. Inoue et al.<sup>100</sup> observed austenite single phase structures in splat quenched Fe-1.6%C-17%Cr steels. They attributed this to the combined effects of supercooling of the austenite phase, increased solid solubilities of carbon and chromium in austenite, and lowering of

$M_s$  temperature by the dissolution of these elements. Several investigators<sup>101-110</sup> also reported an enhancement in austenite retention in splat quenched steels. They suggested that the retention of austenite in rapidly solidified steels was associated with (1) the enrichment of alloying elements in austenite, (2) fine as-solidified austenite grain size, and (3) lack of carbide precipitation. It is apparent from the above discussion that the retention of austenite in laser processed alloys is a result of increased solid solubilities of carbon and chromium which, in turn, increased austenite shear strength. However, the transformation of austenite in single pass alloys to martensite in multiple pass alloys, subject to melt penetration depths, suggests that the austenite was weakened by the degree of solid state thermal cycles involved. The weakening of austenite was attributed to the depletion of alloying elements caused by the high heat inputs (this is also substantiated by the furnace heat treatments). But the transformation of weakened austenite to martensite was essentially related to the high quench rates obtained in laser processing because conventional heat treated and water quenched single pass alloys did not reveal the presence of martensite in the microstructures. Donachie and Ansell<sup>77</sup> proposed that austenite shear strength is considerably lower at high quench rates during solid state quenching and, hence, the transformation to martensite can occur more easily. This might provide a possible explanation for the martensitic transformation in multiple pass laser processed alloys. However, there is no substantial evidence for this supposition in this investigation.

TRANSFORMATIONS OF ALLOYS ( $>30\%Cr$ ) BEYOND THE GAMMA PHASE FIELD--

Optical and transmission electron microscopy studies of laser processed alloys containing chromium 30% and more revealed essentially a dislocated ferritic structure with  $M_{23}C_6$  carbides at the grain boundaries and within the matrix (Figures 90 and 91). The phase transformation sequence for these alloys, under equilibrium conditions, is given as follows:  $L \rightarrow L + \alpha \rightarrow L + \alpha + M_{23}C_6 \rightarrow \alpha + M_{23}C_6$ .  $M_{23}C_6$  carbide, formed directly from the melt, was not prevented by the rapid solidification. This also indicates that there is no difference in the phase transformation sequence for these alloys between equilibrium and rapid solidification.

#### 4.4.4. Fe-0.5%C-Cr System.

SCANNING ELECTRON MICROSCOPY--Figures 92a-d are the representative micrographs showing the transverse section and microstructures of laser processed Fe-0.5%C-Cr alloys. The transformation structures of these steels consists of martensite, austenite and ferrite depending on the chromium content. Though scanning electron microscopy could not identify these phases unambiguously, thin foil transmission electron microscopy studies, shown in the following section, revealed that (1) 10%Cr alloy (Figure 92b) consisted of a mixture of dislocated and twinned lath martensites, (2) 20%Cr alloy (Figure 92c) contained a mixture of austenite and ferrite phases, and (3) 40%Cr alloy (Figure 92d) exhibited a cellular ferritic structure surrounded by  $M_{23}C_6$  carbides at the cell boundaries.

## TRANSMISSION ELECTRON MICROSCOPY--

Martensitic Transformations of 10%Cr alloy--Transmission electron microscopy (TEM) studies of laser processed 10%Cr alloy resulted in a microstructure consisting of a mixture of dislocated/twinned lath martensites (Figure 93). The lath martensite had occurred as packets and the individual martensitic laths were seen as a fine substructure within packets. Regular parallel and large laths were frequently observed. The formation of twins within lath martensite may be related to high quench rates. The effect of quench rate on martensitic morphology and substructure had been studied by several investigators. Boniszewski<sup>93</sup> observed a transition from dislocated lath to twinned plate martensite with an increase in quench rate in carbon and alloy steels. Messler et al.<sup>78</sup> found that increasing the quench rate caused an increase in twin density in lath structures. Donachie and Ansell<sup>77</sup> showed that fast quenched high carbon steels were composed of twinned plates compared to slow quenched specimens. Thomas<sup>75</sup> postulated that fast cooling retains solutes in solution resulting in twinned plate martensites. Sare and Honeycombe<sup>103</sup> observed twinned plate martensites in splat quenched Fe-4%Mo-0.2%C steels which was different from dislocated lath martensite in solid state quenched material. Donachie and Ansell<sup>77</sup> explained the morphological change at high quench rates to be due to a change in the deformation mode of parent austenite.

Isolated pools and thin films of retained austenite were observed at the interlath, packet and prior austenite grain boundaries (Figure 121). The presence of retained austenite in quenched steels was

attributed to several microstructural parameters including grain size,  $M_s$  temperature, austenite shear strength, and carbide precipitation. In the present study, the retention of austenite is believed to be due to high austenite shear strength caused by the enrichment of alloying elements. In addition to retained austenite, fine  $M_3C$  carbides, dispersed homogeneously at the lath boundaries and within laths, were observed (Figure 94).

Transformation of 20%Cr Alloy--TEM studies of 20%Cr alloy revealed a microstructure consisting of twinned/dislocated austenite and dislocated ferrite grains (Figures 95a-d). The presence of strong FCC reflections and the associated twin spots in the diffraction patterns implied that the dark grains with convoluted grain boundaries in the micrographs 95a-d (also Figure 96) were austenite containing a high density of lattice defects. There is no morphological difference observed between austenite and ferrite. Further, there is no evidence of any carbide precipitation in the microstructures of this alloy. Several investigators<sup>101-110</sup> into the effects of splat quenching on the microstructures of Fe-Ni, Fe-Ni-C, Fe-Mo-C, Fe-Cr-C, Fe-W-C and high speed tool steels had shown an enhancement in austenite retention compared to solid state quenched specimens. This was attributed to the increased solid solubilities of alloying elements in austenite, lack of carbide precipitation, fine as-solidified austenite grain size, and supercooling of austenite phase.

Transformation of 40%Cr Alloy--In contrast to martensitic and austenitic/ferritic structures of 10 and 20%Cr alloys, laser processed 40%Cr alloy exhibited essentially a dislocated ferritic structure with grain boundaries containing  $M_{23}C_6$  carbides (Figure 97a-d). The cellular morphology of ferrite, a characteristic of solidification structure, suggests that it is a high temperature delta ferrite; therefore, subsequent solid state transformation to alpha ferrite may not have occurred. This conclusion is based on the equilibrium diagram considerations and the results obtained by other investigators in rapidly solidified alloys. Sare and Honeycombe<sup>101</sup> in splat quenched M2 tool steel and Fe-0.5%C-10% Mo alloys, Rayment and Cantor<sup>102</sup> in splat quenched Fe-0.5%C-23%W alloys, and Strutt et al.<sup>15</sup> in laser melted tool steels, had shown a similar cellular ferritic structure and concluded it to be delta ferrite. The cell boundaries were enriched with  $M_{23}C_6$  carbides (Figure 98). The equilibrium transformation sequence was not altered by rapid solidification for this alloy composition.

MICROHARDNESS--Knoop microhardness studies conducted on the fusion zones as a function of chromium content (and, thereby, the microstructures) indicated that 10%Cr alloy had a hardness of 730 KHN ( $R_c 60$ ) followed by 20%Cr alloy with a hardness of 588 KHN ( $R_c 54$ ) and 40%Cr alloy with a hardness of 316 KHN ( $R_c 31$ ). It is worthwhile to note that austenite/ferrite structures of laser processed Fe-0.5%C-20%Cr alloy possessed a hardness close to that of martensitic 10%Cr alloy.

GENERAL DISCUSSION--The results of thin foil transmission electron microscopy studies of laser processed Fe-0.5%Cr alloys have shown that chromium has a potential effect on the stabilization of austenite under rapid solidification conditions. First, the solid state transformation of austenite to martensite and  $M_3C$  carbides had occurred in 10%Cr alloy. Second, the alloy containing 20%Cr did not permit the transformation of austenite to martensite or equilibrium carbide/ferrite mixture. Finally 40%Cr alloy contained a dislocated cellular ferritic structure with cell boundaries enriched with  $M_{23}C_6$  carbides, which is similar to the equilibrium solidification microstructures. Thus, depending on the chromium content of an alloy, the equilibrium solid state transformations were either suppressed or followed under rapid solidification conditions. The equilibrium solidification sequence<sup>23</sup> and the predicted rapid solidification sequence for these alloys are shown on the next page.

#### 4.4.5. Fe-1.0%Cr System.

SCANNING ELECTRON MICROSCOPY--Figures 99a-d present the transverse section and microstructures of laser processed Fe-1.0%Cr alloys. The transformation structure of 10%Cr alloy consisted of plate martensite in an austenite matrix. Alloys containing 20 and 40%Cr exhibited fine solidification structures. Transmission electron microscopy is required to identify the solid state transformation structures of these alloys.

Fe-0.5%C-Cr SYSTEM

Alloy	10% Cr	20% Cr	40% Cr
Equilibrium solidification sequence	L → L + δ → L + δ + γ → γ + K <sub>1</sub> + K <sub>2</sub> → α + K <sub>1</sub> + K <sub>2</sub>	L → L + δ → L + δ + γ → α + γ → α + γ + K <sub>1</sub>	L → L + δ → L + δ + K <sub>1</sub> → δ + K <sub>1</sub> → α + K <sub>1</sub>
Rapid solidification sequence	L → L + δ → L + δ + γ → α' + K <sub>c</sub>	L → L + δ → L + δ + γ → α + γ	L → L + δ → L + δ + K <sub>1</sub> → δ + K <sub>1</sub>

Key: α = ferrite; δ = ferrite; γ = austenite; K<sub>1</sub> = M<sub>23</sub>C<sub>6</sub> carbide; K<sub>2</sub> = M<sub>7</sub>C<sub>3</sub> carbide; α' = martensite; K<sub>c</sub> = M<sub>3</sub>C carbide.

## TRANSMISSION ELECTRON MICROSCOPY--

Martensitic Transformations in 10% Cr Alloy--Figures 100a to d are the representative thin foil transmission electron micrographs of 10%Cr alloy illustrating the morphology and substructure of martensite in austenite matrix. The martensite morphology was characterized by nonparallel and lenticular plates. The martensite plates were found to be at an angle to each other. There was a size variation among the martensite plates which was attributed<sup>74</sup> to continued partitioning of austenite through the transformation. There was very little evidence of any discontinuity, corresponding to the martensite mid-rib, observed in any of the martensite plates. The habit planes of these plates, as revealed by trace analysis, were often (225)<sub>γ</sub> in concurrence with the observations of Shimizu et al.<sup>97</sup> in water quenched and sub-zero treated

Fe-1.0%C-8%Cr alloy. The substructure of plate martensite essentially contained fine transformation twins (Figures 101a and b). The mode of twinning was found to be  $(112)_\alpha$  type. A dislocation substructure within the plates was seldom observed. The microstructure of this alloy also contained lath martensites in a few areas (Figures 101c and d).

The electron diffraction analysis of the microstructures of 10%Cr alloy did not reveal the presence of any carbide reflection. Due to the complexities arising from double diffraction spots, the carbides, if any, present in the microstructures could not be uniquely identified. It is possible that the carbides might have been present in the microstructure but probably on a finer scale. It is important at this stage to point out that significant amounts of  $M_3C$  carbide were observed (and had been identified without any difficulty) in laser processed Fe-0.5%C-10%Cr alloys produced under the same laser beam conditions. The major difference in the microstructures between 0.5%C-10%Cr and 1.0%C-10%Cr alloys was the martensitic morphology, namely plate martensite in the latter and lath martensite in the former. It appears that plate martensitic morphology has minimized the precipitation of carbide during the rapid thermal cycle involved in multiple pass laser melting.

Transformation Behavior of 20%Cr Alloy--Transmission electron microscopy studies of laser processed 20%Cr alloy revealed a cellular microstructure consisting of predominantly austenite with small amounts of ferrite and  $M_{23}C_6$  carbide (Figures 102 and 103). The substructure of cellular austenite was found to contain dislocations, twins and

stacking faults. The identification of ferrite required diffraction and dark field analysis. The cell boundaries contained appreciable amounts of  $M_{23}C_6$  carbide.

Transformation of 40%Cr Alloy--The transformation structure of 40%Cr alloy exhibited a cellular ferritic structure with cell boundaries containing  $M_{23}C_6$  carbides (Figures 104 and 105). This is similar to the transformation structures of laser processed Fe-0.5%C-40%Cr alloys described earlier.

GENERAL DISCUSSION--The overall picture which emerges from thin foil transmission electron microscopy studies of laser processed, rapidly solidified Fe-1.0%C-Cr steels is that the phase transformation mechanism has varied depending on the chromium content of the alloy. First considerable amounts of austenite had transformed to plate martensite in 10%Cr alloy but no evidence of such a transformation was observed when the chromium content of the alloy was increased to 20%. Further, 20%Cr alloy exhibited  $M_{23}C_6$  carbides at the grain boundaries but the presence of carbide was not detected in 10%Cr alloy. The microstructure of 40%Cr alloy contained presumably a high temperature delta ferrite but rapid quenching did not stabilize the high temperature  $M_7C_3$  carbide.

The equilibrium solidification and solid state transformation sequences, obtained from a binary section of the ternary Fe-Cr-C phase diagram,<sup>23</sup> are shown in the following table. Also given are the

predicted phase transformation sequences under rapid solidification conditions as achieved in the present investigation.

Alloy	10% Cr	20% Cr	40% Cr
Equilibrium solidification sequence	$L \rightarrow L + \gamma \rightarrow \gamma + K_2 \rightarrow \alpha + \gamma + K_2$	$L \rightarrow L + \delta \rightarrow L + \delta + \gamma \rightarrow L + \gamma + K_1 \rightarrow \gamma + K_1 + K_2 \rightarrow \alpha + \gamma + K_1 + K_2$	$L \rightarrow L + \delta \rightarrow L + \delta + K_2 \rightarrow \delta + K_1 \rightarrow \alpha + K_1$
Rapid solidification sequence	$L \rightarrow L + \gamma \rightarrow \gamma \rightarrow \alpha' + \gamma$	$L \rightarrow L + \delta \rightarrow L + \delta + \gamma \rightarrow L + \delta + \gamma + K_1 \rightarrow \delta + \gamma + K_1$	$L \rightarrow L + \delta \rightarrow L + \delta + K_2 \rightarrow \delta + K_1$

Key:  $\alpha$  = ferrite;  $\delta$  = ferrite;  $\gamma$  = austenite;  $K_1$  =  $M_{23}C_6$  carbide;  $K_2$  =  $M_7C_3$  carbide;  $\alpha'$  = martensite.

The observations of martensitic structures in 10%Cr alloy suggest that this alloy had undergone solid state transformations. However, the lack of carbide precipitation indicates that the carbide reactions had been arrested by rapid quenching. The observations of cellular morphologies of austenite and ferrite (direct products of solidification) in 20%Cr alloy suggest that solid state transformations were completely suppressed by rapid quenching. The rapid cooling transformation sequence of 40%Cr alloy is very similar to the equilibrium sequence except that the ferrite observed may be a high temperature delta ferrite as evident from the cellular morphology. It is interesting to note that

rapid solidification had permitted the transformation of  $M_3C_3$  carbide to  $M_{23}C_6$  carbide in this alloy.

4.4.6. General Discussion/Summary of Solid State Transformation Structures. Optical, scanning and thin foil transmission electron microscopy studies of the microstructures of laser processed Fe-C-Cr alloys indicated the complex phase transformation mechanisms associated with rapid solidification processing. However, some generalities can be made, especially regarding the chromium content of the alloy on the phase transformation sequences. The results of microstructural features obtained in this investigation are summarized in the following table. Also shown are the equilibrium phases in parentheses.

Alloy System Cr Content	Fe-0.2%Cr	Fe-0.5%Cr	Fe-1.0%Cr
10%	Lath martensite + $M_3C$ carbide + Retained austenite  (Ferrite + $M_{23}C_6$ )	Lath martensite + $M_3C$ carbide + Retained austenite  (Ferrite + $M_7C_3$ + $M_{23}C_6$ )	Plate martensite Retained austenite  (Ferrite + $M_7C_3$ )
20%	Ferrite + Austenite  (Ferrite + $M_{23}C_6$ )	Ferrite + Austenite  (Ferrite + $M_{23}C_6$ )	Austenite + $M_{23}C_6$ Ferrite  (Ferrite + $M_{23}C_6$ )
40%	Equiaxed Ferrite + $M_{23}C_6$  (Ferrite + $M_{23}C_6$ )	Cellular Ferrite + $M_{23}C_6$  (Ferrite + $M_{23}C_6$ )	Cellular Ferrite + $M_{23}C_6$  (Ferrite + $M_{23}C_6$ )

The most significant finding of this study was the transformation of austenite to martensite in 10%Cr alloys and the retention of high temperature austenite in 20%Cr alloys regardless of carbon contents (0.2 - 1.0%). Further, there was no evidence of any carbide precipitation in laser processed Fe-C-20%Cr alloys (the exception being Fe-1.0% C-20%Cr) in contrast to Fe-C-10%Cr alloys which suggest that there is an increased solid solubility of carbon and chromium in austenite (assuming the solubility of chromium in ferrite and austenite are the same) of 20%Cr alloys. It, therefore, appears that the strength of austenite containing chromium is higher than the austenite containing carbon. A comparison of the microstructures of rapidly solidified, laser processed Fe-0.2%C-20%Cr and Fe-1.0%C-10%Cr alloys confirms this feature. Hence, it is postulated that under rapid solidification conditions, the substitutional chromium has a greater effect in increasing the strength of austenite than the interstitial carbon and, thereby, increases the resistance to shear and diffusion-controlled transformations. Additional experimental data such as the composition of austenite (carbon and chromium) and hardness are required to confirm this hypothesis. The results obtained by Inoue et al.<sup>100</sup> in splat quenched Fe-C-Cr steels (Figure 106) are similar to the present investigation, but there seems to be a disagreement in a few cases. They observed austenite single phase structures in alloys of the type Fe-C-20%Cr for carbon levels greater than 0.5%. But the present investigation had shown duplex austenite/ferrite structures in such alloys. Further,

they did not report  $M_{23}C_6$  carbides in rapidly solidified Fe-1.0%C-20%Cr steels which had been observed in this investigation.

Another interesting observation is the complete suppression of equilibrium solid state carbide precipitations in laser processed Fe-C-20%Cr alloys. But, the existence of equilibrium solidification  $M_{23}C_6$  carbide in Fe-1.0%C-20%Cr alloys indicates that rapid solidification could not prevent the equilibrium liquid to solid reactions. The absence of  $M_3C$  carbide in 20%Cr alloys in contrast to 10%Cr alloys suggest that chromium reduces the diffusivity of carbon and keeps it in solution. Further, the formation of nonequilibrium  $M_3C$  carbide (instead of equilibrium  $M_3C_3$  and  $M_{23}C_6$  carbides) in laser processed Fe-C-10%Cr alloys shows the major role of kinetics in controlling the solid state carbide transformations.

The micrographs of laser processed ferritic Fe-C-40%Cr alloys showed different morphologies of ferrite depending on the carbon content of the alloy. In Fe-0.2%C-40%Cr alloys, the ferrite possessed equiaxed grain morphology and the microstructures did not indicate any evidence of solute segregation. On the other hand, Fe-0.5%C(1.0%C)-40%Cr alloys exhibited a cellular solidification morphology of ferrite with the segregation of carbon and chromium to the intercellular boundaries. Sare and Honeycombe<sup>101</sup> observed elongated grain morphology and cellular morphology of delta ferrite in splat quenched Fe-0.2%C-4%Mo and Fe-0.5%C-10%Mo alloys, respectively. They proposed that the degree of undercooling obtained in rapid quenching relative to the equilibrium liquid to solid freezing range decides the solidification morphologies of

ferrite phases. If the undercooling is more than the equilibrium liquid to solid freezing range, then the alloy will solidify as a homogeneous solid solution resulting in a grain morphology. On the contrary, if the undercooling is less than the equilibrium liquid to solid freezing range, then the solidification will commence above the solidus and considerable solute segregation will occur resulting in a cellular solidification morphology. In the present investigation, the equilibrium liquid to solid freezing range is nearly the same ( $210^{\circ}\text{C}$ ) for both Fe-0.2%C-40%Cr and Fe-1.0%C-40%Cr alloys. Assuming the above hypothesis is valid, then the degree of undercooling achieved between Fe-0.2%C-40%Cr and Fe-1.0%C-40%Cr alloys should be different for a given cooling rate. The present work confirms the earlier observations regarding the change in morphology of ferrite where increase in carbon content is concerned. But the effect of carbon in changing the degree of undercooling and, thereby, changing the solidification mode from plane front to cellular is emphasized.

## 6. CONCLUSIONS

The effects of rapid melting and subsequent quenching on the solidification behavior and solid state transformation structures of laser surface alloyed Fe-Cr, Fe-Ni, Fe-Cr-Ni and Fe-Cr-C systems were investigated. The principal results and conclusions are as follows:

1. The laser parameters and coating variables should be closely controlled to obtain the satisfactory results.
2. The fineness of solidification structures indicated that the cooling rates attained were of the order  $10^3 - 10^6$ °C/sec.
3. The microstructures of Fe-Cr alloys were ferritic irrespective of composition and cooling rate.
4. The microstructures of Fe-Ni and Fe-Cr-Ni alloys were a mixture of ferrite and martensite.
5. Unique microstructures of nonequilibrium austenite and equilibrium ferrite were observed in alloys of the type Fe-20%Cr-C. The substructure and morphology of austenite were a function of the carbon content.

## REFERENCES

1. E. M. Breinan, B. H. Kear, and C. M. Banas, "Physics Today", 29, 11, 44 (1976).
2. J. P. Ayres, and R. J. Schaefer, "Consolidation of Plasma-Sprayed Coatings by Laser Remelting", Proc. on the SPIE Vol. 198, Aug. 27-28, 1979, San Diego.
3. L. S. Weinman, J. N. Devault, and P. Moore, "Properties of Rapidly Solidified Laser Surface Alloyed, Low Carbon Steels", Applications of Lasers in Materials Processing, April 18-20, 1979, Washington, DC.
4. F. D. Seaman and D. S. Gnanamuthu, "Using the Industrial Laser to Surface Harden and Alloy", Metals Progress, p. 67, August 1975.
5. W. E. Wood, "Laser Remelting of Surface Alloyed 6150 Steel", Oregon Graduate Center, 1979.
6. P. Moore, C. Kim and L. S. Weinman, "Topographical Characteristics of Laser Surface Melted Metals", Laser-Solid Interactions and Laser Processing, Nov. 28 - Dec. 1, 1978, Boston, MA.
7. D. Beck, and S. M. Copley, "Solidification of Superalloy Melts Produced by Laser Irradiation", Rapid Solidification Processing and Principles, Edited Mehrabian, Cohen, Claitors, 1978.
8. T. R. Anthony, and H. E. Cline, "Journal of Applied Physics", 49, 3, 1298, (1978).
9. T. R. Anthony, and H. E. Cline, "Journal of Applied Physics", 48, 9, 3888, (1977).
10. L. S. Weinman, and J. N. Devault, "A Microprobe Study of Rapidly Solidified Laser Surface Alloyed Low Carbon Steels", Symposium on 'Laser-Solid Interactions and Laser Processing', Nov. 28 - Dec. 1, 1978, Boston, MA.
11. L. S. Weinman and C. Kim, "Rapid Solidification Processing and Principles", Edited Mehrabian, Claitors, 1978.
12. E. M. Breinan, and B. H. Kear, "Rapid Solidification of Laser Processing of Materials for Microstructure and Properties", Rapid Solidification Processing and Principles, Edited Mehrabian, Cohen, Claitors, 1978.
13. J. P. Carstens and G. L. Whitney, "Industrial Applications of High Power Lasers", United Tech. Research Center.

14. P. Moore, C. Kim, and L. S. Weinman, "Processing and Properties of Laser Surface Melted Titanium Alloys", ASM Conference--Applications of Lasers in Materials Processing, April 18-20, 1979, Washington, DC.
15. Y. W. Kim, P. R. Strutt, and H. Nowotny, "Laser Melting and Heat-Treatment of M2 Tool Steel", to appear in Metallurgical Transactions.
16. P. R. Strutt, M. Tuli, H. Nowotny, and B. H. Kear, "Laser Surface Melting of High Speed Tool Steels", Mat. Sci. & Engineering, 36, (1978), 217).
17. P. R. Strutt, D. A. Gilbert, and H. Nowotny, "Heat Treatment of Laser Melted M2 Tool Steel", Proceedings of Laser Materials Processing--Material Research Conference, Nov. 1978, Boston.
18. Laser Institute of America, "Guide for Material Processing by Lasers".
19. J. F. Reedy, "Change of Reflectivity of Metallic Surfaces during Irradiation by CO<sub>2</sub>-TEA Laser Pulses", IEEE Journal of Quantum Electronics, Feb. 1976, pp. 137-162, Vol. QE-12, No. 2.
20. T. J. Wieting and J. L. Derosa, "Effects of Surface Condition on the Infrared Absorptivity of 304 Stainless Steel", J. Appl. Phys., 50 (2), February 1979.
21. T. J. Wiering and J. T. Schriempf, "Infrared Absorptances of Partially Ordered Alloys at Elevated Temperatures", J. Appl. Phys., 47 (9), Sept. 1976.
22. W. W. Duley, D. J. Semple, and M. Gravel, "Coupling Coefficient for CW CO<sub>2</sub> Laser Radiation on Stainless Steel", Optics and Laser Technology, Dec. 1979, p. 313.
23. T. E. Zarecz and M. A. Saiti, "Metal Reflectivity Under High Intensity Optical Radiation", Applied Physics Letters, Vol. 26, No. 4, Feb. 1975.
24. J. N. Hill and J. Spalding, "Surface Treatments by Laser", Optics and Laser Technology, Dec. 1974, p. 276.
25. T. R. Anthony and H. E. Cline, "Surface Normalization of Sensitized Stainless Steel by Laser Surface Melting", J. Appl. Phys., Vol. 49, No. 3, March 1978.
26. P. Duwez, "Structure and Properties of Alloys Rapidly Quenched from the Liquid State", Trans. ASM, 60, 607 (1967).

27. S. S. Charschan (Editor), "Lasers in Industry".
28. AWS "Welding Handbook", Vol. I.
29. "Handbook of Stainless Steels", Peckner and Bernstein.
30. E. V. Locke, E. D. Hoag, and R. A. Hella, IEEE Journal of Quantum Electronics, QE-8, 2 (1972) 132.
31. E. V. Locke and R. A. Hella, IEEE Journal of Quantum Electronics, QE-10, 2 (1974) 179.
32. E. M. Breinan and C. M. Banas, "Evaluation of Basic Laser Welding Capabilities", Tech. Report, United Technologies Research Center, 1975.
33. H. E. Cline and T. R. Anthony, J. Appl. Phy., 48 (9) (1977) 3895.
34. Y. Arata and I. Miyamoto, Trans. JWRI, 1, 1 (1972) 11.
35. J. F. Ready, "Industrial Applications of Lasers", Academic Press.
36. C. Kim and L. S. Weinman, Scripta Met., 12 (1978) 57.
37. J. A. A. Ketelaar, J. P. Colpa and F. N. Hooge, Journal of Chemical Physics, 23 (1955) 413.
38. E. J. Morgan-Warren, Welding Journal, 3 (1979) 76-s.
39. Metallurgy of Welding.
40. G. E. Linnert, Welding Metallurgy, AWS, Vol. 2, 1967.
41. R. Mehrabian, S. Kou, S. C. Hsu and A. Munitz, Proc. Mat. Res. Soc. Symposium on Lasers and Laser-Solid Interactions, Nov. 1978, Boston, MA.
42. W. W. Duley, CO<sub>2</sub> Lasers--Effects and Applications, 1976, p. 128.
43. J. Mazumdar and W. M. Steen, J. Appl. Phy., 51 (1980) 941.
44. H. E. Cline and T. R. Anthony, J. Appl. Phy., 48 (1977) 3895.
45. L. E. Greenwald, E. M. Breinan and B. H. Kear, "Laser-Solid Interactions and Laser Processing", 1978, S. D. Ferris (ed.), p. 129.
46. H. Jones, "Rapidly Quenched Metals", Proc. 2nd International Conference, MIT Press.

47. W. E. Brower, R. Strachan and M. C. Flemings, AFS Cast Metals Research Journal, 12 (1970) 176.
48. H. Matyja, B. C. Giessen and N. J. Grant, J. Inst. Metals, 96 (1968) 30.
49. M. H. Burden and H. Jones, J. Inst. Metals, 98 (1970) 249.
50. J. A. McComb, S. Nenno and M. Meshii, J. Phys. Soc. Japan, 19 (1970) 1691.
51. J. V. Wood and R. W. K. Honeycombe, J. Mater. Science, 9 (1974) 1183.
52. P. G. Boswell and G. A. Chadwick, J. Materials Science, 12 (1977) 1879.
53. J. S. Pascover and S. V. Radcliffe, Trans. AIME, 242 (1968) 673.
54. A. Gilbert and W. S. Owen, Acta Met., 10 (1962) 45.
55. J. M. Wallbridge and J. G. Parr, JISI, 204 (1966) 119.
56. M. J. Bibby and J. G. Parr, JISI, 202 (1964) 100.
57. W. D. Swanson and J. G. Parr, JISI, 202 (1964) 104.
58. T. L. Wilson, J. K. Jackson, and R. E. Miner, Trans. AIME, 245 (1969) 2185.
59. R. H. Goodenow and K. F. Hehemann, Trans. AIME, 233 (1965) 1777.
60. J. F. Grubb and R. N. Wright, Met. Trans., 10A (1979) 1247.
61. R. W. K. Honeycombe, Metal Science, (1980) 201.
62. J. V. Bee and R. W. K. Honeycombe, Met. Trans., 9A (1978) 587.
63. T. B. Massalski, Acta. Met., 6 (1958) 243.
64. C. S. Roberts, B. L. Averbach and M. Cohen, Trans. ASM, 45 (1953) 576.
65. R. H. Aborn, Trans. ASM, 48 (1956) 51.
66. A. R. Cox, Iron and Steel Institute, (1968) 539.
67. W. C. Leslie, Acta Met., 9 (1961) 1004.

68. K. F. Hale and M. McLean, JISI, 201 (1963) 331.
69. M. G. H. Wells and J. F. Butler, Trans. ASM, 59 (1966) 427.
70. G. R. Speich and P. R. Swann, JISI, 203 (1965) 480.
71. J. S. Pascover and S. V. Radcliffe, Acta Met., 17 (1969) 321.
72. G. R. Speich, Metals Handbook, ASM, 8 (1973) 425.
73. P. M. Kelly and J. Nutting, JISI, (1961) 199.
74. G. Krauss and A. R. Marder, Met. Trans., 2 (1971) 2343.
75. G. Thomas, Met. Trans., 2 (1971) 2373.
76. J. V. Bee and R. W. K. Honeycombe, Met. Trans., 10A (1979) 1213.
77. S. J. Donachie and G. S. Ansell, Met. Trans., 6A (1975) 1863.
78. R. W. Messler, G. S. Ansell and V. I. Lizunov, Trans. ASM, 62 (1969) 362.
79. G. S. Ansell and A. Arrott, Trans. AIME, 227 (1963) 1080.
80. H. R. Woehrle, W. R. Clough and G. S. Ansell, Trans. ASM, 59 (1966) 784.
81. S. K. Das and G. Thomas, Met. Trans., 1 (1970) 325.
82. B. V. N. Rao and G. Thomas, Met. Trans., 11A (1980) 441.
83. G. Thomas, Met. Trans., 9A (1978) 439.
84. J. A. Mathews, Amer. Soc. Steel Treating, 8 (1925) 565.
85. E. P. Klier and A. R. Troiano, Trans. AIME, 162 (1945) 175.
86. A. R. Marder and G. Krauss, Trans. ASM, 60 (1967) 651.
87. B. V. N. Rao, T. Y. Koo and G. Thomas, Proc. of EMSA, (1975) 30.
88. N. C. Law, P. R. Howell and D. V. Edmonds, Metal Science, 13 (1979) 507.
89. S. Clark and G. Thomas, Met. Trans., 6A (1975) 969.
90. E. M. Breinan and G. S. Ansell, Met. Trans., 1 (1970) 1513.
91. G. M. ... Met. Trans., 1 (1970) 3000

92. R. G. Davies and C. L. Magee, *Met. Trans.*, 1 (1970) 2927.
93. J. Boniszewski, "Physical Properties of Martensite and Bainite", JISI, SR 93.
94. B. P. J. Sandvik and H. P. Nevalainen, *Metals Technology*, 6 (1981) 213.
95. K. Shimizu, M. Oka and C. M. Wayman, *Acta Met.*, 18 (1970) 1005.
96. G. R. Speich and W. C. Leslie, *Met. Trans.*, 3 (1972) 1043.
97. K. Shimizu and Z. Nishiyama, *Met. Trans.*, 3 (1972) 1055.
98. R. W. K. Honeycombe and F. B. Pickering, *Met. Trans.*, 3 (1972) 1099.
99. Z. Nishiyama, "Martensitic Transformation", Academic Press, 1977.
100. A. Inoue, T. Iwadachi, T. Minemura and T. Masumoto, *Trans. JIM*, 22 (1981) 197.
101. I. R. Sare and R. W. K. Honeycombe, "Rapidly Quenched Metals", Section I, N. J. Grant and B. C. Giessen (ed.) 1976.
102. J. J. Rayment and B. Cantor, *Met. Trans.*, 12A (1981) 1557.
103. I. R. Sare and R. W. K. Honeycombe, *J. Mat. Sci.*, 13 (1978) 1991.
104. Y. Inokuti and B. Cantor, *Metal Science*, 5 (1979) 269.
105. J. J. Rayment and B. Cantor, *Metal Science*, 3 (1978) 156.
106. R. C. Ruhl and M. Cohen, *Trans. Met. Soc. AIME*, 245 (1969) 253.
107. I. R. Sare and R. W. K. Honeycombe, *Metal Science*, 5 (1979) 269.
108. J. V. Wood and R. W. K. Honeycombe, *J. Mat. Sci.*, 9 (1974) 1183.
109. J. V. Wood and R. W. K. Honeycombe, *Mat. Sci. Eng.*, 23 (1976) 107.
110. H. Jones and C. Surayanarayana, *J. Mat. Sci.*, 8 (1973) 705.

## MATERIALS

### Substrates:

	Weight percentage				
	C	Si	Mn	S	P
Pure iron	0.01	0.01	0.01	0.003	0.008
0.2% C steel	0.18	0.08	0.68	0.01	0.007
0.5% C steel	0.45	0.13	0.63	0.020	0.010
1.0% C steel	0.95	0.10	0.45	0.017	0.013

### COATINGS:

Chromium

Nickel

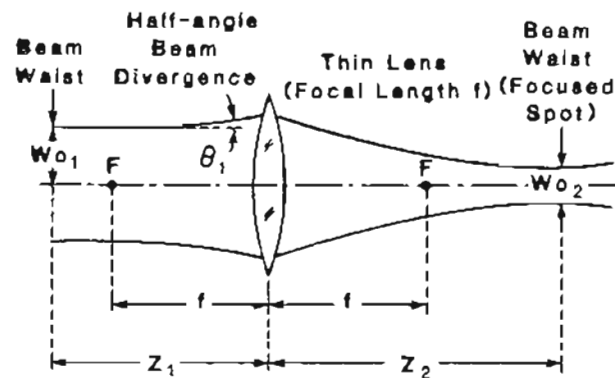
Table I. CHEMICAL COMPOSITIONS OF MATERIALS.

**CHROMIUM ELECTRO-DEPOSITION****Bath Composition****Chromic Trioxide 250 gms/liter****Sulfuric Acid 2.5 gms/liter****CONDITIONS****Temperature 65 c****Current Density 0.3 Amp/cm.cm****Voltage 6Volts****Anode Lead-6%Tin****NICKEL ELECTRO-DEPOSITION****Bath Composition (Watt's Bath)****Nickel Sulfate 300 gms/liter****Nickel Chloride 45 gms/liter****Boric Acid 35 gms/liter****Hydrogen Peroxide 10 ppm****CONDITIONS****Temperature 50 c****Current Density 0.05 Amp/cm.cm****Voltage 6Volts****Anode Graphite****Table II. ELECTROPLATING CONDITIONS.**

<u>LASER:</u>	
Wavelength	10.6 Micrometers (Infrared)
Power Output	Nominal 1000 watts TEM <sub>00</sub> (95% Gaussian) Operating Range: 1500 watts multimode, 1200 watts TEM <sub>00</sub>
Beam Diameter	Approximately 13 millimeters at the TEM <sub>00</sub> 1/e <sup>2</sup> intensity limits.
Beam Divergence	1.4 milliradians
Beam Jitter	Less than ±0.2 milliradian
Power Output Stability	Less than ±5% variation
<u>GENERAL:</u>	
Power Requirements	460 volts ac (nominal) 3-phase, 60 Hz, 40 kW (50 Hz or 230 volts ac optional)
Gas Requirements	Separate Helium, Nitrogen, and Carbon Dioxide regulated to 15 PSIG or premixed bottles of these gases in the proper proportions
Water Cooling	8 Gallons per minute, 40 PSIG
Laser Head Size	4 feet high by 5 feet wide by 5 feet long
Laser Head Weight	2850 pounds
Power Supply Size	6 1/2 feet high by 5 feet wide by 2 feet deep
Power Supply Weight	2300 pounds
Vacuum Pump	Frame-mounted on anti-vibration pads with independent on-off switch
Auxiliary Vacuum Port	2-inch standard flange with blocking port for coupling to an external pump
Gas Consumption	CO <sub>2</sub> - 0.08 SCFH He - 1.8 SCFH N <sub>2</sub> - 0.4 SCFH

Table III. CO<sub>2</sub> GAS TRANSPORT LASER SPECIFICATIONS.

## SPOT SIZE DETERMINATION



### Spot Size At Focal Point ( $W_{02}$ )

$$W_{02} = \frac{\lambda f}{\pi W_{01}}$$

### Spot Size Away From Focal Point

The equation relating  $W_0$  and  $W(Z)$  is:

$$W(Z) = W_{02} \left[ 1 + \left( \frac{\lambda Z}{\pi W_{02}^2} \right)^2 \right]^{1/2}$$

Table IV. BEAM SIZE DETERMINATION.

LASER: Continuous Wave CO<sub>2</sub> Gas Transport Type  
(10.6  $\mu\text{m}$  Wavelength)

POWER: 1500 Watts (Multimode)  
1200 Watts (TEM<sub>00</sub> mode)

FOCUSSING OPTICS: ZNSE Lens 6.25 cm(2.5 in) F.L

BEAM DIAMETER: 0.0066-1.3 cm(0.0026-0.5120 in)

SCAN RATE: 0.4233-8.466 cm/sec (10-200 in/min)

SHIELDING GAS: 90% Argon-10% Helium

Table V. LASER OPERATING PARAMETERS.

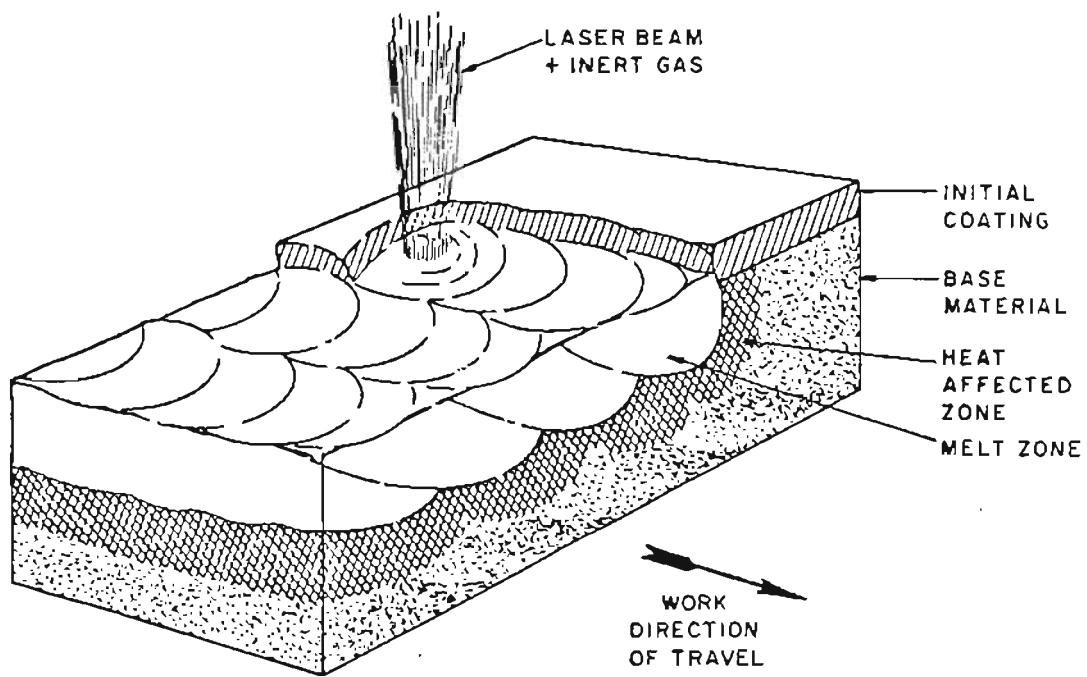


Figure 1. A SCHEMATIC OF LASER SURFACE ALLOYING PROCESS.

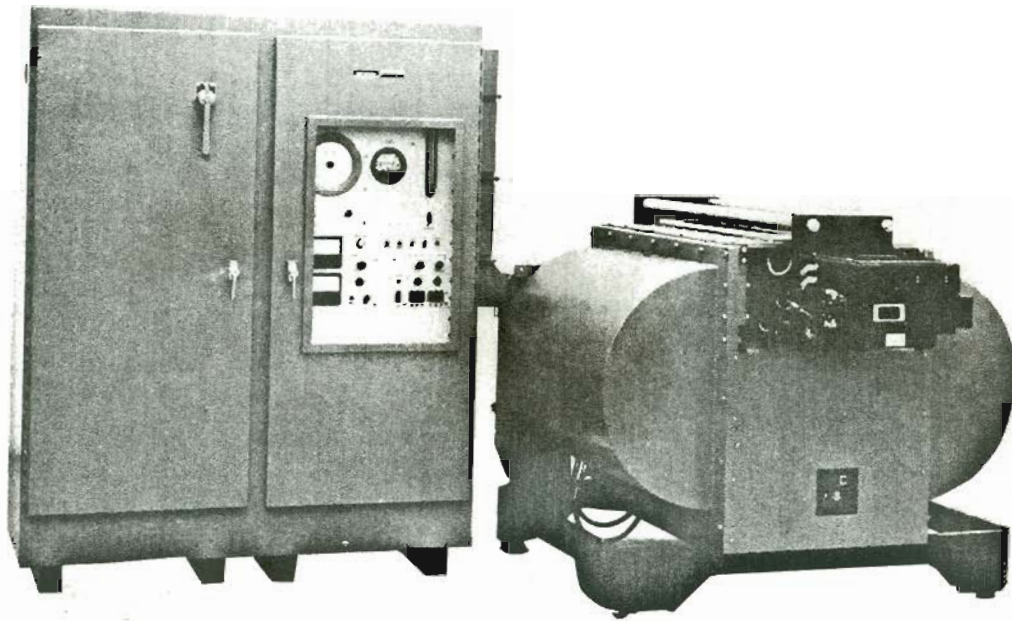


Figure 2. THE CO<sub>2</sub> GAS TRANSPORT LASER (GTE SYLVANIA MODEL 971).

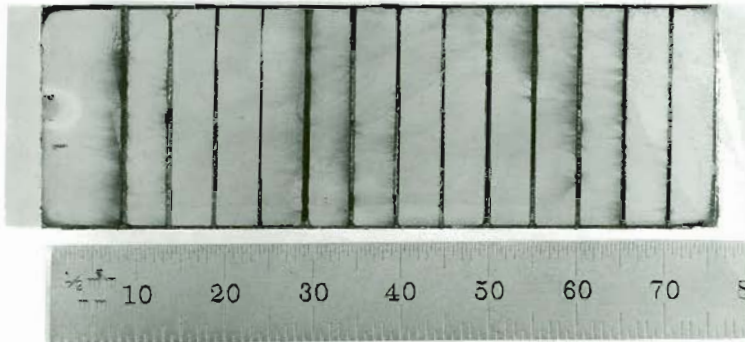
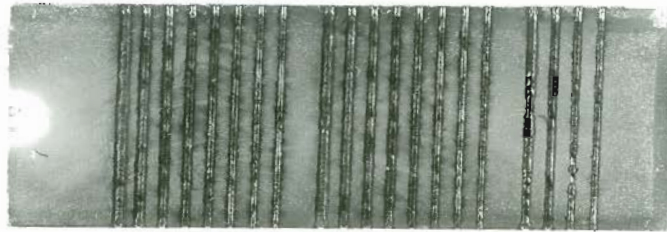
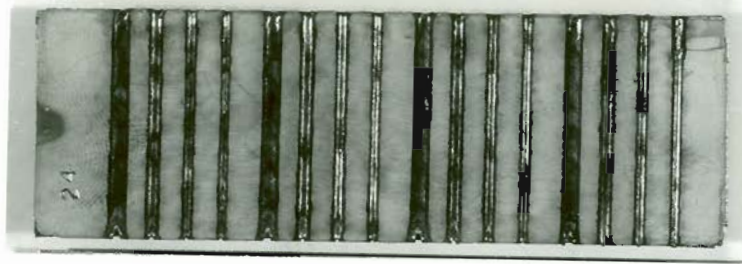


Figure 3. SURFACE APPEARANCES OF LASER ALLOYED SPECIMENS.

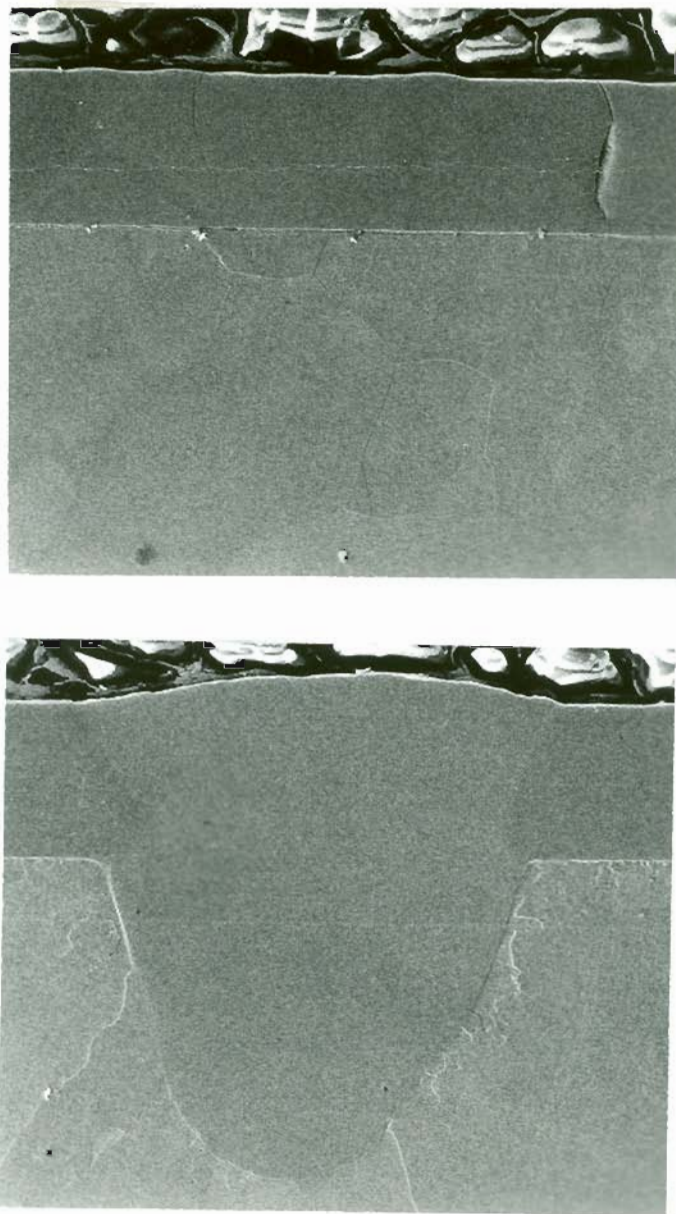


Figure 4. SCANNING ELECTRON MICROGRAPHS SHOWING

- a) THE TRANSVERSE SECTION OF CHROMIUM COATING ON AN IRON SUBSTRATE
- b) THE TRANSVERSE SECTION OF LASER ALLOYED FUSION ZONE

MAGNIFICATION: 50x.

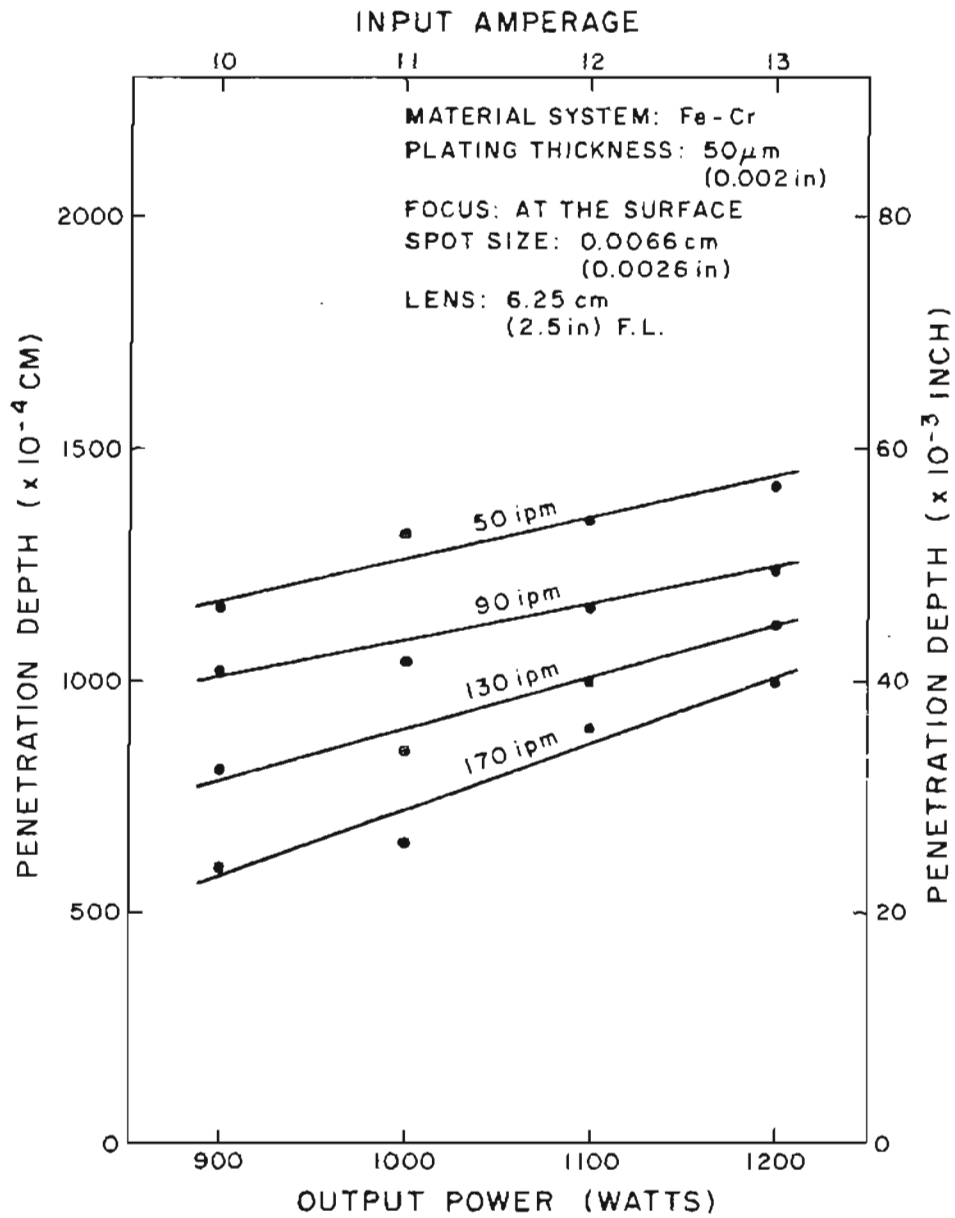


Figure 5. EFFECT OF LASER POWER ON MELT PENETRATION OF Fe-Cr ALLOYS.

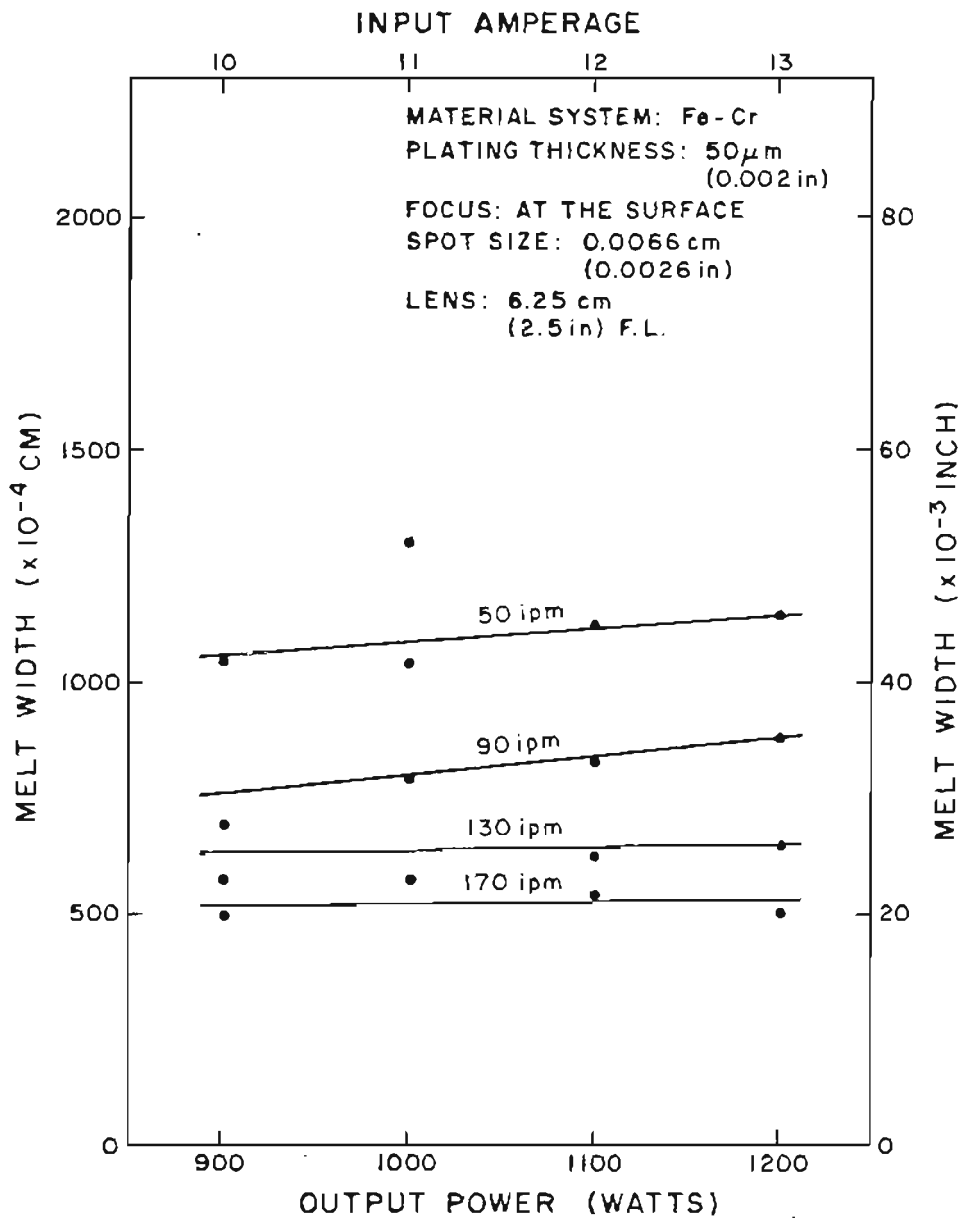


Figure 6. EFFECT OF LASER POWER ON MELT WIDTH OF Fe-Cr ALLOYS.

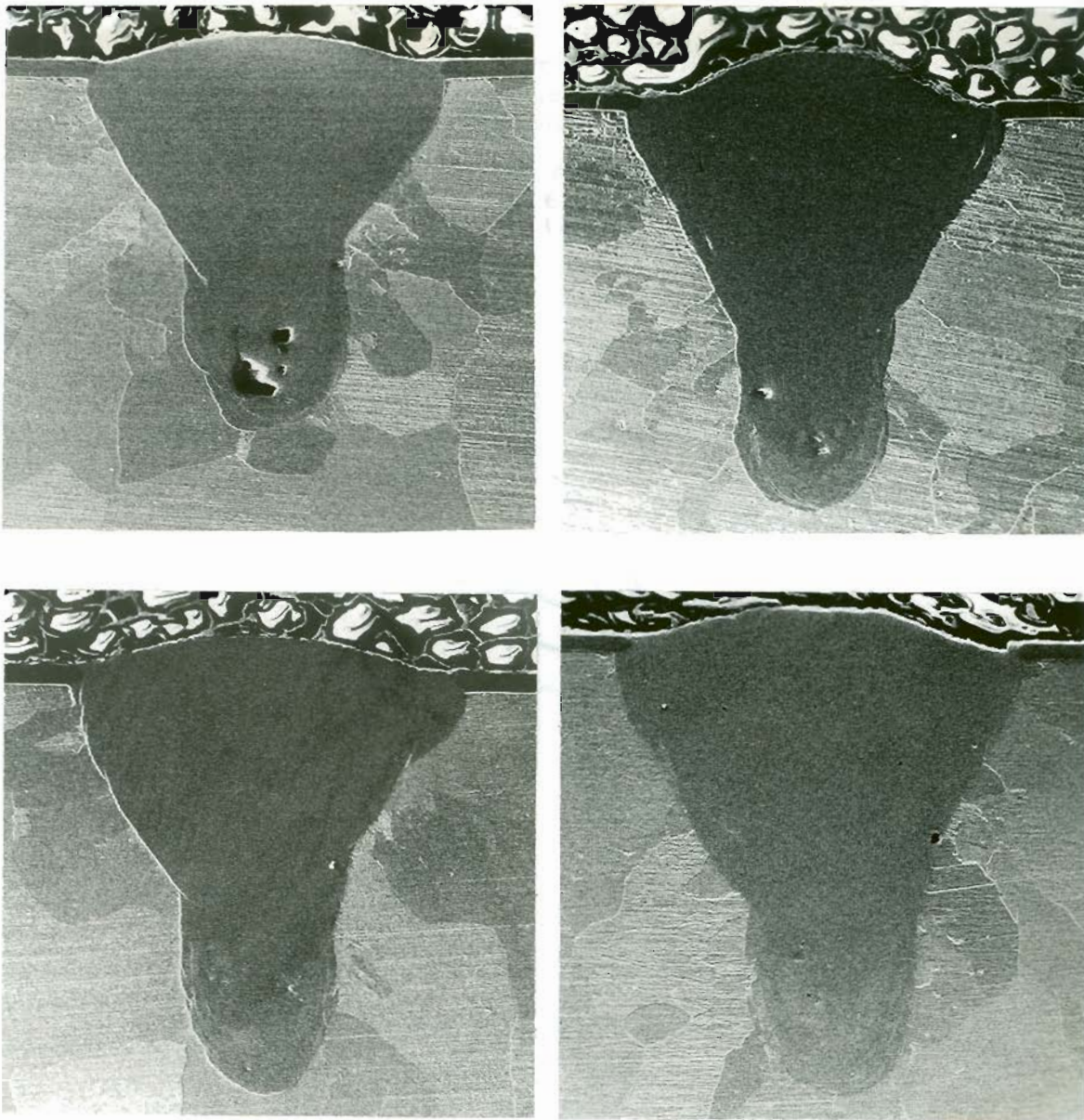


Figure 7. SCANNING ELECTRON MICROGRAPHS SHOWING THE VARIATION OF FUSION ZONE SIZE WITH LASER POWER

a) 900 WATTS, b) 1000 WATTS, c) 1100 WATTS,  
d) 1200 WATTS.

MAGNIFICATION: 50x.

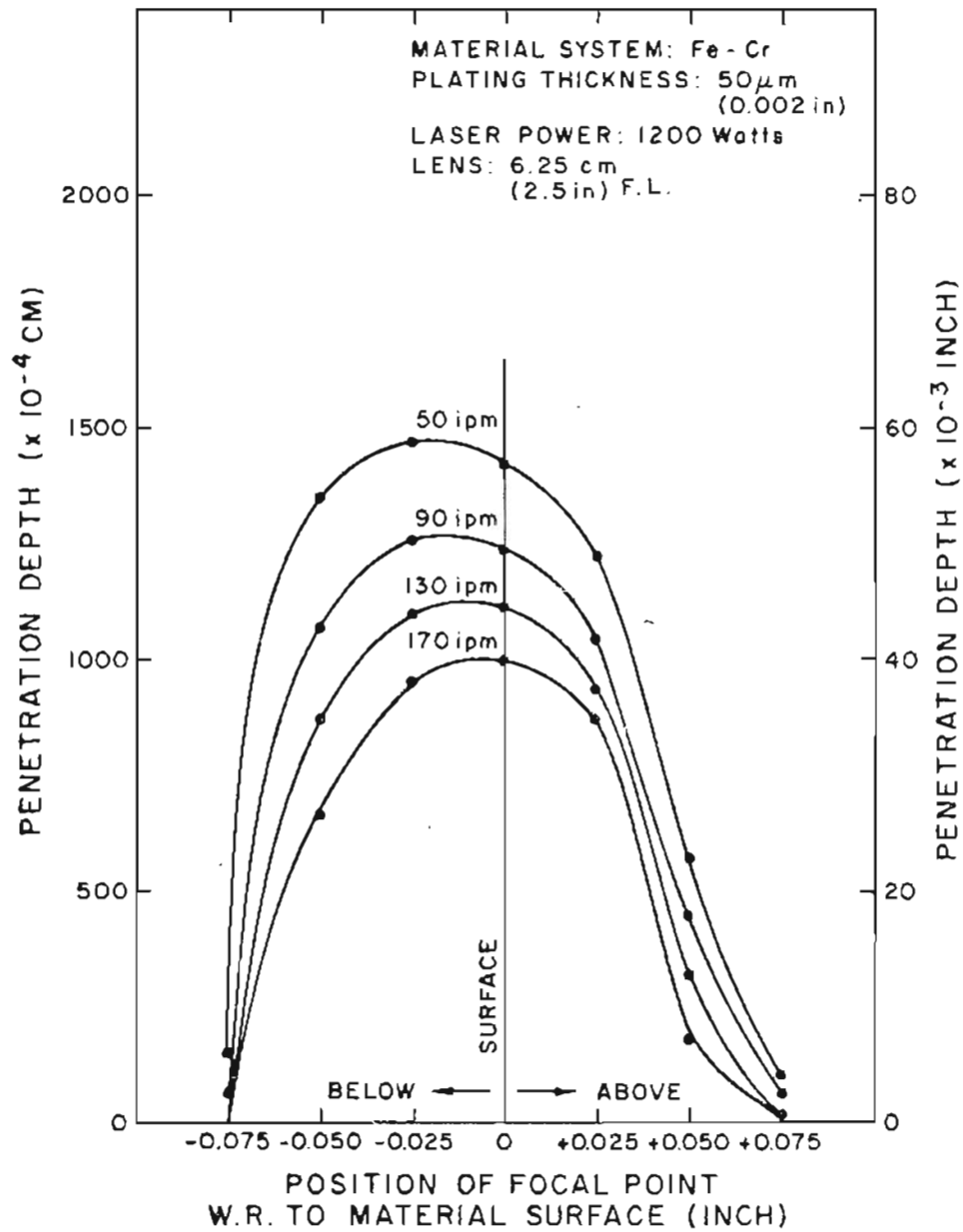


Figure 8. EFFECT OF FOCAL POSITION ON MELT PENETRATION OF Fe-Cr ALLOYS.

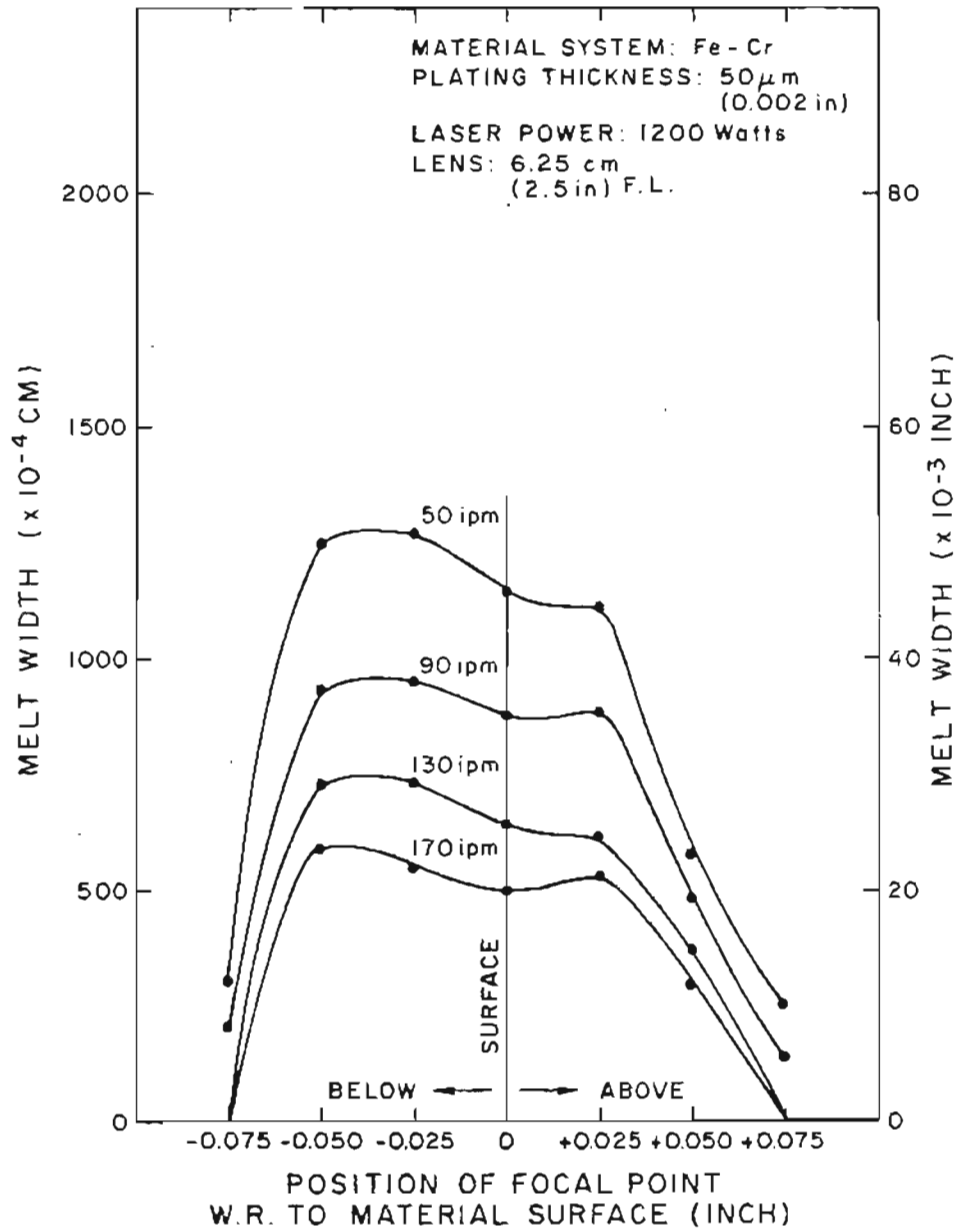


Figure 9. EFFECT OF FOCAL POSITION ON MELT WIDTH OF Fe-Cr ALLOYS.

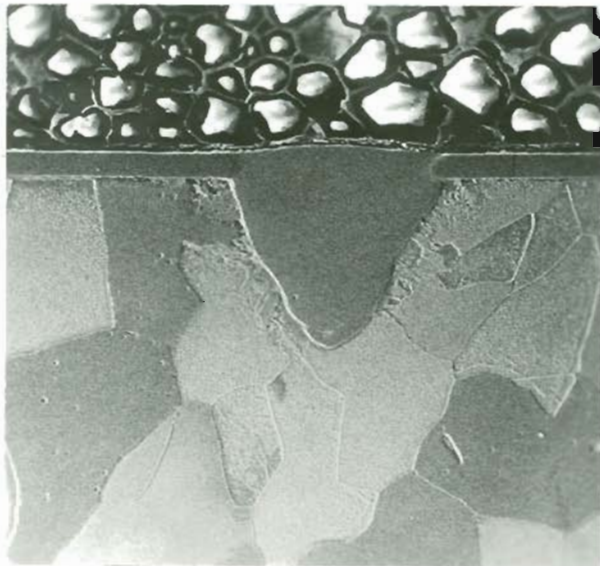
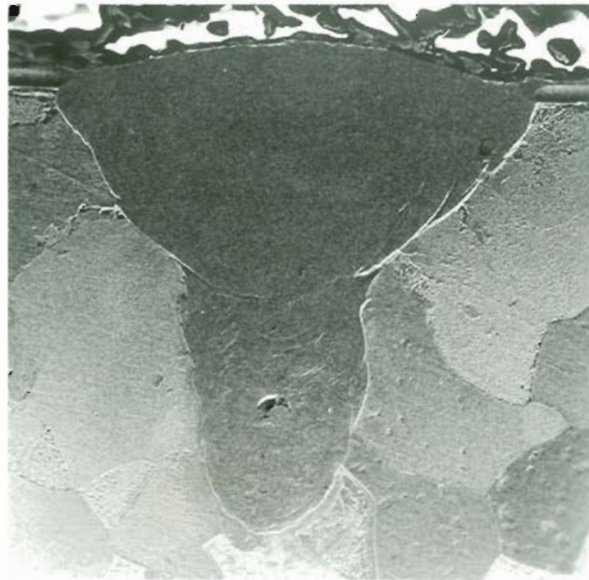


Figure 10. SCANNING ELECTRON MICROGRAPHS SHOWING THE EFFECT OF FOCUSING ON FUSION ZONE GEOMETRY

- a) FOCUS: 0.050 INCH BELOW THE SPECIMEN SURFACE
- b) FOCUS: 0.050 INCH ABOVE THE SPECIMEN SURFACE

MAGNIFICATION: 50x.

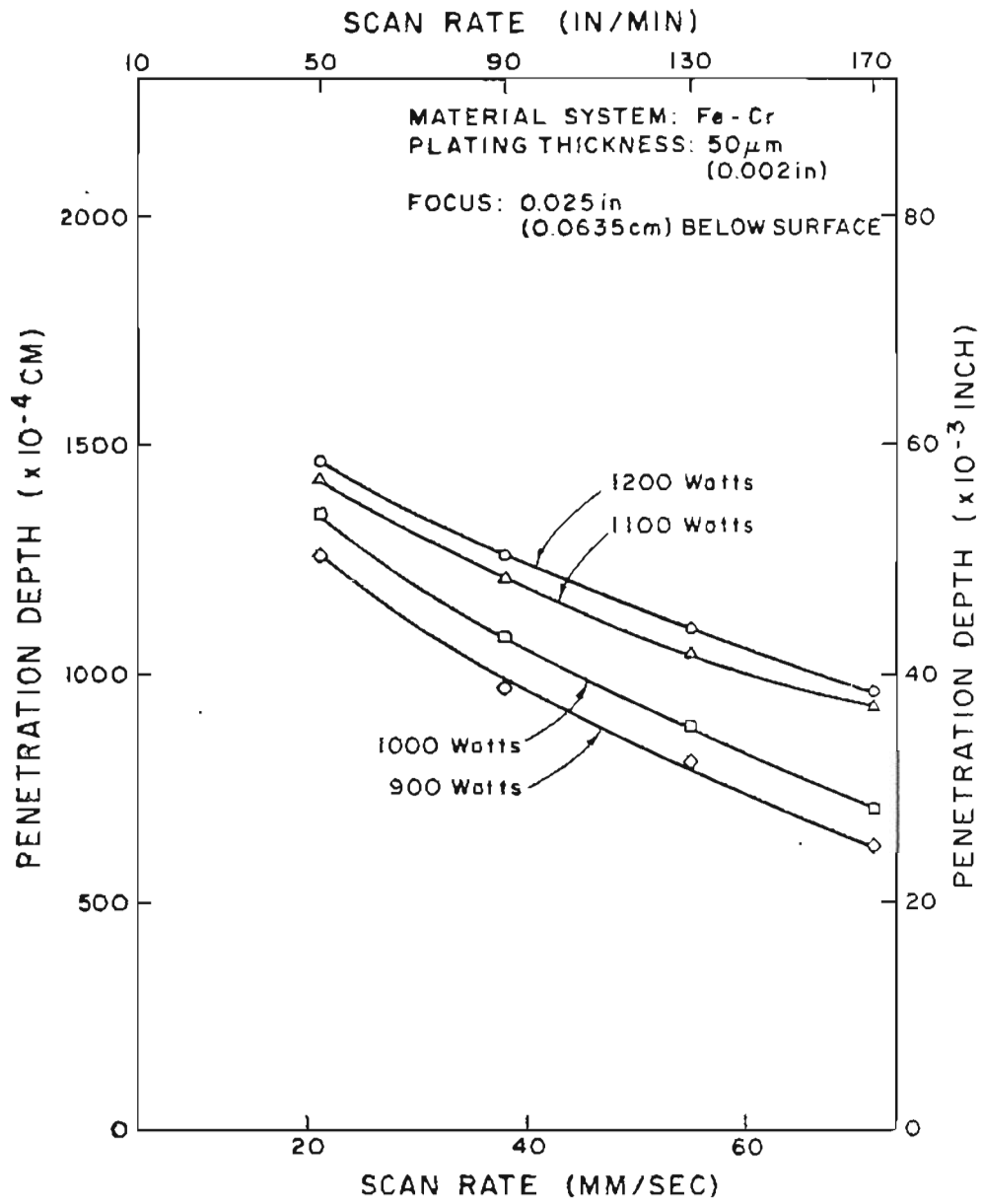


Figure 11. EFFECT OF SCAN RATE ON MELT PENETRATION OF Fe-Cr ALLOYS.

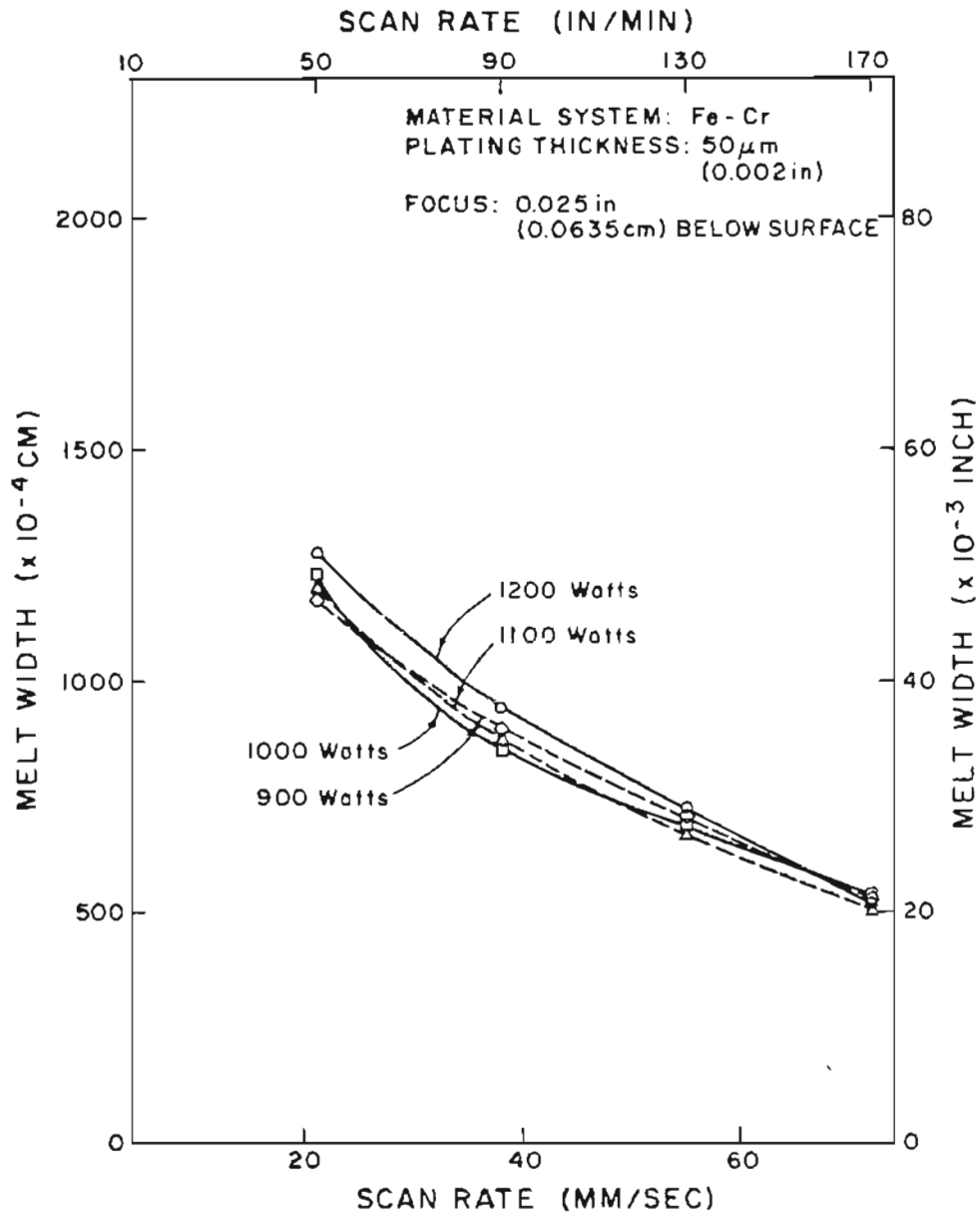


Figure 12. EFFECT OF SCAN RATE ON MELT WIDTH OF Fe-Cr ALLOYS.

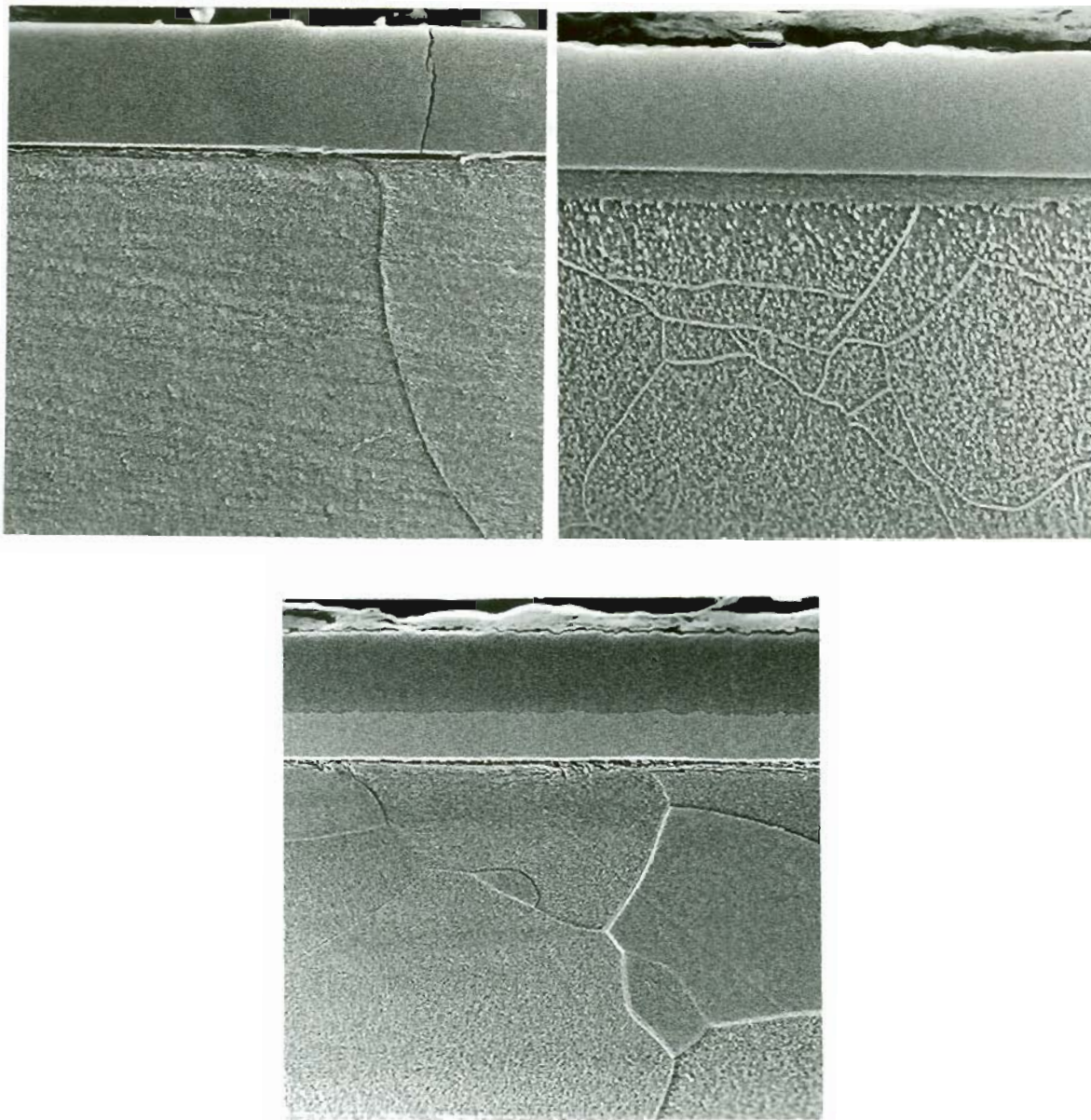


Figure 13. SCANNING ELECTRON MICROGRAPHS OF THE TRANSVERSE SECTIONS OF ELECTRODEPOSITED COATINGS

a) CHROMIUM, b) NICKEL, c) CHROMIUM/NICKEL.

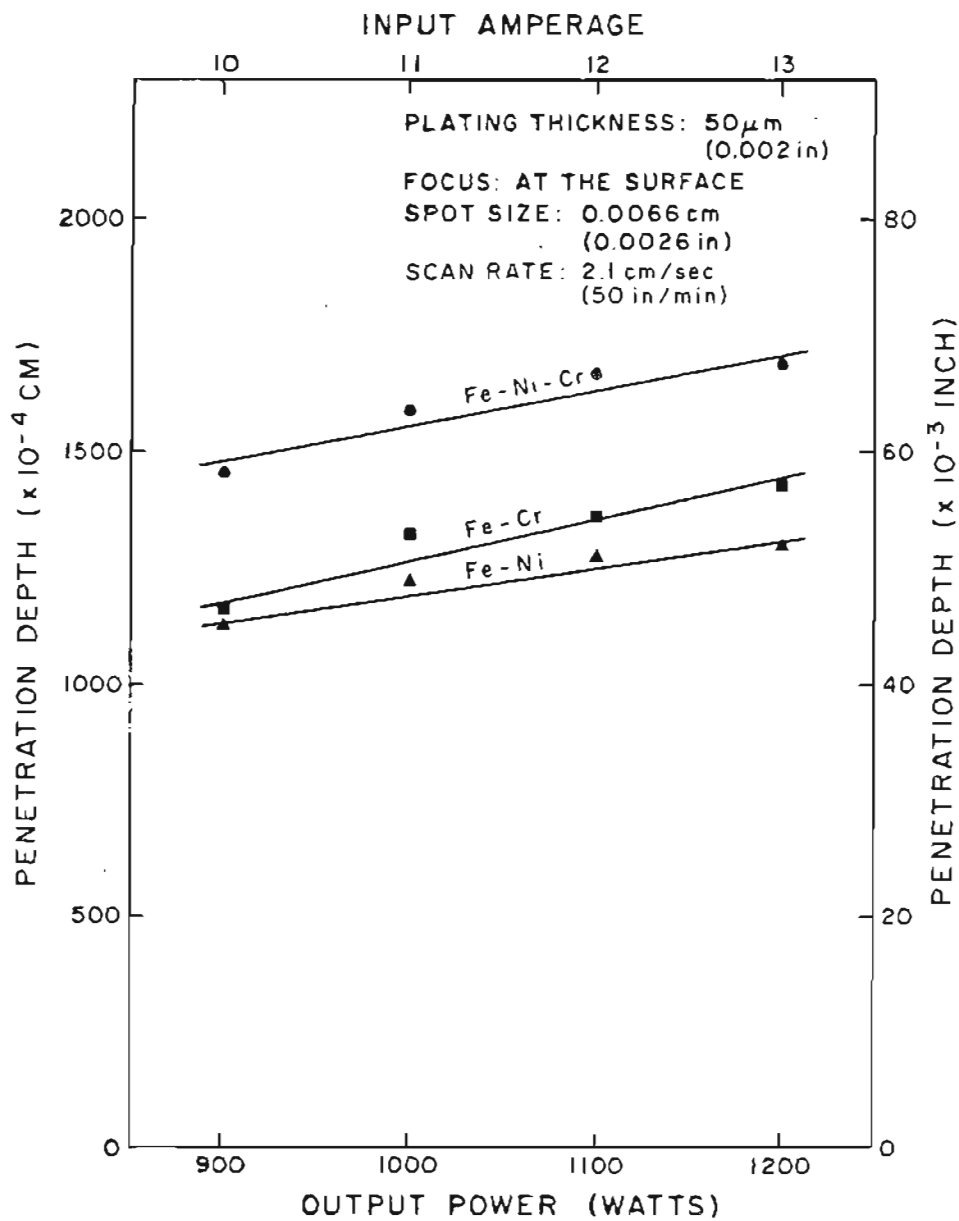


Figure 14. EFFECT OF COATING COMPOSITION ON MELT PENETRATION OF Fe-Cr, Fe-Ni AND Fe-Cr-Ni ALLOYS FOR VARIOUS LASER POWERS.

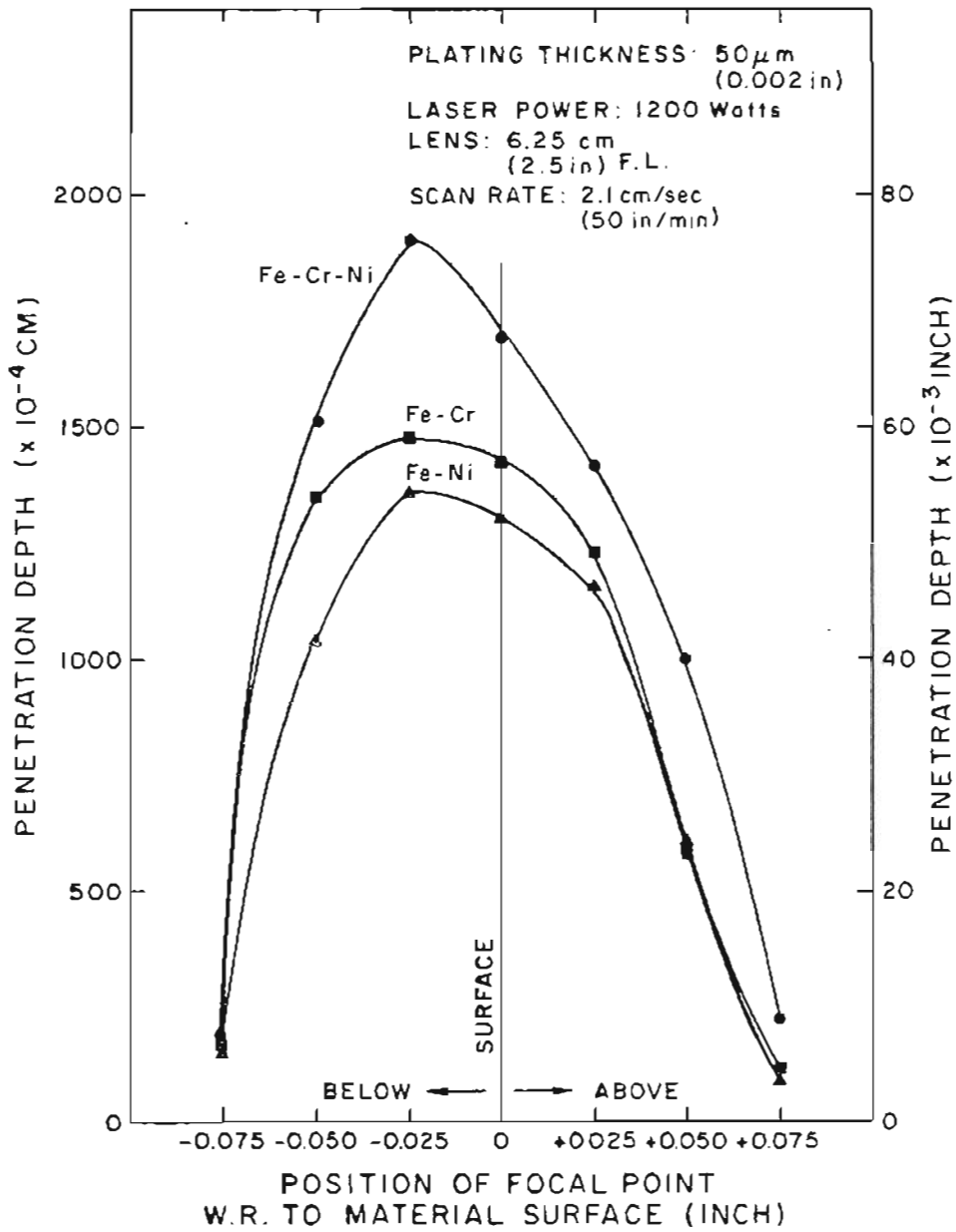


Figure 15. EFFECT OF COATING COMPOSITION ON MELT PENETRATION OF Fe-Cr, Fe-Ni AND Fe-Cr-Ni ALLOYS FOR VARIOUS FOCAL POSITIONS.

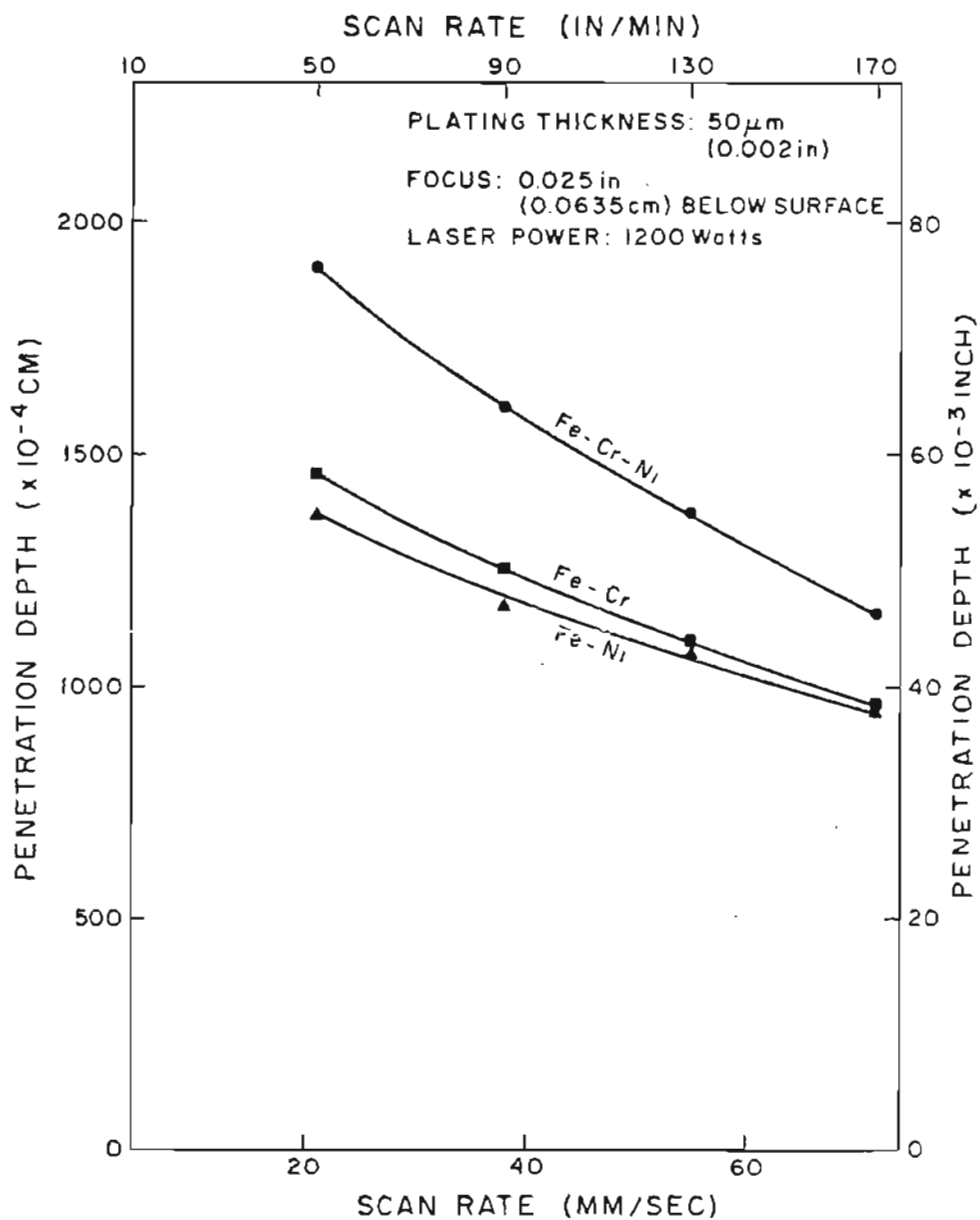


Figure 16. EFFECT OF COATING COMPOSITION ON MELT PENETRATION OF Fe-Cr, Fe-Ni, AND Fe-Cr-Ni ALLOYS FOR DIFFERENT SCAN RATES.

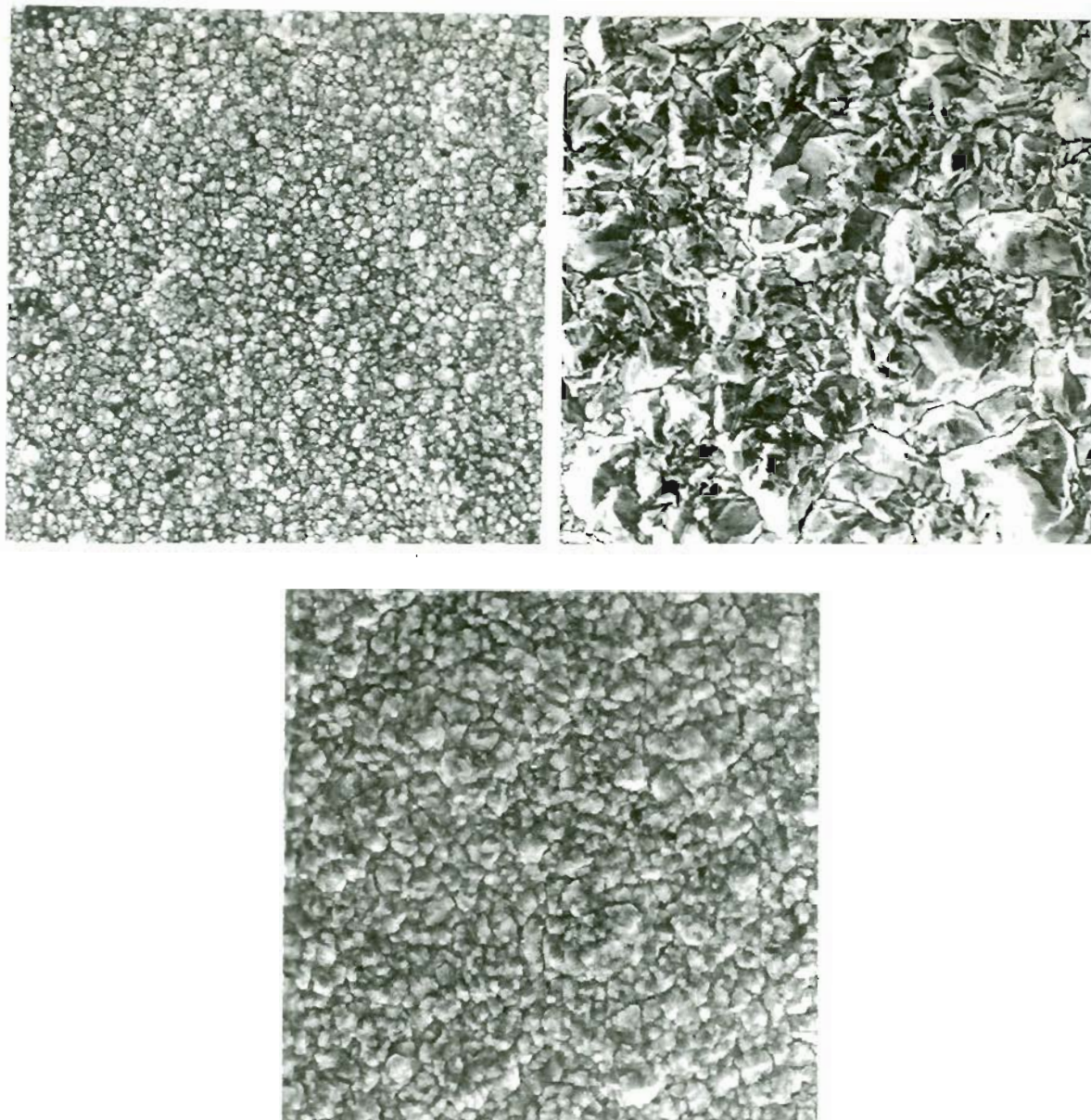


Figure 17. SCANNING ELECTRON MICROGRAPHS SHOWING THE ELECTRODEPOSITED COATING MORPHOLOGIES

a) CHROMIUM, b) NICKEL, c) CHROMIUM/NICKEL

MAGNIFICATION: 1000x.

## PROPERTIES OF ELEMENTS STUDIED

ELEMENT	THERMAL CONDUCTIVITY Watts/cm C	THERMAL DIFFUSIVITY $\text{cm}^2/\text{sec}$
Iron	0.835	0.2082
Chromium	0.948	0.2023
Nickel	0.94	0.2354
304Stainless steel	0.168	0.0535
Copper	4.01	1.1403

Figure 18. THERMAL PROPERTIES OF ALLOYING ELEMENTS.

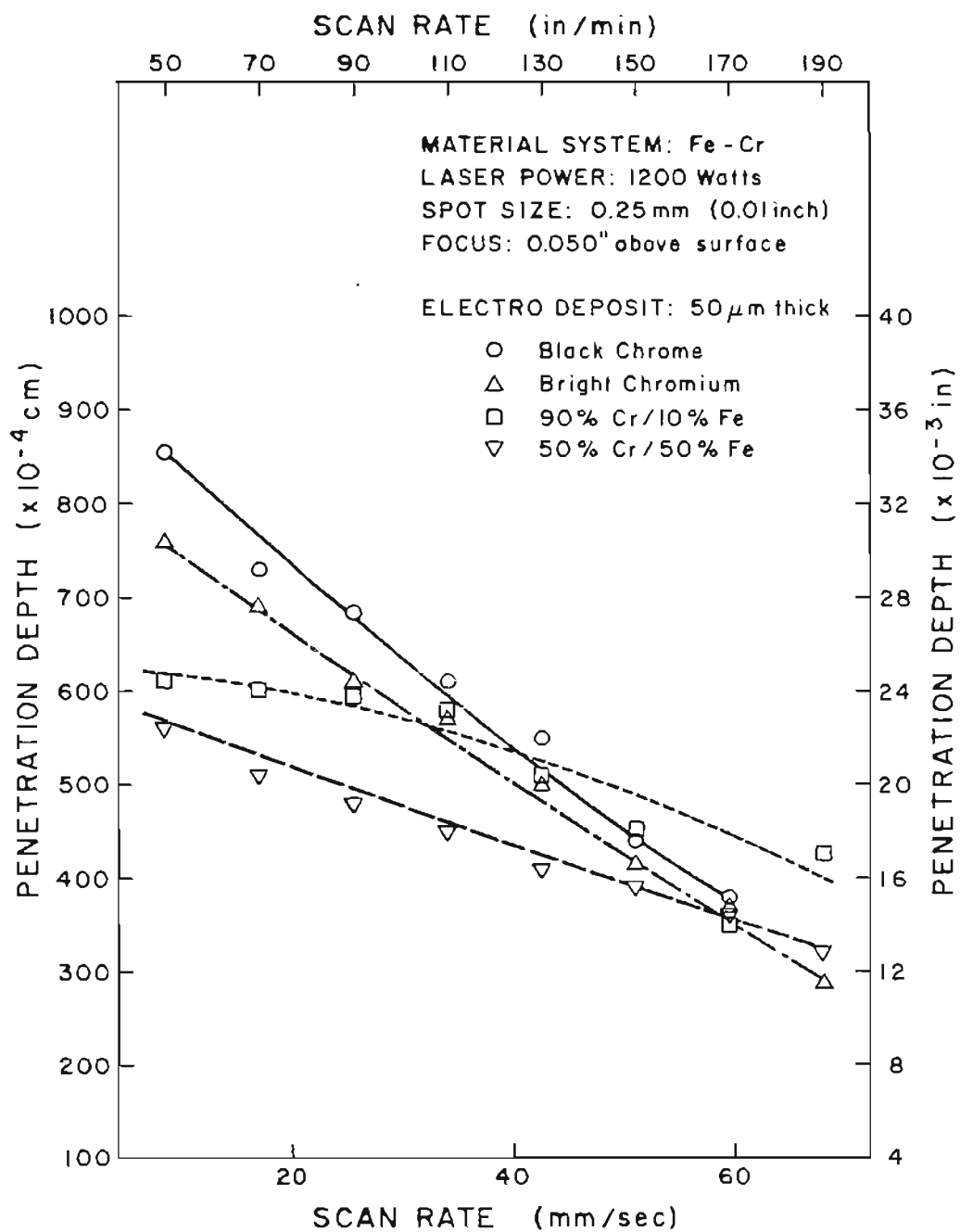


Figure 19. EFFECT OF COATING MORPHOLOGY ON MELT PENETRATION OF Fe-Cr ALLOYS.

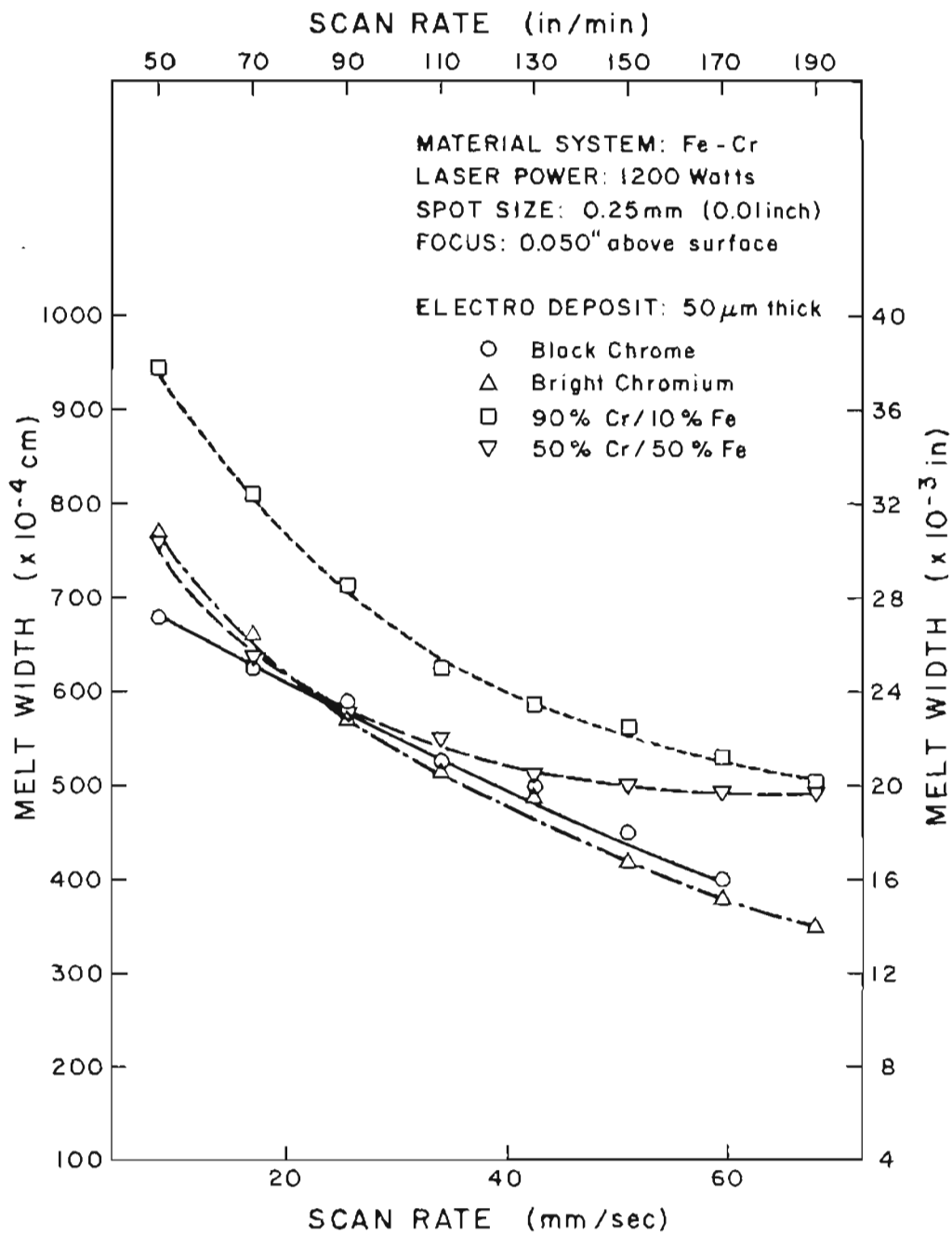


Figure 20. EFFECT OF COATING MORPHOLOGY ON MELT WIDTH OF Fe-Cr ALLOYS.

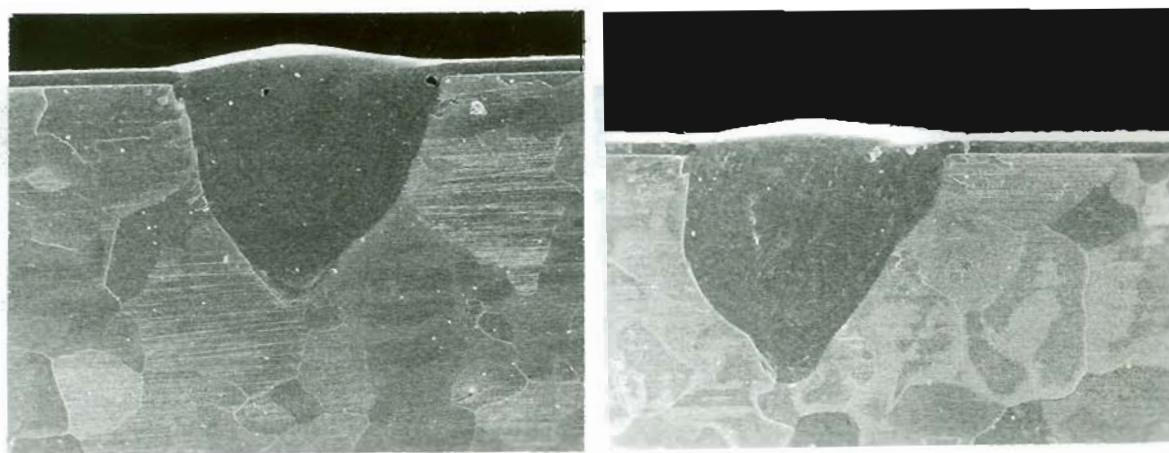
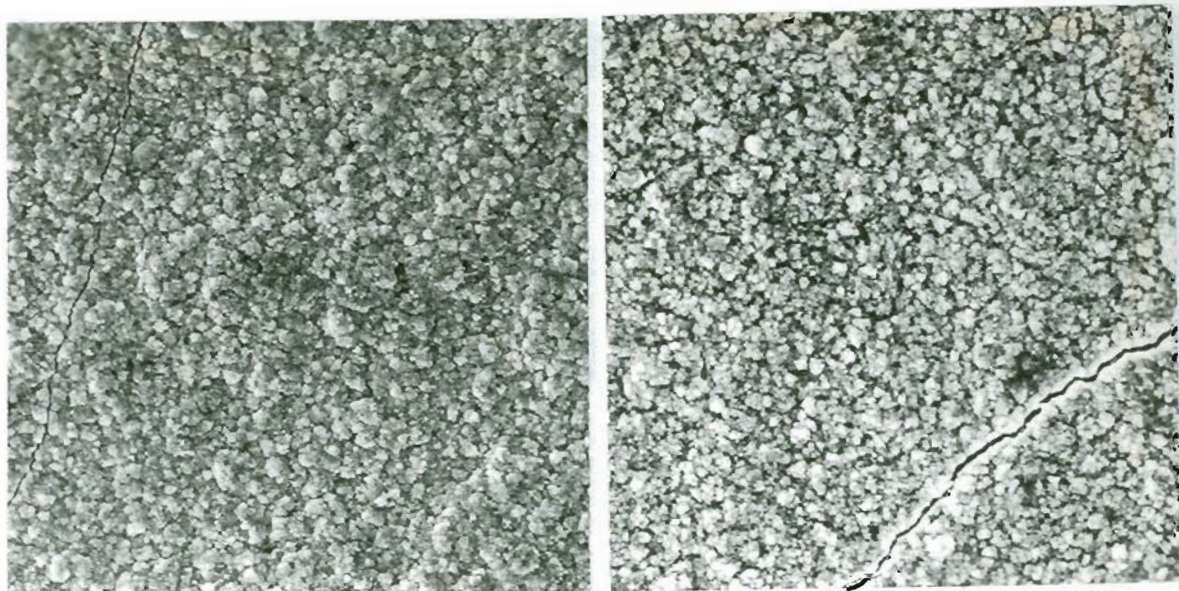


Figure 21. SCANNING ELECTRON MICROGRAPHS SHOWING THE COATING MORPHOLOGIES AND THE TRANSVERSE SECTIONS OF FUSION ZONES

a) AND b) BRIGHT CHROMIUM  
 c) AND d) BLACK CHROMIUM

MAGNIFICATION: a),c) = 1000x; b),d) = 50x.

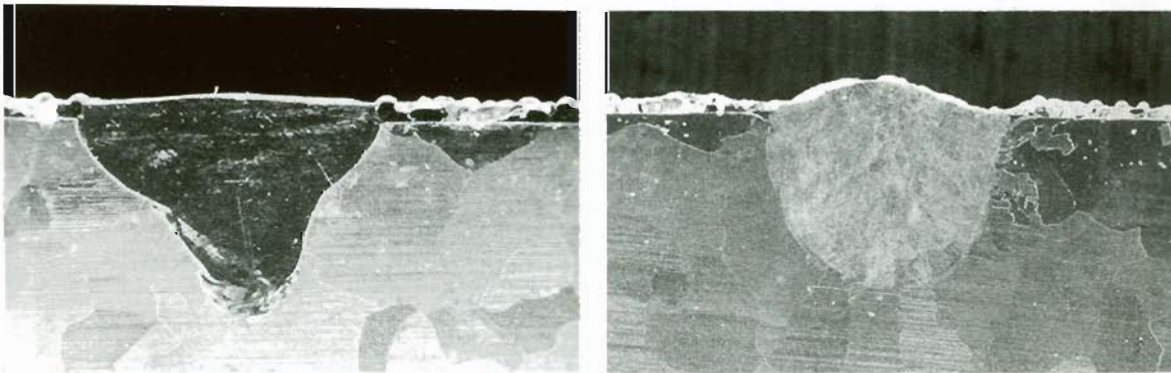
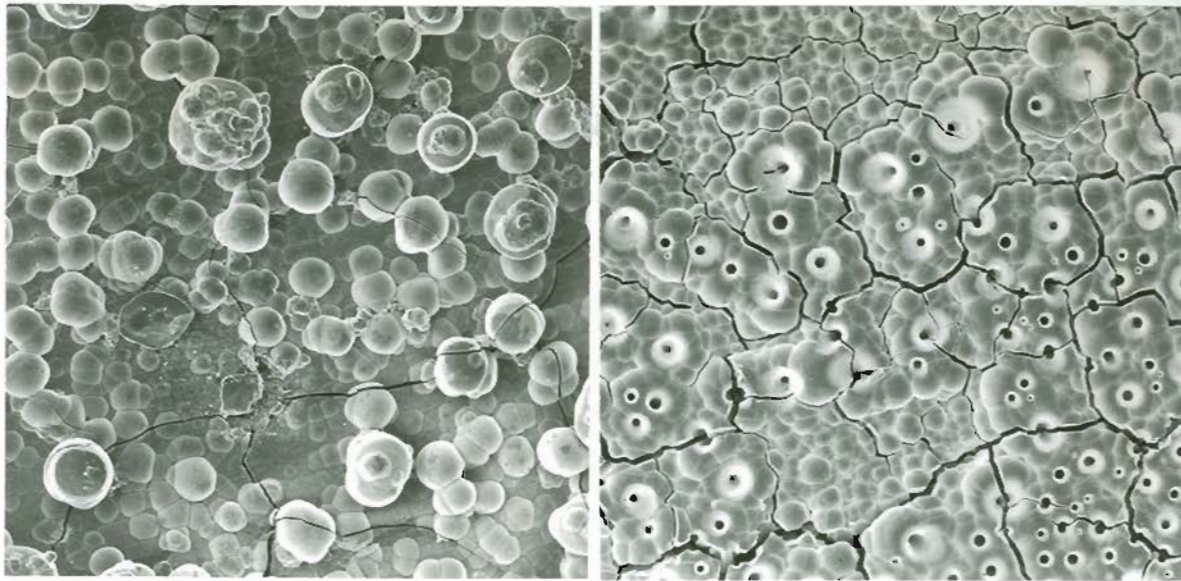


Figure 22. SCANNING ELECTRON MICROGRAPHS SHOWING THE COATING MORPHOLOGIES AND THE TRANSVERSE SECTIONS OF FUSION ZONES

(a) AND (b): 90% Cr/10%Fe ALLOY COATING

(c) AND (d): 50% Cr/50%Fe ALLOY COATING

MAGNIFICATION: (a), (c) 1000x  
(b), (d) 50x.

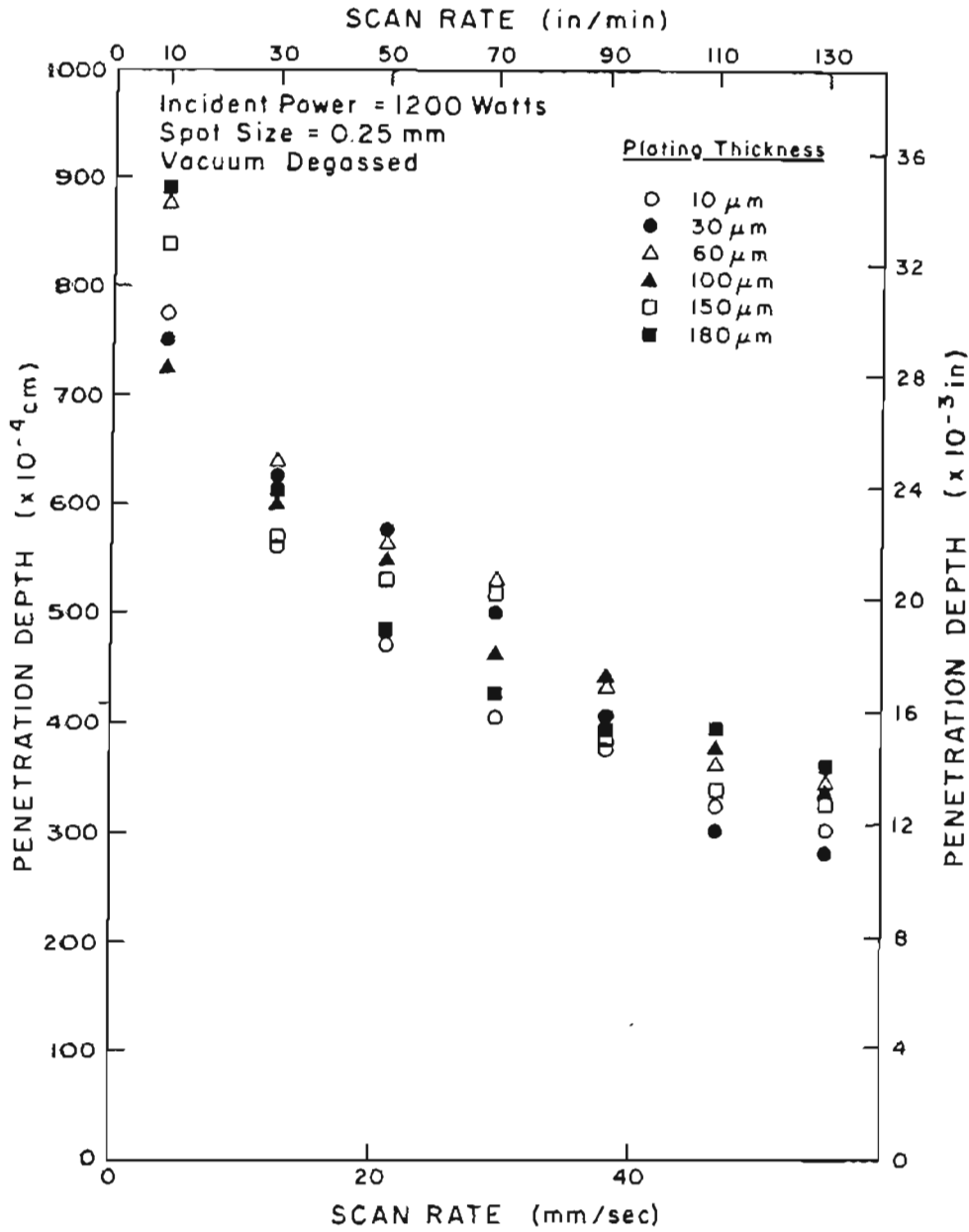


Figure 23. EFFECT OF CHROMIUM COATING THICKNESS ON MELT PENETRATION OF Fe-Cr ALLOYS.

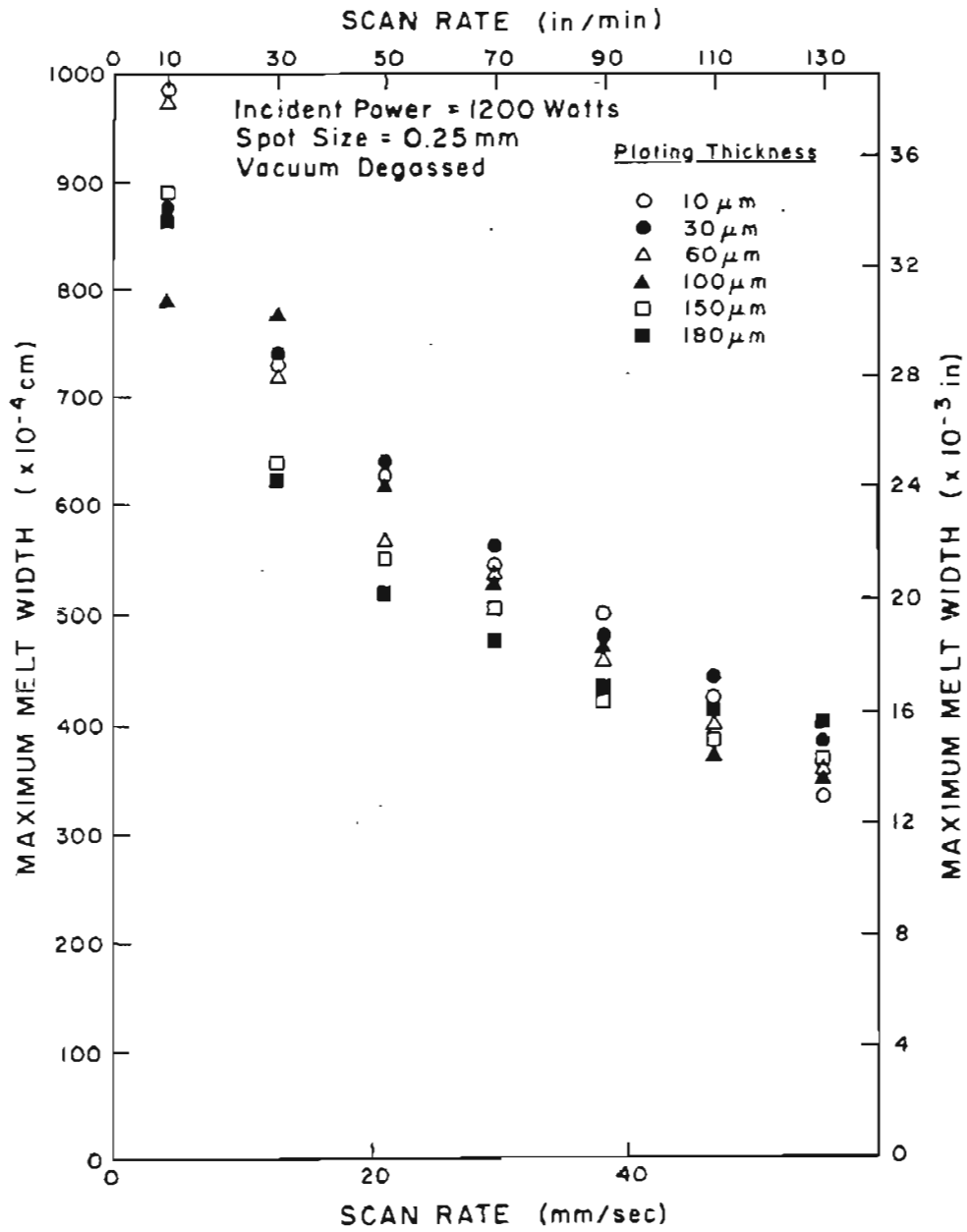


Figure 24. EFFECT OF CHROMIUM COATING THICKNESS ON MELT WIDTH OF Fe-Cr ALLOYS.

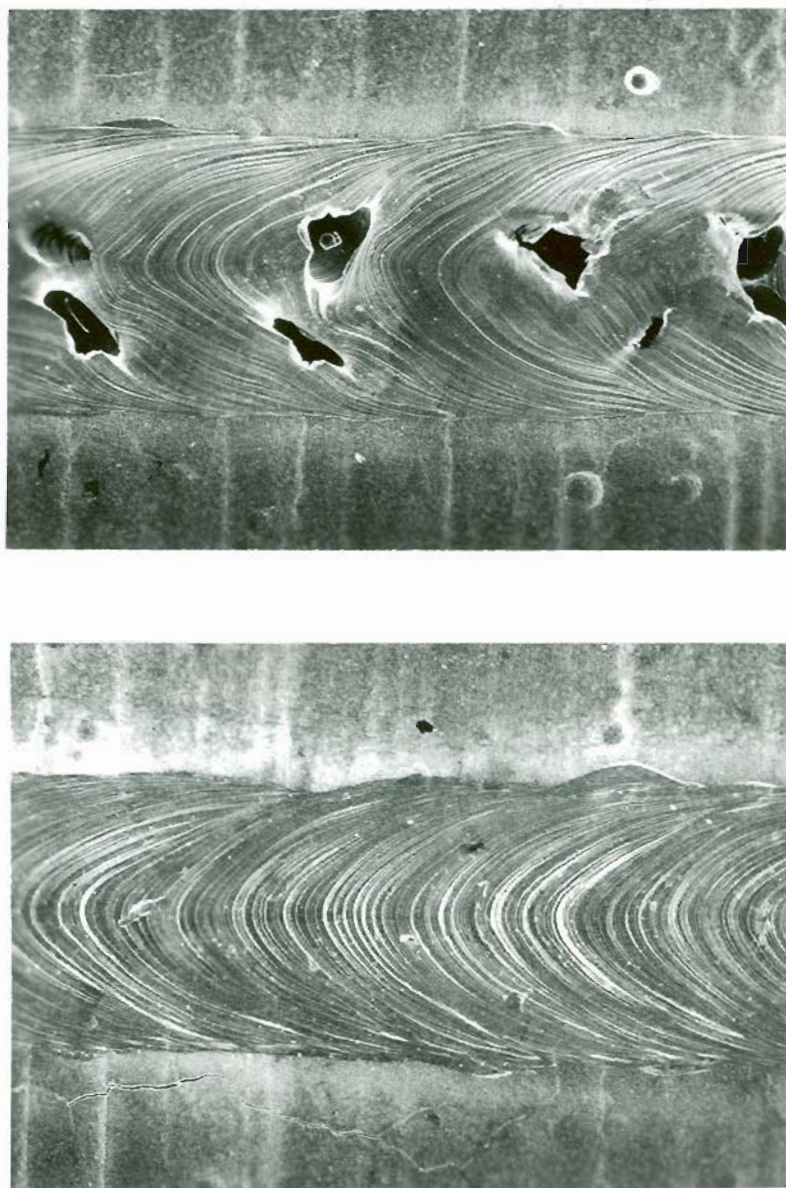


Figure 25. SCANNING ELECTRON MICROGRAPHS SHOWING THE EFFECT OF TRAPPED HYDROGEN ON THE LASER ALLOYED SURFACES

- a) BEFORE DEGASSING
- b) AFTER DEGASSING.

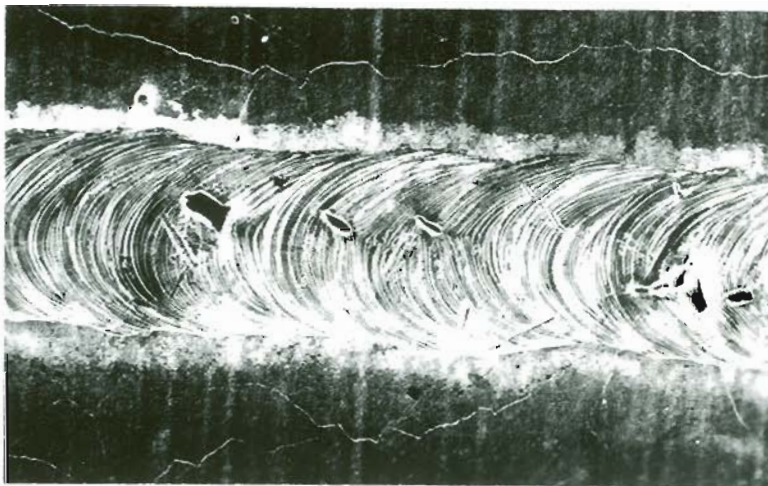
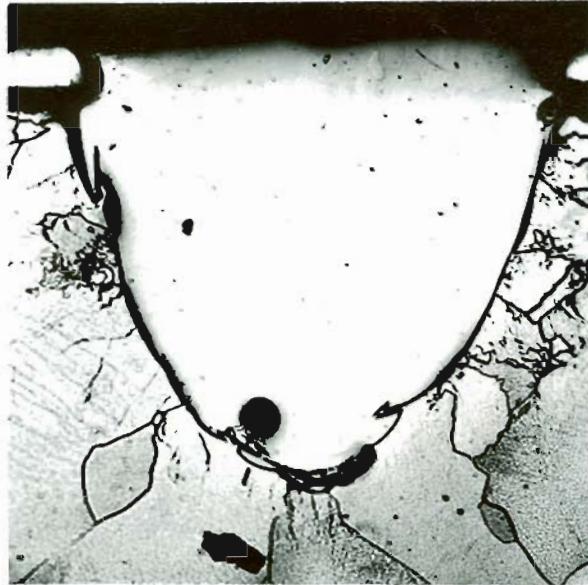


Figure 26. OPTICAL AND SCANNING ELECTRON MICROGRAPHS SHOWING THE EFFECT OF TRAPPED HYDROGEN ON POROSITY OF LASER ALLOYED SURFACES AS A FUNCTION OF SCAN RATE

a) AND b) 30 in/min.

MAGNIFICATION: a) 120x, b) 50x.



Figure 26. OPTICAL AND SCANNING ELECTRON MICROGRAPHS SHOWING THE EFFECT OF TRAPPED HYDROGEN ON POROSITY OF LASER ALLOYED SURFACES AS A FUNCTION OF SCAN RATE

c) AND d) 60 in/min.

MAGNIFICATION: c) 120x, d) 50x.

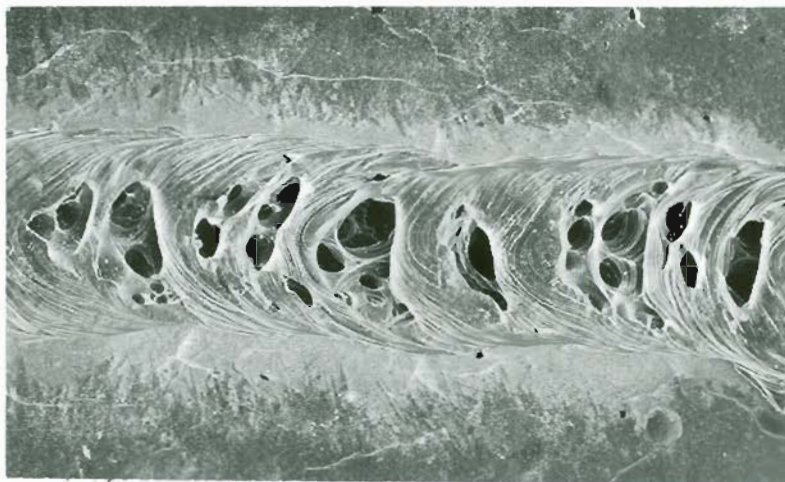


Figure 26. OPTICAL AND SCANNING ELECTRON MICROGRAPHS SHOWING THE  
(cont.) EFFECT OF TRAPPED HYDROGEN ON POROSITY OF LASER ALLOYED  
SURFACES AS A FUNCTION OF SCAN RATE

e) AND f) 100 in/min.

MAGNIFICATION: e) 120x, f) 50 x.

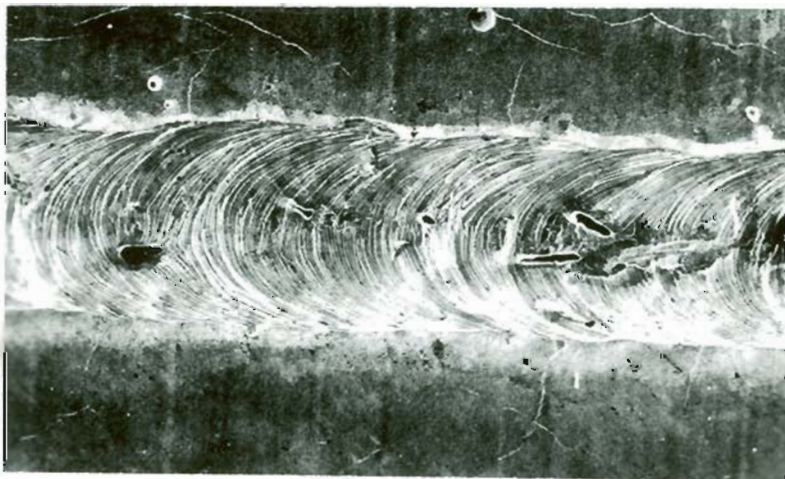
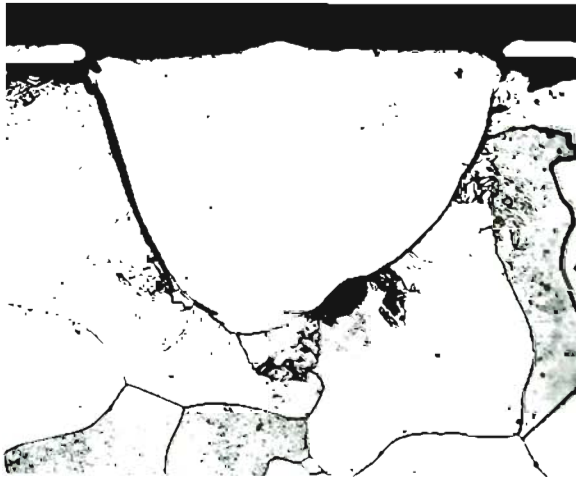


Figure 27. OPTICAL AND SCANNING ELECTRON MICROGRAPHS SHOWING THE EFFECT OF TRAPPED HYDROGEN ON POROSITY OF LASER ALLOYED SURFACES AS A FUNCTION OF COATING THICKNESS

a) AND b) 30 $\mu$ m

MAGNIFICATION: a) 120x, b) 50x.

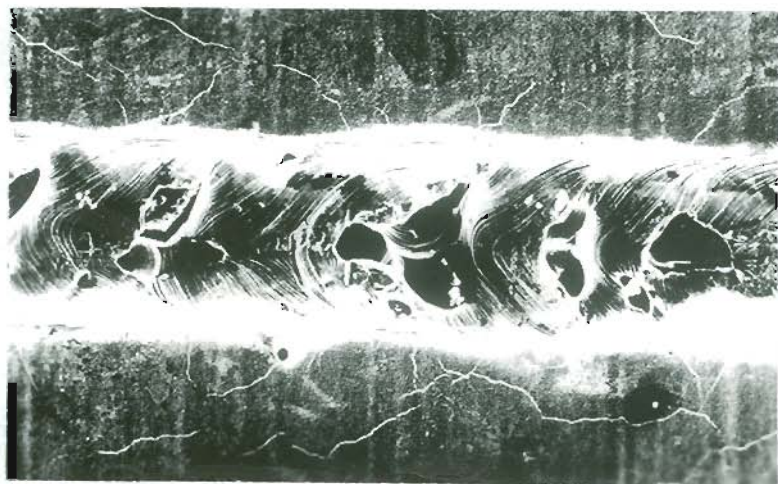


Figure 27. OPTICAL AND SCANNING ELECTRON MICROGRAPHS SHOWING THE  
(cont.) EFFECT OF TRAPPED HYDROGEN ON POROSITY OF LASER ALLOYED  
SURFACES AS A FUNCTION OF COATING THICKNESS

c) AND d)  $60\mu\text{m}$

MAGNIFICATION: c) 120x, d) 50x.

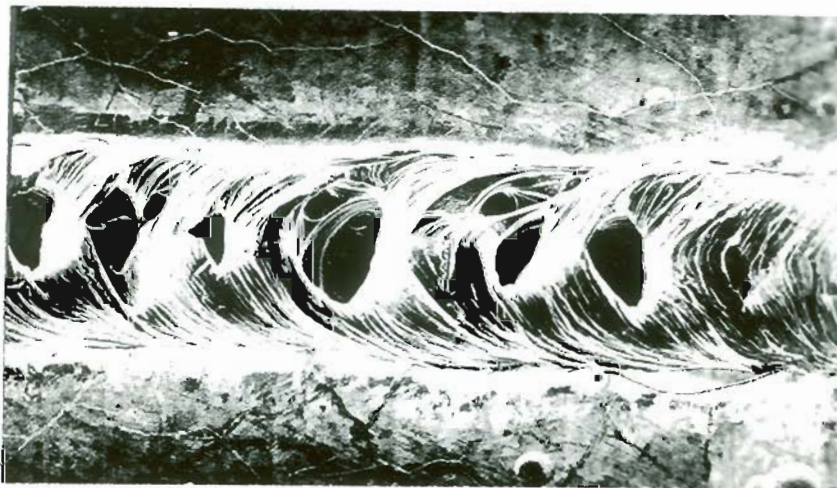
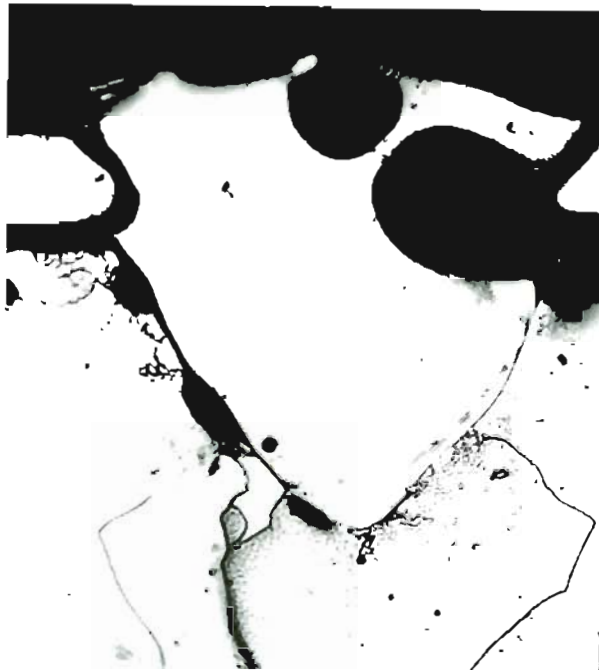


Figure 27. OPTICAL AND SCANNING ELECTRON MICROGRAPHS SHOWING THE  
(cont.) EFFECT OF TRAPPED HYDROGEN ON POROSITY OF LASER ALLOYED  
SURFACES AS A FUNCTION OF COATING THICKNESS

e) AND f) 120 $\mu$ m

MAGNIFICATION: e) 120x, f) 50x.

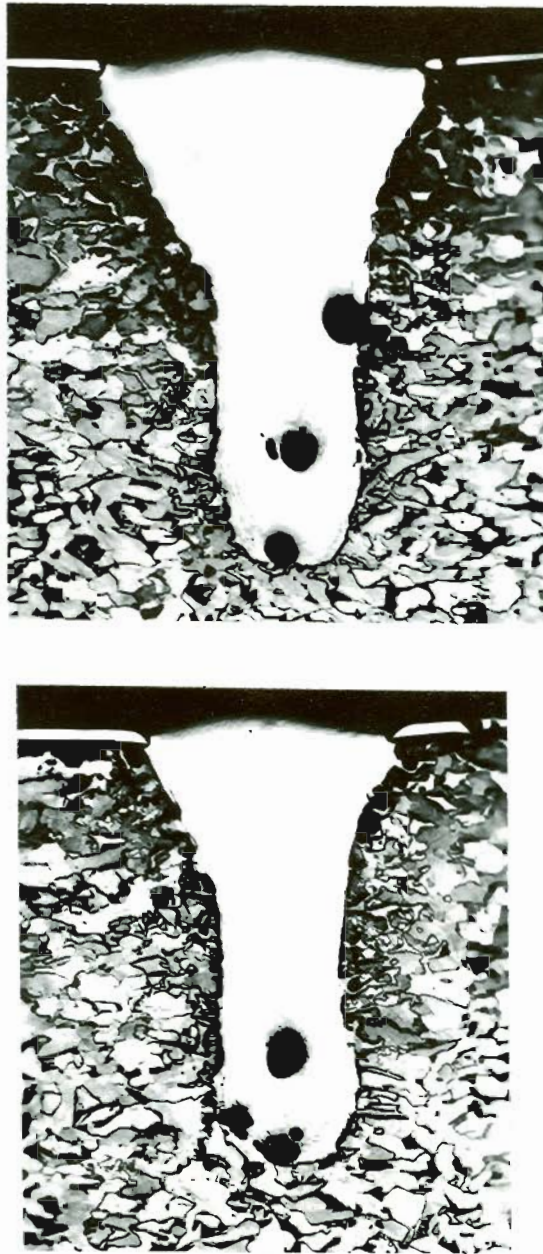


Figure 28. OPTICAL MICROGRAPH SHOWING THE "KEYHOLE" POROSITY IN DEEP PENETRATION FUSION ZONES. MAGNIFICATION: 50x.

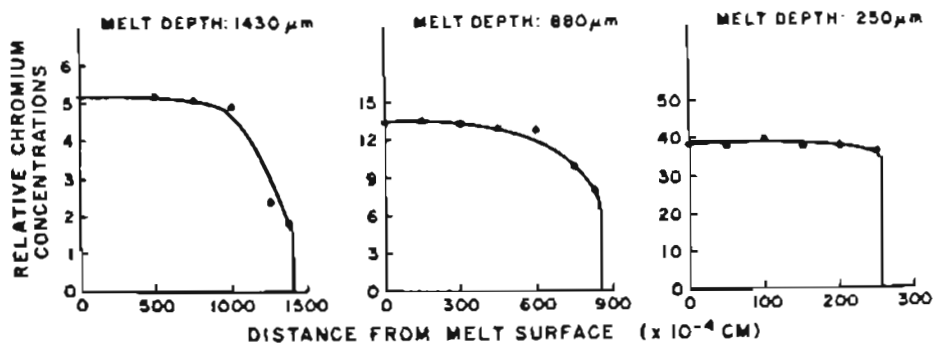
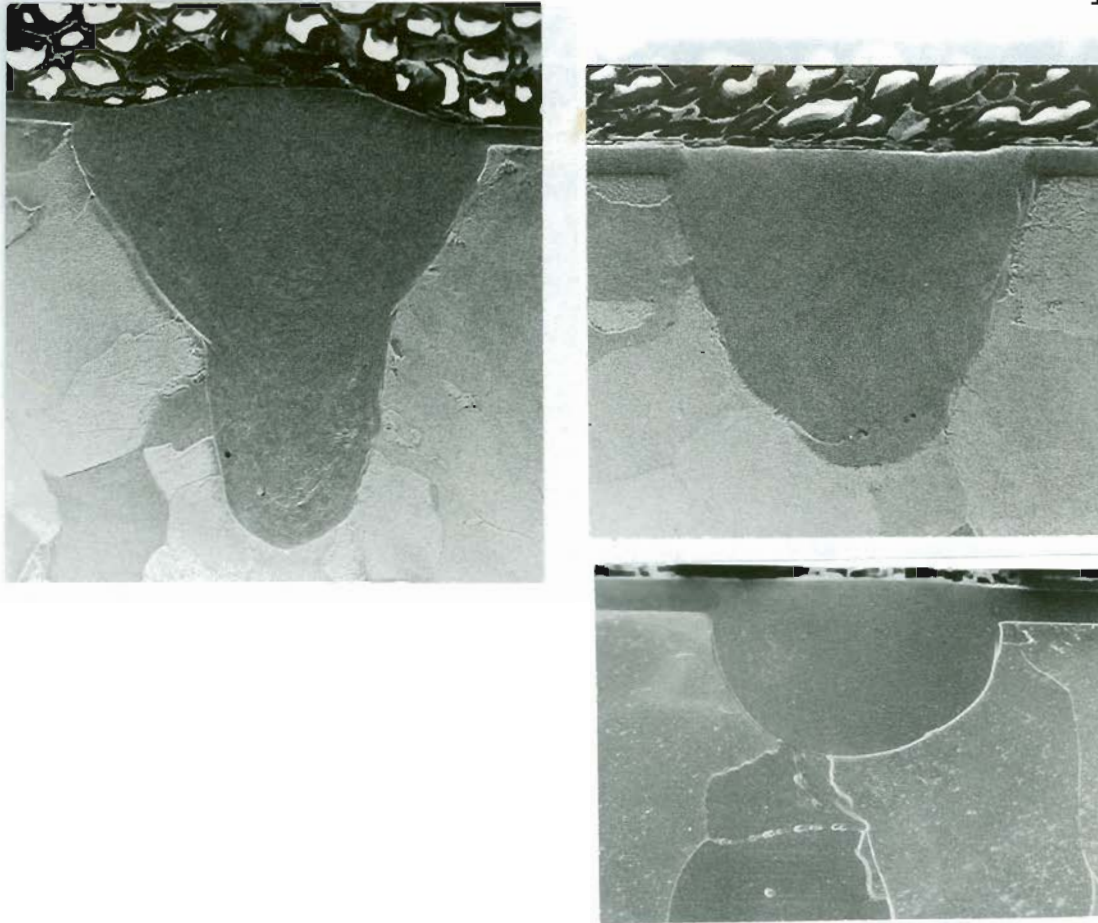


Figure 29. EFFECT OF FUSION ZONE SHAPE ON THE COMPOSITION UNIFORMITY OF FUSION ZONE.

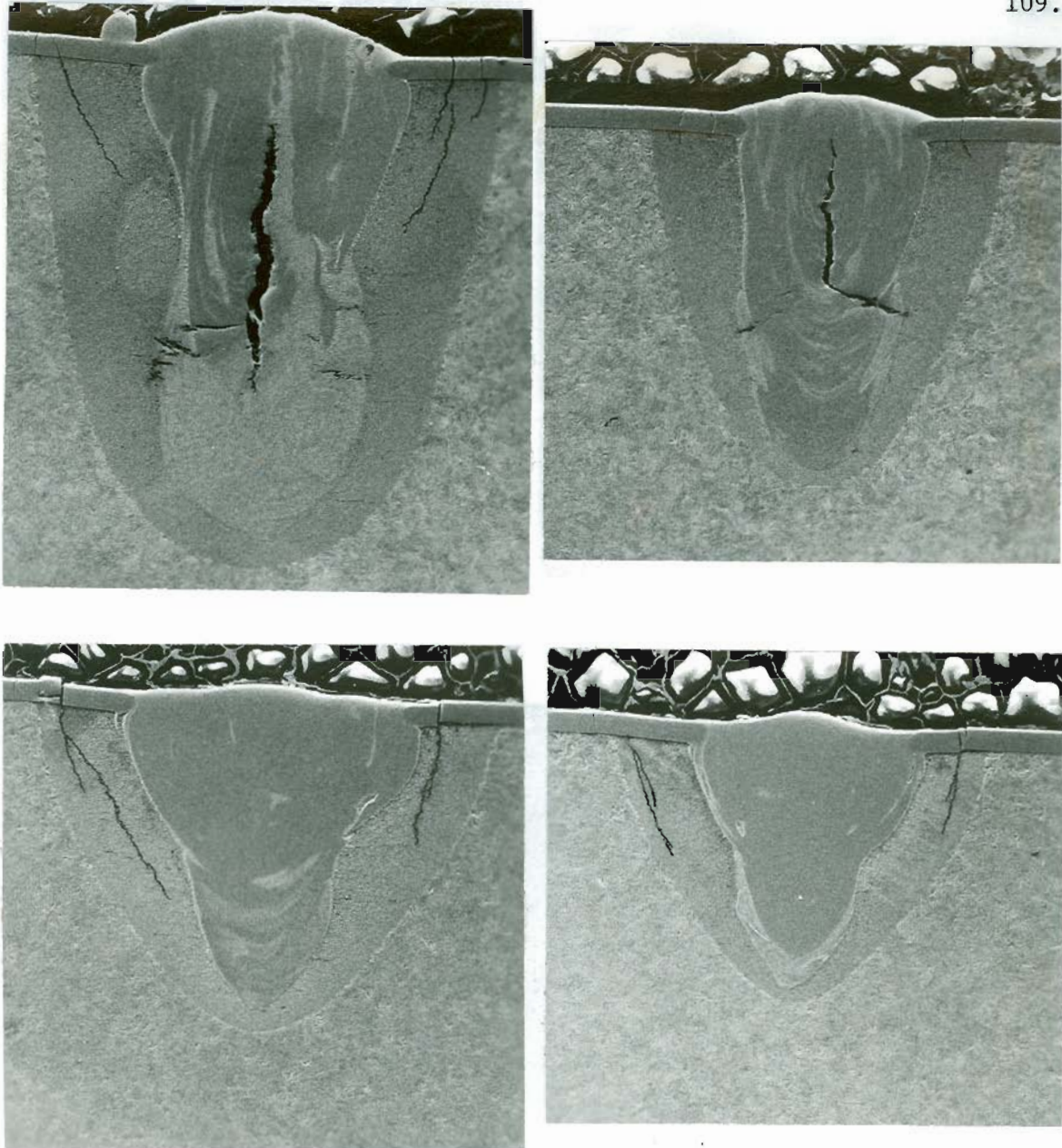


Figure 30. SCANNING ELECTRON MICROGRAPHS SHOWING THE EFFECT OF FUSION ZONE SIZE AND SHAPE ON THE CRACK SUSCEPTIBILITY OF Fe-1.0%Cr ALLOYS. MAGNIFICATION: 50x.

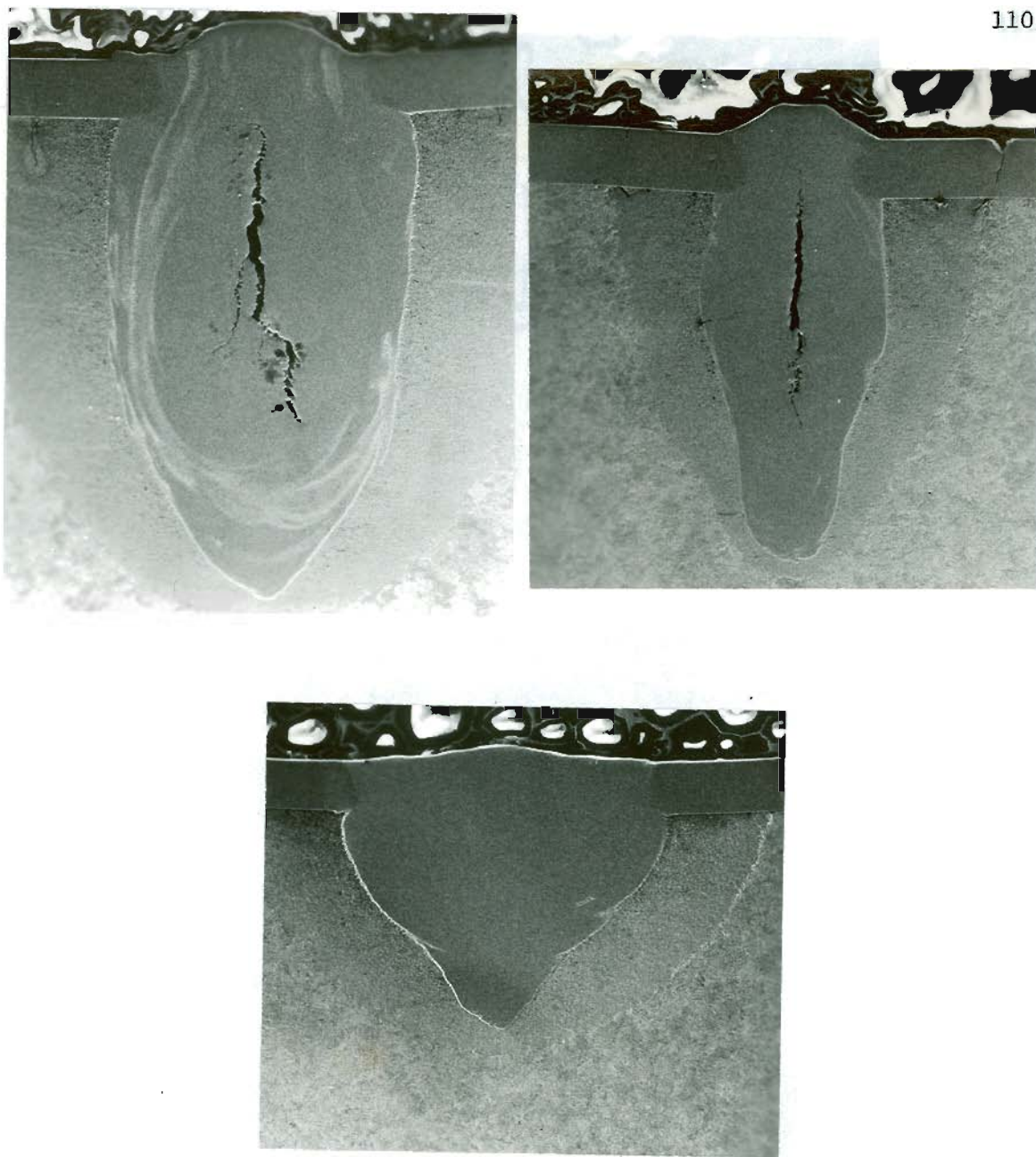


Figure 31. SCANNING ELECTRON MICROGRAPHS SHOWING THE EFFECT OF FUSION ZONE SIZE ON THE CRACK SUSCEPTIBILITY OF Fe-1.0%C-Cr ALLOYS. MAGNIFICATION: 50x.

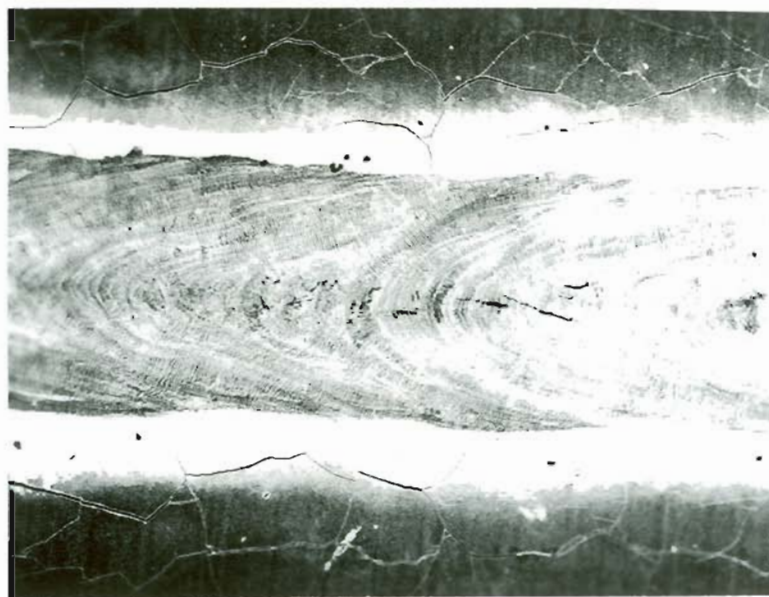
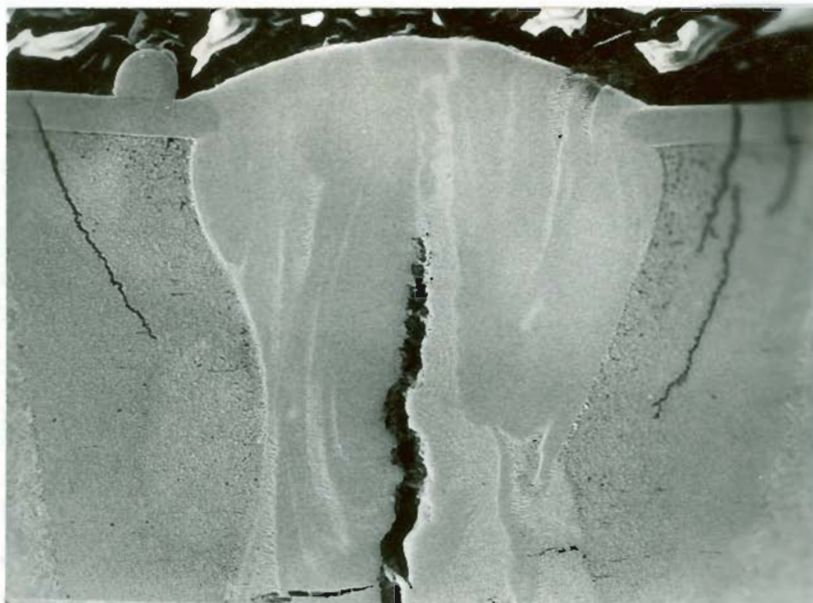


Figure 32. SCANNING ELECTRON MICROGRAPHS SHOWING

- a) THE HEAT AFFECTED ZONE CRACKS; 100x
- b) THE CRACKS IN THE COATING ADJACENT TO THE MELT PASS;  
50x.

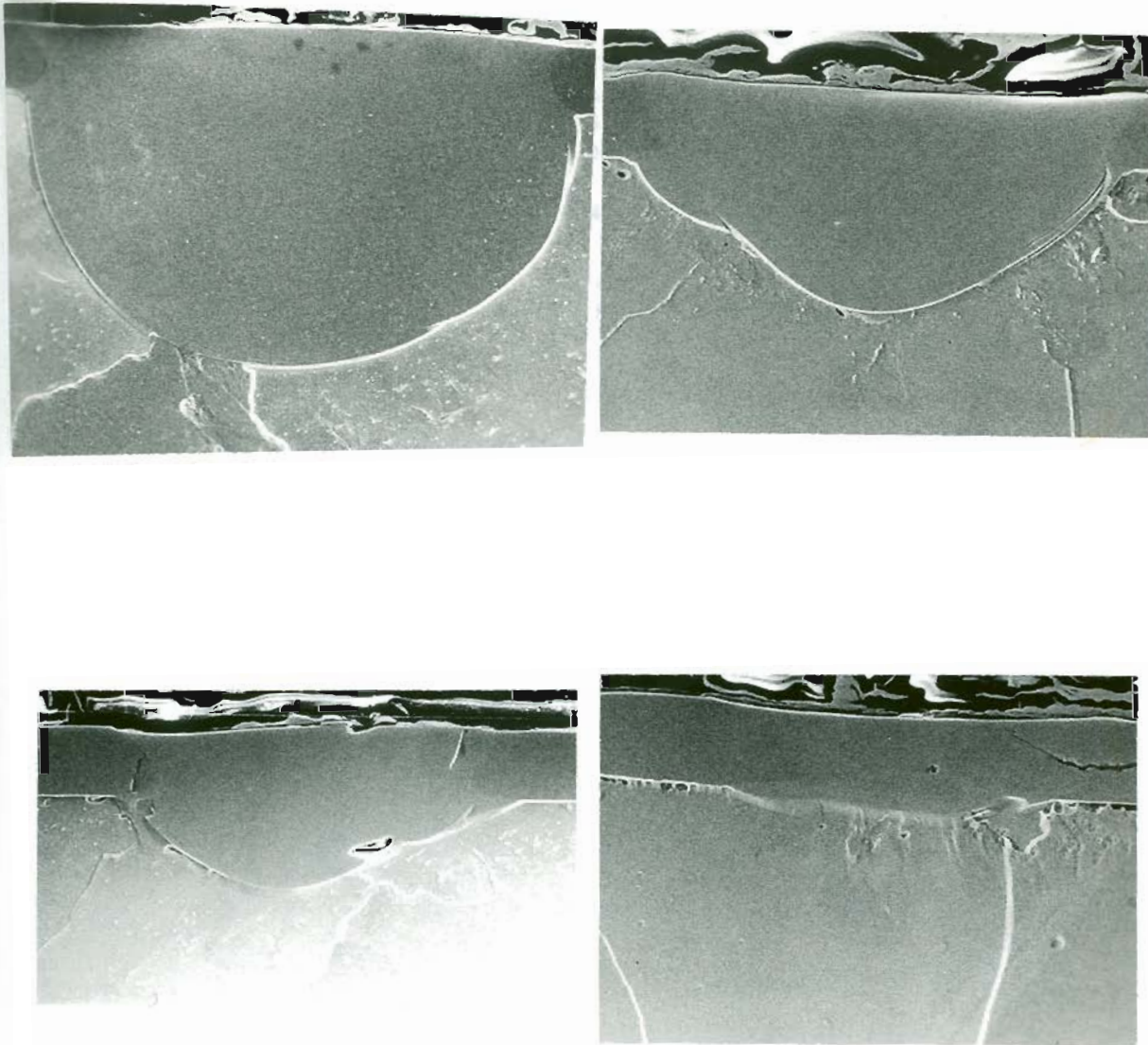


Figure 33. SCANNING ELECTRON MICROGRAPHS SHOWING THE SEMICIRCULAR FUSION ZONES. MAGNIFICATION: 200x.

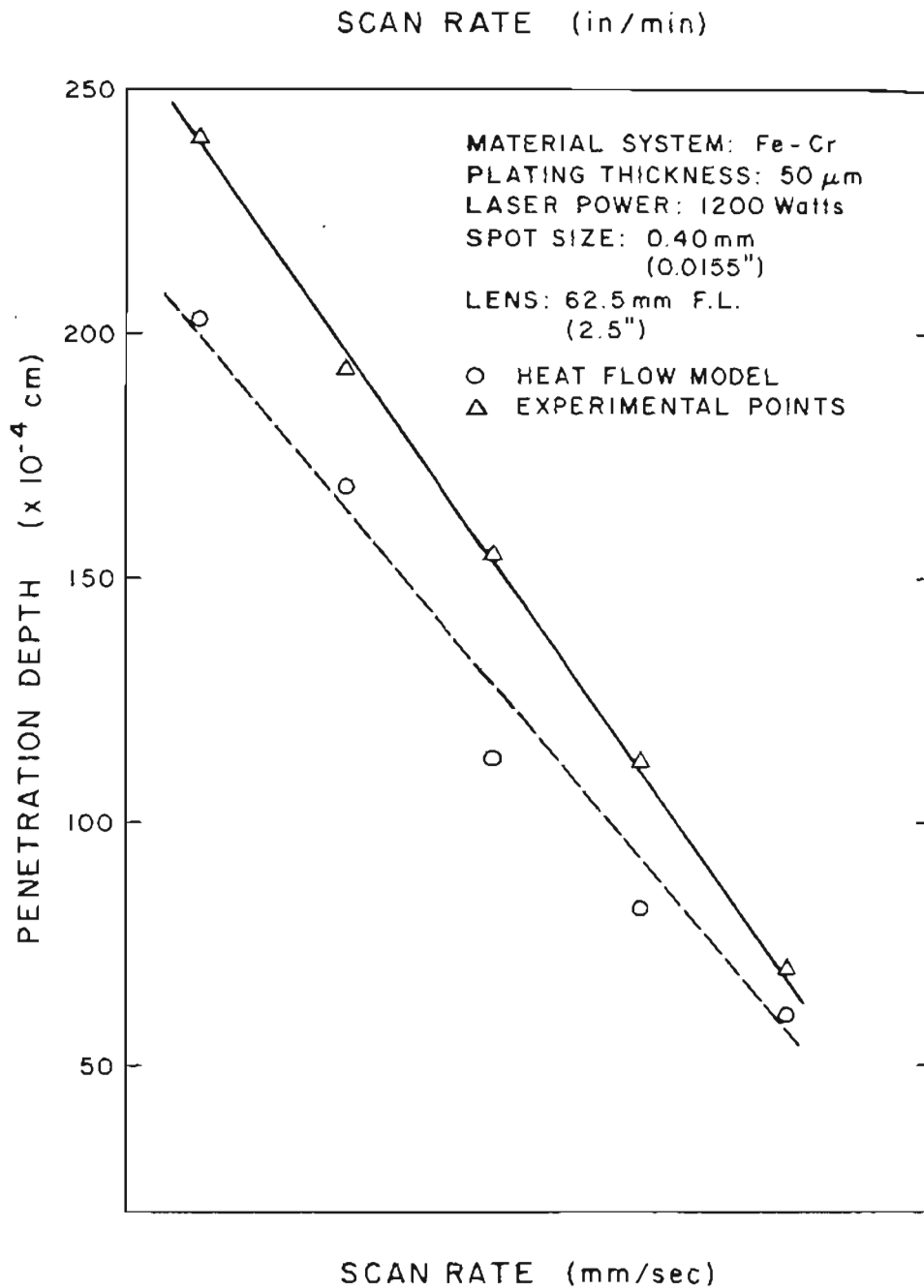


Figure 34. EFFECT OF SCAN RATE ON MELT PENETRATION OF Fe-Cr ALLOYS AS PREDICTED BY A ONE-DIMENSIONAL HEAT TRANSFER MODEL.

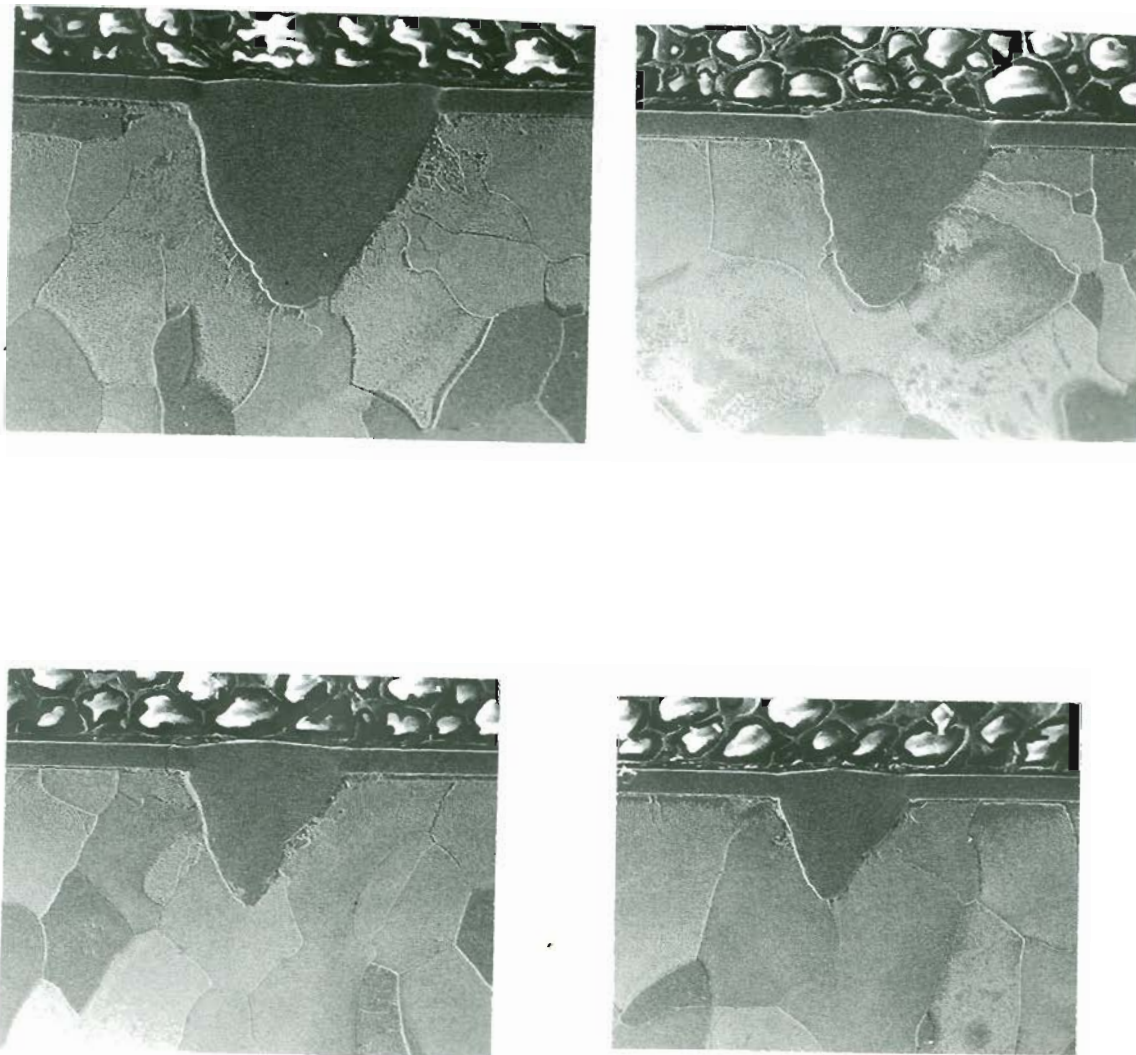


Figure 35. SCANNING ELECTRON MICROGRAPHS SHOWING THE TRIANGULAR FUSION ZONES. MAGNIFICATION: 50x.

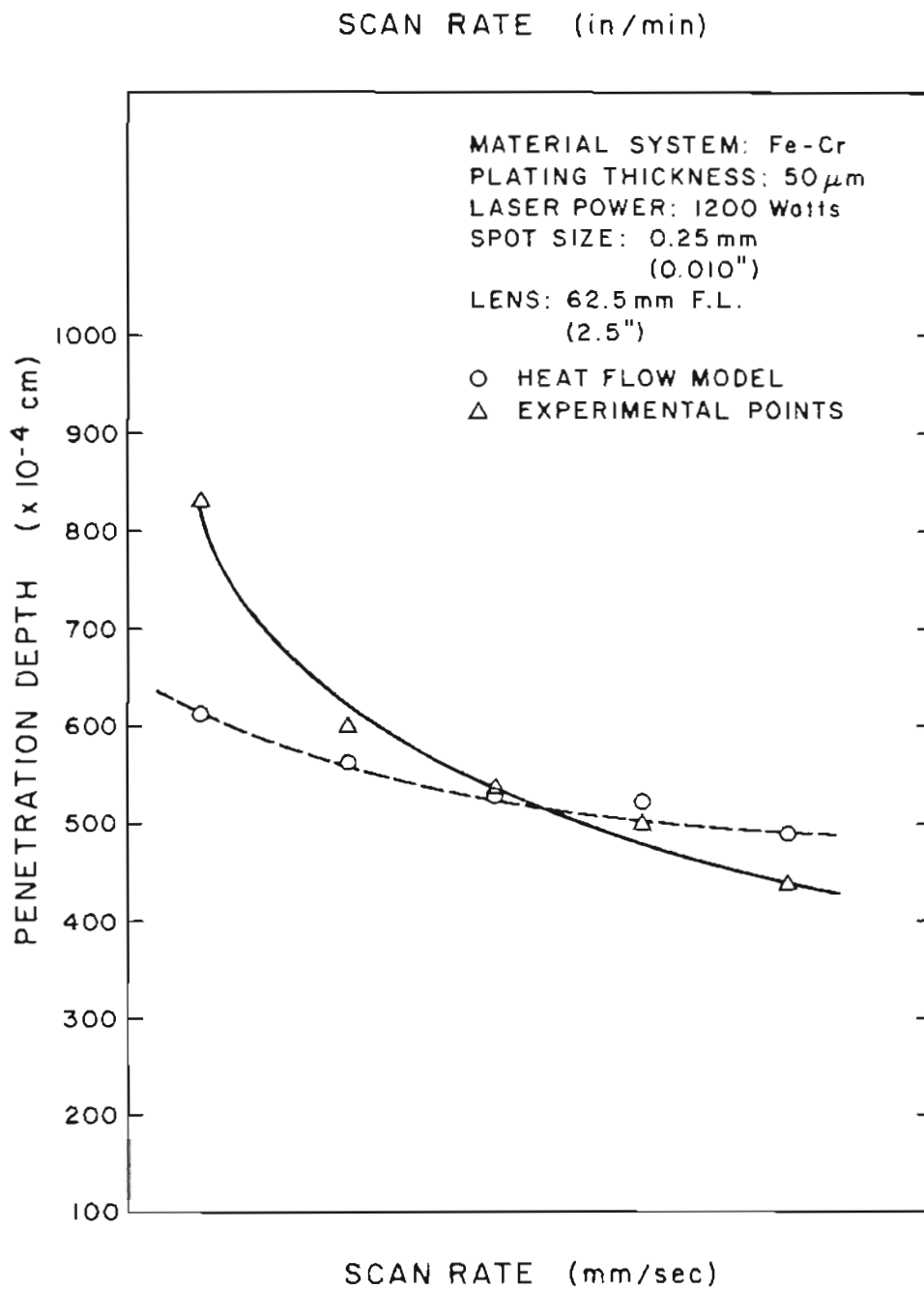


Figure 36. EFFECT OF SCAN RATE ON MELT PENETRATION OF Fe-Cr ALLOYS AS PREDICTED BY A THREE-DIMENSIONAL HEAT TRANSFER MODEL.

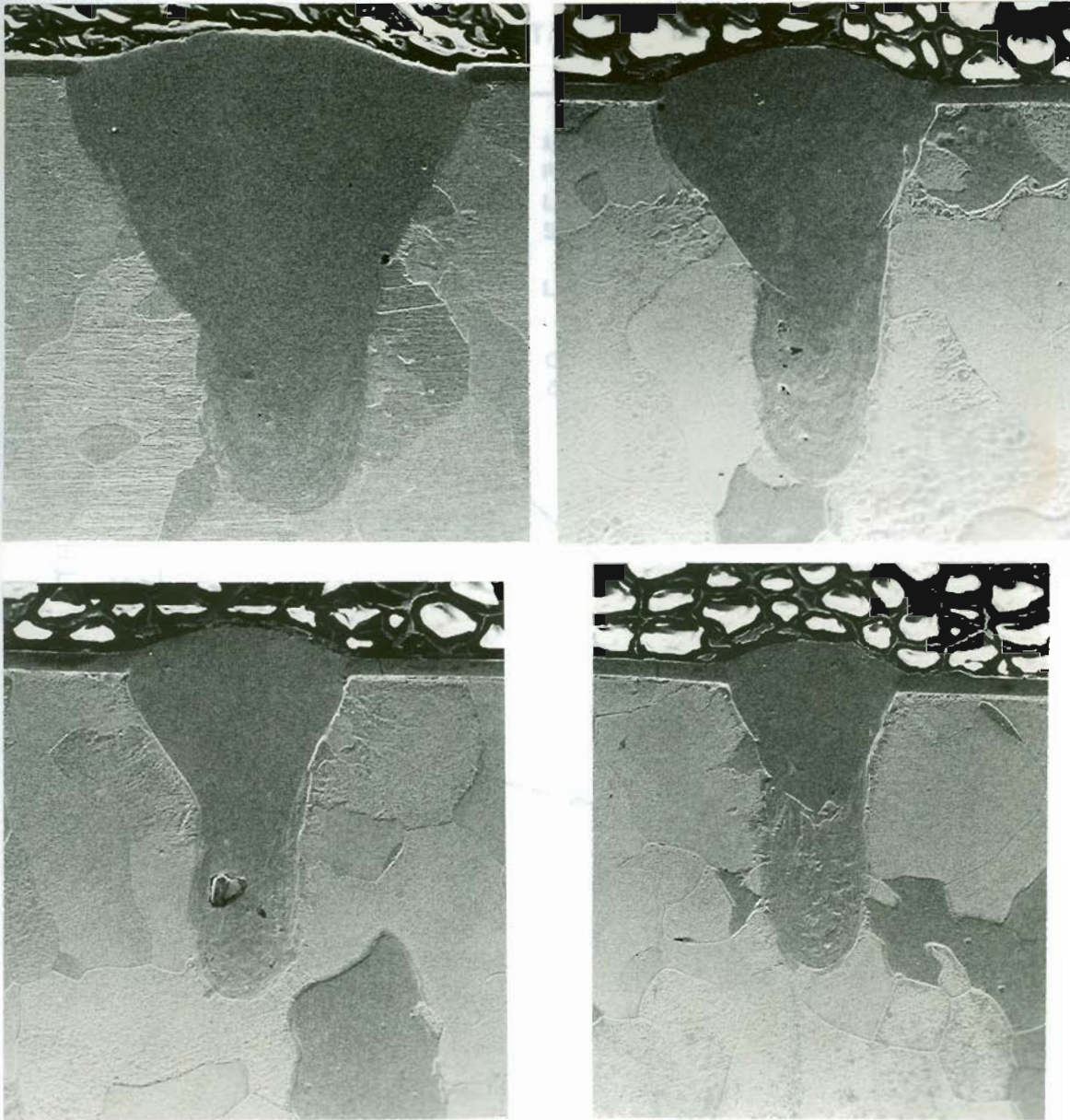


Figure 37. SCANNING ELECTRON MICROGRAPHS SHOWING THE HOUR-GLASS FUSION ZONES.

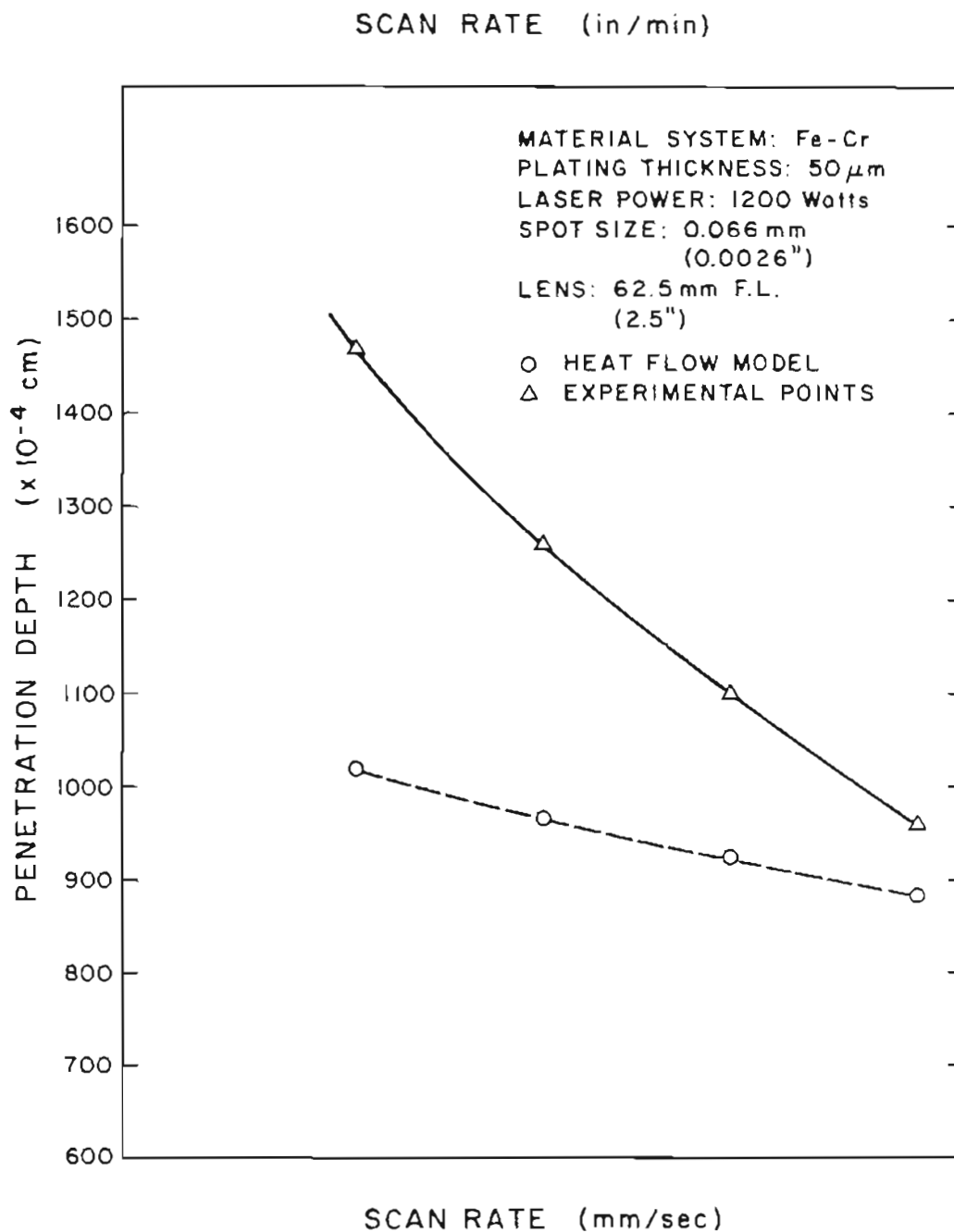


Figure 38. EFFECT OF SCAN RATE ON MELT PENETRATION OF Fe-Cr ALLOYS AS PREDICTED BY A THREE-DIMENSIONAL HEAT TRANSFER MODEL.

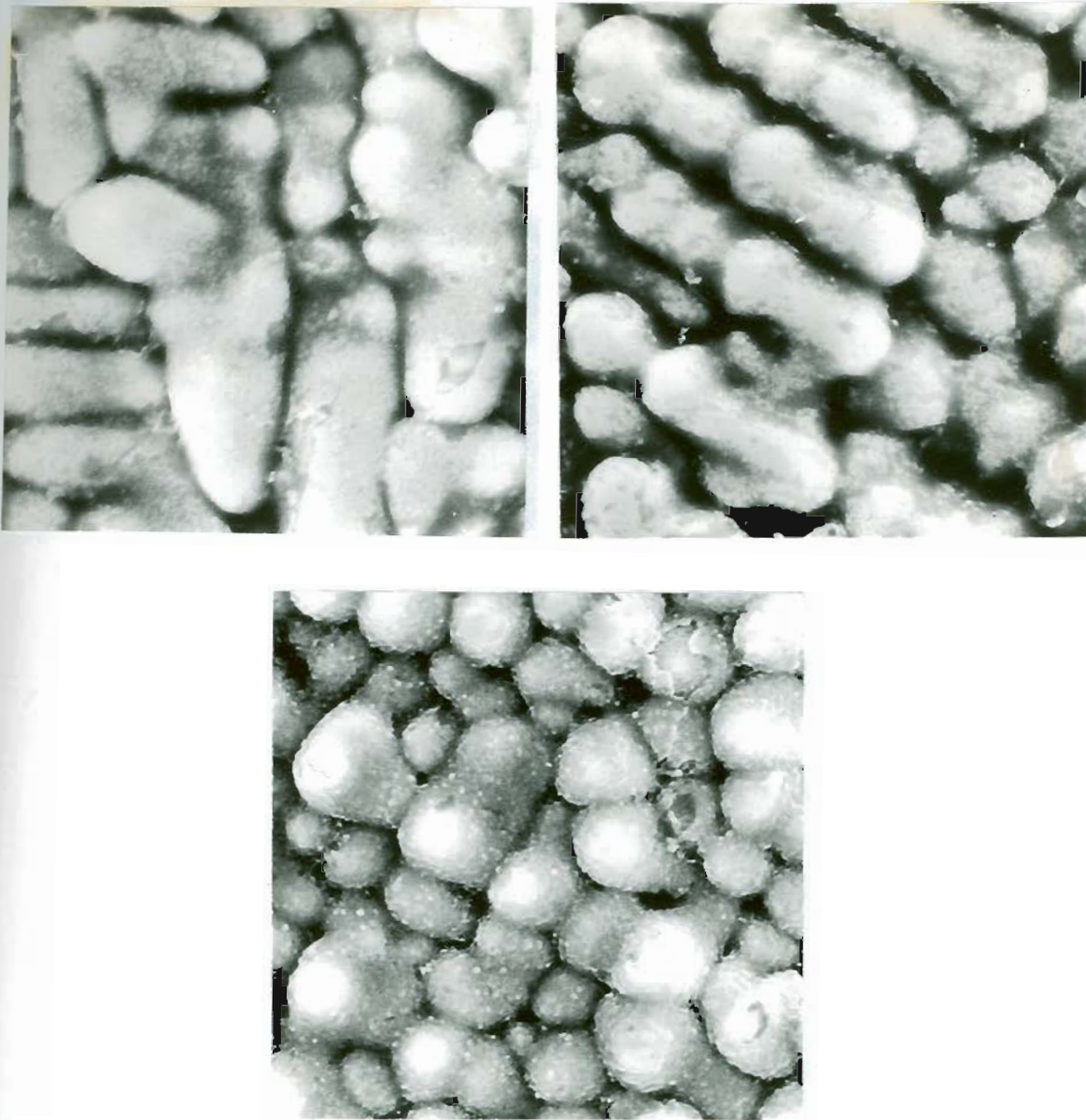


Figure 39. SCANNING ELECTRON MICROGRAPHS SHOWING THE SOLIDIFICATION STRUCTURES OF Fe-1.0%Cr ALLOYS WITH PENETRATION DEPTHS OF

a) 1500 $\mu$ m, b) 1340 $\mu$ m, c) 1150 $\mu$ m

MAGNIFICATION: 5000x.

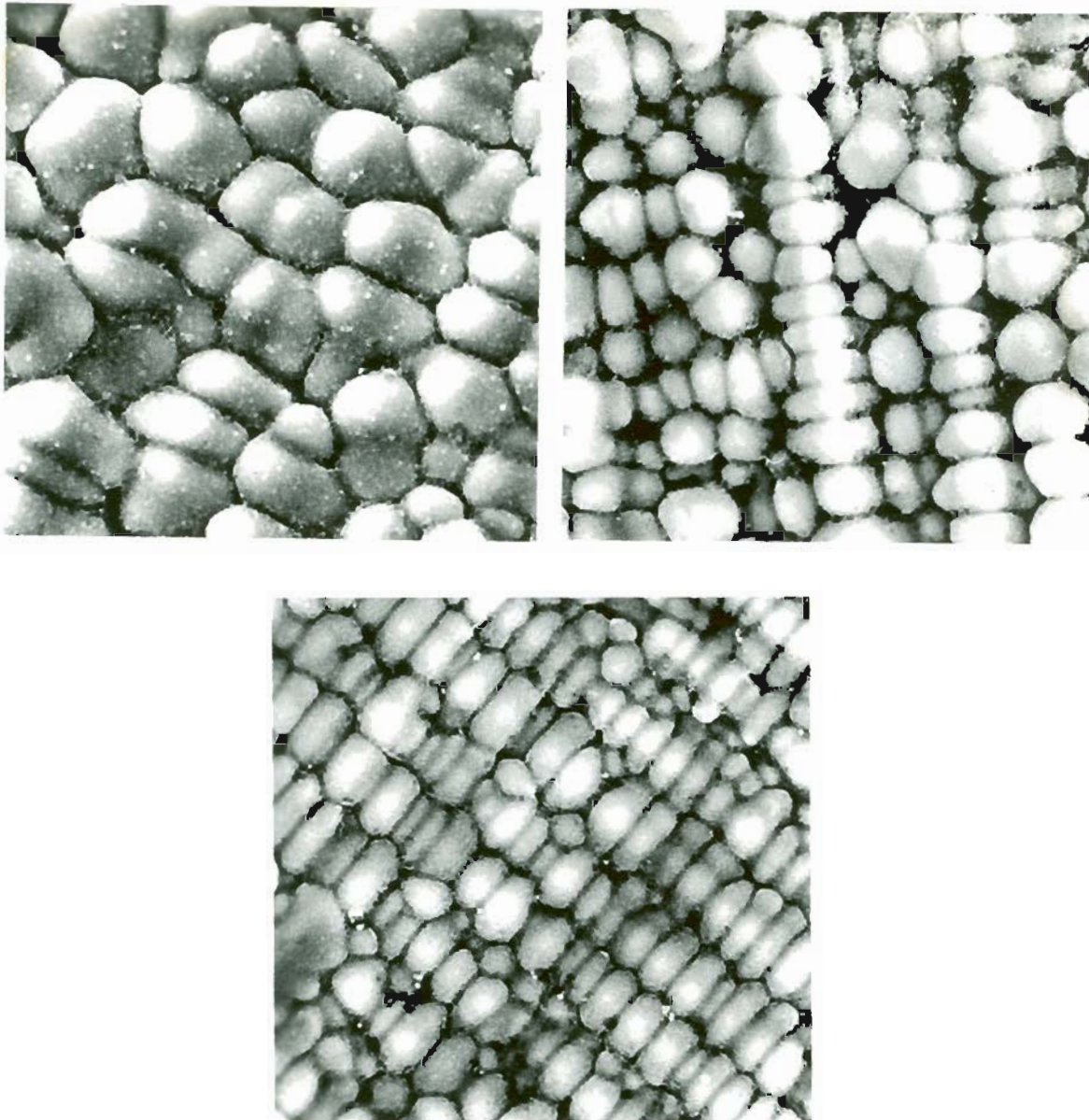


Figure 40. SCANNING ELECTRON MICROGRAPHS SHOWING THE SOLIDIFICATION STRUCTURES OF Fe-1.0%Cr ALLOYS WITH PENETRATION DEPTHS OF

a) 1000 $\mu$ m, b) 790 $\mu$ m, c) 700 $\mu$ m.

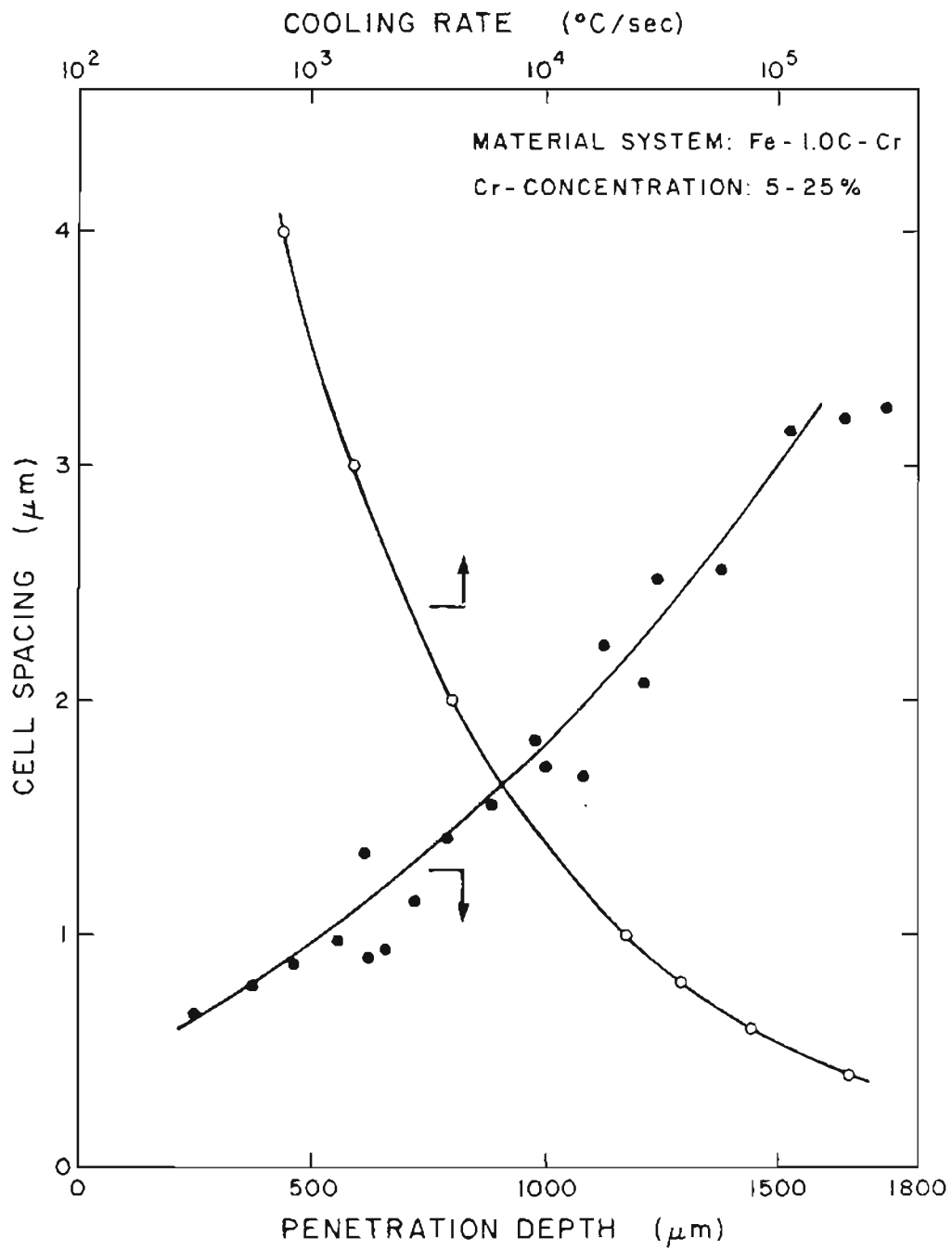


Figure 41. EFFECT OF PENETRATION DEPTH ON THE CELL SPACING OF SOLIDIFICATION STRUCTURES OF Fe-C-Cr ALLOYS.

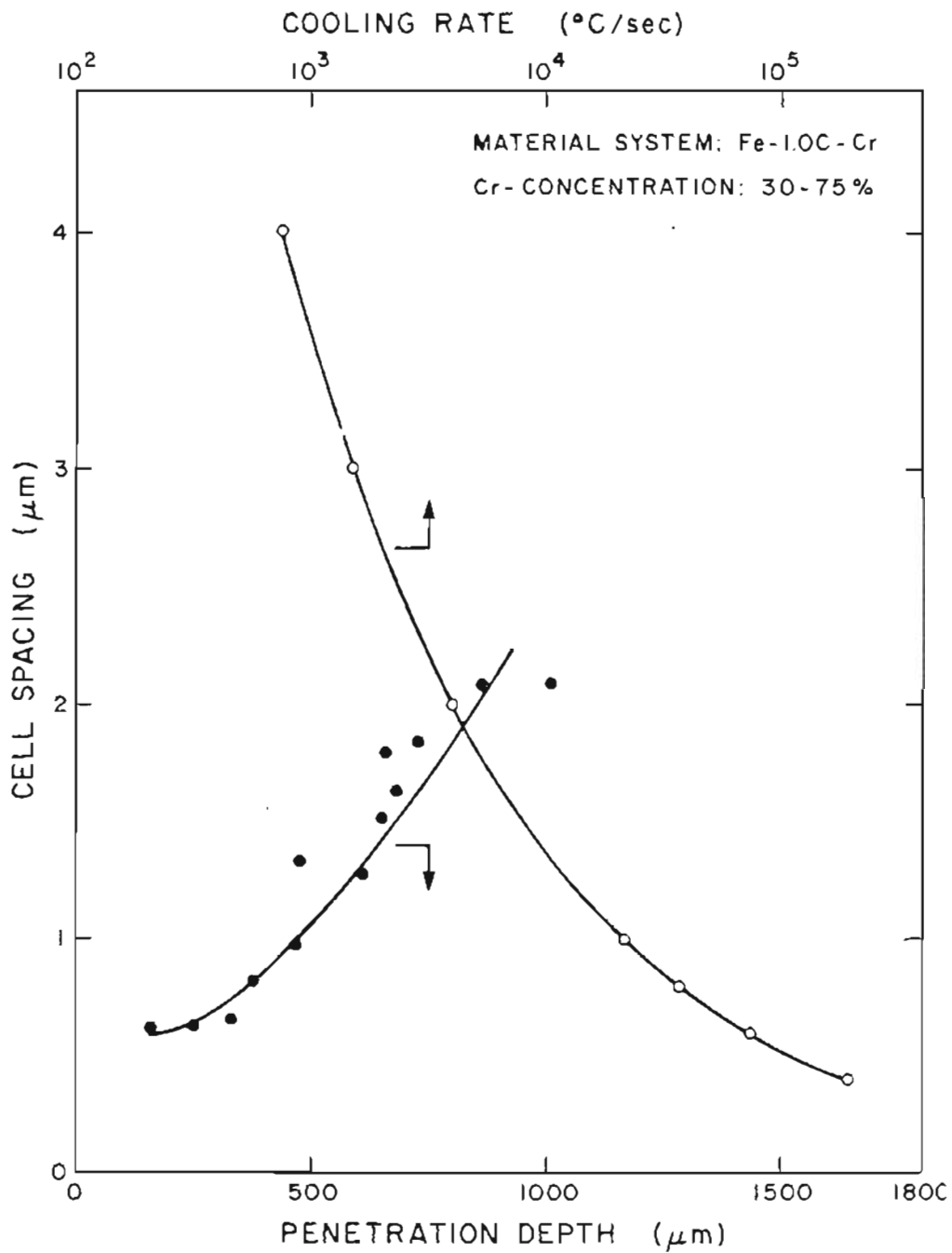


Figure 42. EFFECT OF PENETRATION DEPTH ON THE CELL SPACING OF SOLIDIFICATION STRUCTURES OF Fe-C-Cr ALLOYS.

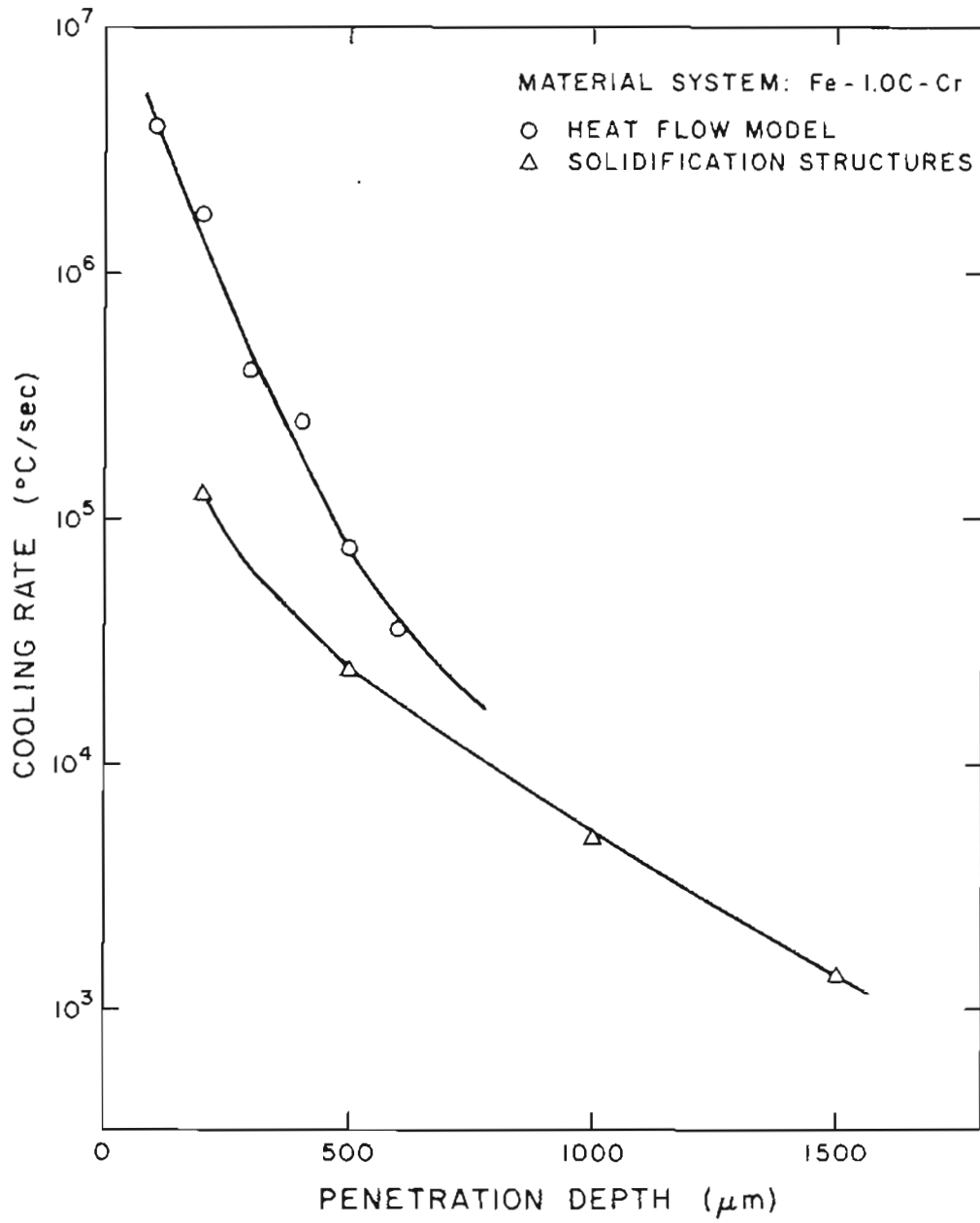


Figure 43. EFFECT OF PENETRATION DEPTH ON THE SOLIDIFICATION COOLING RATES AS PREDICTED BY HEAT TRANSFER MODELS AND SOLIDIFICATION STRUCTURES.

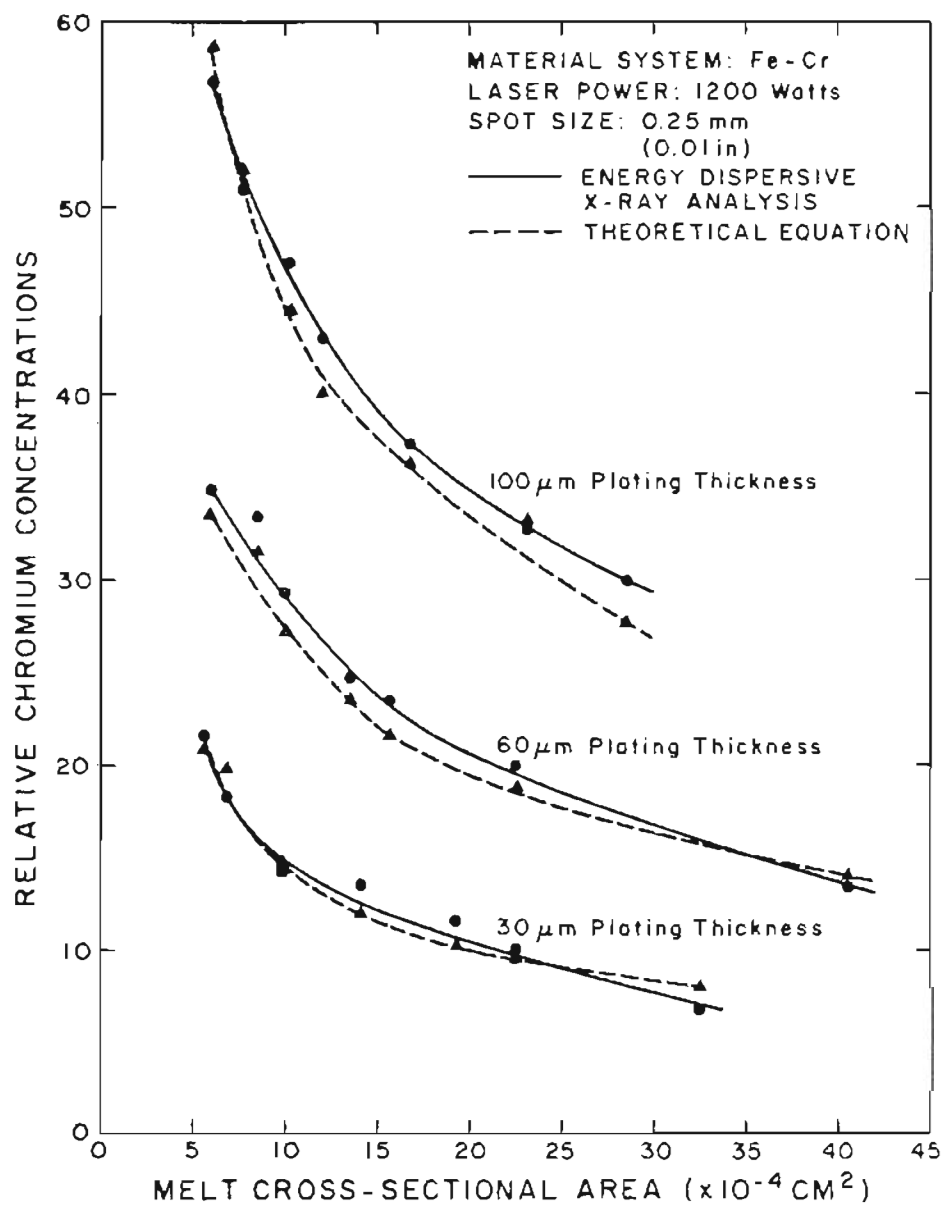


Figure 44. EFFECT OF COATING THICKNESS AND FUSION ZONE CROSS-SECTIONAL AREA ON THE ALLOY CONTENT OF FUSION ZONE.

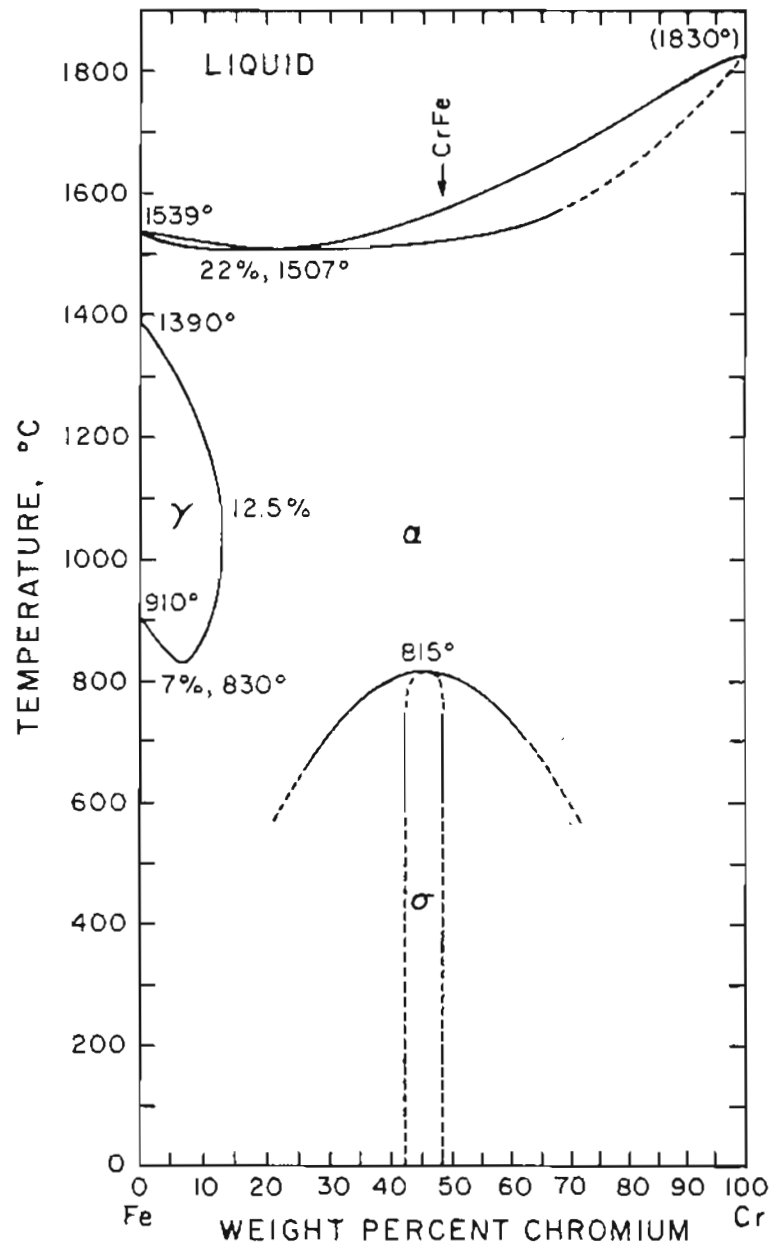


Figure 45. THE Fe-Cr PHASE DIAGRAM.

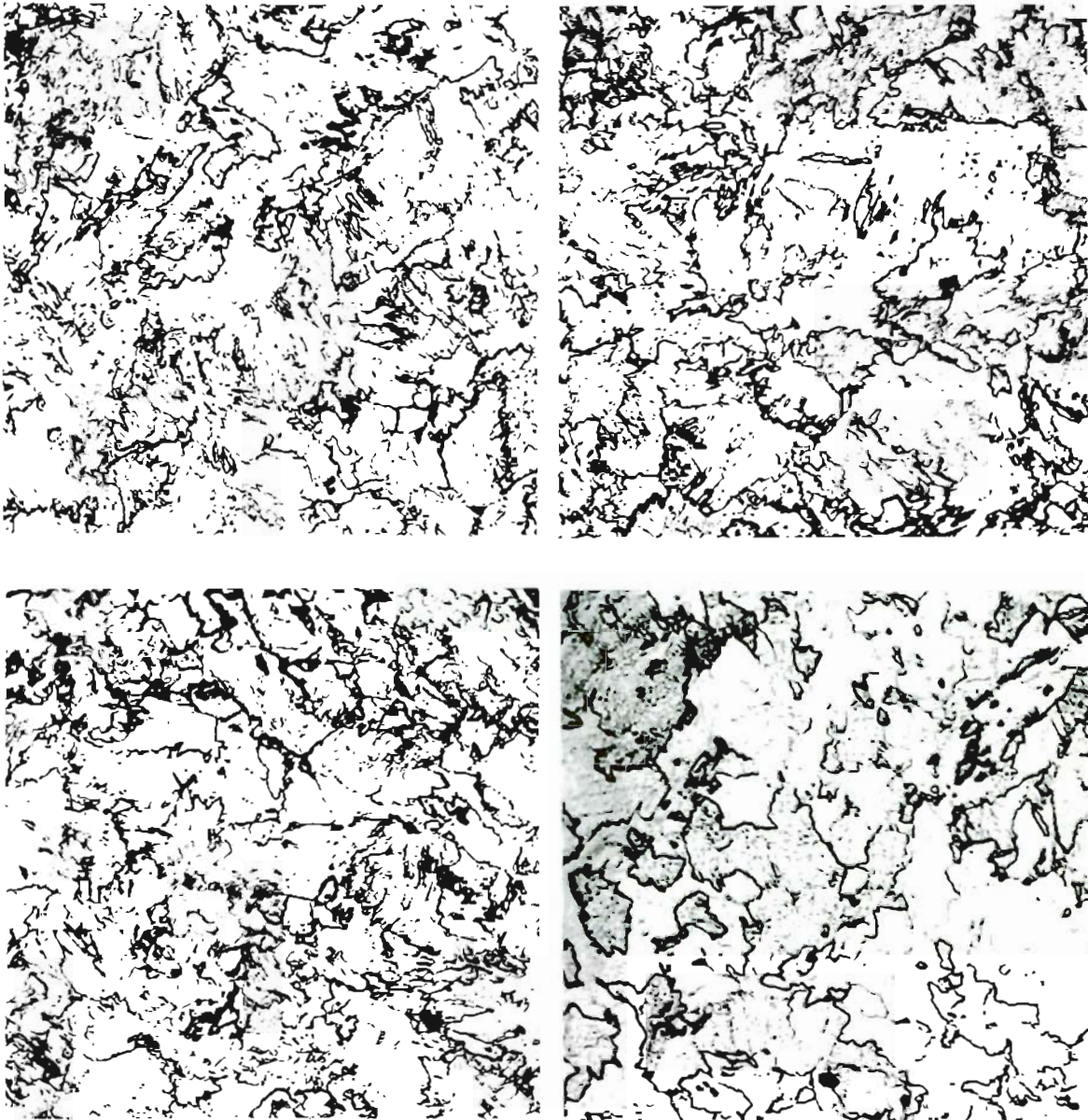


Figure 46. LIGHT MICROGRAPHS OF LASER PROCESSED Fe-Cr ALLOYS SHOWING THE MASSIVE FERRITE STRUCTURES

a) 4%Cr, b) 5%Cr, c) 7%Cr, and d) 10%Cr

MAGNIFICATION: 250x.

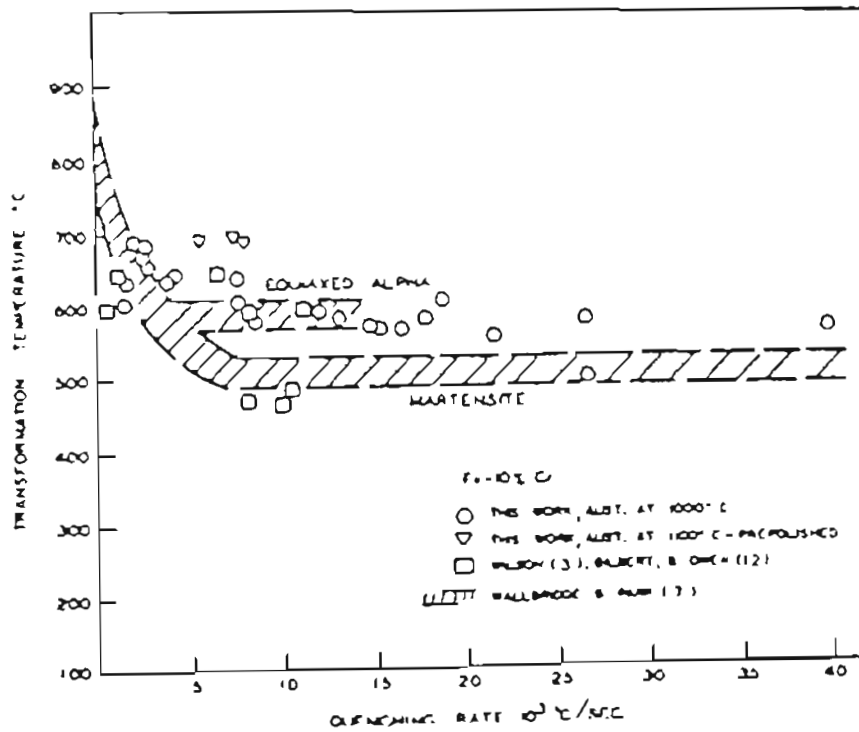


Figure 47. EFFECT OF QUENCH RATE ON THE TRANSFORMATION TEMPERATURE AND STRUCTURE OF Fe-10%Cr ALLOY [AFTER PASCOVER AND RADCLIFFE(53)].

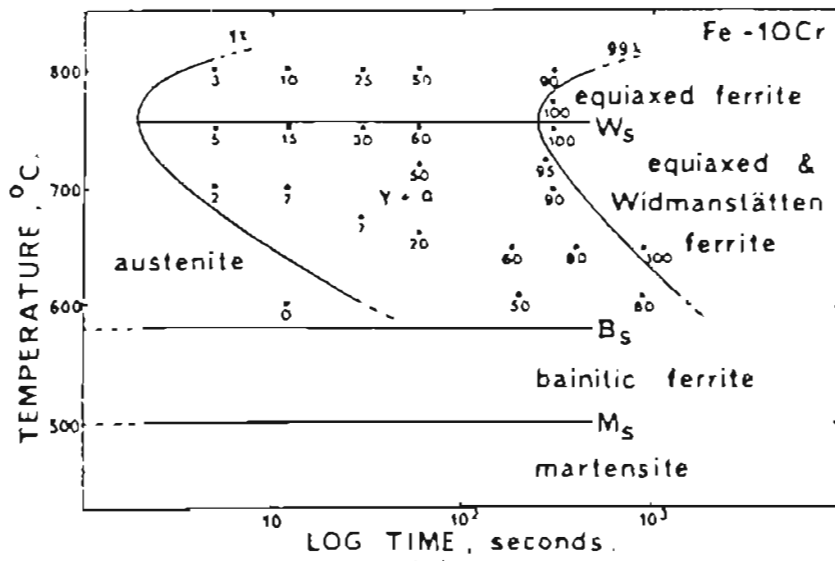


Figure 48. A TTT DIAGRAM FOR Fe-10%Cr ALLOY.

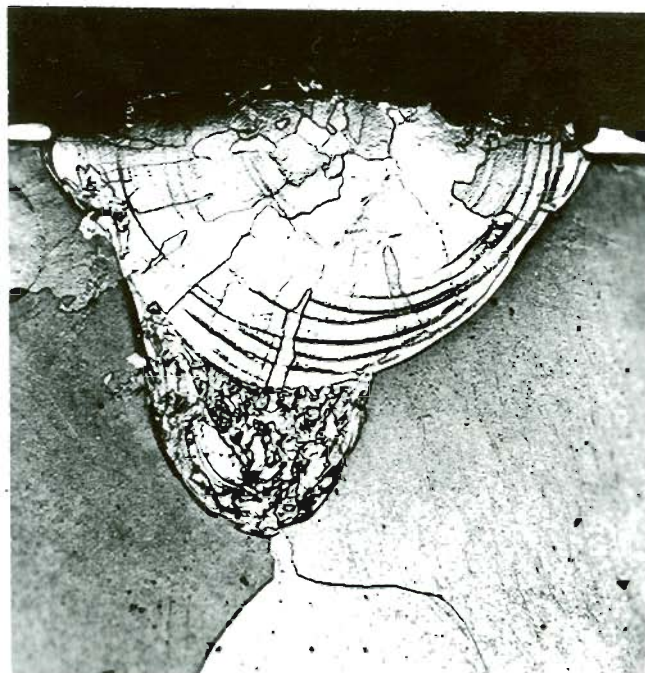


Figure 49. LIGHT MICROGRAPH OF A Fe-Cr ALLOY SHOWING THE VARIATION IN THE MORPHOLOGY OF FERRITE FROM THE BOTTOM TO THE TOP SURFACE OF FUSION ZONE AS A FUNCTION OF CHROMIUM CONTENT. MAGNIFICATION: 160x.

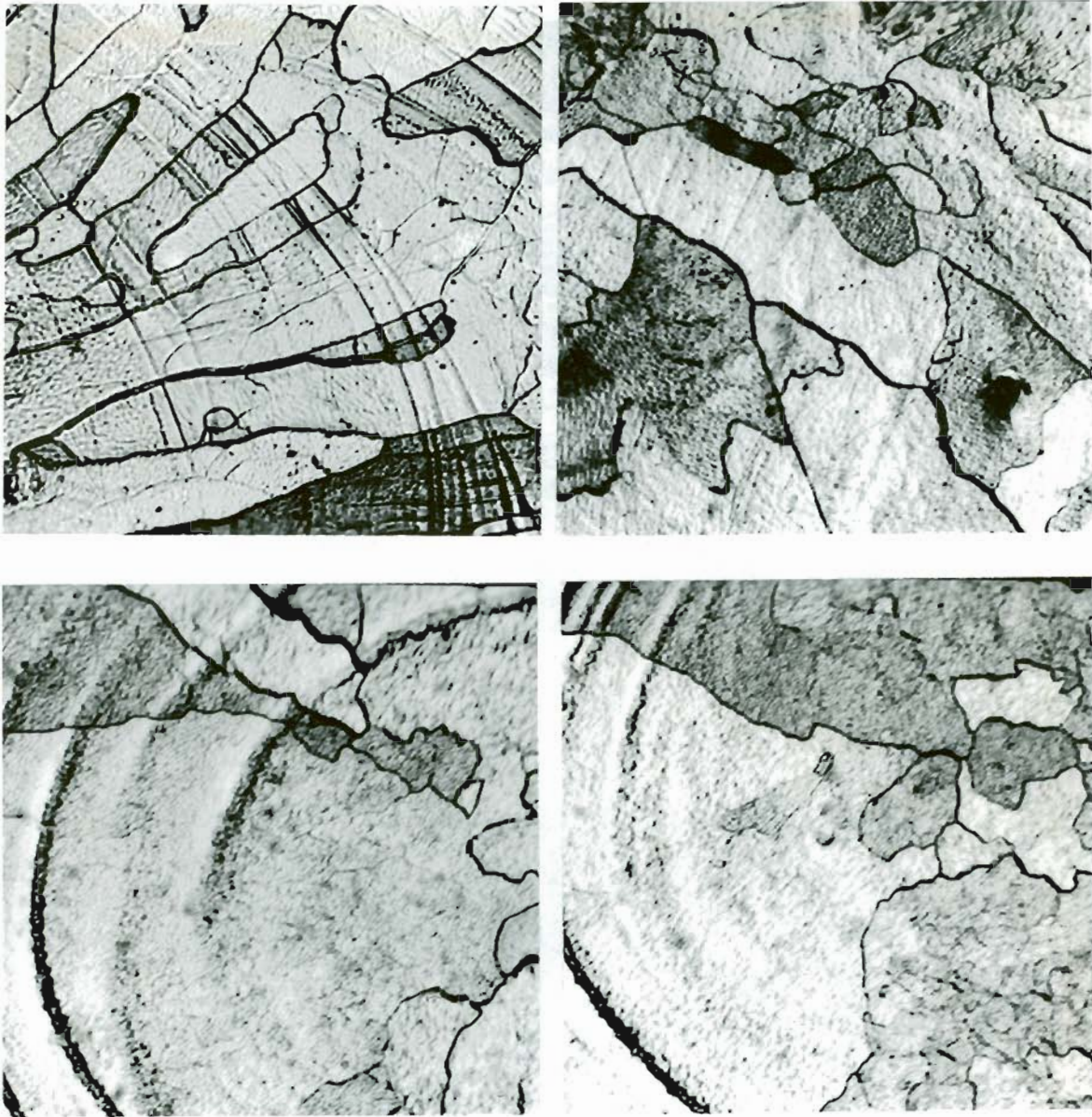


Figure 50. LIGHT MICROGRAPHS OF LASER PROCESSED Fe-Cr ALLOYS SHOWING THE EQUIAXED FERRITIC STRUCTURES

a) 20%Cr, b) 25%Cr, c) 30%Cr, d) 50%Cr

MAGNIFICATION: 400x.

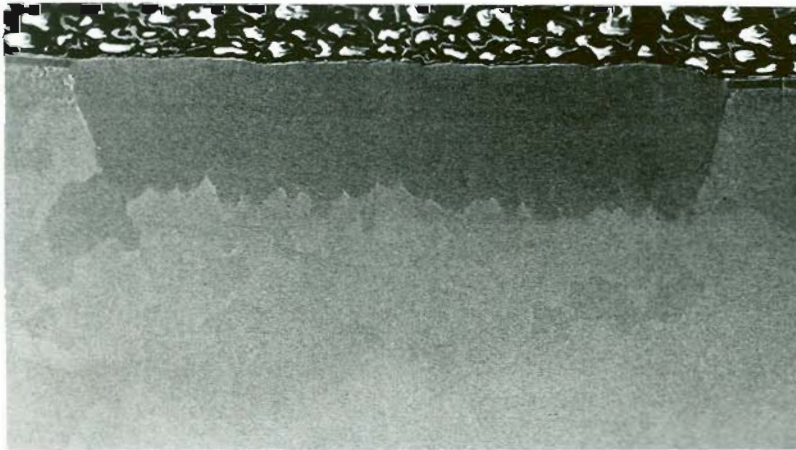


Figure 51. THE LONGITUDINAL AND TRANSVERSE SECTIONS OF "MULTIPLE SCAN" LASER ALLOYED SURFACES. MAGNIFICATION: 50x.

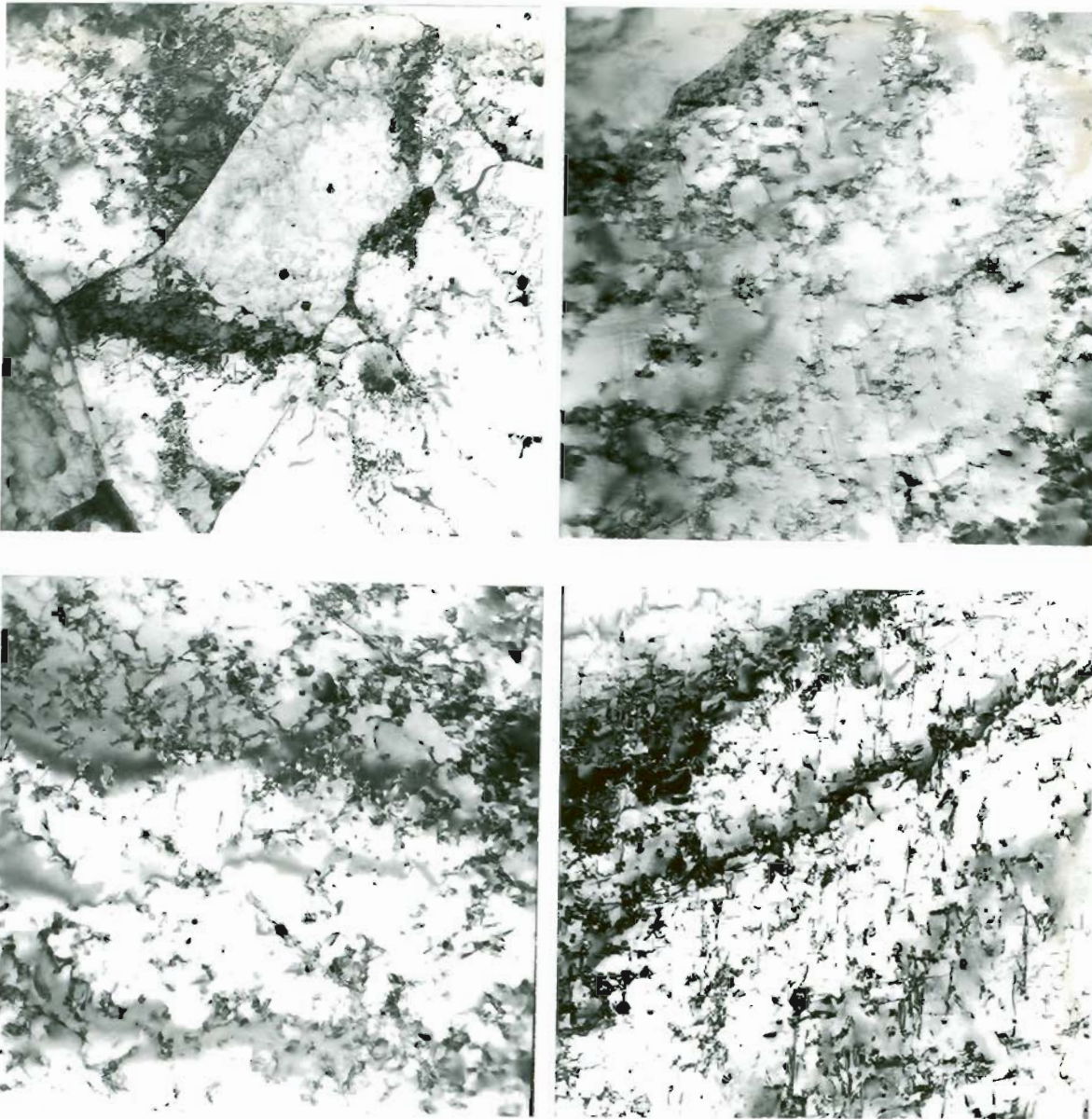


Figure 52. TRANSMISSION ELECTRON MICROGRAPHS OF LASER PROCESSED  
Fe-Cr ALLOYS SHOWING THE FERRITIC STRUCTURES

a) 5%Cr, b) 10%Cr, c) 20%Cr, d) 50%Cr

MAGNIFICATION: 18000x.

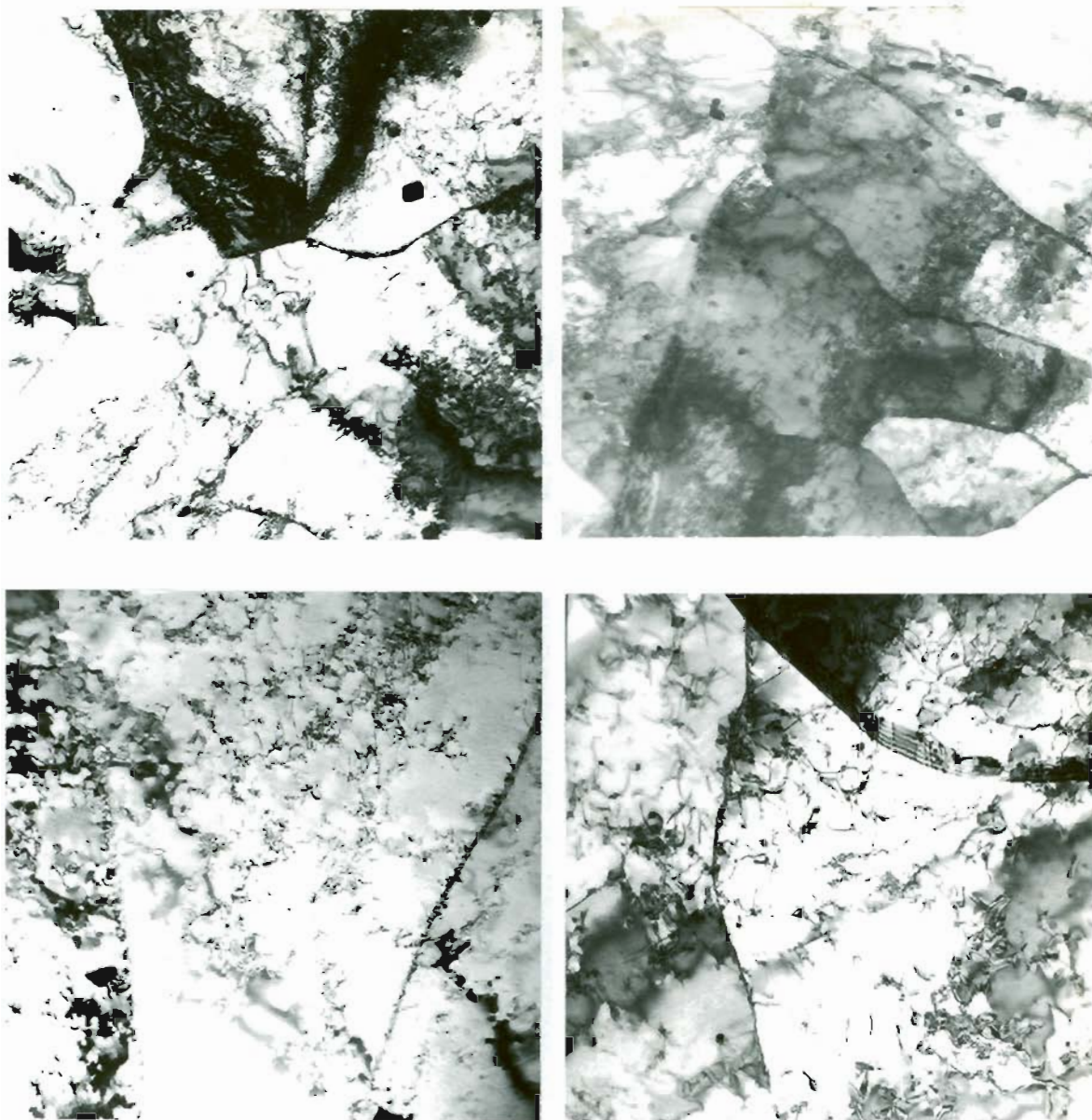


Figure 53. TRANSMISSION ELECTRON MICROGRAPHS OF LASER PROCESSED Fe-Cr ALLOYS SHOWING THE FERRITIC STRUCTURES

- a) 5%Cr (PENETRATION DEPTH: 450 $\mu$ m)
- b) 5%Cr (PENETRATION DEPTH: 120 $\mu$ m)
- c) 20%Cr (PENETRATION DEPTH: 420 $\mu$ m)
- d) 20%Cr (PENETRATION DEPTH: 100 $\mu$ m)

MAGNIFICATION: 18,000x.

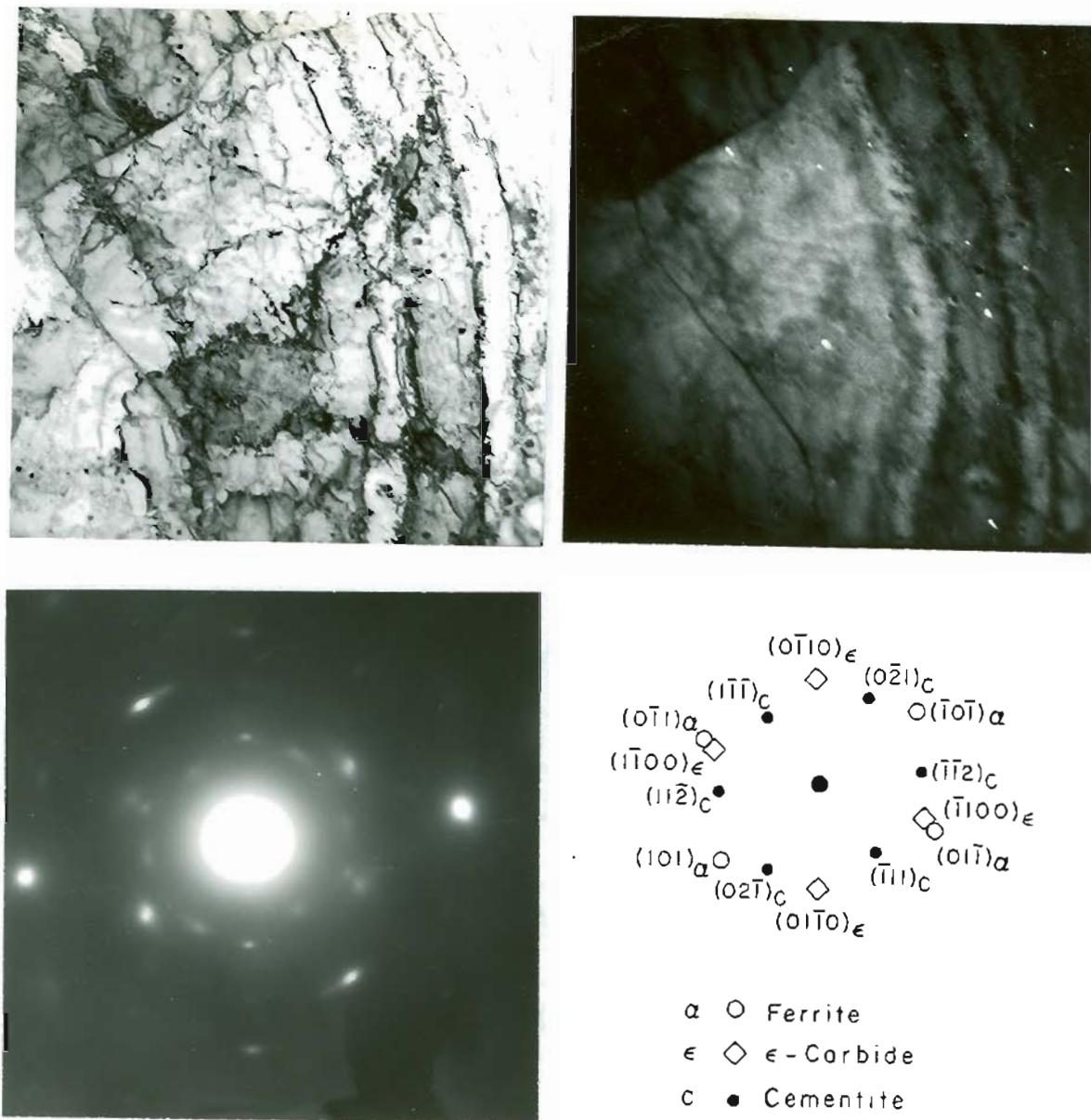


Figure 54. TRANSMISSION ELECTRON MICROGRAPHS OF LASER PROCESSED Fe-10%Cr ALLOY

a) BF, b) DF SHOWING  $\epsilon$ -CARBIDE, c) SAD PATTERN, d) ANALYSIS OF SAD

MAGNIFICATION: 18,000x.

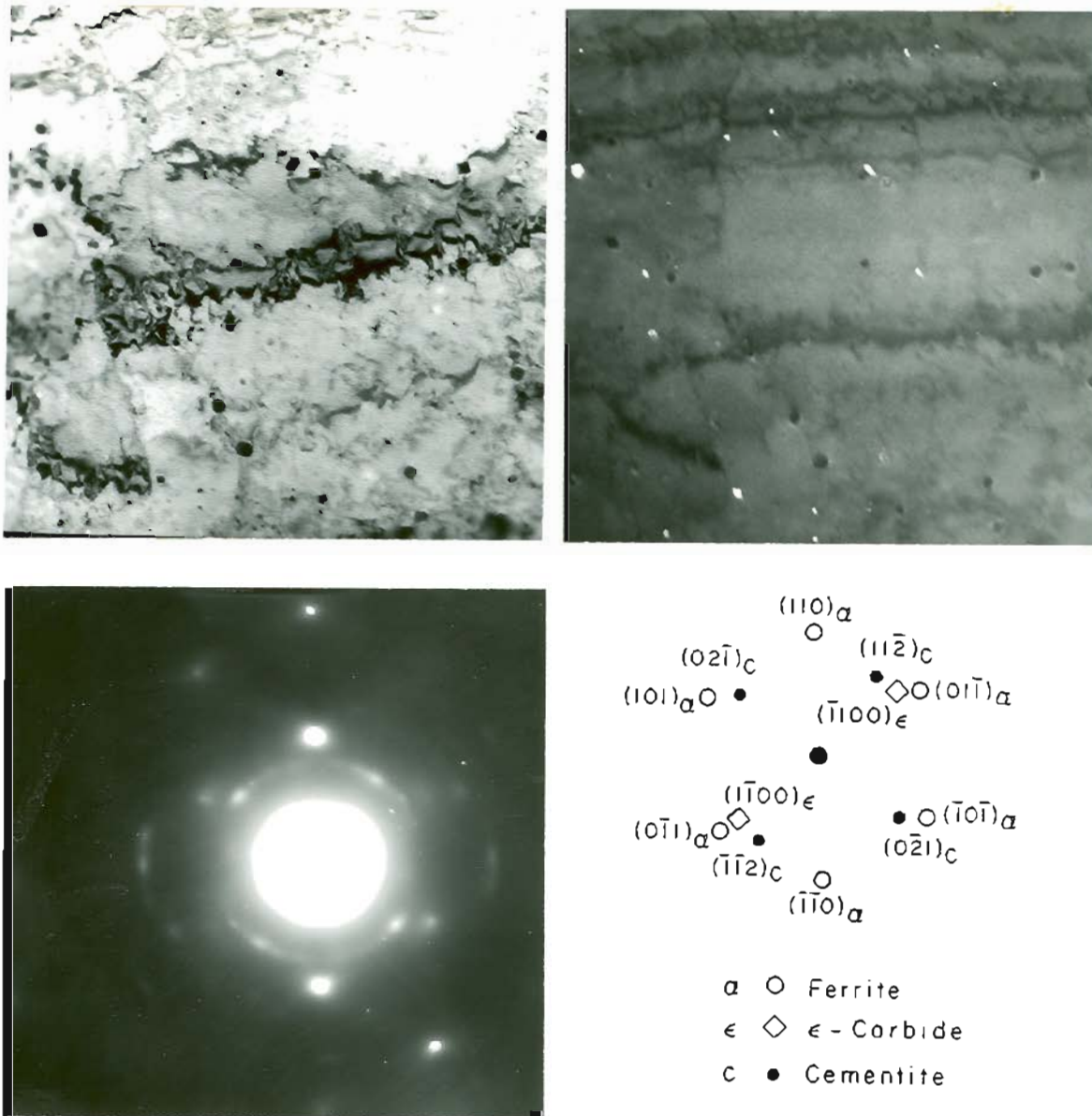


Figure 55. TRANSMISSION ELECTRON MICROGRAPHS OF LASER PROCESSED Fe-10%Cr ALLOY

a) BF, b) DF SHOWING  $M_3C$  CARBIDE, c) SAD PATTERN, d) SCHEMATIC OF SAD

MAGNIFICATION: 18,000x.

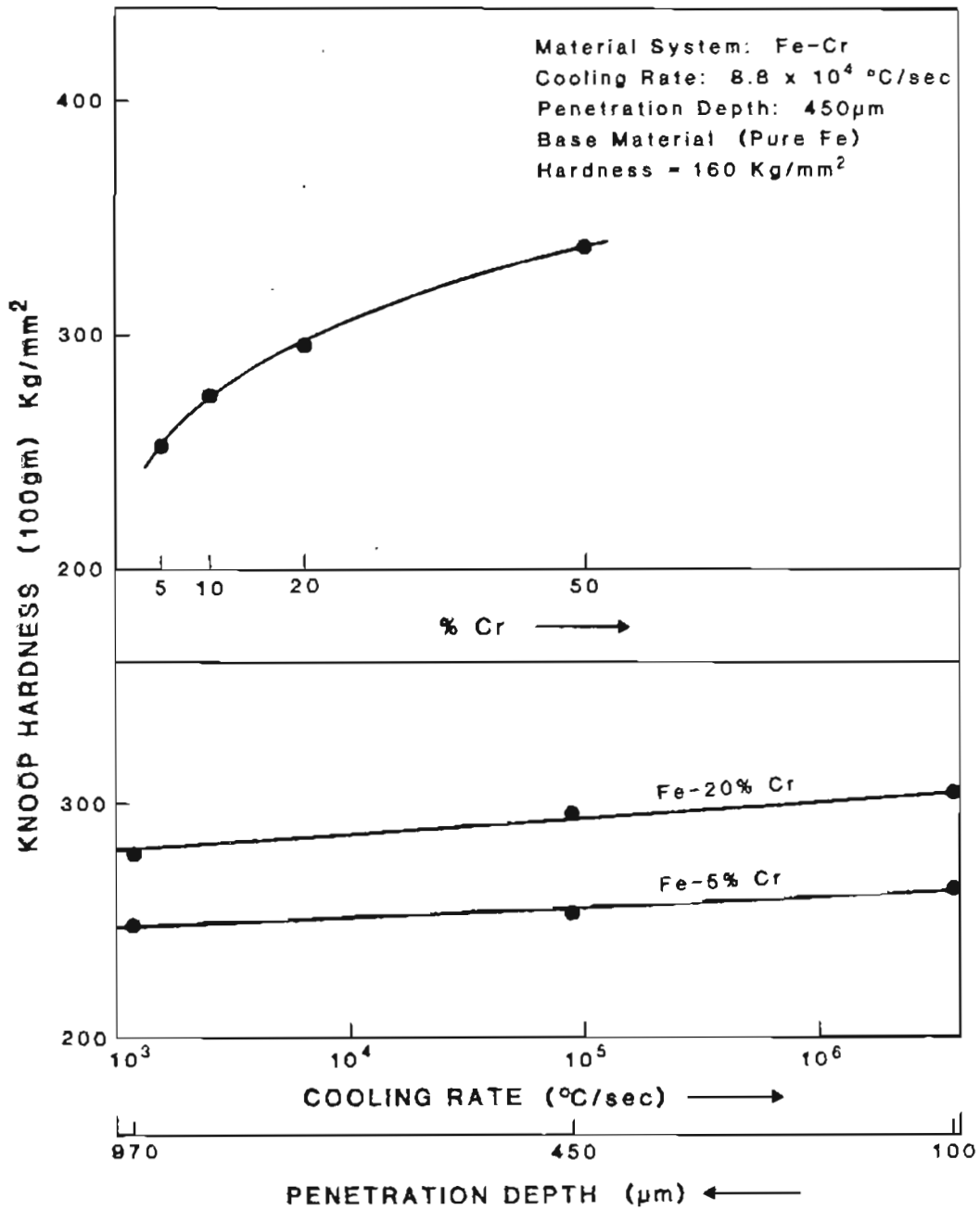


Figure 56. EFFECT OF COMPOSITION AND COOLING RATE ON THE MICRO-HARDNESS OF Fe-Cr ALLOYS.

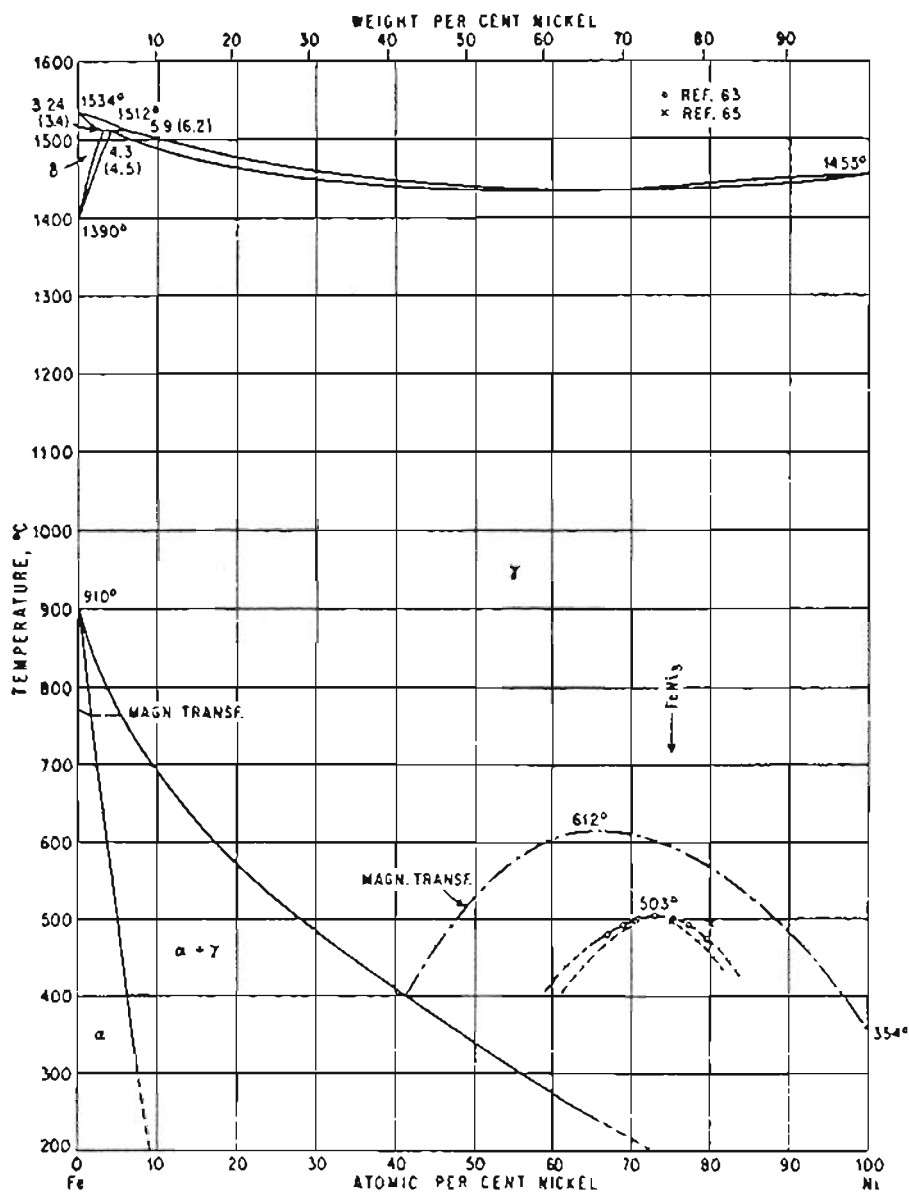


Figure 57. THE Fe-Ni EQUILIBRIUM DIAGRAM.

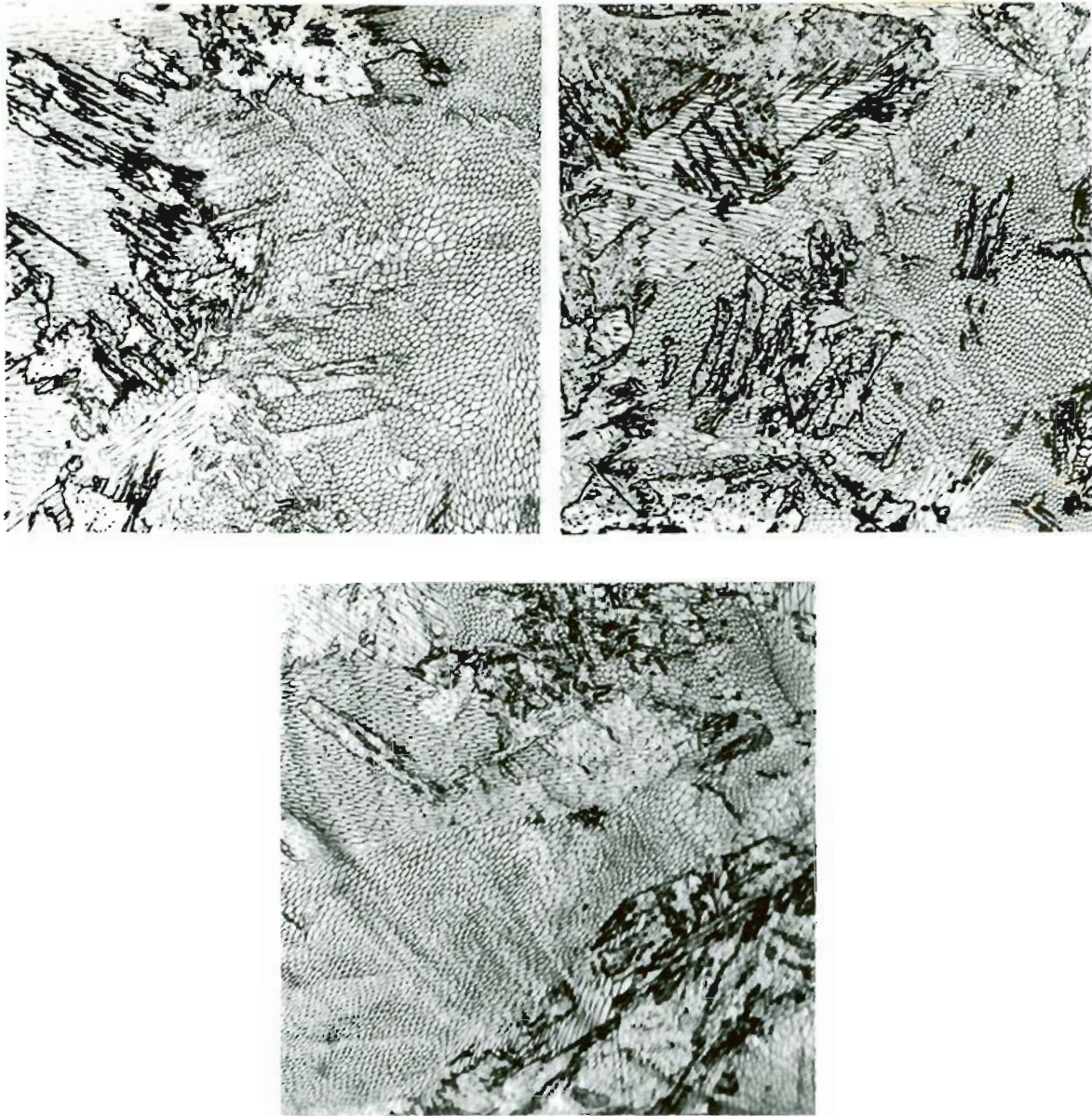


Figure 58. LIGHT MICROGRAPHS OF LASER PROCESSED Fe-Ni ALLOYS

a) 3%Ni, b) 5%Ni, c) 7%Ni

MAGNIFICATION: 250x.

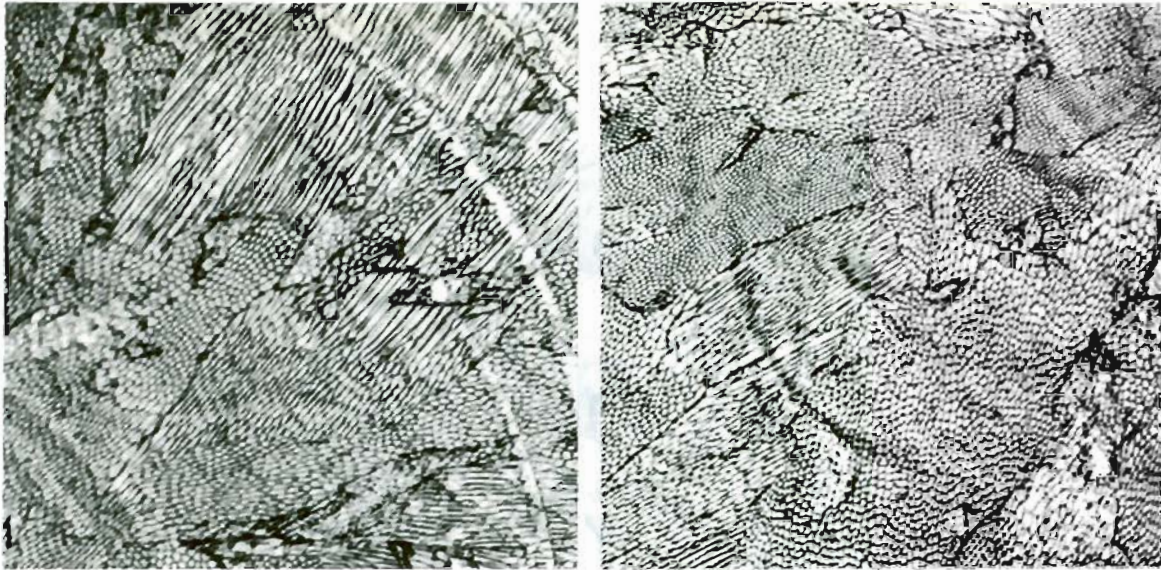


Figure 59. LIGHT MICROGRAPHS OF LASER PROCESSED Fe-Ni ALLOYS

a) 10%Ni, b) 12%Ni, c) 15%Ni

MAGNIFICATION: 250x.



Figure 60. LIGHT MICROGRAPHS OF LASER PROCESSED Fe-Cr-Ni ALLOYS

a) 4%Cr/2%Ni,    b) 6%Cr/2%Ni

MAGNIFICATION: 250x.



Figure 61. LIGHT MICROGRAPHS OF LASER PROCESSED Fe-Cr-Ni ALLOYS  
a) 7%Cr/3%Ni, b) 9%Cr/3%Ni.

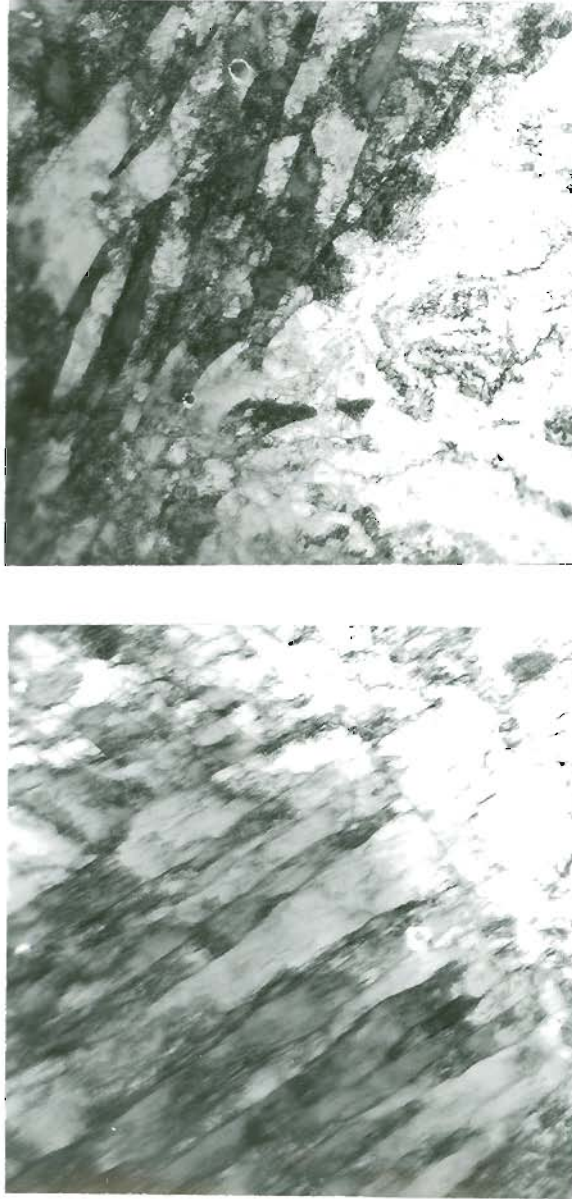


Figure 62. TRANSMISSION ELECTRON MICROGRAPHS OF LASER PROCESSED Fe-5%Ni ALLOY (PENETRATION DEPTH: 500 $\mu$ m). MAGNIFICATION: 18,000x.

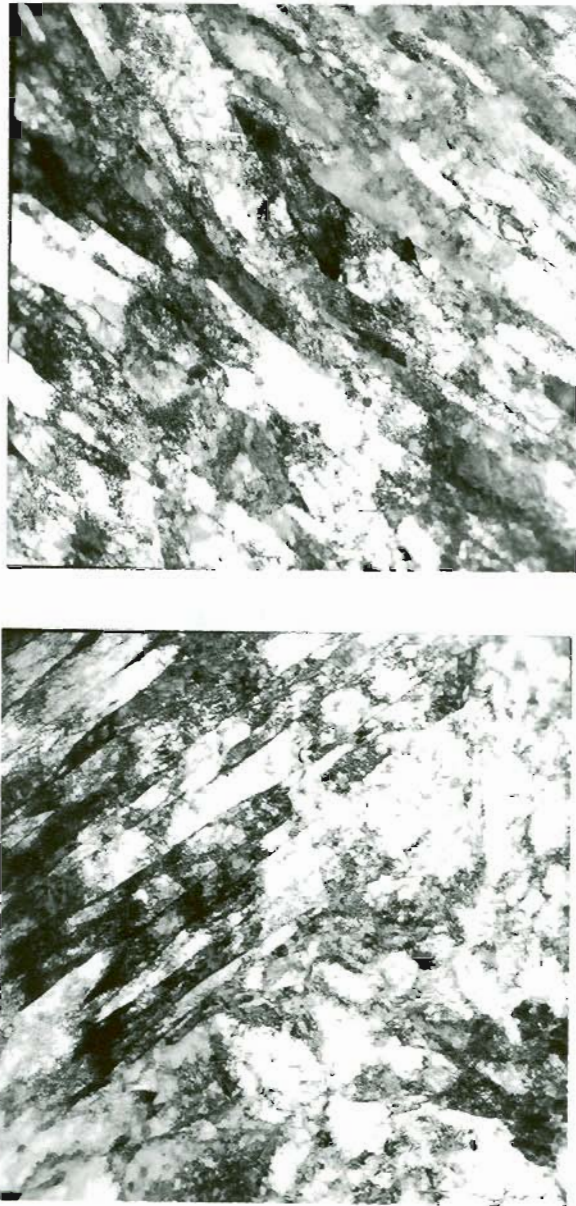


Figure 63. TRANSMISSION ELECTRON MICROGRAPHS OF LASER PROCESSED Fe-6%Cr-2%Ni ALLOY (PENETRATION DEPTH: 625 $\mu$ m). MAGNIFICATION: 18,000x.

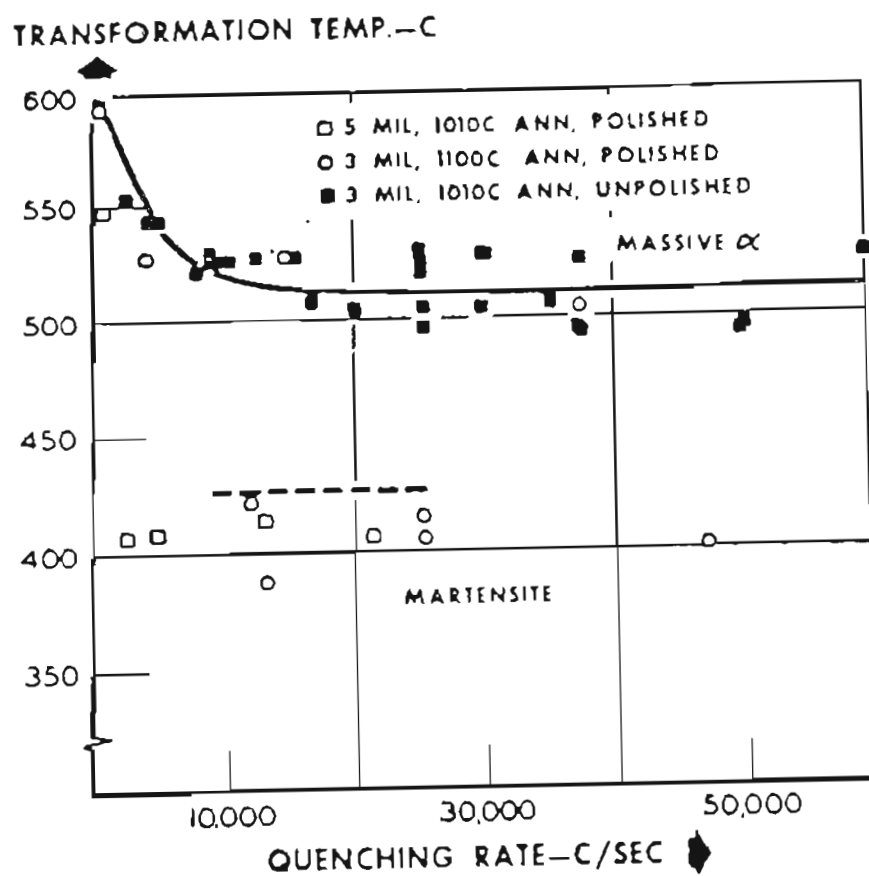


Figure 64. EFFECT OF QUENCH RATE ON THE TRANSFORMATION TEMPERATURE AND STRUCTURE OF Fe-5%Ni ALLOY [AFTER WILSON ET AL (58)].

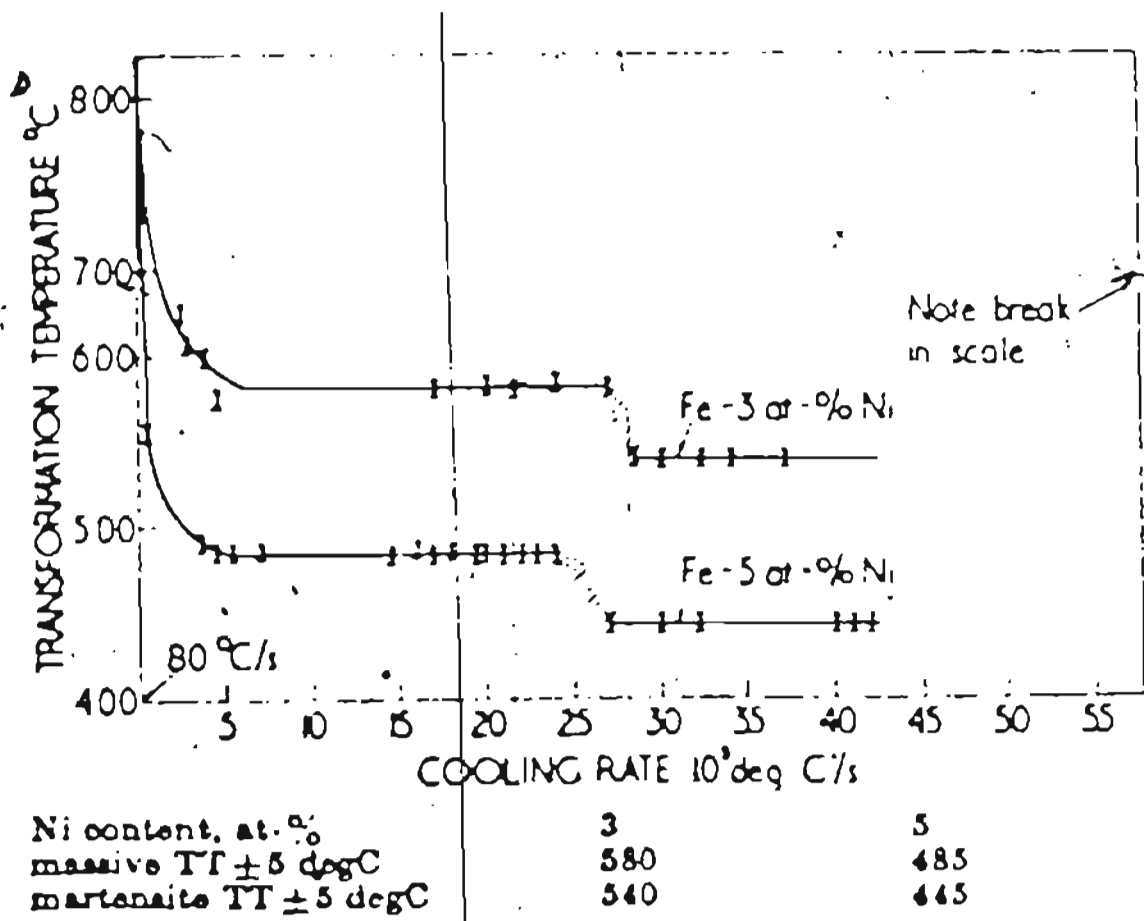


Figure 65. EFFECT OF QUENCH RATE ON THE TRANSFORMATION TEMPERATURE AND STRUCTURE OF Fe-5%Ni ALLOY [AFTER SWANSON AND PARR (57)].

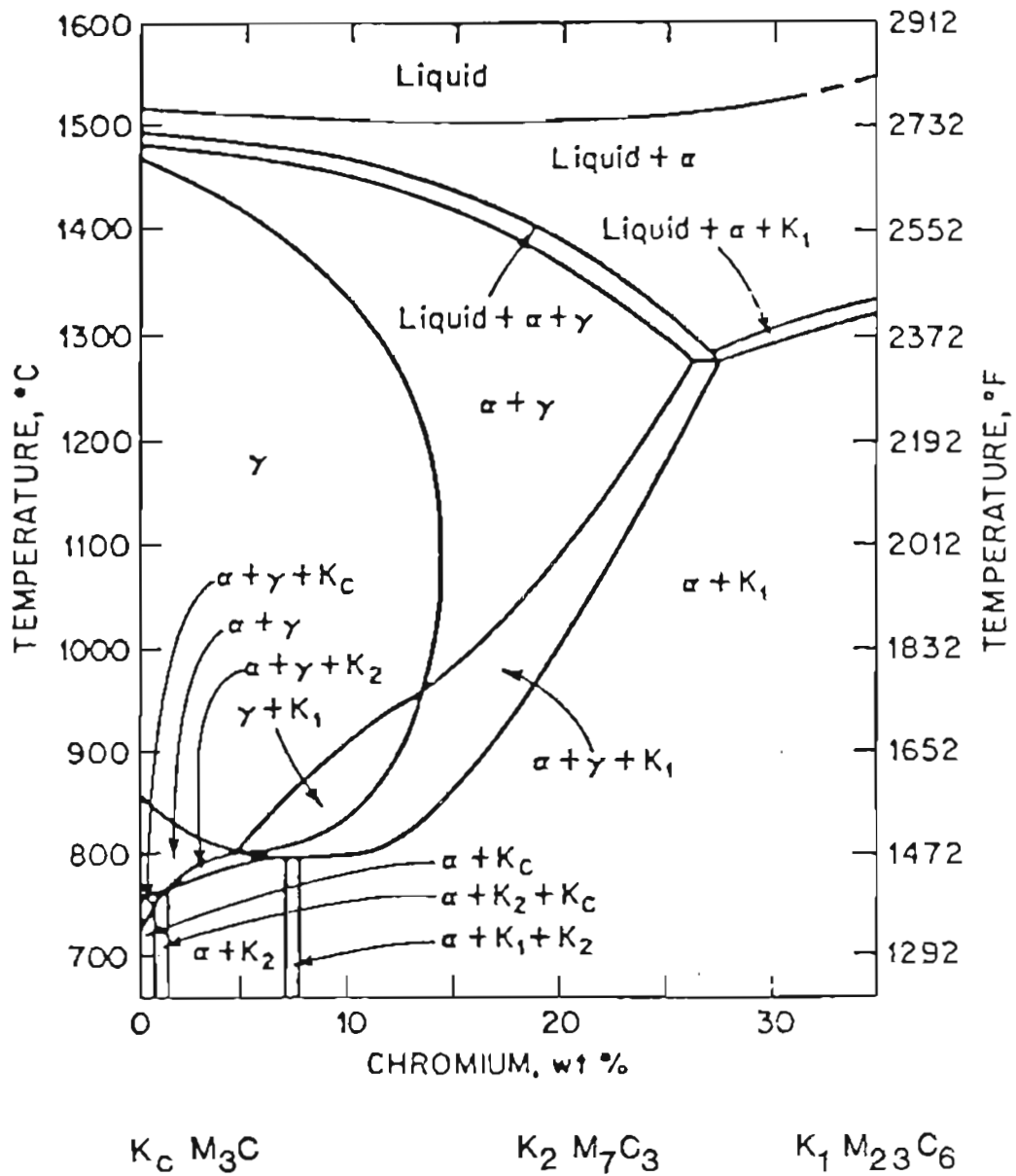


Figure 66. THE Fe-0.2%C-Cr PHASE DIAGRAM.

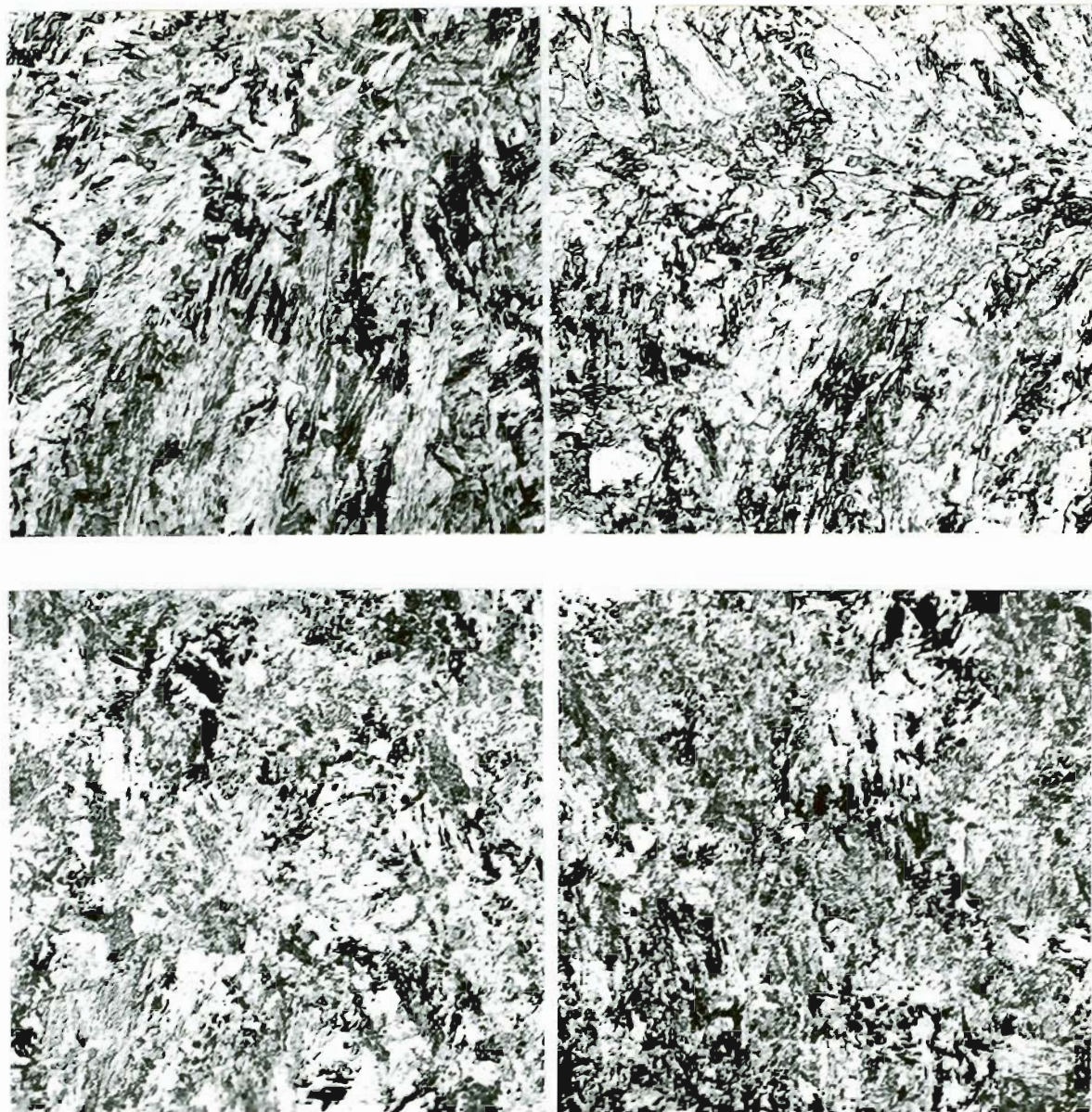


Figure 67. LIGHT MICROGRAPHS OF LASER PROCESSED Fe-0.2%C-Cr ALLOYS

a) 5%Cr (SINGLE SCAN),    b) 10%Cr (SINGLE SCAN),  
c) 5%Cr (MULTIPLE SCAN),    d) 10%Cr (MULTIPLE SCAN)

MAGNIFICATION: 250x.

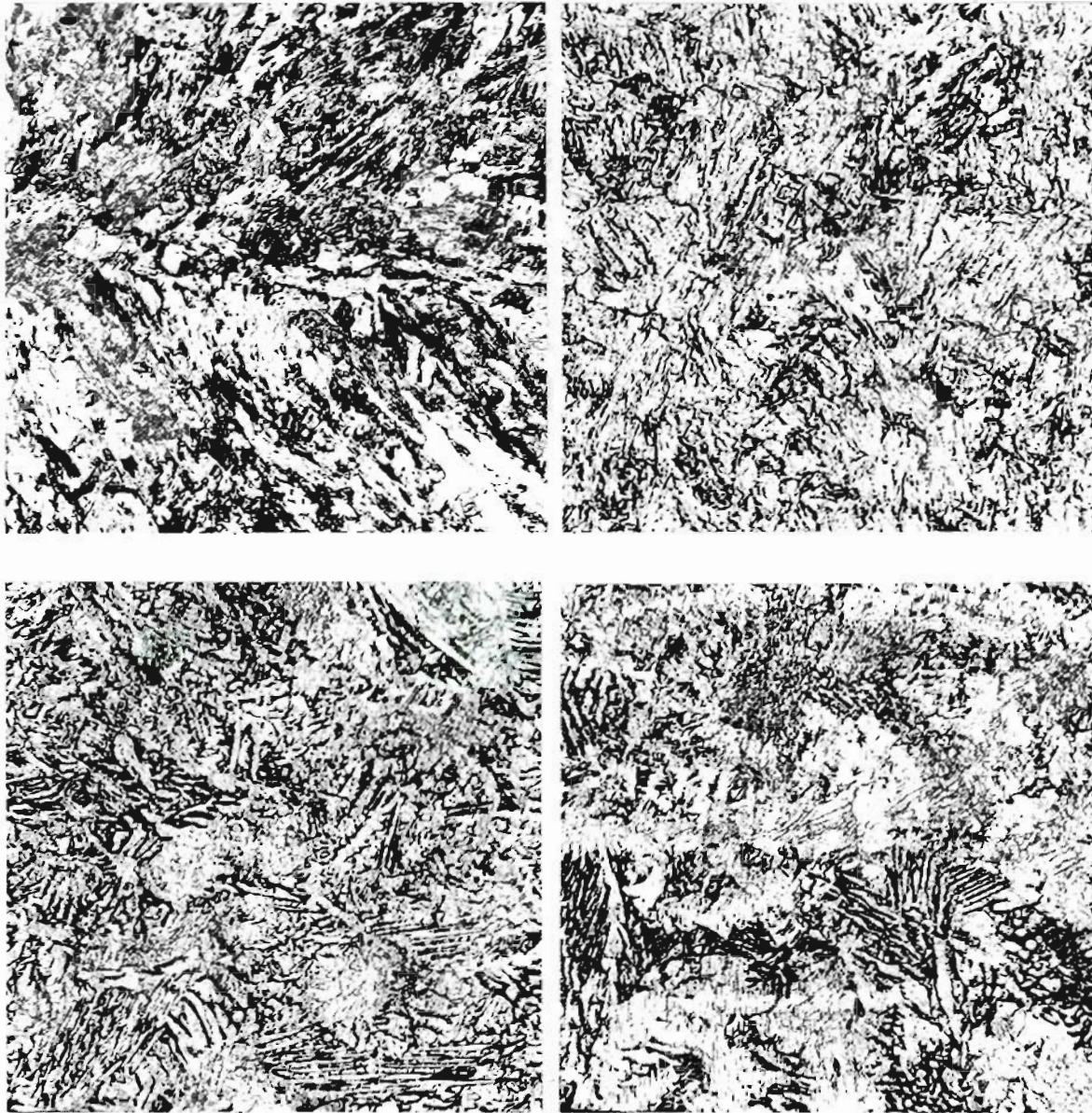


Figure 68. LIGHT MICROGRAPHS OF LASER PROCESSED Fe-0.2%C-Cr ALLOYS

a) 7%Cr, b) 12%Cr, c) 13%Cr, d) 14%Cr

MAGNIFICATION: 250x.

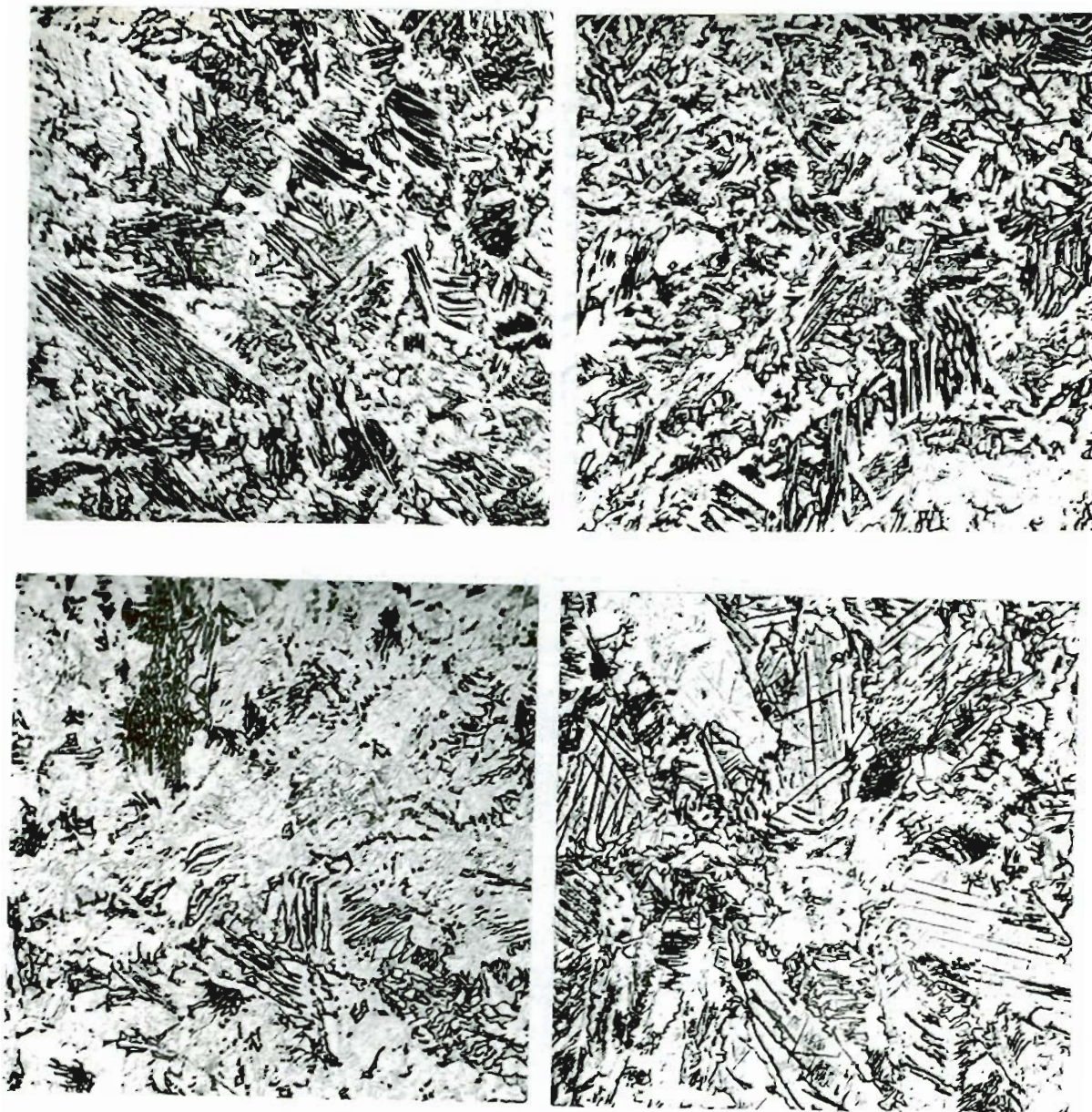


Figure 69. LIGHT MICROGRAPHS OF LASER PROCESSED Fe-0.2% C-Cr ALLOYS

a) 15%Cr, b) 16%Cr, c) 17%Cr, d) 18%Cr

MAGNIFICATION: 250x.



Figure 70. LIGHT MICROGRAPHS OF LASER PROCESSED Fe-0.2%C-Cr ALLOYS

a) 20%Cr, b) 23%Cr, c) 30%Cr

MAGNIFICATION: 250x.

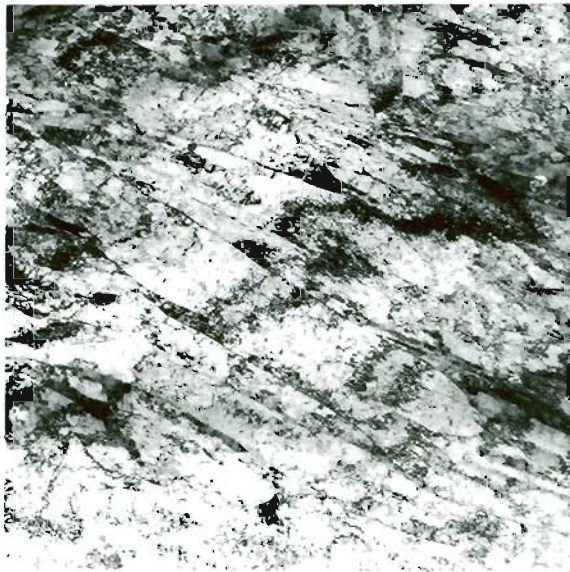
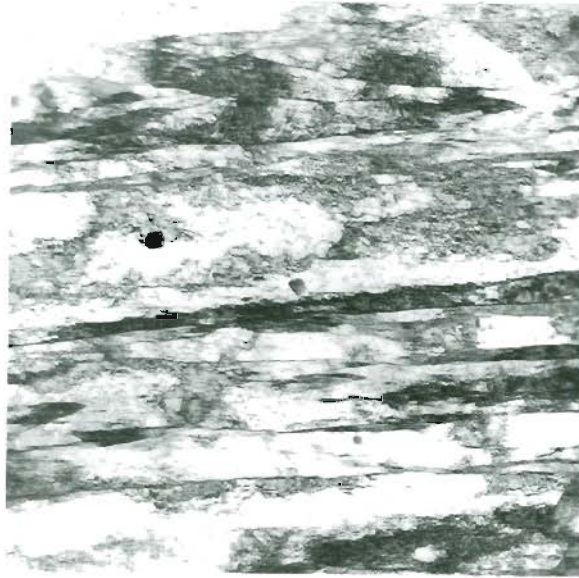


Figure 71. TRANSMISSION ELECTRON MICROGRAPHY OF LASER PROCESSED Fe-0.2%C-5%Cr ALLOY SHOWING THE LATH MARTENSITIC STRUCTURES (PENETRATION DEPTH: 1500 $\mu$ m). MAGNIFICATION: 18,000 $\times$ .

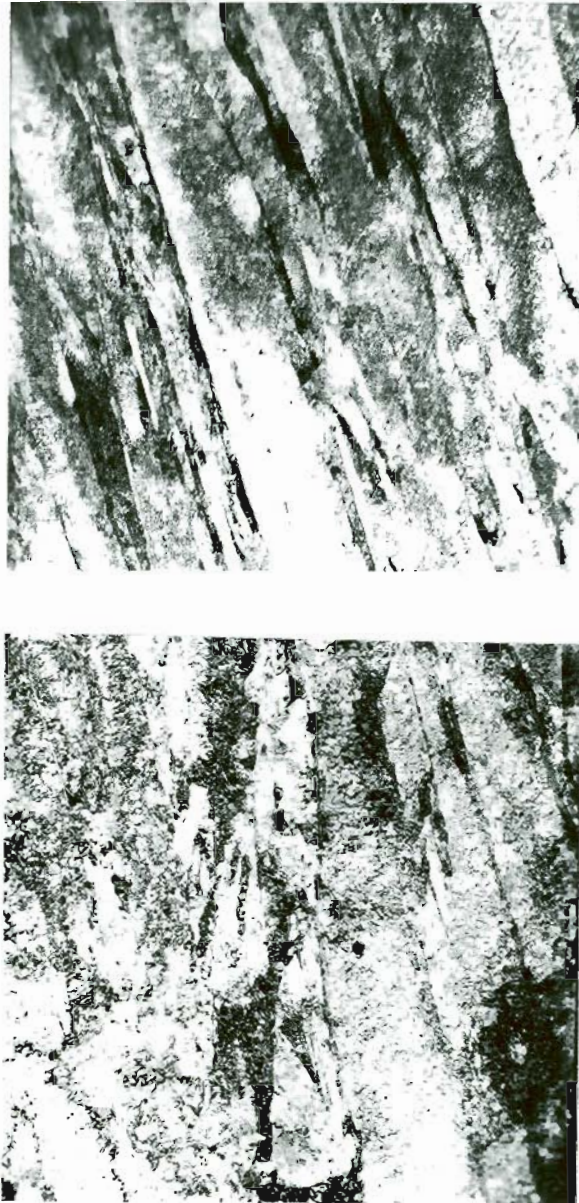


Figure 72. TRANSMISSION ELECTRON MICROGRAPHS OF LASER PROCESSED Fe-0.2%C-5%Cr ALLOY SHOWING THE LATH MARTENSITIC STRUCTURES (PENETRATION DEPTH: 600 $\mu$ m). MAGNIFICATION: 18,000x.

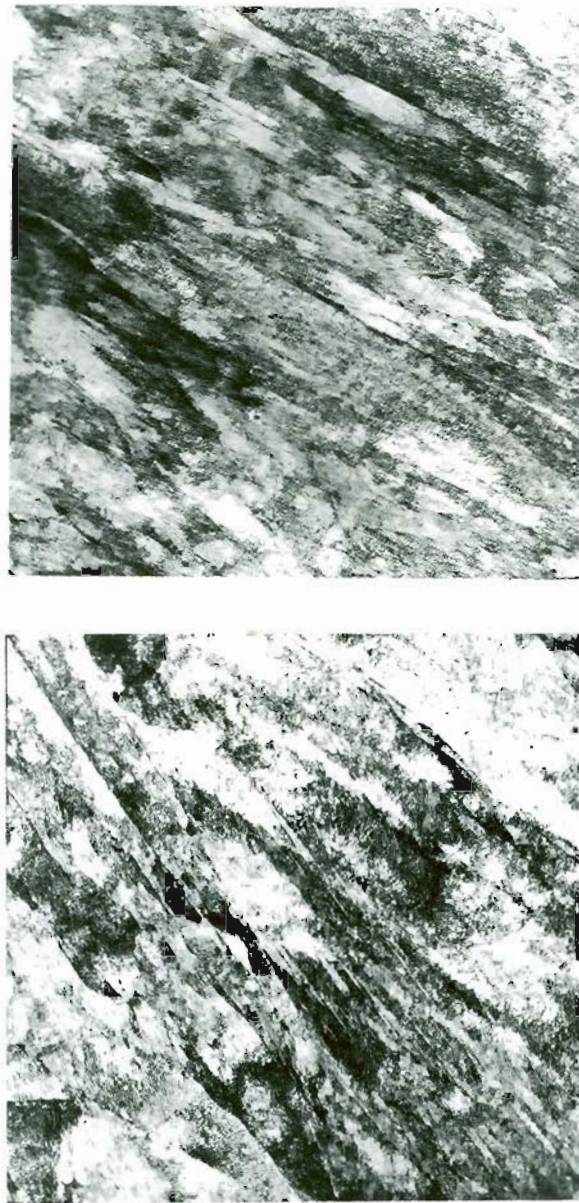


Figure 73. TRANSMISSION ELECTRON MICROGRAPHS OF LASER PROCESSED Fe-0.2%C-5%Cr ALLOY SHOWING THE LATH MARTENSITIC STRUCTURES (PENETRATION DEPTH: 200 $\mu$ m). MAGNIFICATION: 18,000x.

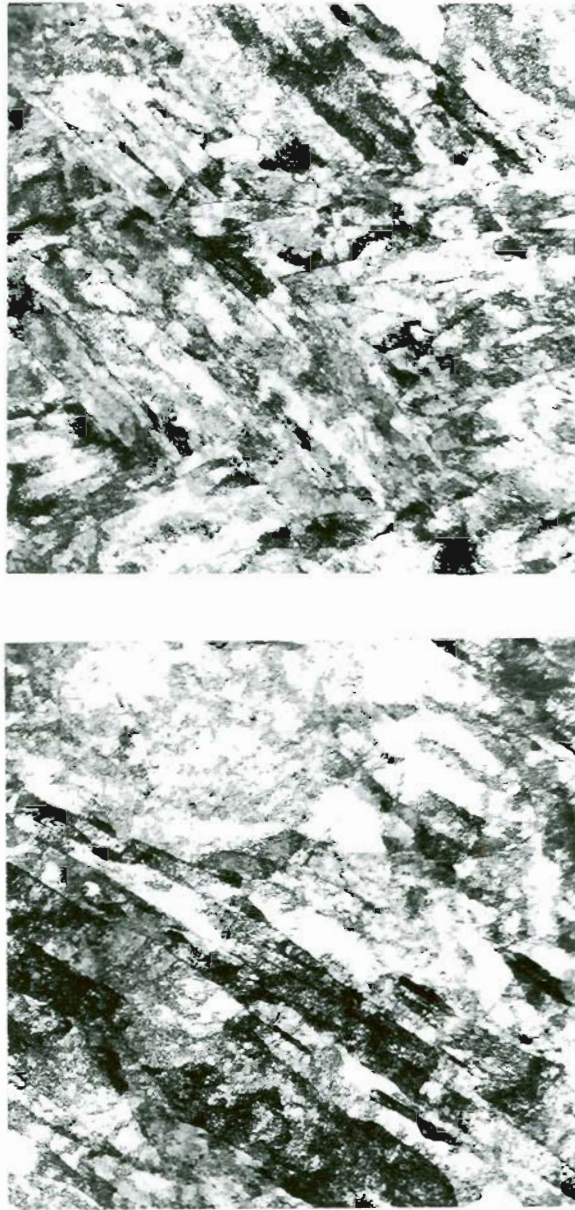


Figure 74. TRANSMISSION ELECTRON MICROGRAPHS OF LASER PROCESSED Fe-0.2%C-10%Cr ALLOY SHOWING THE LATH MARTENSITIC STRUCTURES (PENETRATION DEPTH: 1000 $\mu$ m). MAGNIFICATION: 18,000x.

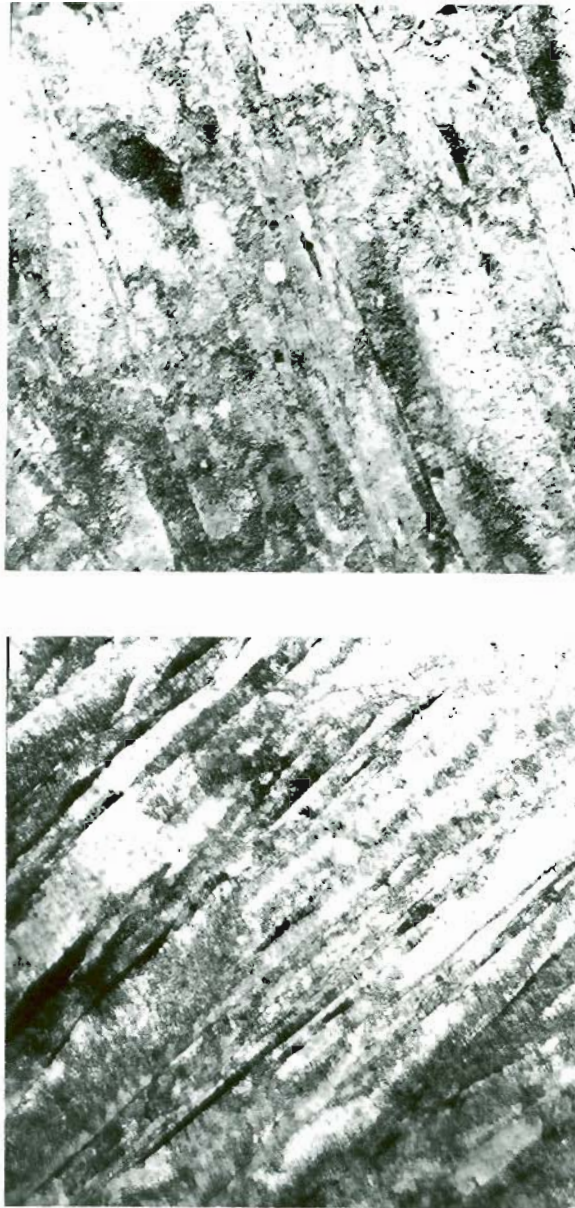


Figure 75. TRANSMISSION ELECTRON MICROGRAPHS OF LASER PROCESSED Fe-0.2%C-10%Cr ALLOY SHOWING THE LATH MARTENSITIC STRUCTURES (PENETRATION DEPTH: 600 $\mu$ m). MAGNIFICATION: 18,000 $\times$ .

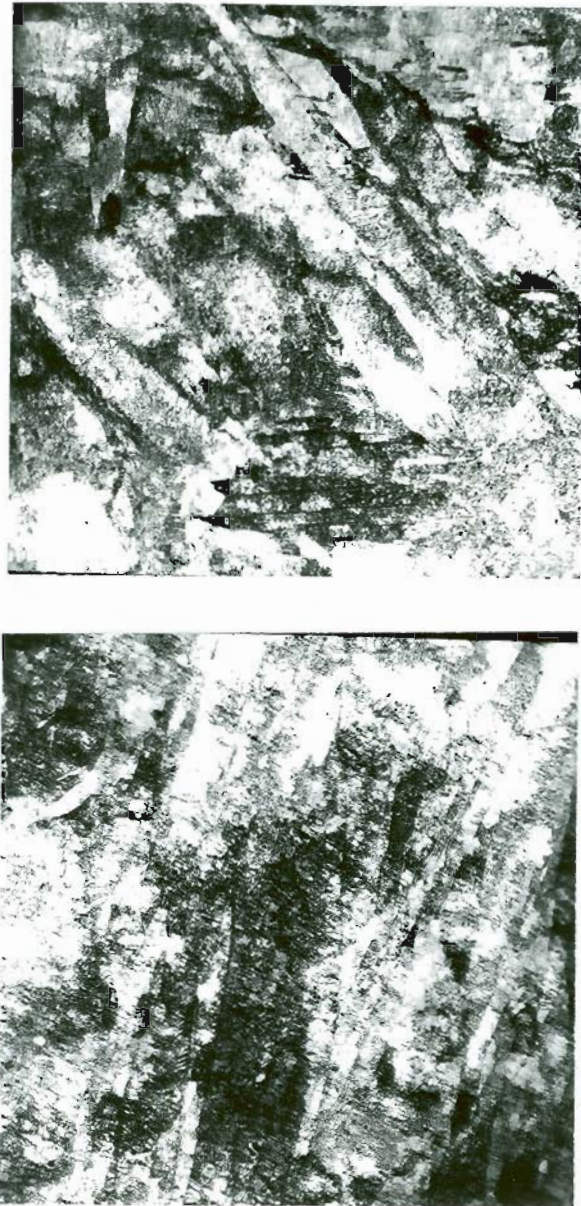


Figure 76. TRANSMISSION ELECTRON MICROGRAPHS OF LASER PROCESSED Fe-0.2%C-10%Cr ALLOY SHOWING THE LATH MARTENSITIC STRUCTURES (PENETRATION DEPTH: 150 $\mu$ m). MAGNIFICATION: 18,000 $\times$ .

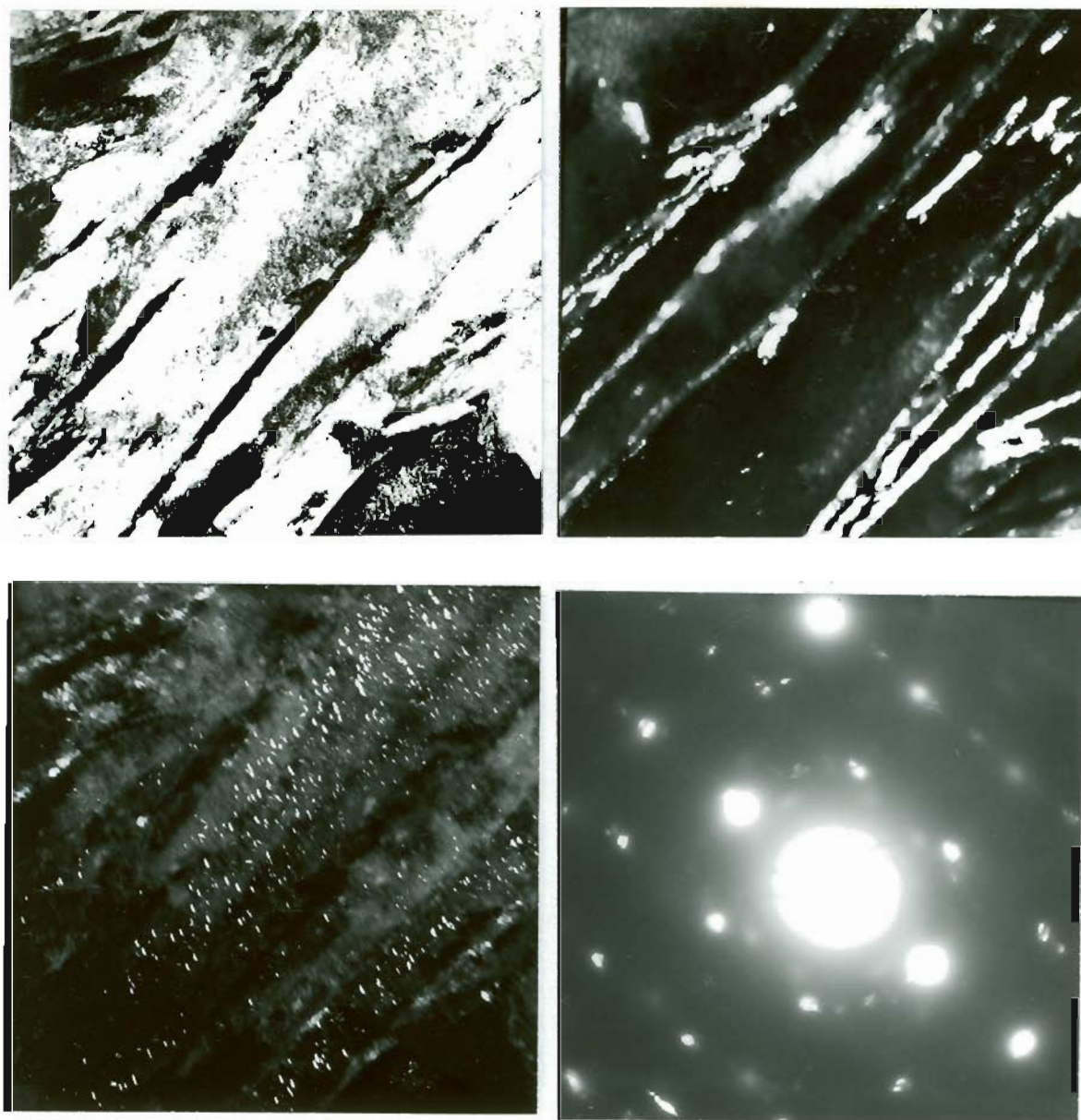


Figure 77. TRANSMISSION ELECTRON MICROGRAPHS OF LASER PROCESSED Fe-0.2%C-5%Cr ALLOY (PENETRATION DEPTH: 1500 $\mu$ m)

a) BF, b) DF SHOWING RETAINED AUSTENITE  
c) DF SHOWING  $\epsilon$ -CARBIDE, d) SAD PATTERN

MAGNIFICATION: 18,000 $\times$ .

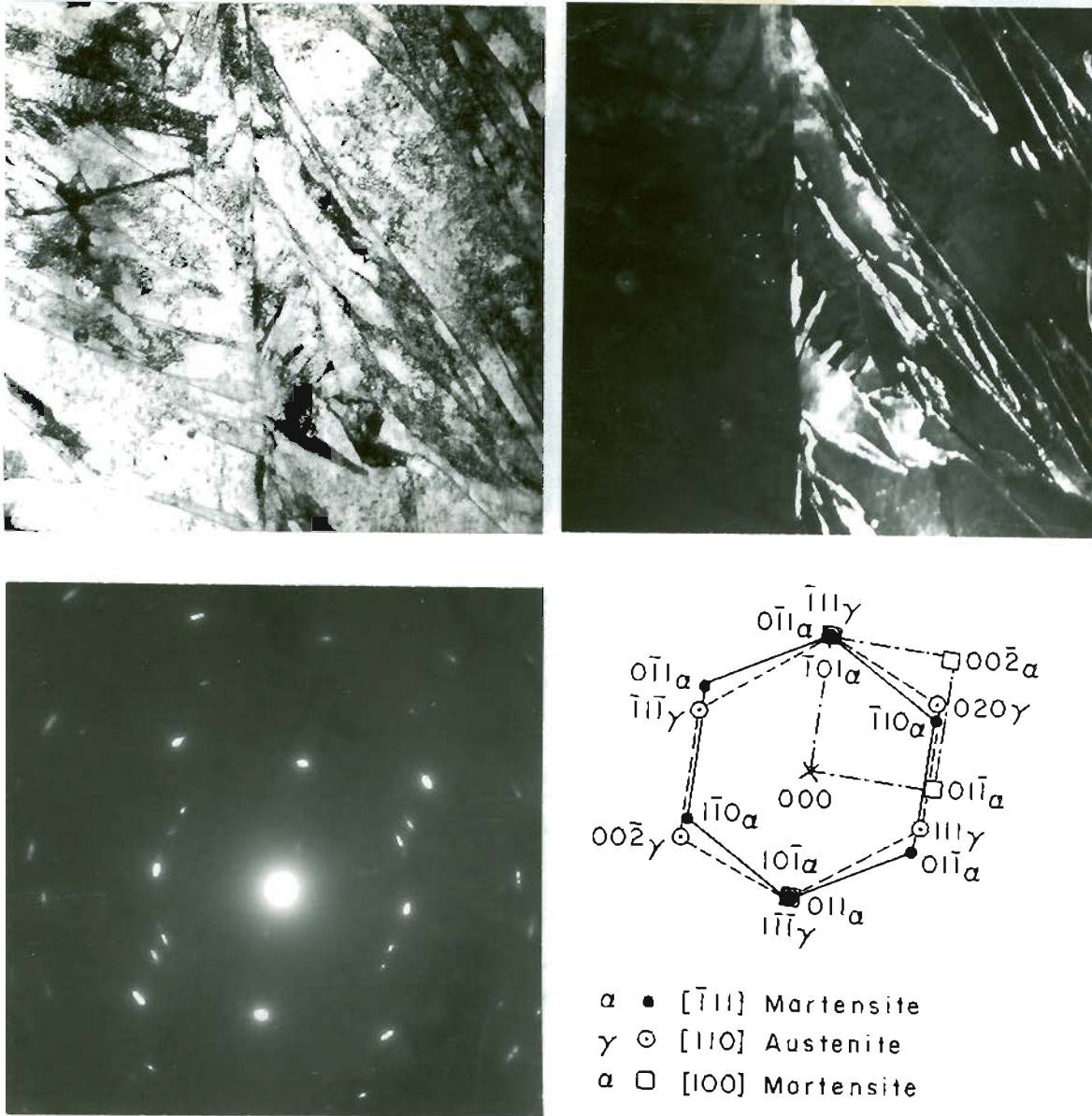


Figure 78. TRANSMISSION ELECTRON MICROGRAPHS OF LASER PROCESSED Fe-0.2%C-5%Cr ALLOY (PENETRATION DEPTH: 600 $\mu$ m)

a) BF, b) DF SHOWING RETAINED AUSTENITE,  
c) SAD PATTERN, d) ANALYSIS OF SAD

MAGNIFICATION: 18,000x.

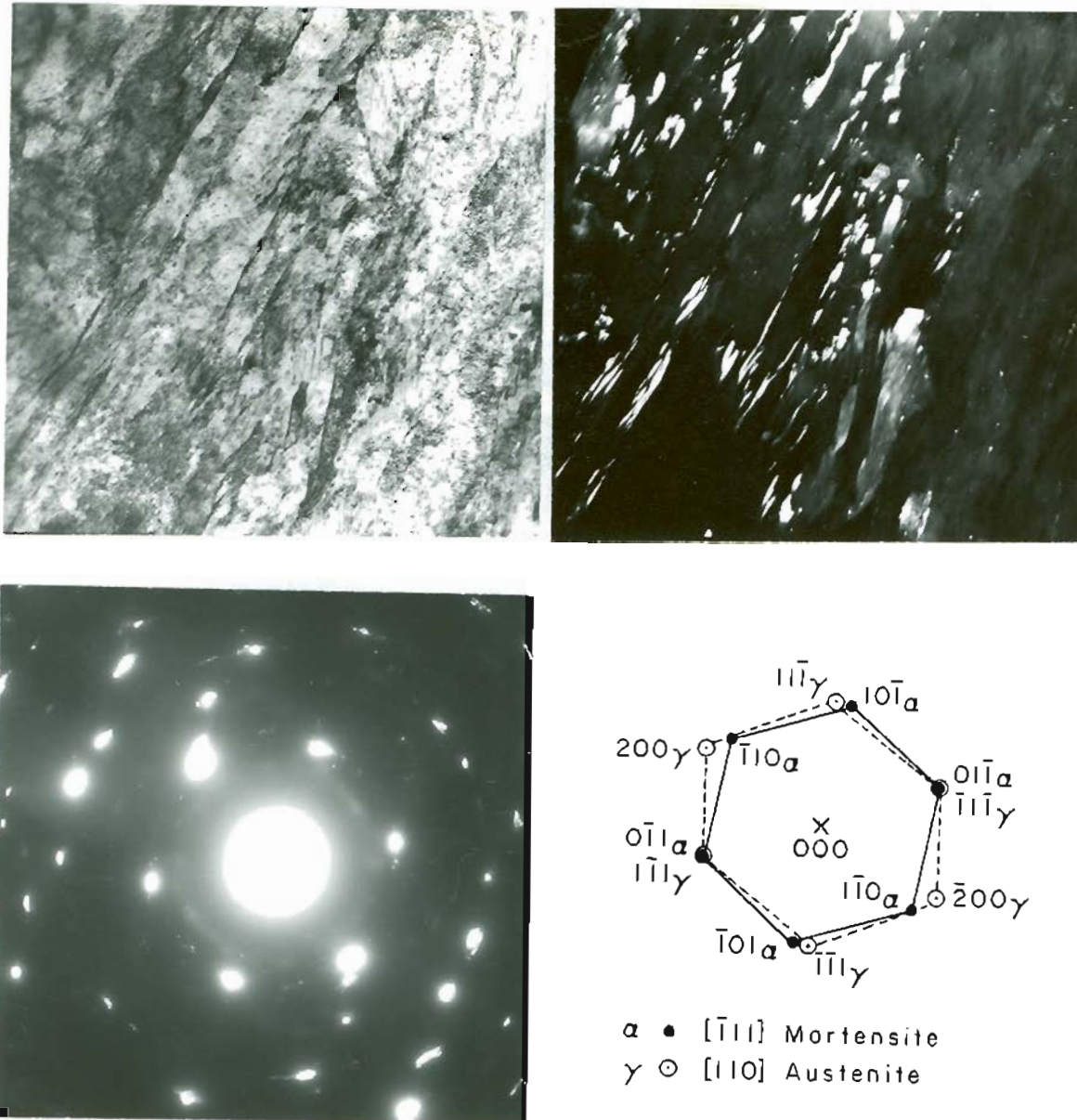


Figure 79. TRANSMISSION ELECTRON MICROGRAPHS OF LASER PROCESSED Fe-0.2%C-10%Cr ALLOY (PENETRATION DEPTH: 600 $\mu$ m)

a) BF, b) DF SHOWING RETAINED AUSTENITE,  
c) SAD PATTERN, d) ANALYSIS OF SAD

MAGNIFICATION: 18,000x.

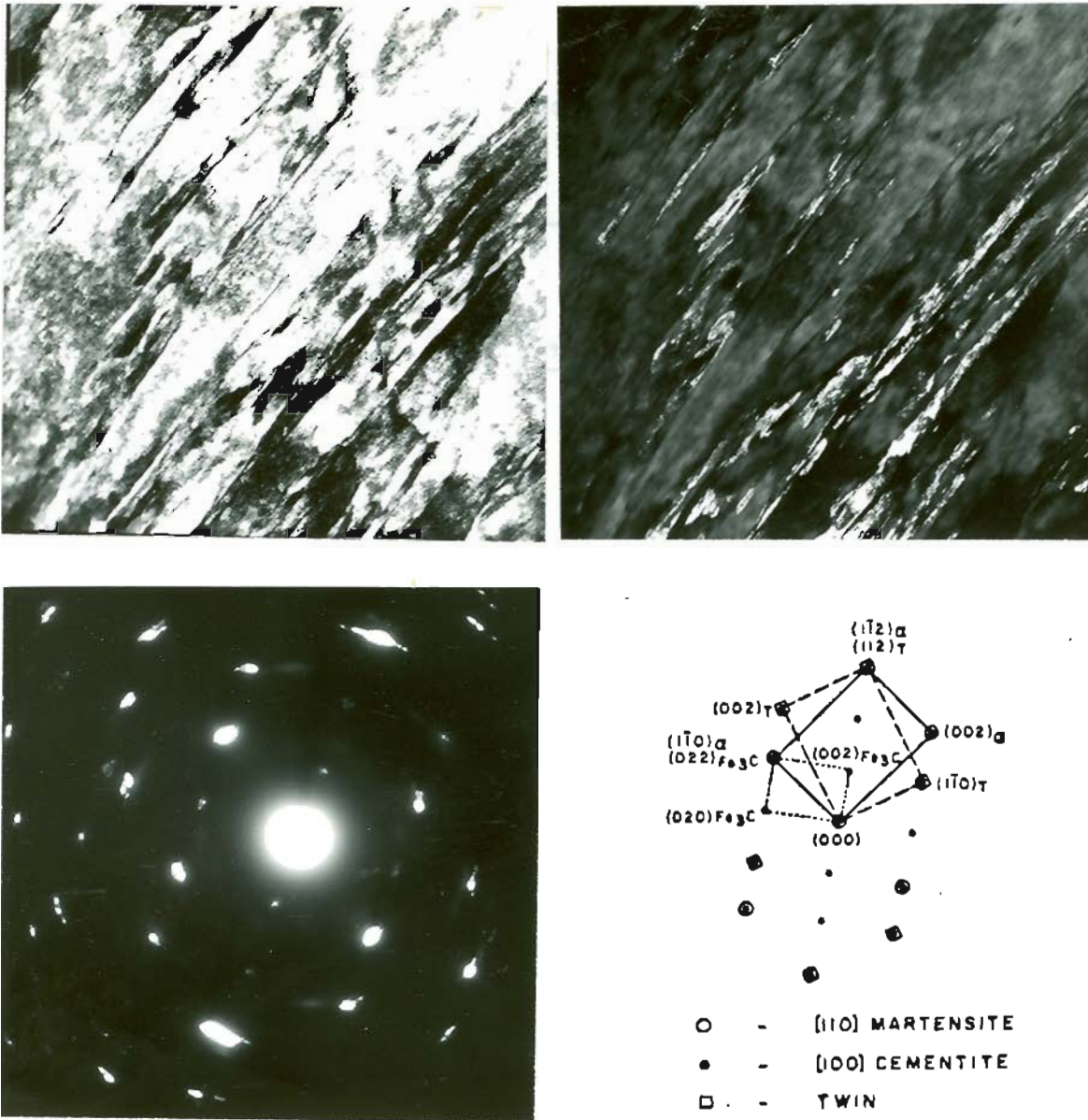


Figure 80. TRANSMISSION ELECTRON MICROGRAPHS OF LASER PROCESSED Fe-0.2%C-5%Cr ALLOY (PENETRATION DEPTH: 600 $\mu$ m)

a) BF, b) DF SHOWING  $M_3C$  CARBIDE  
c) SAD PATTERN, d) ANALYSIS OF SAD

MAGNIFICATION: 18,000x.

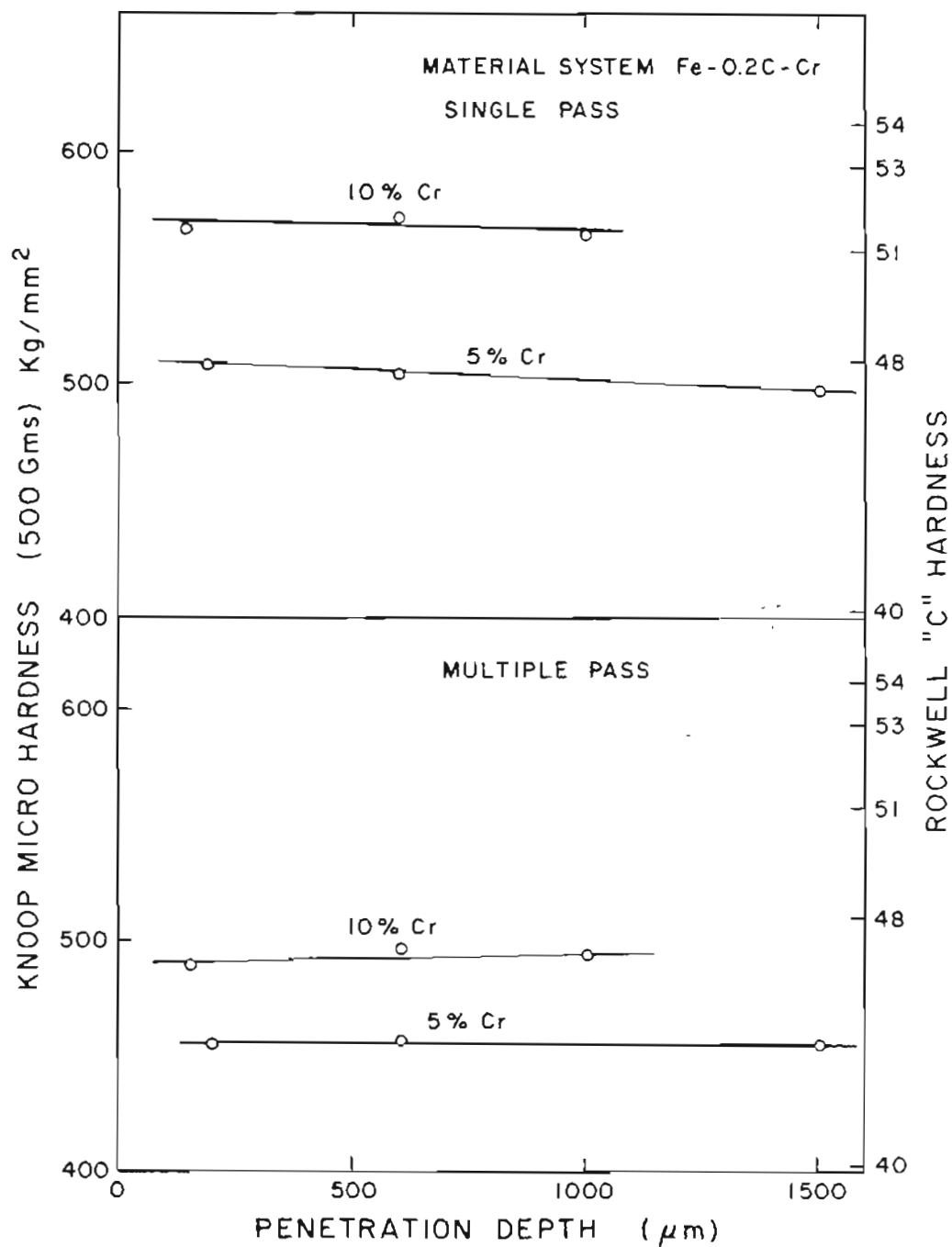


Figure 81. EFFECT OF COOLING RATE ON THE MICROHARDNESS OF Fe-0.2%Cr ALLOYS.

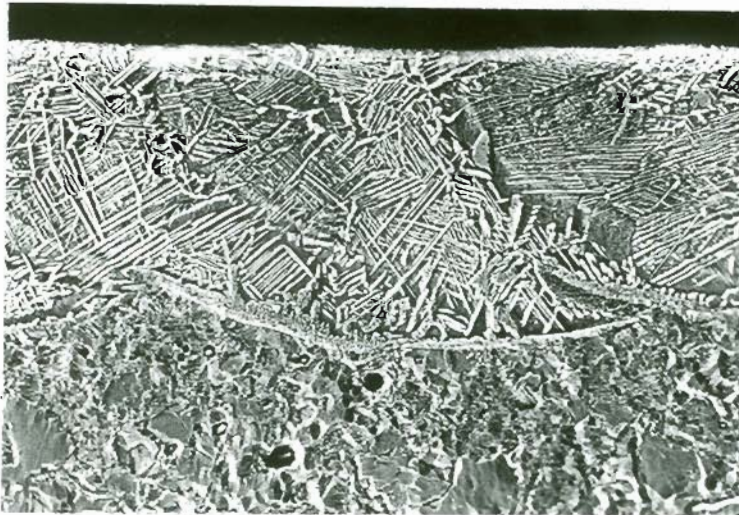
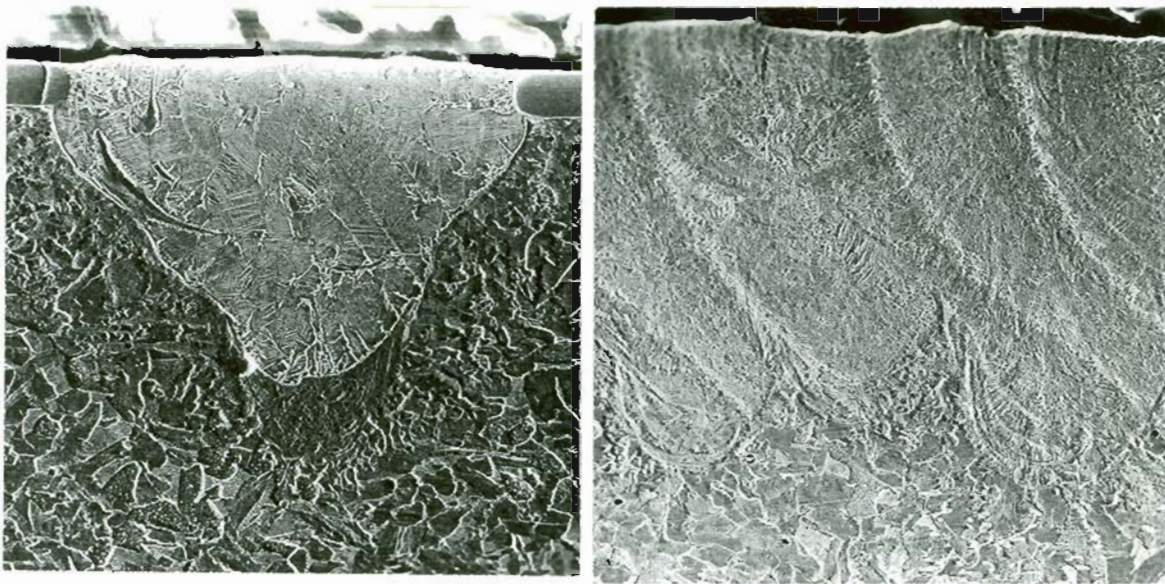


Figure 82. SCANNING ELECTRON MICROGRAPHS SHOWING THE TRANSVERSE SECTIONS OF FUSION ZONES CONTAINING 20%Cr

- a) SINGLE SCAN (PENETRATION DEPTH: 600 $\mu$ m)
- b) MULTIPLE SCAN (PENETRATION DEPTH: 600 $\mu$ m)
- c) MULTIPLE SCAN (PENETRATION DEPTH: 120 $\mu$ m)

MAGNIFICATION: a) 100x, b) 100x, c) 300x.

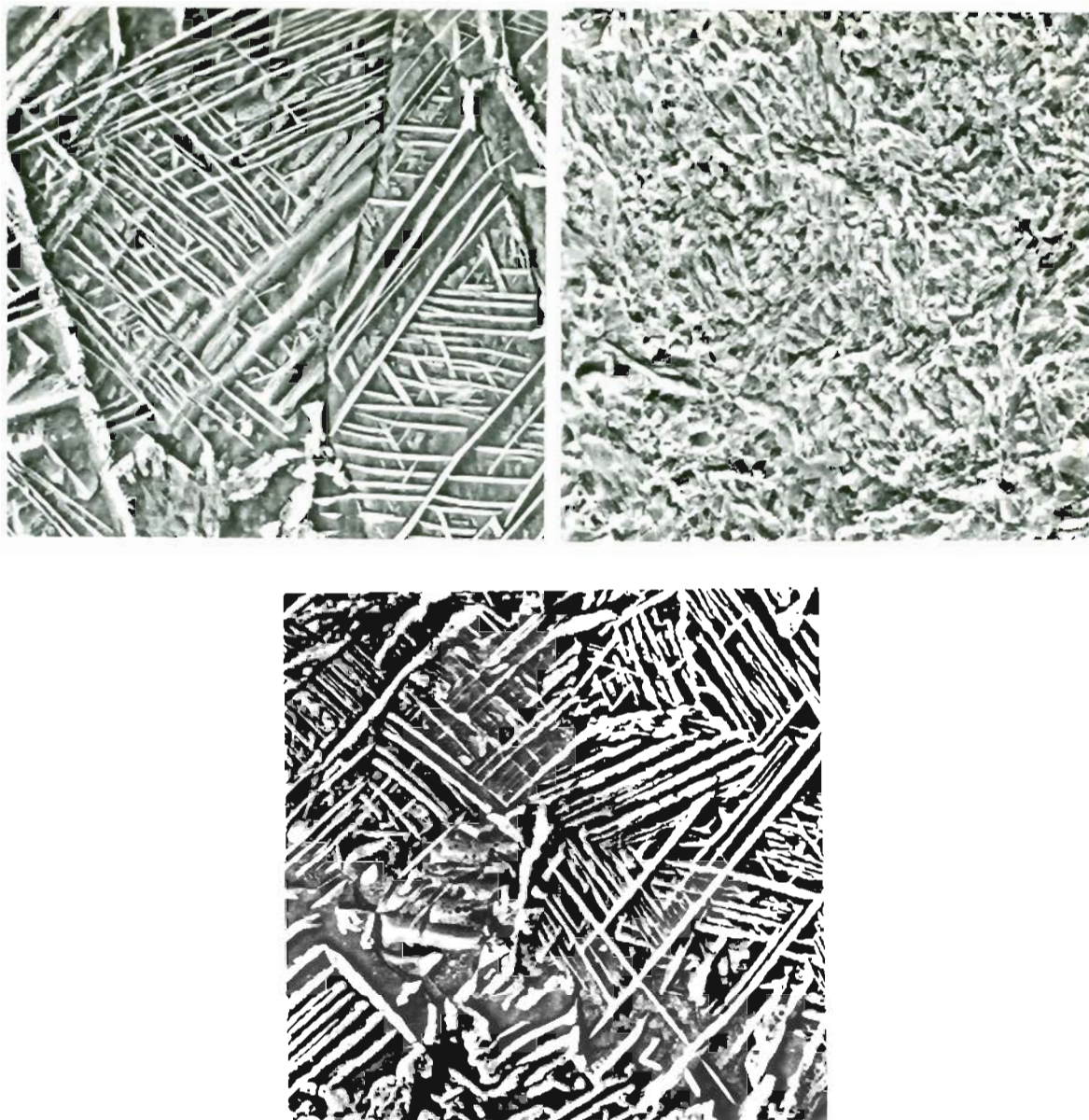


Figure 83. SCANNING ELECTRON MICROGRAPHS SHOWING THE MICROSTRUCTURES OF LASER PROCESSED Fe-0.2%C-20%Cr ALLOYS

- a) SINGLE SCAN (PENETRATION DEPTH: 600 $\mu$ m)
- b) MULTIPLE SCAN (PENETRATION DEPTH: 600 $\mu$ m)
- c) MULTIPLE SCAN (PENETRATION DEPTH: 120 $\mu$ m)

MAGNIFICATION: 1000x.

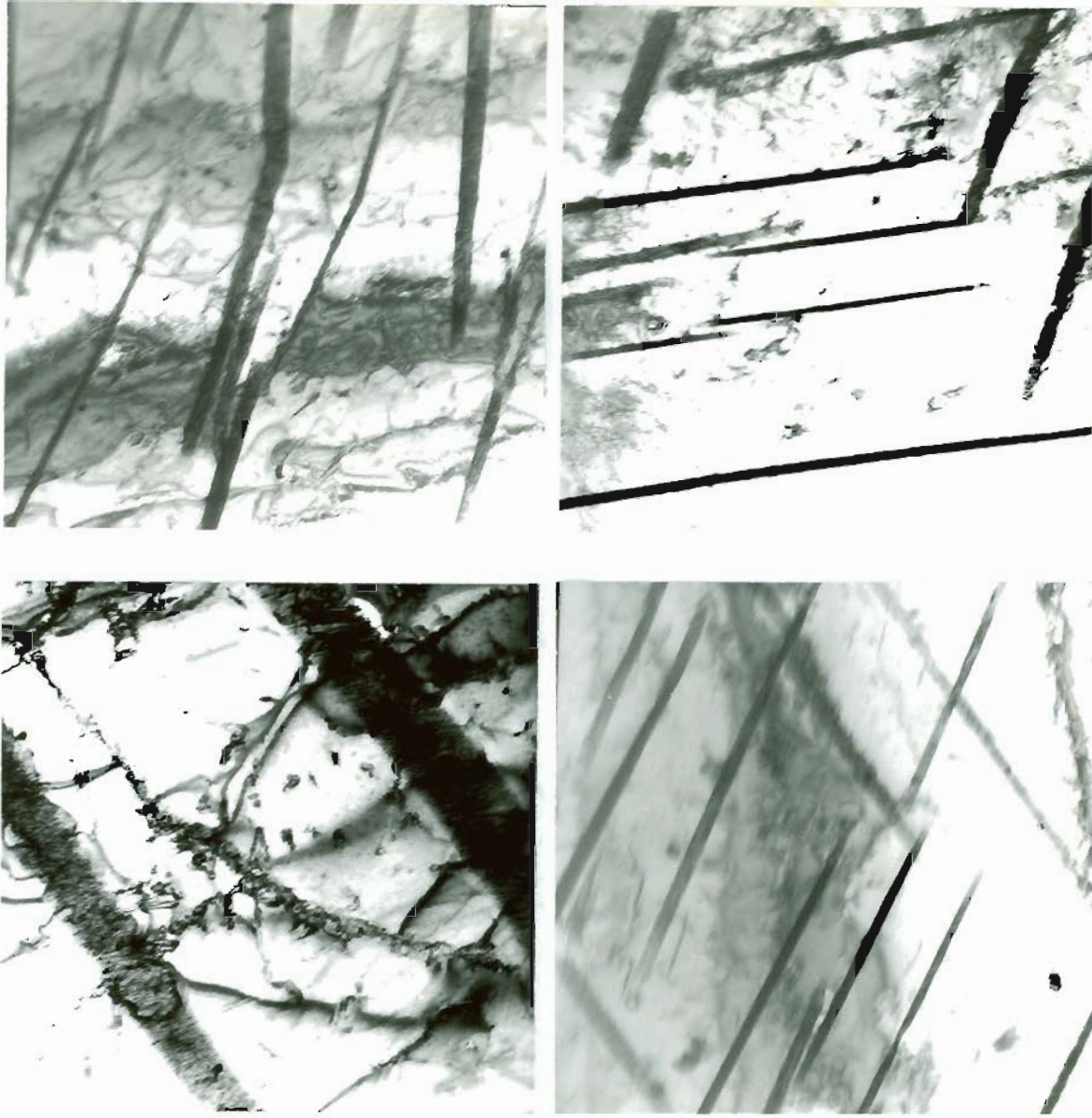


Figure 84. TRANSMISSION ELECTRON MICROGRAPHS OF LASER PROCESSED Fe-0.2%C-20%Cr ALLOY SHOWING THE AUSTENITIC NEEDLES IN A FERRITIC MATRIX (PENETRATION DEPTH: 600 $\mu$ m, SINGLE SCAN) MAGNIFICATION: 18,000x.

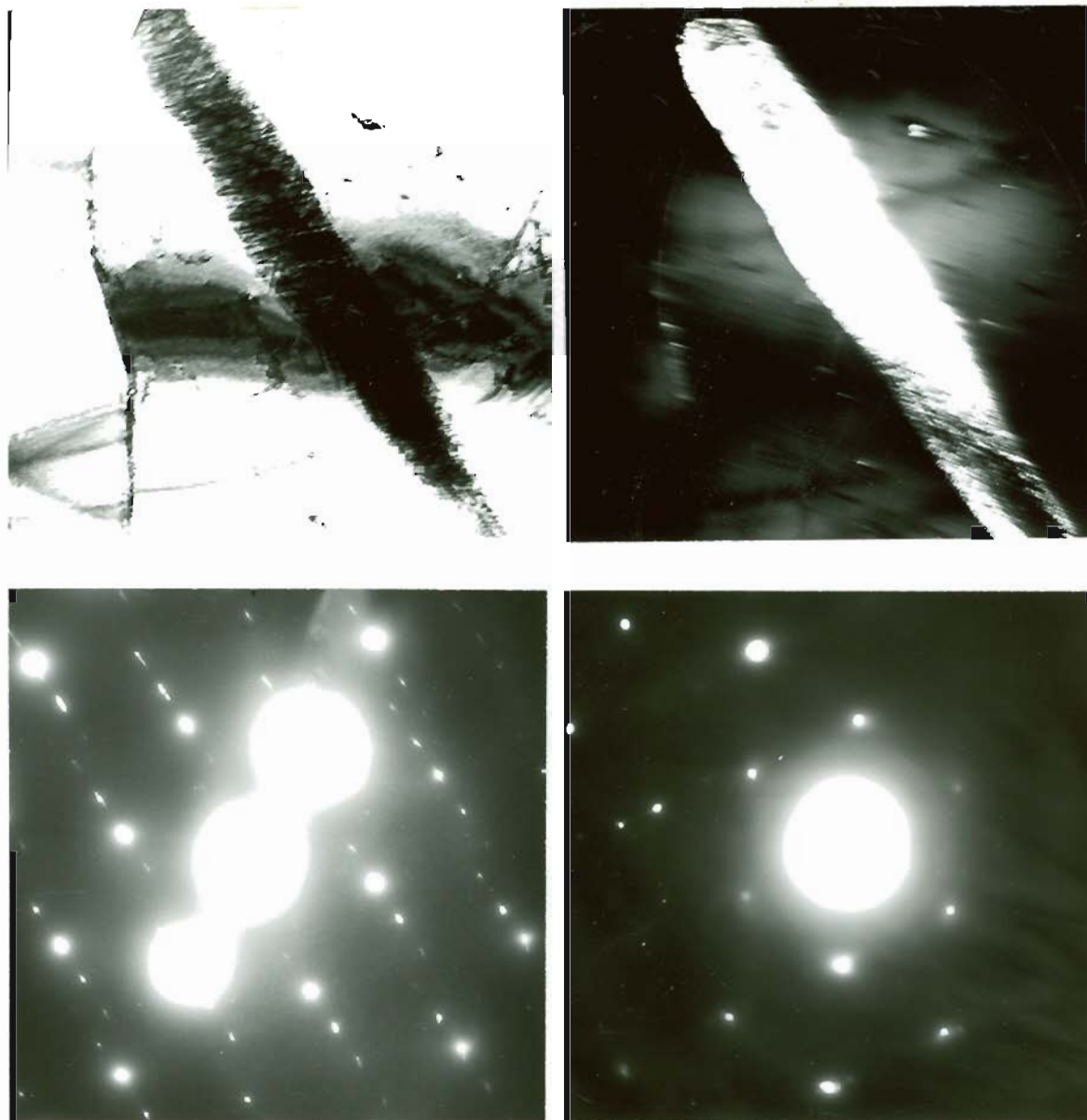


Figure 85. TRANSMISSION ELECTRON MICROGRAPHS OF LASER PROCESSED Fe-0.2%C-20%Cr ALLOY (PENETRATION DEPTH: 600 $\mu$ m, SINGLE SCAN)

- a) BF, b) DF SHOWING THE AUSTENITE,  
c) SAD PATTERN FROM THE AUSTENITE,  
d) SAD PATTERN FROM THE FERRITE

MAGNIFICATION: 18,000 $\times$ .

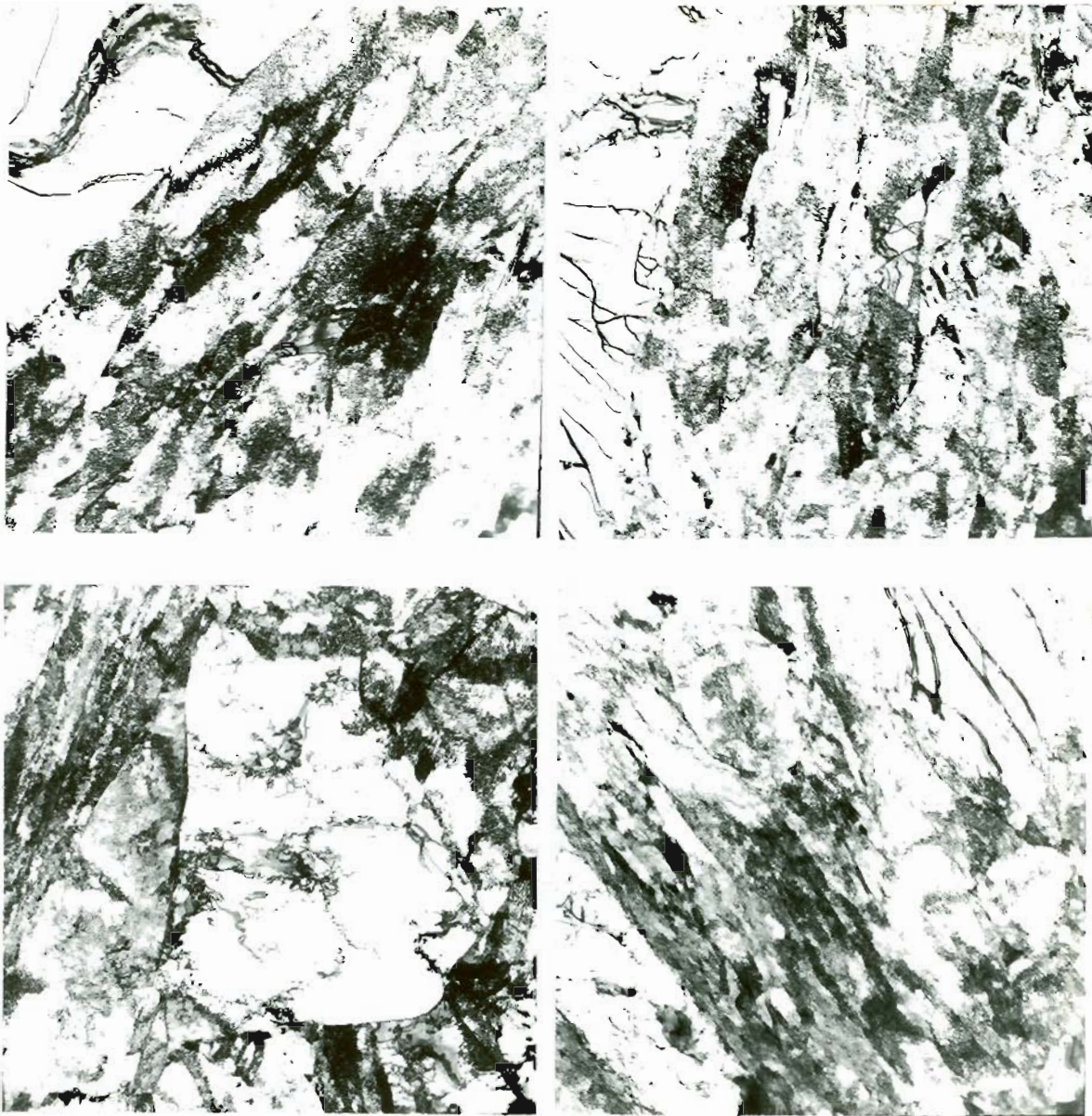


Figure 86. TRANSMISSION ELECTRON MICROGRAPHS OF LASER PROCESSED Fe-0.2%C-20%Cr ALLOY (PENETRATION DEPTH: 600 $\mu$ m, MULTIPLE SCAN). MAGNIFICATION: 18,000x.

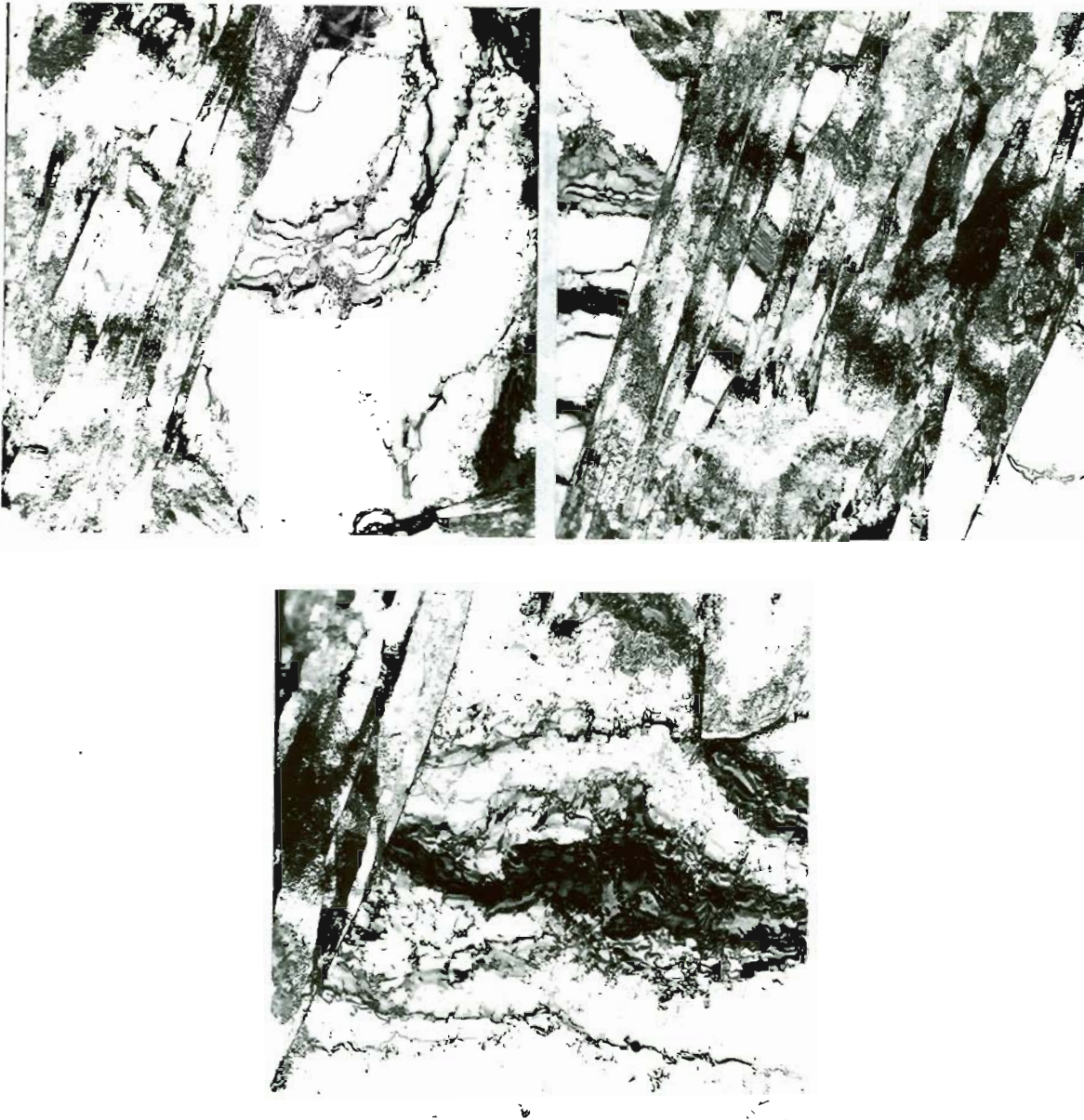


Figure 87. TRANSMISSION ELECTRON MICROGRAPHS OF LASER PROCESSED Fe-0.2%C-20%Cr ALLOY (PENETRATION DEPTH: 600 $\mu$ m, MULTIPLE SCAN). MAGNIFICATION: 18,000 $\times$ .

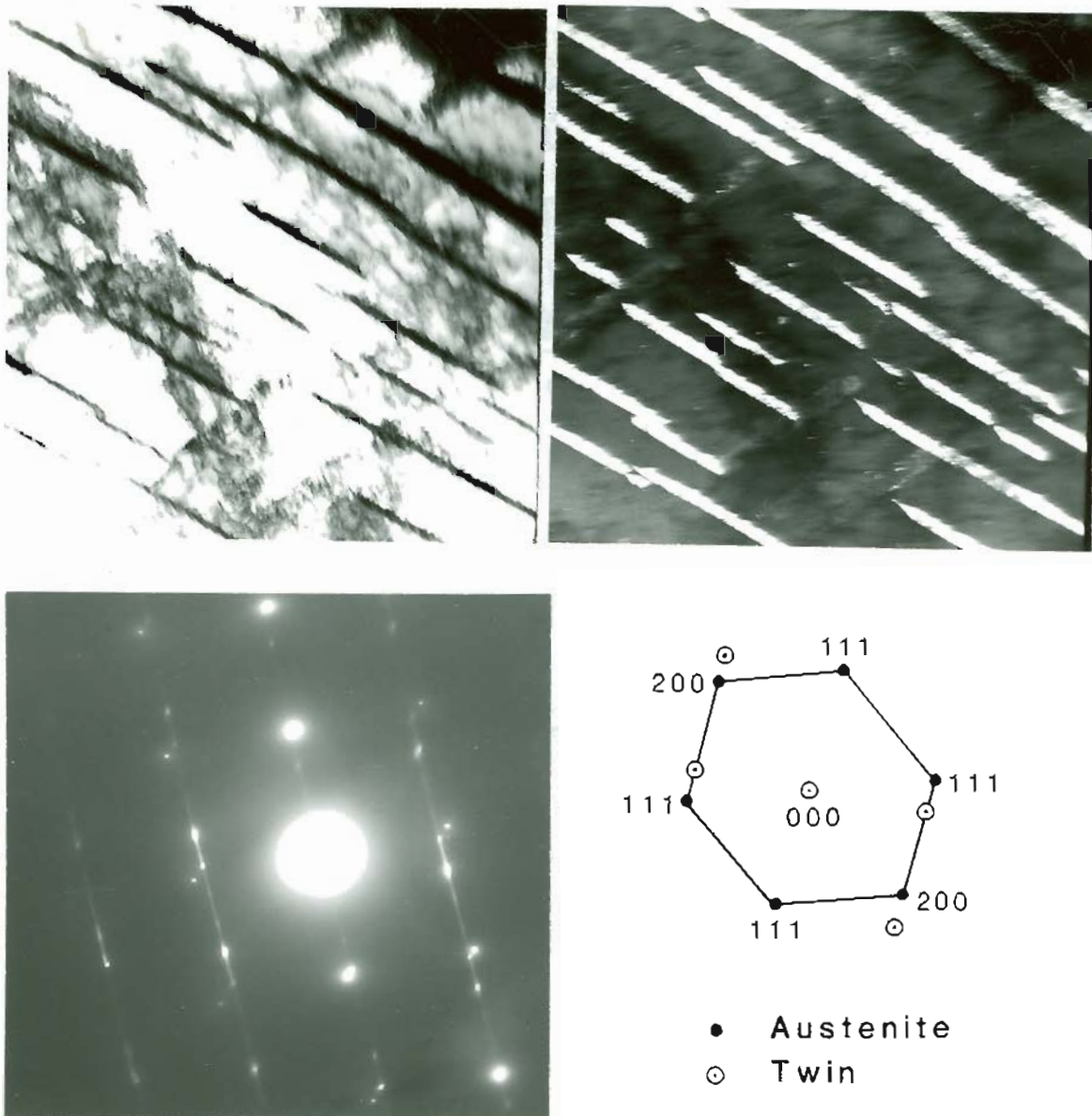


Figure 88. TRANSMISSION ELECTRON MICROGRAPHS OF LASER PROCESSED Fe-0.2%C-20%Cr ALLOY (PENETRATION DEPTH: 120 $\mu$ m, MULTIPLE SCAN)

a) BF, b) DF SHOWING THE AUSTENITIC NEEDLES,  
c) SAD PATTERN, d) ANALYSIS OF SAD

MAGNIFICATION: 18,000x.

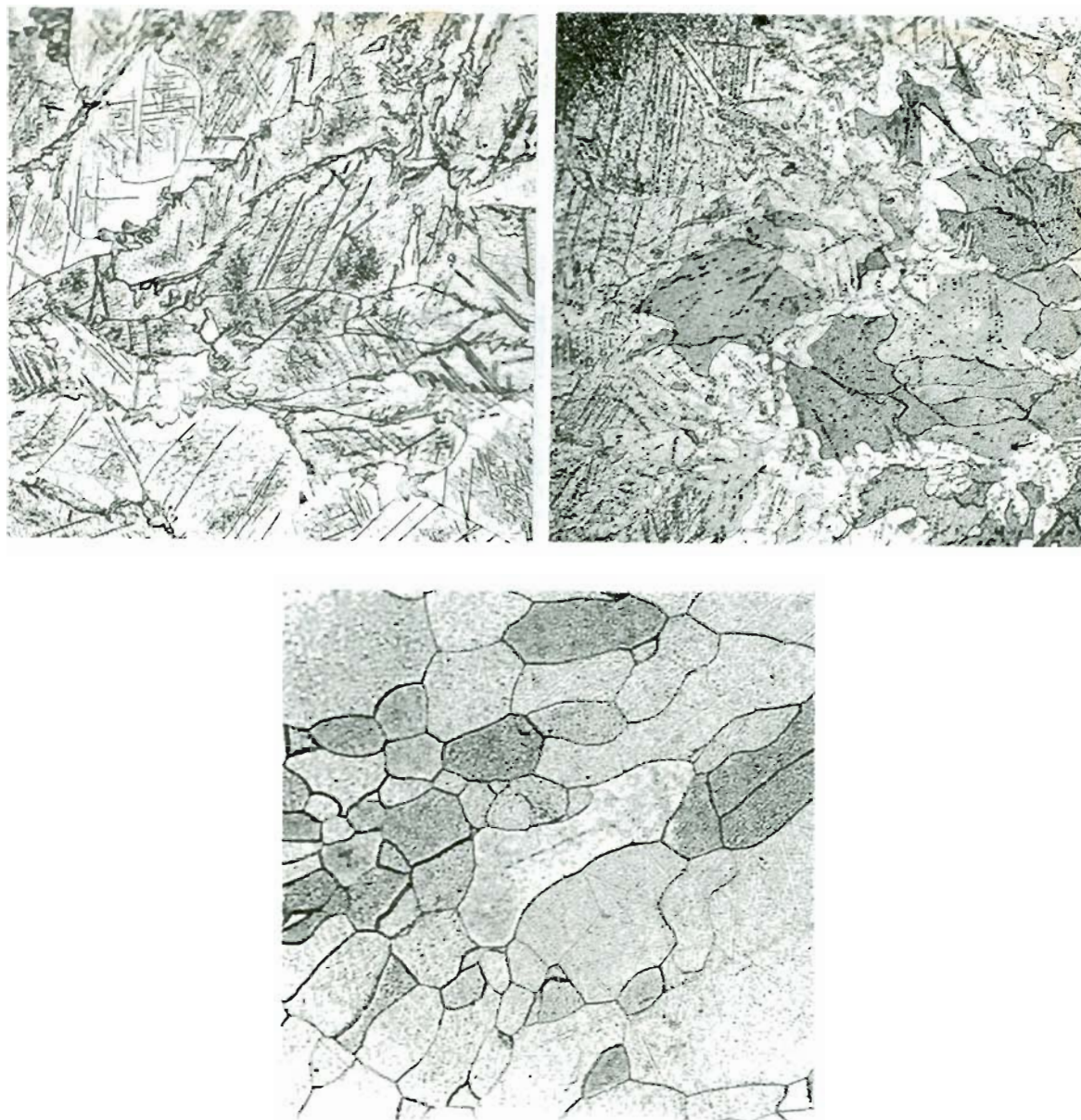


Figure 89. LIGHT MICROGRAPHS OF CONVENTIONALLY FURNACE HEAT TREATED AND WATER QUENCHED "SINGLE SCAN" Fe-0.2%C-20%Cr ALLOYS

- a) AS-LASER PROCESSED AND/OR HEAT TREATED AT 900°C (1 HR),
- b) HEAT TREATED AT 1000°C (1 HR),
- c) HEAT TREATED AT 1200°C (5 MIN)

MAGNIFICATION: 400x.

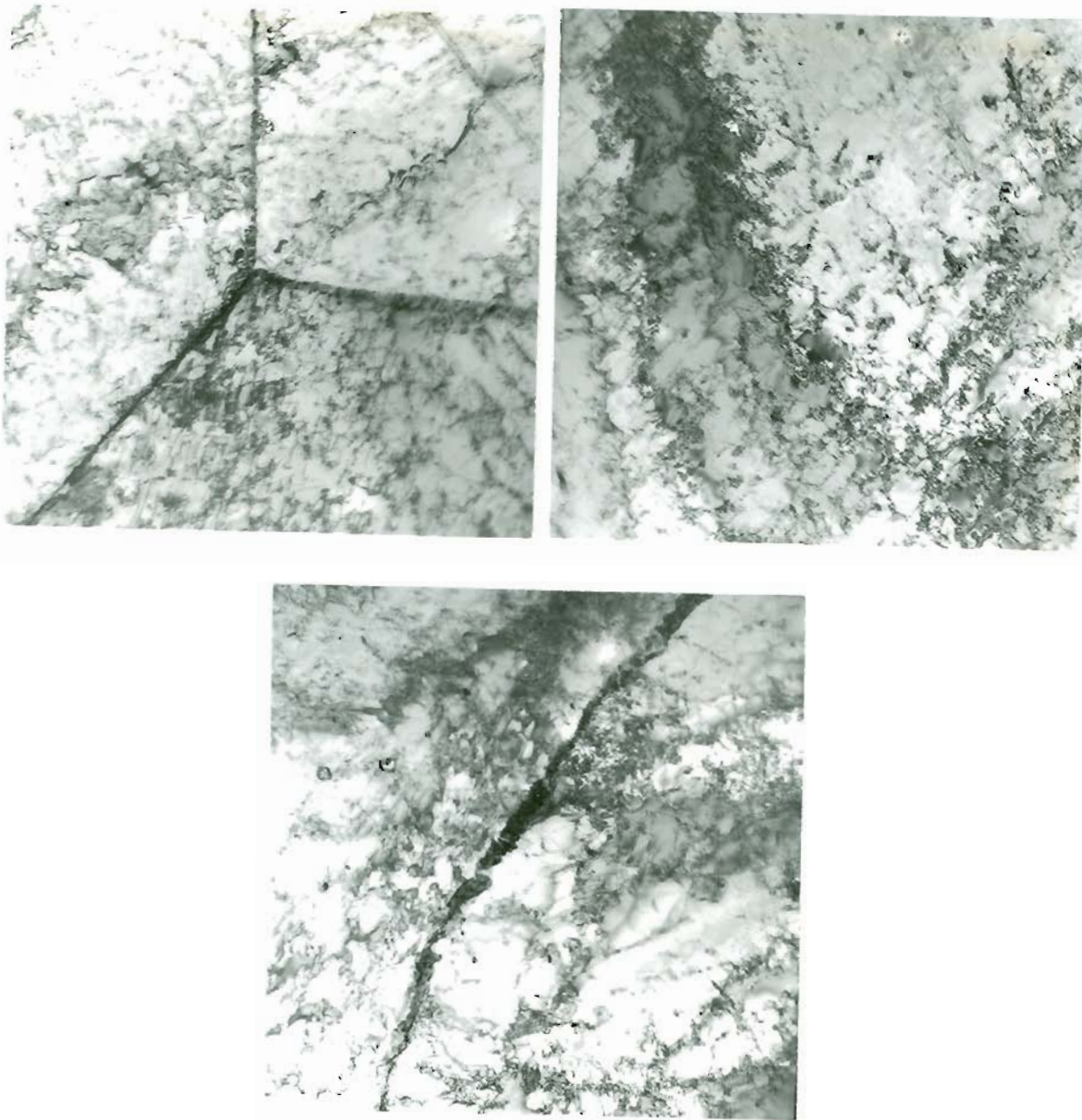


Figure 90. TRANSMISSION ELECTRON MICROGRAPHS OF LASER PROCESSED Fe-0.2%C-30%Cr ALLOY SHOWING THE FERRITIC STRUCTURES (PENETRATION DEPTH: 600 $\mu$ m). MAGNIFICATION: 18,000x.

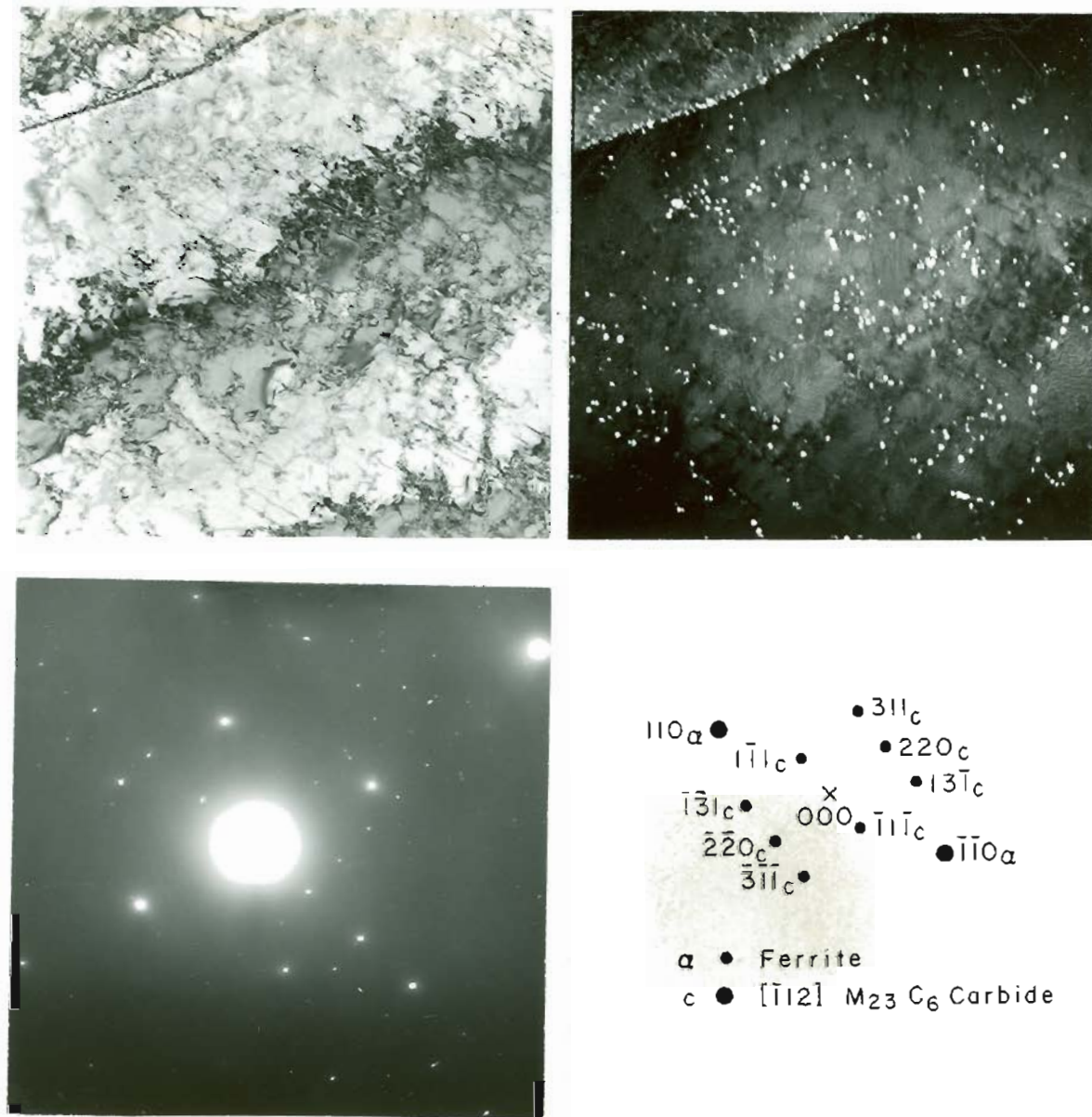


Figure 91. TRANSMISSION ELECTRON MICROGRAPHS OF LASER PROCESSED Fe-0.2%C-30%Cr ALLOY (PENETRATION DEPTH: 600 $\mu$ m)

a) BF, b) DF SHOWING  $M_{23}C_6$  CARBIDE, c) SAD PATTERN,  
d) ANALYSIS OF SAD

MAGNIFICATION: 18,000x.

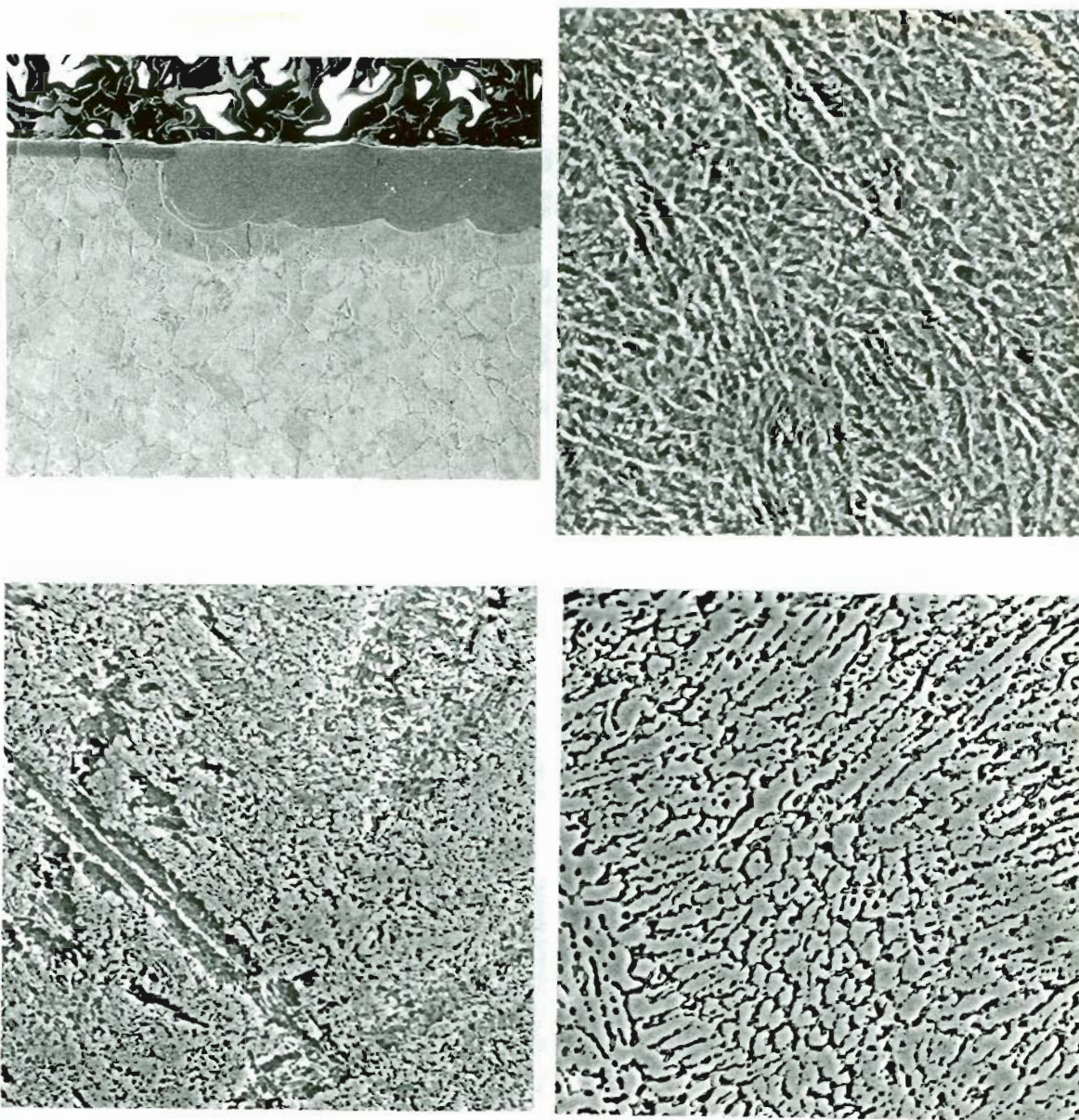


Figure 92. SCANNING ELECTRON MICROGRAPHS OF LASER PROCESSED Fe-0.5%C-Cr ALLOYS

a) A TRANSVERSE SECTION OF THE FUSION ZONE, b) 10%Cr,  
c) 20%Cr, d) 40%Cr

MAGNIFICATION: a) 50x, b),c),d) 1000x.

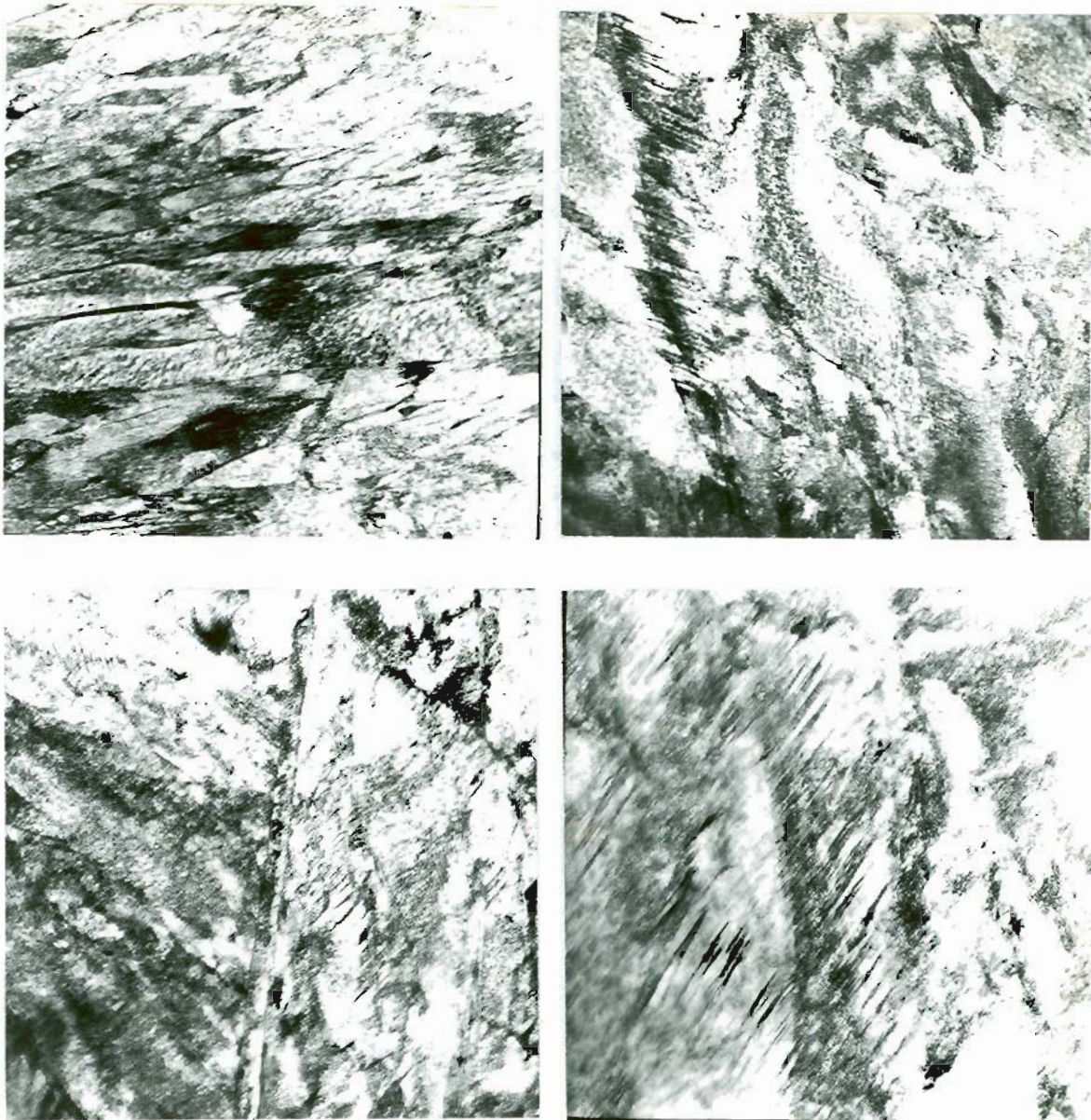


Figure 93. TRANSMISSION ELECTRON MICROGRAPHS OF LASER PROCESSED Fe-0.5%C-10%Cr ALLOY SHOWING THE LATH MARTENSITIC STRUCTURES (PENETRATION DEPTH: 220 $\mu$ m). MAGNIFICATION: 18,000x.

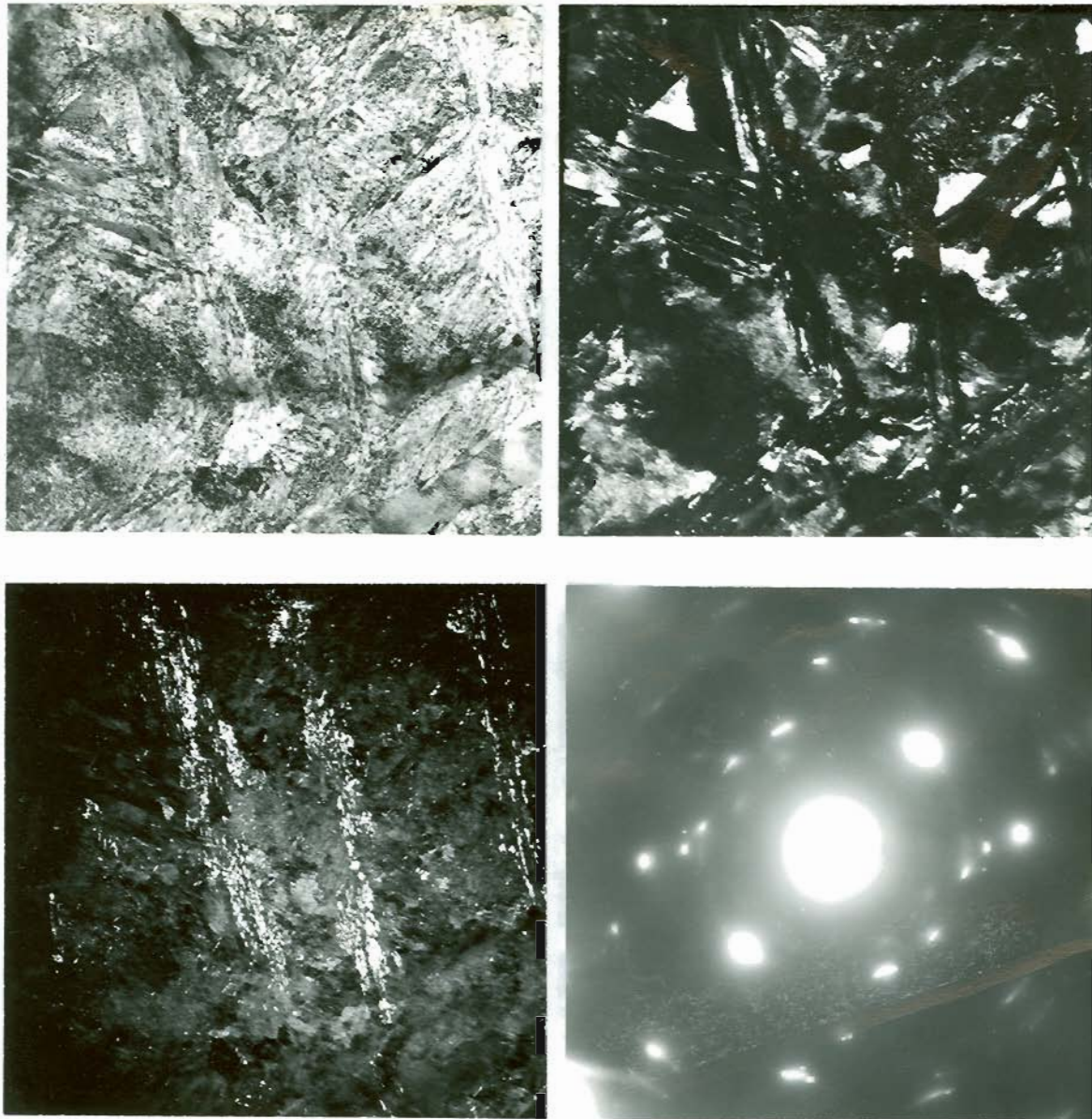


Figure 94. TRANSMISSION ELECTRON MICROGRAPHS OF LASER PROCESSED Fe-0.5%C-10%Cr ALLOY (PENETRATION DEPTH: 220 $\mu$ m)

a) BF, b) DF SHOWING RETAINED AUSTENITE,  
c) DF SHOWING M<sub>3</sub>C CARBIDE, d) SAD PATTERN

MAGNIFICATION: 18,000x.

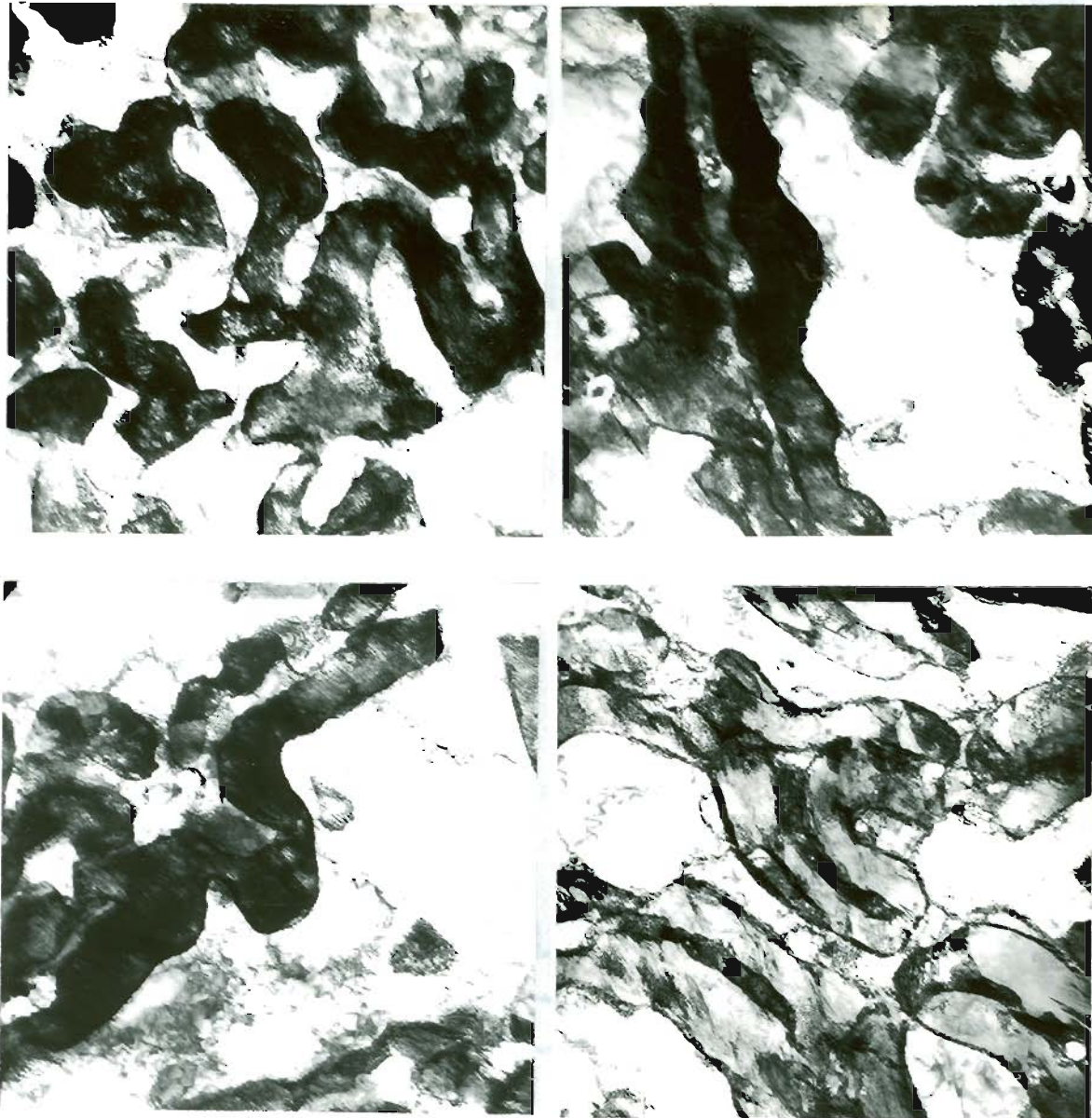


Figure 95. TRANSMISSION ELECTRON MICROGRAPHS OF LASER PROCESSED Fe-0.5C-20Cr ALLOY SHOWING THE AUSTENITE/FERRITE STRUCTURES (PENETRATION DEPTH: 210 $\mu$ m). MAGNIFICATION: 18,000 $\times$ .

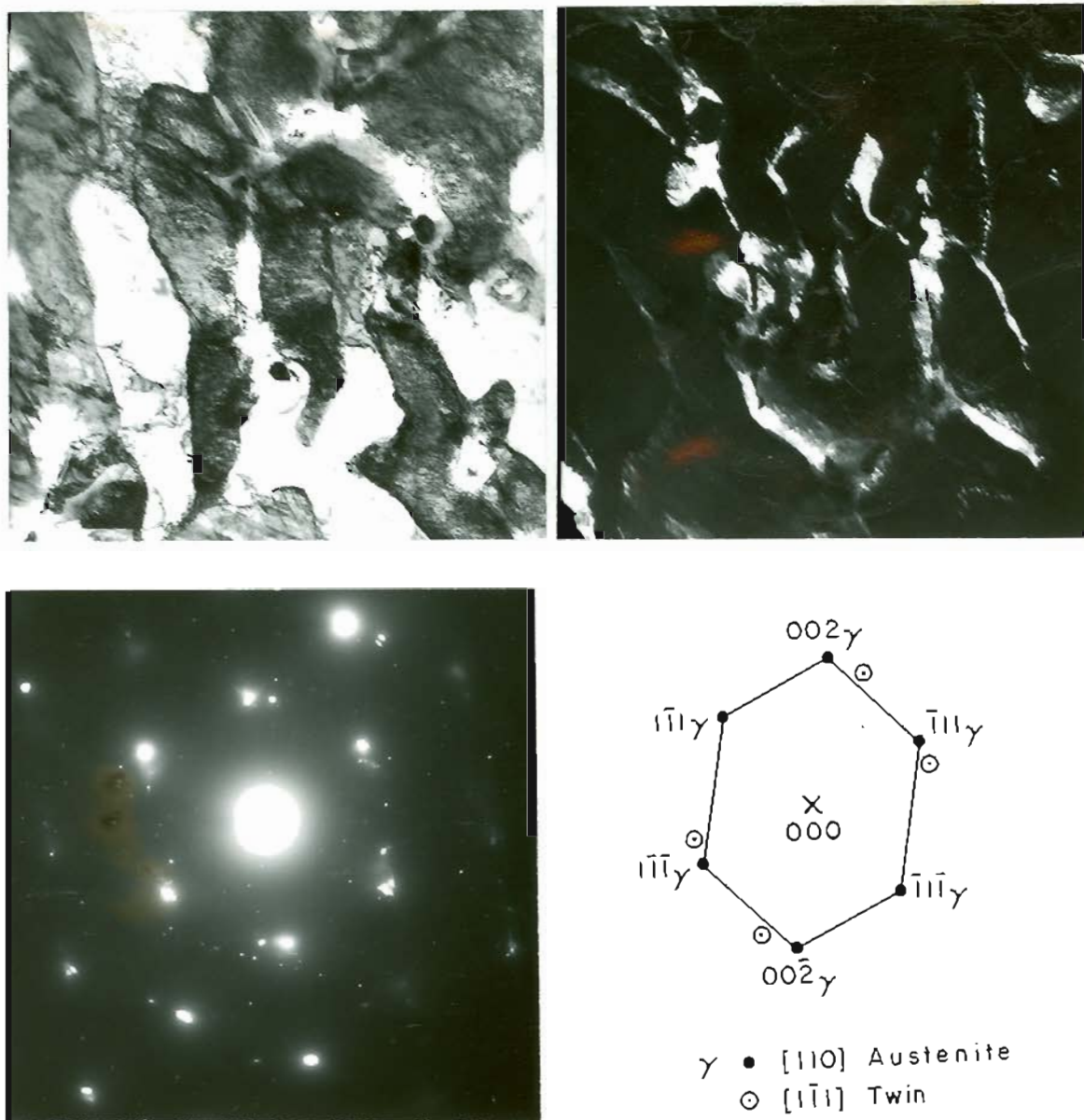


Figure 96. TRANSMISSION ELECTRON MICROGRAPHS OF LASER PROCESSED Fe-0.5%C-20%Cr ALLOY (PENETRATION DEPTH: 210 $\mu$ m)  
 a) BF, b) DF SHOWING THE AUSTENITIC POOLS,  
 c) SAD PATTERN, d) ANALYSIS OF SAD

MAGNIFICATION: 18,000x.

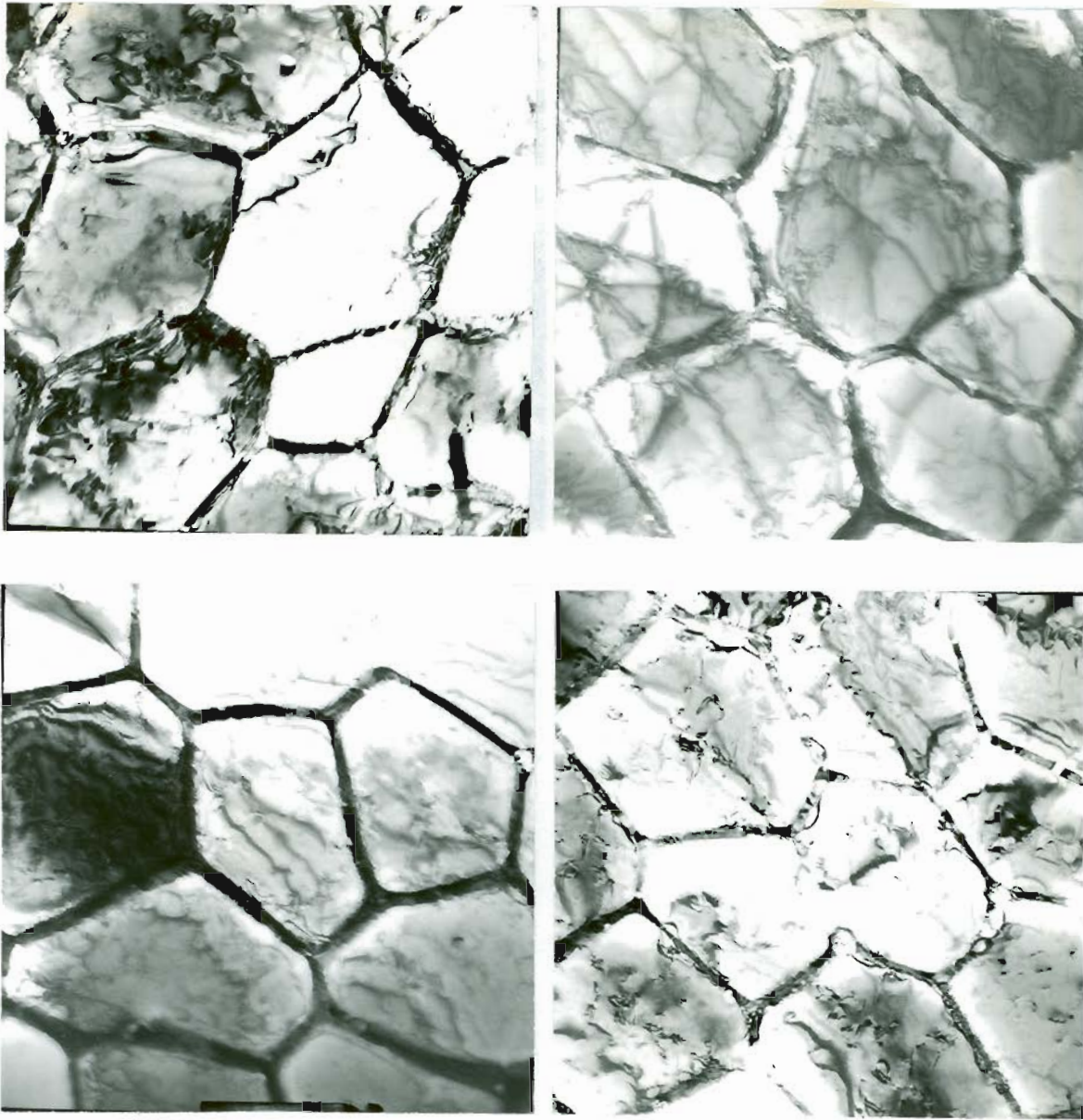


Figure 97. TRANSMISSION ELECTRON MICROGRAPHS OF LASER PROCESSED Fe-0.5%C-40%Cr ALLOY SHOWING THE FERRITIC STRUCTURES (PENETRATION DEPTH: 240 $\mu$ m). MAGNIFICATION: 18,000x.

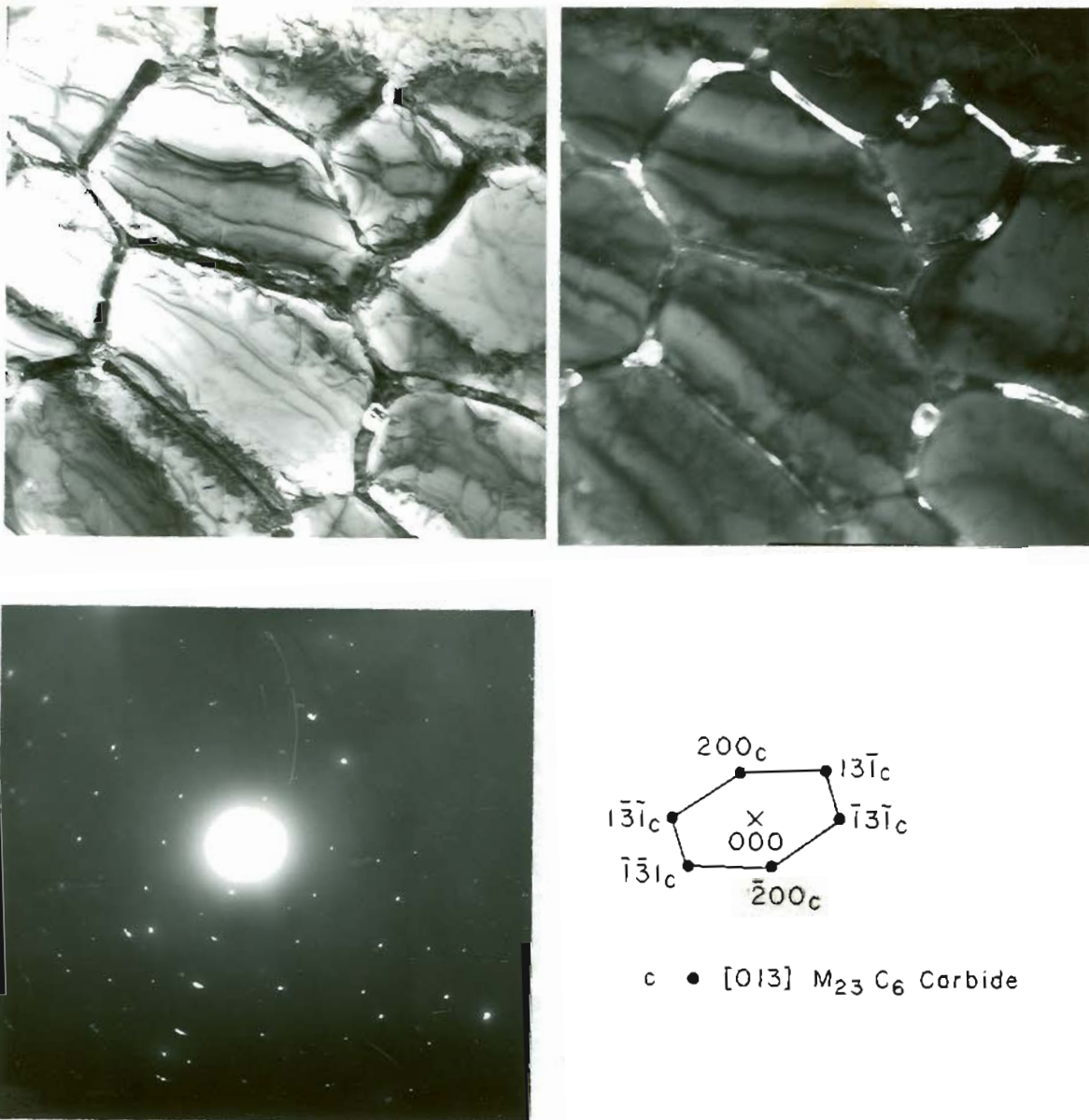


Figure 98. TRANSMISSION ELECTRON MICROGRAPHS OF LASER PROCESSED Fe-0.5%C-40%Cr ALLOY (PENETRATION DEPTH: 240 $\mu$ m)

a) BF, b) DF SHOWING  $M_{23}C_6$  CARBIDE,  
c) SAD PATTERN, d) ANALYSIS OF SAD

MAGNIFICATION: 18,000x.

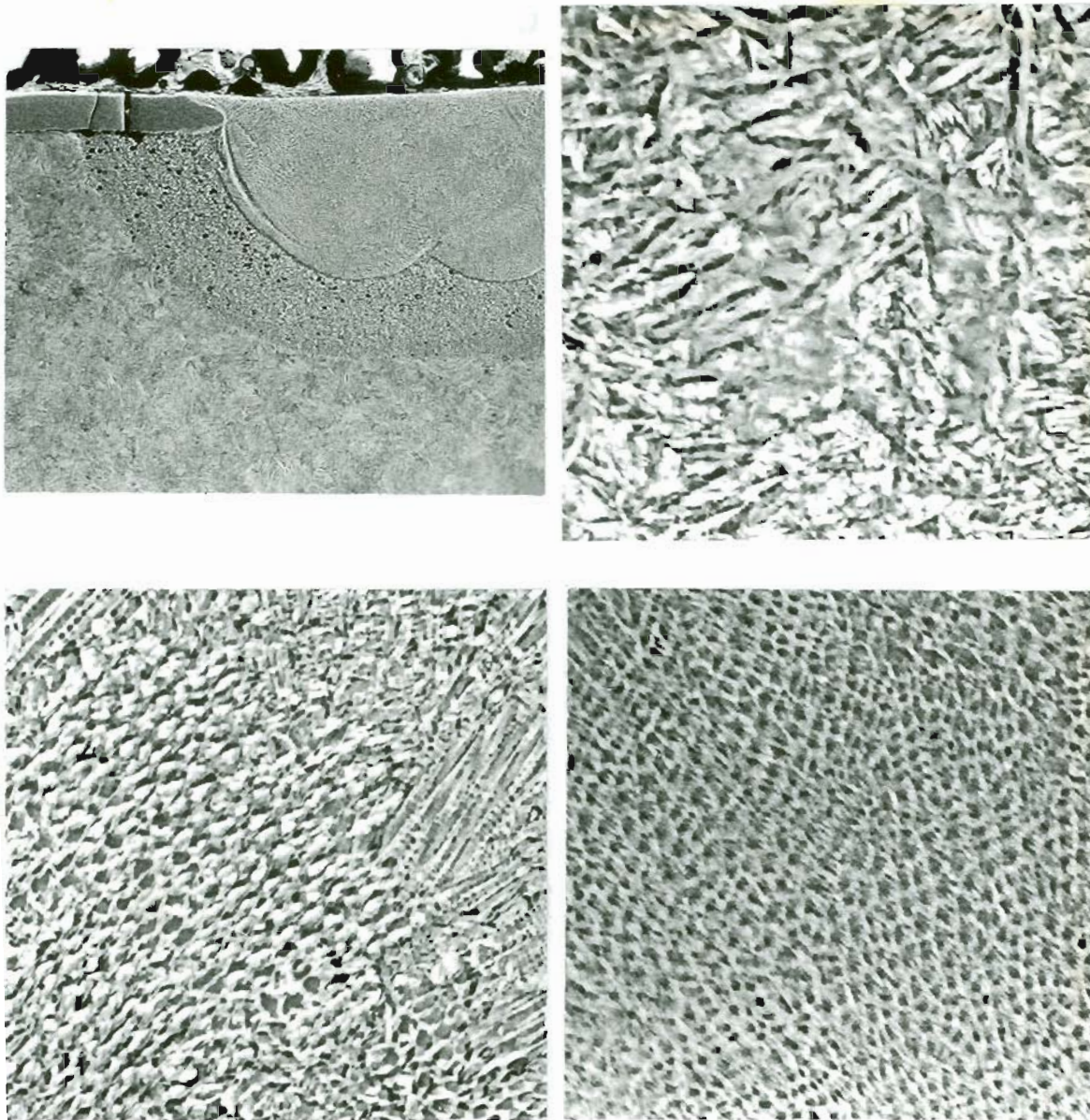


Figure 99. SCANNING ELECTRON MICROGRAPHS OF LASER PROCESSED Fe-1.0%Cr ALLOYS

a) A TRANSVERSE SECTION,    b) 10%Cr,    c) 20%Cr,  
d) 40%Cr

MAGNIFICATION:    a) 100x,    b),c),d) 1000x.

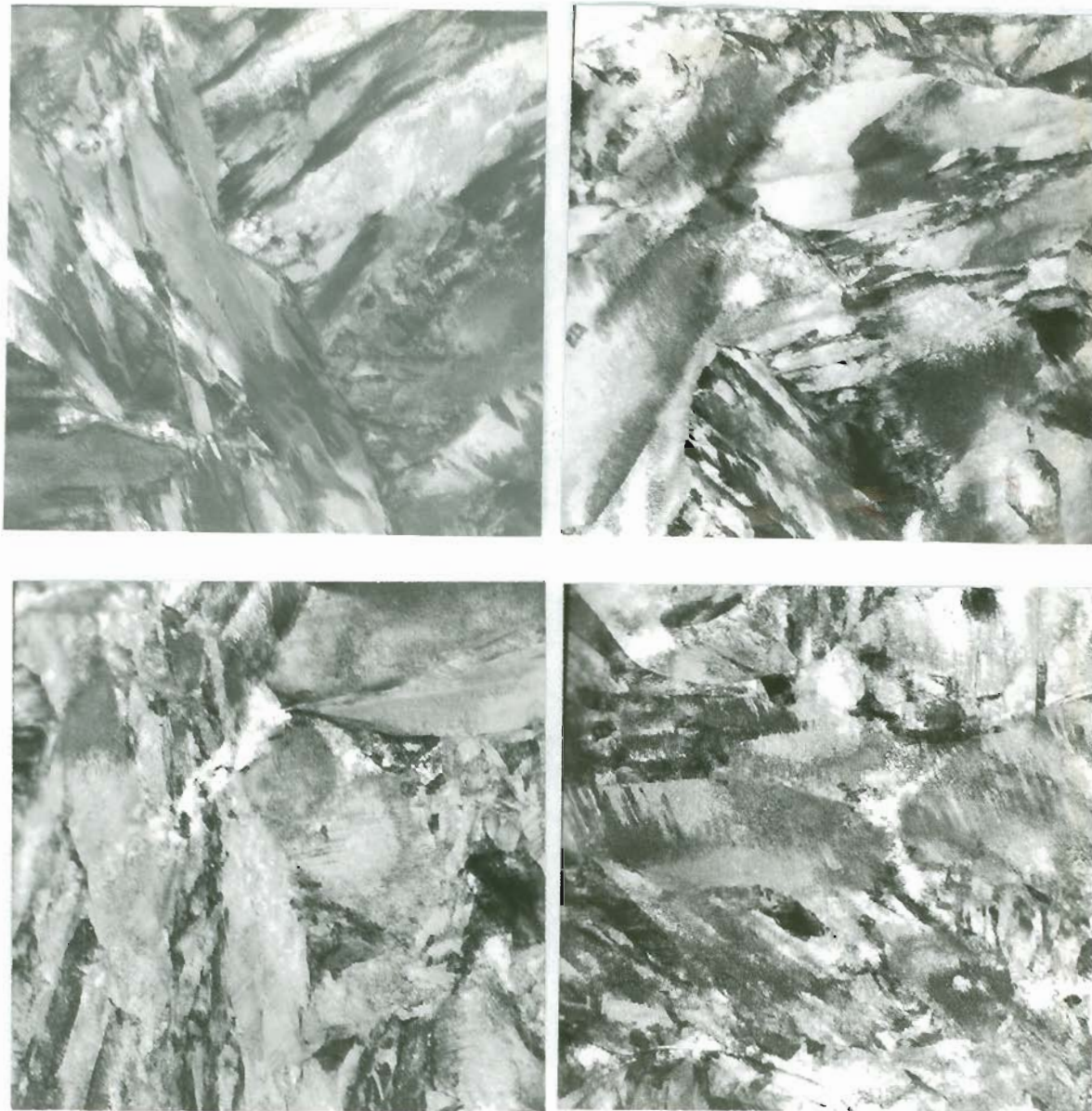


Figure 100. TRANSMISSION ELECTRON MICROGRAPHS OF LASER PROCESSED Fe-1.0%C-10%Cr ALLOY SHOWING THE PLATE MARTENSITIC STRUCTURES (PENETRATION DEPTH: 210 $\mu$ m). MAGNIFICATION: 18,000 $\times$ .

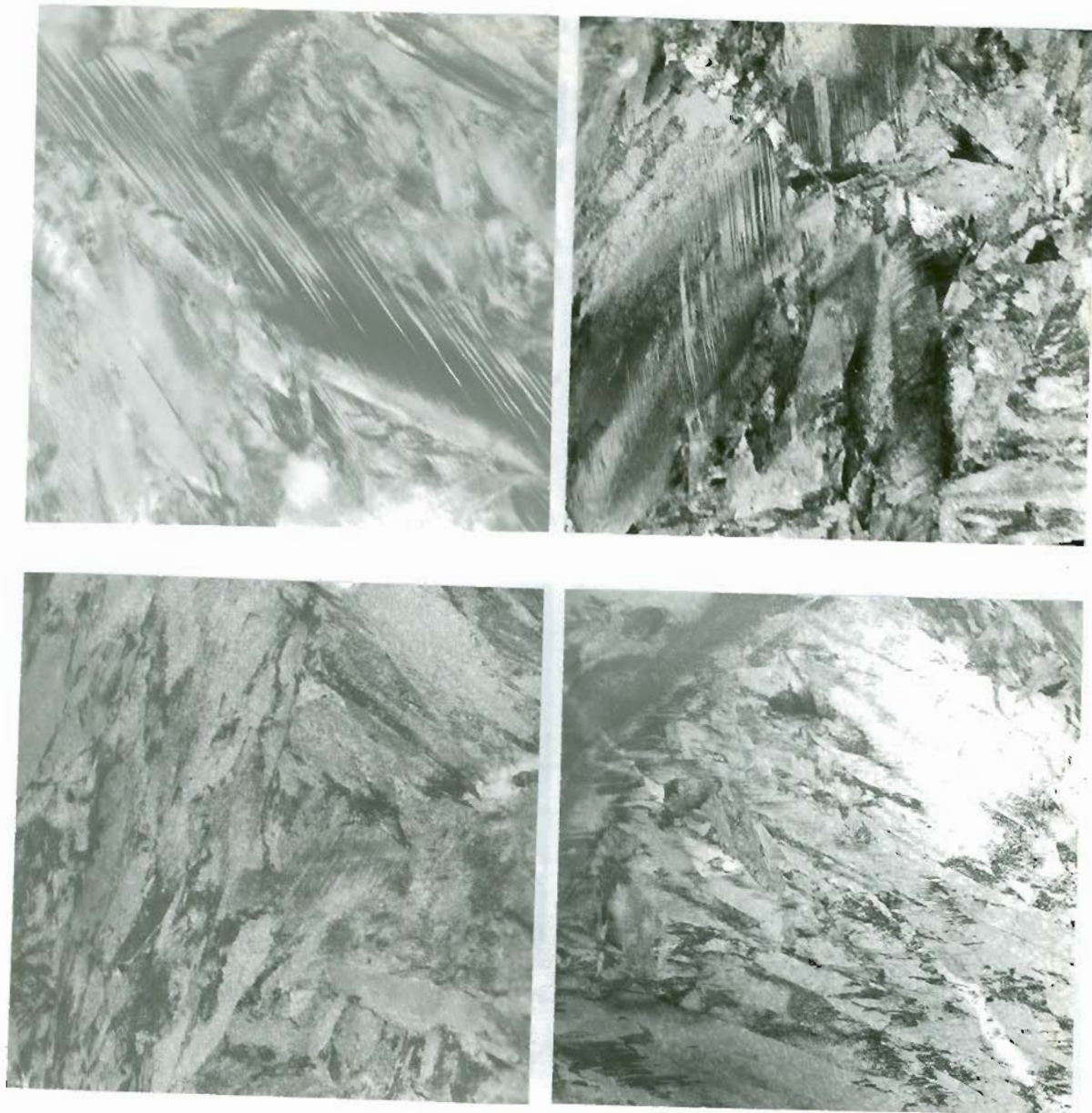


Figure 101. TRANSMISSION ELECTRON MICROGRAPHS OF LASER PROCESSED Fe-1.0%Cr-10%Cr ALLOY SHOWING THE TWINNED PLATE MARTENSITES [a),b)] AND DISLOCATED LATH MARTENSITES [c),d)], (PENETRATION DEPTH: 210 $\mu$ m). MAGNIFICATION: 18,000x.

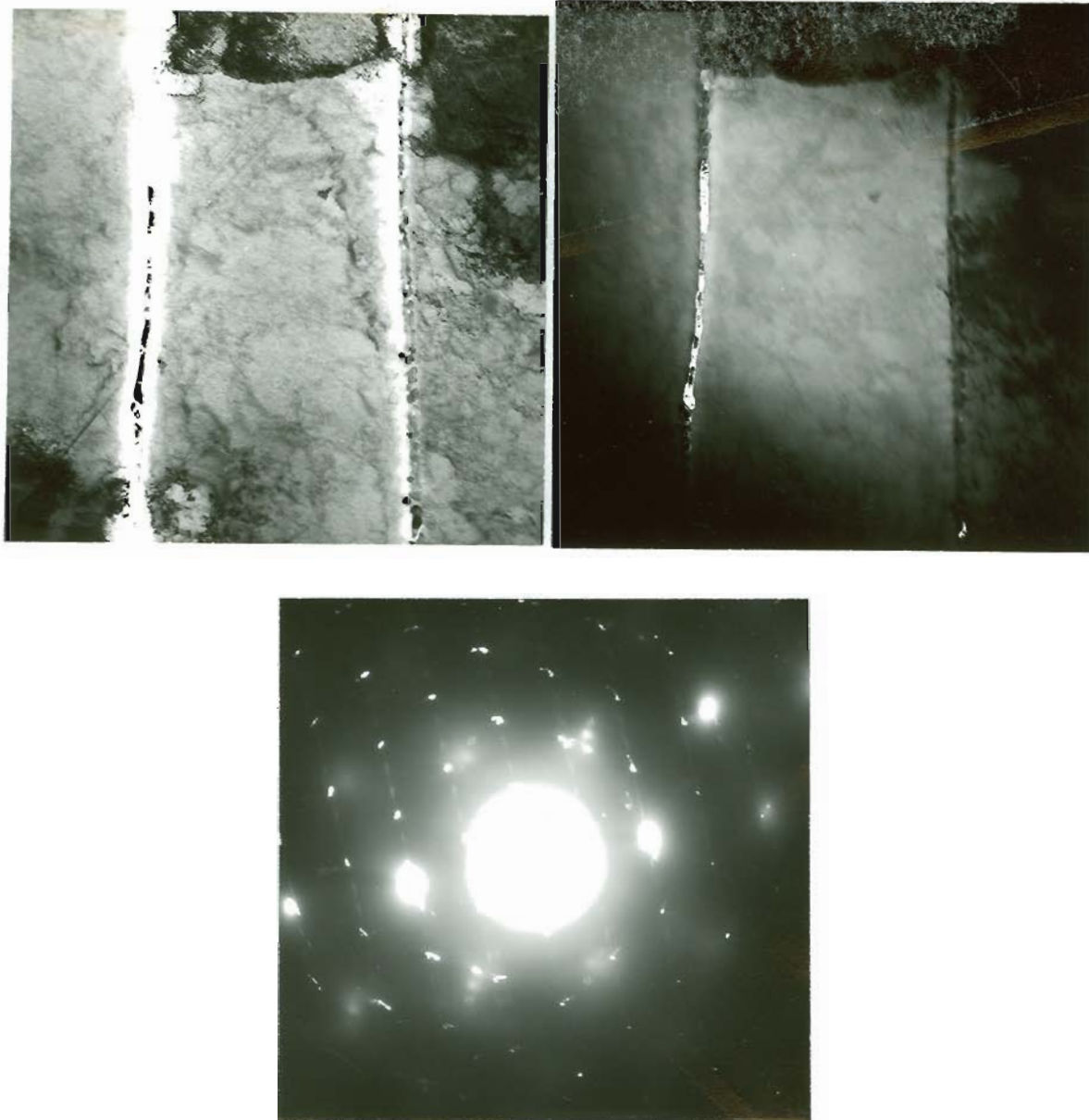


Figure 103. TRANSMISSION ELECTRON MICROGRAPHS OF LASER PROCESSED Fe-1.0%C-20%Cr ALLOY (PENETRATION DEPTH: 240 $\mu$ m)

a) BF, b) DF SHOWING  $M_{23}C_6$  CARBIDE,  
c) SAD PATTERN

MAGNIFICATION: 18,000x.

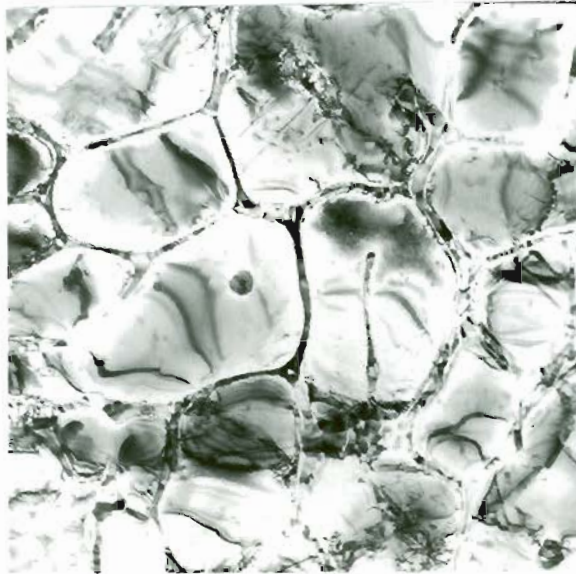
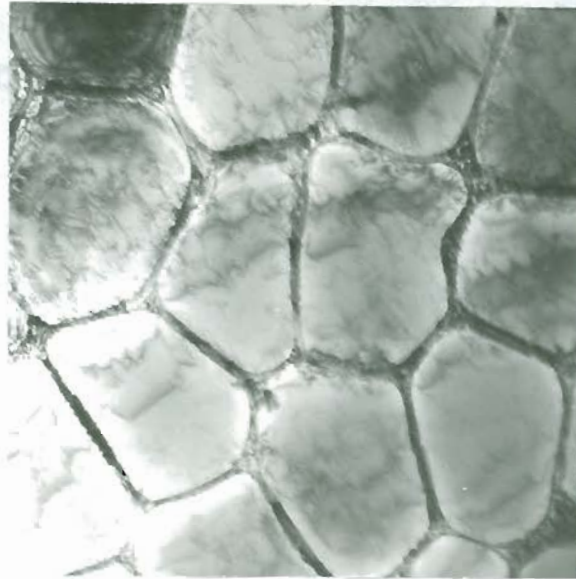


Figure 104. TRANSMISSION ELECTRON MICROGRAPHS OF LASER PROCESSED Fe-1.0%C-40%Cr ALLOY SHOWING THE FERRITIC STRUCTURES (PENETRATION DEPTH: 220 $\mu$ m). MAGNIFICATION: 18,000x.

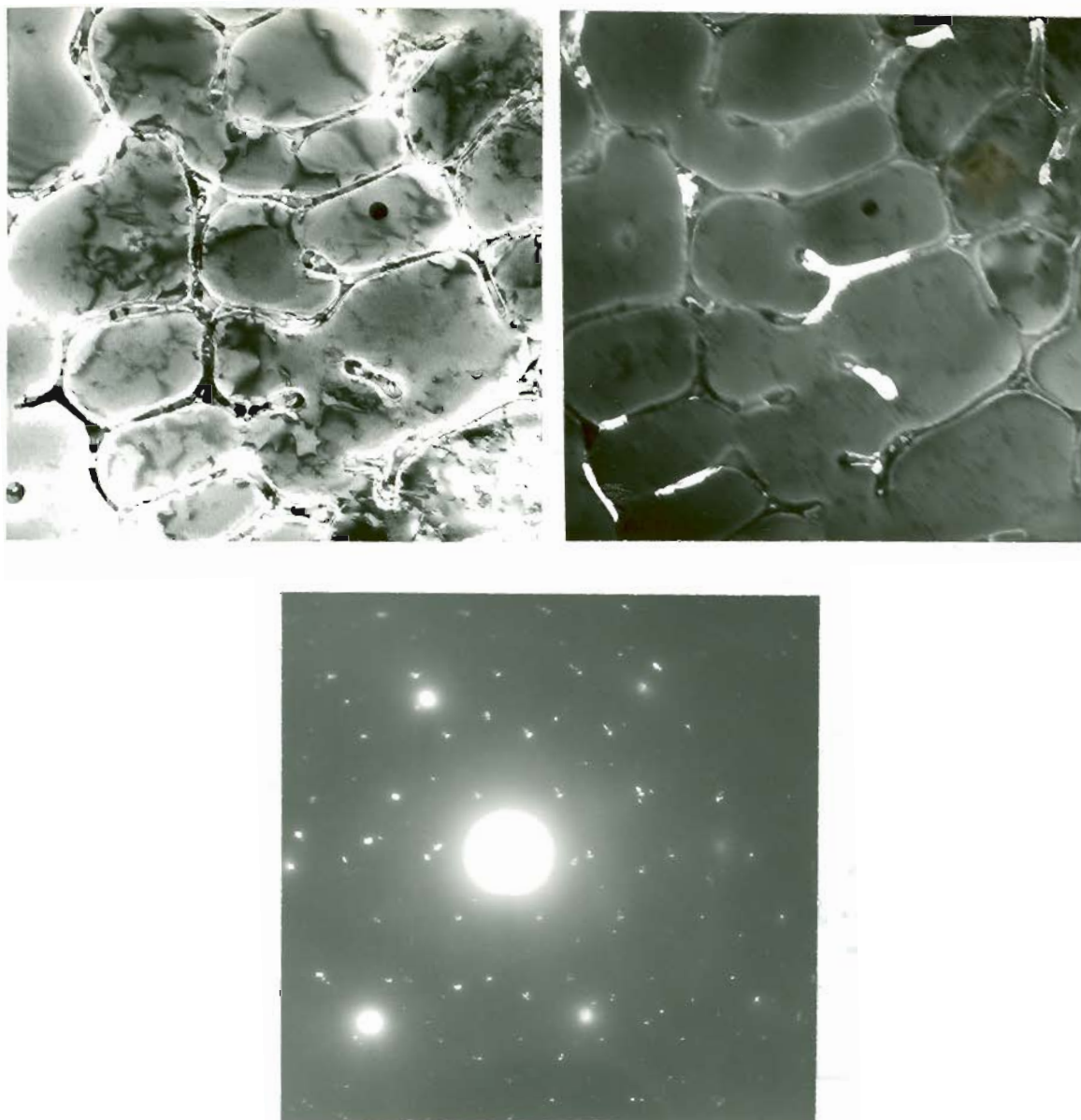


Figure 105. TRANSMISSION ELECTRON MICROGRAPHS OF LASER PROCESSED Fe-1.0%C-40%Cr ALLOY (PENETRATION DEPTH: 220 $\mu$ m)

a) BF, b) DF SHOWING M<sub>23</sub>C<sub>6</sub> CARBIDE,  
c) SAD PATTERN

MAGNIFICATION: 18,000 $\times$ .

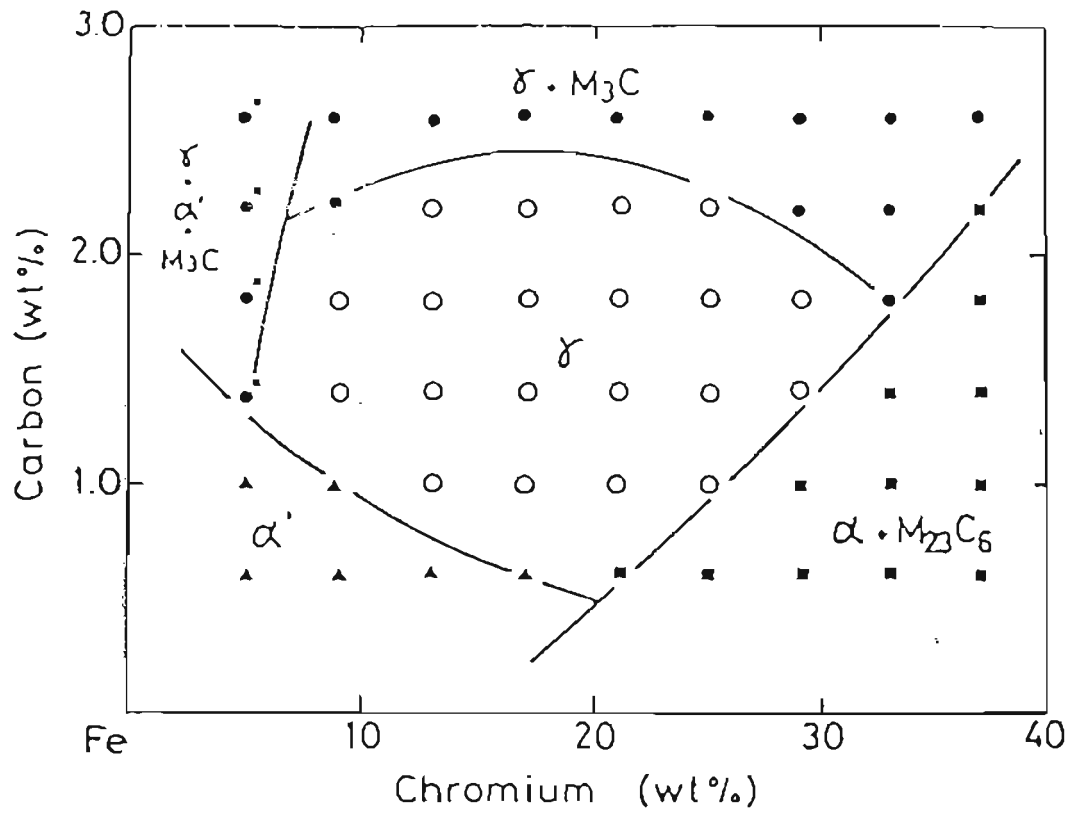


Figure 106. A NON-EQUILIBRIUM DIAGRAM FOR "SPLAT-COOLED" Fe-C-Cr ALLOYS [AFTER INOUE ET AL (100)].

## VITA

The author was born in Kalipatty, a small village in southern India, on October 2, 1953. From 1962 until 1968, he attended Government High School specializing in general engineering courses. He was then educated at Madras University, receiving a Bachelor's degree in Chemistry with distinction in 1972. Then he joined Indian Institute of Science, Bangalore, and received a Bachelor's degree in Metallurgical Engineering with distinction in 1975, and a Master's degree in Mechanical Engineering with distinction in 1977. He also obtained the first rank in Master's degree program. Then he worked as a Development Engineer at India Pistons Ltd., a leading automobile industry in India, from 1977 to 1978. He left his job to pursue higher studies in Materials Science and Engineering at the Oregon Graduate Center, where he completed the requirements for his Ph.D. in March 1982.

The author has accepted a position as Assistant Professor in the Department of Mechanical Engineering, Iowa State University, starting in August, 1982.